DESIGN AND USE OF SURFACE MODIFIERS AS TOOLS FOR UNDERSTANDING AND CONTROLLING INTERFACES IN ORGANIC ELECTRONICS

A Thesis
Presented to
The Academic Faculty

by

O'Neil L. Smith

In Partial Fulfillment
of the Requirements for the Degree
Doctor of Philosophy in the
School of Chemistry and Biochemistry

Georgia Institute of Technology
May 2014

DESIGN AND USE OF SURFACE MODIFIERS AS TOOLS FOR UNDERSTANDING AND CONTROLLING INTERFACES IN ORGANIC ELECTRONICS

Approved by:

Dr. Seth R. Marder, Advisor
School of Chemistry and Biochemistry
Georgia Institute of Technology

Dr. Joseph W. Perry, Co-Advisor
School of Chemistry and Biochemistry
Georgia Institute of Technology

Dr. Andrew Lyon
School of Chemistry and Biochemistry
Georgia Institute of Technology

Dr. Kenneth Sandhage
School of Material Science and Engineering
Georgia Institute of Technology

Dr. Vladimir Tsukruk
School of Material Science and Engineering
Georgia Institute of Technology

Date Approved: March, 12, 2014

To my parents and my wife

ACKNOWLEDGEMENTS

I would like to extend my gratitude to everyone who played an instrumental role in supporting me throughout my Ph.D. studies at Georgia Tech. First I would like to thank my advisor, Dr Marder, for accepting me in his group and for demonstrating the patience necessary for me to climb the learning curve as a scientist. I must say thank you to my co-advisor, Dr. Perry, for integrating me into his group and providing me with scientific tools and mentorship that was required for me to develop my scientific skills. I would like to acknowledge and thank Dr Sergio Paniagua, Anthony Giordano, Dr. Mohanalingam Kathaperumal , Yunsang Kim, Dr. Stephen Barlow, Dr Tim Parker, and Dr Cristina Rumi for their support and the many constructive scientific discussions. Thanks to my mentees, Emily Li, Katherine Henry and Phillip Nwachokor who were always enthusiastic about learning science. I must say thank you to Dr Lawrence Bottomley, Megan Mann, Dr Erin Ratcliff, Dr Scott Saavedra and Saehan Park for teaching me the fundamentals of electrochemistry. Thanks also to Dr Pemberton, and Zachary Lachance for their assistance with IRRAS measurements. I would like to also acknowledge Dr Kippelen and his group for allowing me to use their instrumentation when needed. I must also acknowledge the Center for Organic Photonics and Electronics (COPE) for their fellowship award. I would like to thank all the members of both the Marder and Perry groups and for all their assistance over the years. I would like to thank the Smith family and Dr Dixon who were very supportive of me all the way throughout my Ph.D. studies.

Finally, I would like to thank my wife, Allia, for all her support and for being my anchor throughout the process.

TABLE OF CONTENTS

LIST OF TABLES

LIST OF FIGURES

LIST OF SYMBOLS AND ABBREVIATIONS

AFM	atomic force microscopy
BD	bond dipole
BT	barium titanate
CA	contact angle
CB	conduction band
CV	cyclic voltammetry
CSWV	cyclic square wave voltammetry
DFT	density functional theory
DSC	detergent/solvent-cleaned
ETL	electron transport layer
HTL	hole transport layer
IMFP	inelastic mean free path
IRRAS	infrared-reflection absorption spectroscopy
ITO	indium tin oxide
NMR	nuclear magnetic resonance spectroscopy
OPV	organic photovoltaic
PA	phosphonic acid
SAM	self-assembled monolayer
SEE	secondary electron edge
SEM	scanning electron microscopy
TCO	transparent conductive oxide
TGA	thermogravimetric analysis

UPS	ultraviolet photoelectron spectroscopy
VB	valence band
VBM	valence band maximum
WF	work function
XPS	X-ray photoelectron spectroscopy

SUMMARY

This thesis focuses on the use of surface modifiers as tools for probing and/or controlling interfaces. Surface modification of transparent conducting oxides (TCOs) with organic and organometallic modifiers can be used as a tool for mediating interfacial energetics as well as probing the kinetics of charge-transfer at the metal oxide/organic interface. The synthetic tunability of these modifiers allows us to design molecules based on various parameters, which include the nature of the binding, spacer, and terminal groups. Based on this framework, several modifiers were synthesized and used to investigate surface energy tuning as well as charge injection kinetics as a function of molecular structure. More specifically, we use XPS/UPS to examine the evolution of the chemical structure and frontier orbital levels of the TCO/organic interface as a function of the chosen surface modifier. In addition, we investigate the impact that various molecular binding groups have on mediating the kinetics of charge-transfer.

In the last section of this body of work we examine the development of dielectric nanocomposite films for capacitor applications. More specifically, we examine the use of phosphonic acid modifiers to functionalize barium titanate nanoparticles in order to provide miscibility with a suitable polymer host. The effect of various modifiers on the dielectric properties not nanocomposite thin films were examined.

CHAPTER 1 INTRODUCTION

1.1 Surfaces and interfaces

Surfaces and interfaces (i.e. the boundary between different media) are of key scientific interest for many technological processes; thereby making efforts to understand their chemistry and physics of critical importance. In biology, for example, the surface tension of water allows for the arrangement of lipids into membranes that are important for functions such as compartmentalization, cellular regulation and a myriad of other processes that are important for life.[1, 2] Heterogeneous catalysis, which focuses on chemistry at surfaces, is another area that has garnered a lot of attention. Here, efforts are geared at developing a thorough molecular-level understanding of the chemistry that occurs at catalytically active surface sites and their material dependence.[3-5] Gaining a proper understanding of these effects is not only of academic interest but will also help in the design of better and/or less expensive catalysts for a significant number of industrial processes. The development of antifouling protective coatings is yet another area of surface science where research is being conducted in an effort to safeguard against corrosion related failure of structures such as bridges, buildings, aircraft and automobiles.[6, 7] Solutions to the formidable challenges faced in this area require an understanding of surface structure and chemical composition such that appropriate antifouling measures can be taken. Understanding and controlling the fundamental mechanisms of heat transfer across boundaries is an integral step in solving many of the scientific challenges in areas of thermoelectrics,[8] thermal interface materials,[9-11] and

heat sinks.[12, 13] In electrochemistry the processes occurring at the electrode-electrolyte interface are monitored in order to provide insight into numerous redox phenomena.[14, 15] Similarly, in organic electronic applications, the interface between the metal or metal oxide electrode and the adjacent organic layer plays an essential role in determining how effectively charges are injected and/or collected and, as a result, affects overall performance of the device.[16-18] Therefore, being able to control these interfaces is important for the development of organic electronic devices. With today's growing interest in nanoscale technologies it should now be clear that there is significant academic, technological and economical imperative for understanding and controlling surfaces and interfaces owing to both their ubiquitous nature as well as the increasingly dominant role that they continue to play in device architectures.

The abrupt termination of the solid structure at the surface confers different chemical and physical properties on the surface relative to that associated with the bulk of the material.[19] The under-coordinated atoms at the surface are often geometrically displaced (surface reconstruction) and experience an entirely different chemical environment relative to those in the bulk.[19, 20] Consequently, the electronic structure and, by extension, chemical, physical and electronic properties at the surface generally differ from the rest of the material.

In this body of work we are primarily interested in understanding, probing and controlling the metal oxide-organic interfaces often encountered in organic electronic devices, specifically organic photovoltaic (OPVs) and dielectric nanocomposite films. This chapter is meant to provide introductory and background information that will aid in understanding the subsequent chapters. It begins by providing a brief overview of organic

electronics with an emphasis on the significance of the metal oxide-organic hybrid interfaces often encountered in the two previously mentioned device platforms. Next a general description of the electronic structure of metal oxides is presented before honing in on the structure of indium tin oxide and barium titanate, which are two prominently utilized oxides in the field of OPVs and nanocomposite dielectrics, respectively. The design and use of organic monolayers to control the chemical, physical and electronic properties of metal oxide surfaces will then be introduced. Emphasis will be placed on how organic small molecules can be used to modulate work function, wettability and charge transfer processes. This will allow us to transition into the use of electroactive monolayer to probe the kinetics of electron transfer at metal oxide-organic interfaces.

1.2 A brief introduction to organic electronics

Organic electronics is the fields of science and technology that focuses on the integration and use of carbon-based materials in the development of devices.[21, 22] The driving force behind the development of organic-based devices is rooted in the potential to produce light-weight, flexible devices.[21, 23, 24] Additionally, the development of organic electronics could potentially lead to a significant reduction in production cost as expensive lithography techniques, often used with traditional semiconductor technology, can now be replaced with cheaper processing techniques such as spin coating, ink-jet printing or roll-to-roll production. There is also great interest in having malleable materials that are capable of being molded into desired shapes and undergo rigorous deformation while preserving their electrical and optical properties for applications such as integrated circuits,[25-28] pressure sensors[25, 29] and bioelectronics.[30]

Unlike conventional silicon technology, organic materials offer a high degree of synthetic flexibility, which allows for systematic tuning of their optical and electronic properties. In organic semiconductors both these properties are intrinsically linked to the ionization potential (the minimum amount of energy required to remove an electron; IP) and the electron affinity (the energy required to add an electron to a neutral molecule or atom; EA) of the organic material. Organic semiconductors with low IP generally facilitate hole injection and are considered to be electron-donor molecules while those with a high EA favor electron injection and are described as electron-acceptors. Donor and acceptor materials that are able to preferentially and efficiently transport the injected carriers can be further categorized as hole transporting and electron transporting, respectively.[31] A key parameter that governs charge carrier mobility in the donor and acceptor materials is the overlap of the frontier orbitals between adjacent molecules or polymer chains. Unfortunately, the weakness of the intermolecular coupling, together with the molecular packing and morphology often limits the achievable mobility in organic semiconductor (10^{-6} to 1 cm^2 $V^{-1}s^{-1}$).[31] In contrast, prototypical amorphous silicon semiconductors, which generally have a rigid three-dimensional structure and wide conduction and valence bands are able to achieve mobilities in the range of 10 cm^3 $V^{-1}s^{-1}$.[21, 31, 32] Furthermore, in inorganic silicon technology doping with elements such as boron or phosphorus is usually done to create semiconductors in which the holes or electrons are the majority carriers, respectively.

1.2.1 Interfaces in OPVs

Organic photovoltaics is one of the most researched areas in the broader field of organic electronics. The motivation behind the development OPVs is its potential to be a significant parts of solving today's growing energy challenge. As can be seen in Figure 1.1 OPVs device platforms are comprised of a hole-transporting layer, an electron-transporting layer, a transparent conductive oxide (TCO), hole selective contact and an electron selective contact.

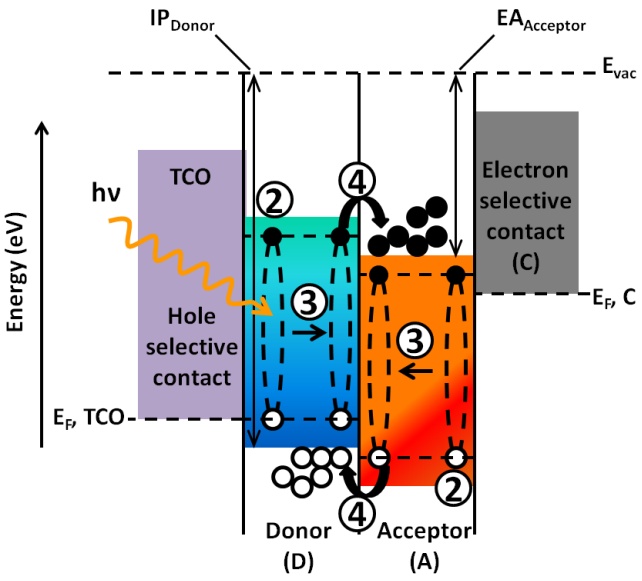

Figure 1.1 Frontier orbital energy offsets in planar organic heterojunction OPV. The processes involved in charge generation in OPVs, except for the first step of light absorption, are also depicted by numbers. Holes are indicated by hallow circles and electrons by filled circles. The ionization potential of the donor (IP_{Donor}) and the electron affinity of the acceptor ($EA_{Acceptor}$) are also shown. Modified from Kippelen and Bredas.[32]

Upon the absorption of light in OPVs (step 1; not shown) a coulombically bound electron-hole pair (exciton) is generated (step 2), which then diffuses to an interface between the donor and acceptor (step 3) where the charges get separated (exciton dissociation) and transferred into the acceptor or donor layer (step 4). The holes then get transported to the hole-selective contact and the electrons to the electron-selective contact where they are collected.[32, 33] The electrode-organic interface is very complex and presents a barrier to the collection of charges if the frontier electronic levels of the adjacent organic layer are not adequately aligned with the electrode's Fermi level (E_F; the energy at which the probability of finding an electron is 0.5 at 0 K).[32] In addition to the alignment of the frontier energy levels, other factors including surface composition, charge density distribution, and electrical heterogeneity of the contact must also be taken into account.

In OPVs the power conversion efficiency (i.e., the efficiency of the solar cell) is given as the ratio of the maximum power output over the incident solar power (P_{solar}). This efficiency is usually determined by generating current density-voltage curves (Figure 1.2) and calculating the efficiency by substituting the fill factor (FF; equation 1.2) into equation 1.1. Here V_{oc} is the open circuit voltage (i.e. the voltage when the current density is zero), J_{sc} is the current density at zero voltage (i.e. short-circuit current), P_{max} is the maximum output power, and V_{max} and J_{max} are the voltage and current density measured at the point of maximum power.

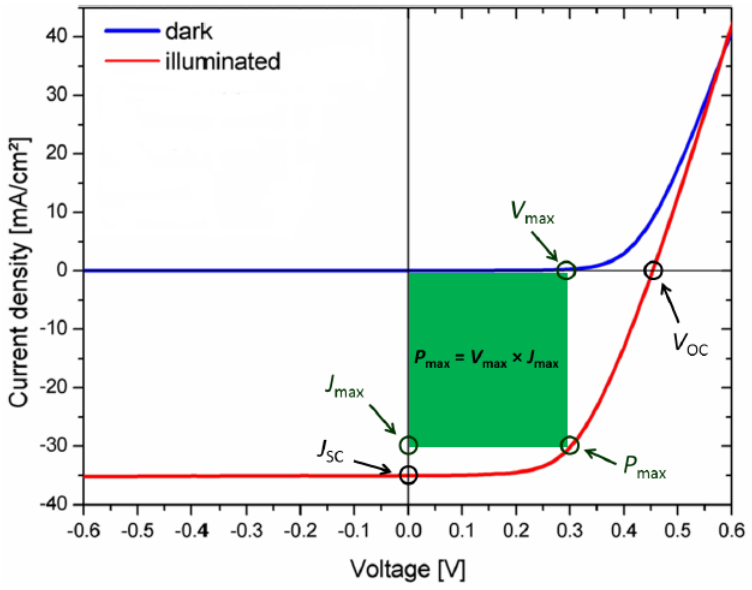

Figure 1.2 Representative current density-voltage curves of a solar cell in the dark and under illumination. Figure adopted from Lin *et al.*[34]

$$\eta = \frac{P_{max}}{P_{solar}} = FF \frac{J_{sc}V_{oc}}{P_{solar}} \qquad \text{(Equation 1.1)}$$

$$FF = \frac{J_{max}V_{max}}{J_{sc}V_{oc}} \qquad \text{(Equation 1.2)}$$

The V_{oc}, in particular, has been shown to significantly depend on the energy level offset at the metal oxide-organic interface.[33, 35, 36] Knesting *et al.*,[37] for example, have shown that the V_{oc} of a polymer/fullerene-based photovoltaic cell has a linear dependence on the work function (the energy difference between the energy level outside a singly ionized system where an electron becomes unbound (E_{vac}) and the Fermi level) of the hole

selective electrode. They observed that the device efficiency improved with increasing work function (Φ) and V_{oc}. These increases in efficiency were also correlated to a reduction in the recombination of charge carriers at the metal oxide-organic interface. Similar results were obtained by Ratcliff *et al*.[38] who also found that in addition to modulating the work function of the TCO the introduction of charge selective interlayers at the hybrid interface further improves the charge colleting efficiency at the metal oxide electrode.

1.2.2 Interfaces in nanocomposite dielectrics

Within the Marder and Perry groups at Georgia Tech we have taken a nanocomposite approach towards the development of dielectric materials. In these systems, easily polarized filler nanoparticles (specifically $BaTiO_3$) are dispersed in a suitable polymer matrix to potentially afford dielectric materials with large energy storage capacity. An important part in the development of nanocomposites is being able to control the chemical and physical properties of the surface of the nanoparticles, which is critical for: (i) minimizing aggregation of the nanoparticles, (ii) passivation of the surface of the nanoparticle and (iii) maximizing the compatibility between the particles and the polymer matrix. As mentioned before, properties at the inorganic-organic interface generally differ from that of the bulk polymer and these properties become increasingly dominant as the nanoparticle size is reduce (i.e. increasing surface area per volume).[39, 40] A comprehensive understanding of the role of the interface must therefore be developed in order to facilitate rational development of dielectric nanocomposite materials.

1.3 Metal oxides in organic electronic applications

As discussed in section 1.2 many organic electronic applications employ metal oxides as an integral part of their device structure. For example, in OPVs, TCOs have found uses as electrodes that provide optical access as well as serving as a port for charge extraction. In some device architecture TCOs are also used as interlayers that mediate the flow of charge between the active layers and the electrodes.[41] The choice of TCO usually depends on whether or not the metal oxide has the appropriate band alignment for charge extraction as well as its physical compatibility with the adjacent layers. The ease of processing, and the cost and availability of the metal oxide are also factors that are usually taken into account.

In a similar manner, the development of dielectric nanocomposites relies on the dispersal of high permittivity particles into a suitable host polymer matrix. The uniform dispersion of nanoparticles in the polymer matrix is crucial to the success of this approach and it must be done in a manner that minimizes both porosity and inhomogeneous electric fields that often lead to premature failure.[42] Here too, being able to manipulate the interface in a manner that reduces loss and maximizes both dielectric strength and storage capacity is crucial to the development of the technology.

1.3.1 Electronic structure of metal oxides

In order to discuss the measures that can be taken to tailor the properties of the hybrid inorganic-organic interface, a description of the metal oxide structure must first be established. From first principles we can recall that when electrons from two valence

atomic orbitals combine to form a chemical bond two new orbitals results: (i) a bonding orbital and (ii) an antibonding orbital, which are lower and higher in energy relative to that of the sum of the energies of the individual electron orbitals, respectively.[43] In solids the concept remains the same; therefore if N electron orbitals combine then N possible energy levels will result half of which will be lowered in energy and half raised in energy. The energy difference between the orbitals that are raised in energy is usually small so the levels smear out forming what can be considered a continuous band; the same is true for the orbitals lowered in energy. Usually the 'bonding' band is filled with electrons creating a so called valence band while the 'antibonding' band is empty forming a conduction band.[44, 45] The electron occupancy of these bands (or the levels therein) follow Fermi-Dirac statistics and is dependent on the temperature (T) and the density of states (DOS) available for population as demonstrated by equation 1.3.

$$f(E) = \frac{1}{1 + e^{\frac{E - E_F}{kT}}} \qquad \text{(Equation 1.3)}$$

where f(E) is the probability of finding an electron at an energy level (E), E_F is the Fermi level as defined previously in section 1.2.1 and k is Boltzmann's constant. The distribution is shown graphically in Figure 1.3.

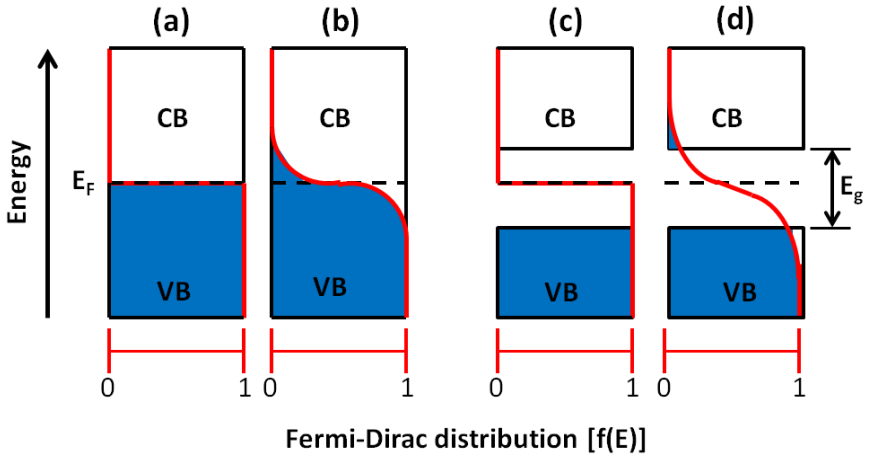

Figure 1.3 Illustration of the filling of bands in (a and b) metals and (c and d) intrinsic metal oxide semiconductors according to Fermi-Dirac distribution statistics (red trace). In the figure, CB represents the conduction band, VB the valence band and E_g the optical band gap. The electronic structure when T = 0 K is depicted in (a) and (c) while T >> 0 K is represented in (b), and (d).

In metals no distinction can be made between the conduction and valence bands because there is significant overlap between the occupied and unoccupied states. This makes it easy for electrons in the valence band to populate the conduction band and, in so doing, render metals as highly conductive materials. In contrast, intrinsic semiconductors have a band gap (E_g) which presents a barrier to the promotion of charges to the conduction band. When the temperature is 0 K only bands at the Fermi level or lower can be populated as shown in (a) and (c) for the metal and the intrinsic semiconductor, respectively. In the semiconductor, the Fermi level is found in the middle of the band gap which reflects that the probability of finding an electron in the VB is very high and very low in the CB but it does not imply an occupiable energy level or density of state (DOS) in the gap. At temperatures much greater than 0 K electrons are promoted to

higher energy levels making it more likely for them to populate the conduction band. In semiconductors, population of the conduction band occurs more readily in materials with smaller band gaps (~ 1-4 eV), which is what distinguishes them from insulators.[14, 44, 45]

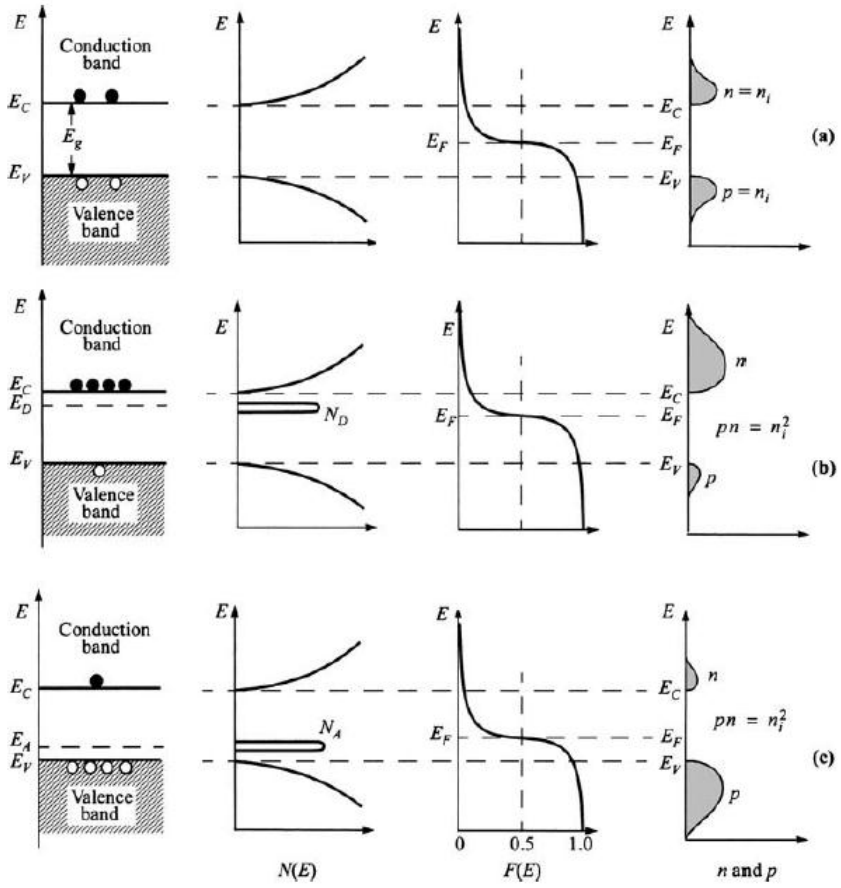

Figure 1.4 Schematic band diagram, density of states, Fermi-Dirac distribution, and carrier concentration for (a) intrinsic, (b) n-type, and (c) p-type semiconductors at thermal equilibrium. In this figure the conduction band minimum (E_c), the valence band maximum (E_v), and the band gap (E_g) are depicted. ED, EA and ND, NA are the energy levels and density of states associated with the donor and acceptor, respectively. The concentration of carriers is represented by n and p for n-type and p-type dopants, respectively. Reproduced from Sze and Ng.[44]

Often times the carrier concentration in intrinsic semiconductors are too low for them to function efficiently as conductive materials so donor impurities are added through a process known as doping in order to boost their conductivity. The doped semiconductors are said to be extrinsic. If the energy levels in the donor that is added to the semiconductor lies close (within a few kT) to the conduction band of the semiconductor such that an appreciable amount of carriers can be promoted to the conduction band under ambient conditions the semiconductor is termed n-type. In this case the majority carriers are electrons and the Fermi level shifts towards the conduction band. In a similar manner, when the dopant levels are closer to the valence band edge p-type semiconductors are created in which the majority carriers are holes and the Fermi level shifts towards the valence band.[14, 44] This is presented graphically in Figure 1.4 along with the corresponding DOS, Fermi-Dirac distribution and carrier concentrations

1.3.1.1 The electronic and crystal structure of indium tin oxide (ITO)

Indium tin oxide (ITO) is to date the most widely used TCO in heterojunction organic photovoltaic (OPV) cells because of its high optical transparency (~90%), electrical conductivity (~10^4 Ω^{-1} cm^{-1}), sheet resistance in units of Ω/□ and its compatibility with current lithographic techniques.[46],[47] The electronic structure of ITO, as depicted in Figure 1.5a, is comprised of a conduction band made up of In(5s) orbitals and a valence band comprised mostly of O (2p) levels. Most commercially available ITO is doped with about 10-14% Sn which creates levels close to or within the conduction band thereby rendering the material conductive.[48] In addition, thermal treatment of the metal oxide during processing often results in the creation of oxygen vacancy sites, which

act as n-type dopants donating two electrons to each vacancy.[49] This further contributes to the conductivity of the semiconductor. Figure 1.5b shows the <100> termination of the bixbyite crystal structure of Indium tin oxide with possible oxygen vacancy shown in white.

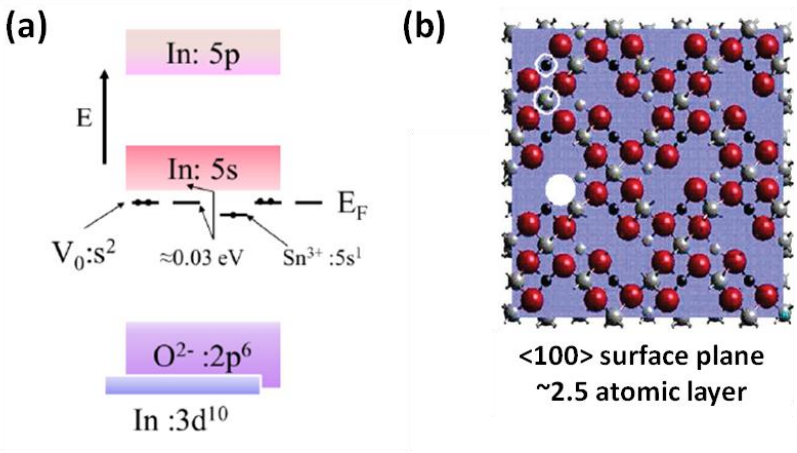

Figure 1.5 Schematic energy-band model for Sn-doped In_2O_3 (a) reproduced from Fan and Goodenough.[48] Crystal structure of the <100> surface of the bixbyite lattice of In_2O_3 (b) reproduced from Warschkow *et al*.[50]

1.3.1.2 Electronic and crystal structure of barium titanate

Barium titanate (BT) is one of the most utilized metal oxides in the field of dielectrics. Figure 1.6 shows the electronic structure of BT, which has a conduction band edge made up of Ti (3d) orbitals and a valence band edge comprised mostly of O(2p) levels and a band gap of approximately 3.2 eV.

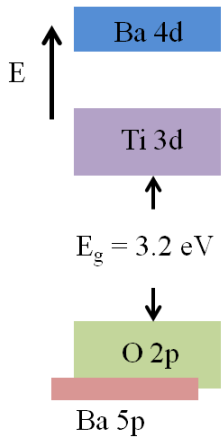

Figure 1.6 Schematic energy-band model for $BaTiO_3$. E_g indicates the optical band gap. Reproduced from Gao *et al*.[51]

The oxide belongs to the perovskite family of compounds that have the general composition of ABO_3. The dielectric properties of BT stems from the ability of the O^{2-} and Ti^{4+} ions to be displaced or become polarized relative to the Ba^{2+} cations in the presence of an electric field. The polarization response, as well as the phase composition of BT, depends on both the size of the particle and temperature. It is generally accepted that the dielectric constant of BT nanoparticle increases over the particle size range of 40 to 140 nm and then decreases from 140 to 450 nm.[52-54] An example of the particle size dependence of the dielectric constant of BT is shown in Figure 1.7. In addition to the change in the dielectric constant, variation in particle size also affects the phase composition of BT.[55, 56] Currently, there is an ongoing debate about what the critical particle size is for BT to transition from a cubic phase to a tetragonal phase at room temperature.[52, 53, 56] Figure 1.8 shows the cubic and tetragonal of crystal structure of BT along with their lattice parameters. Due to the displacement of the atoms in the tetragonal structure, this form of BT has a permanent dipole moment and exhibits

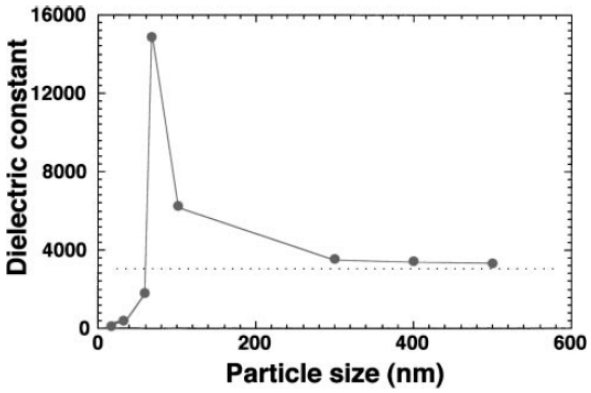

Figure 1.7 Plot showing the dielectric constant of BaTiO3 as a function of particle size. Reproduced from Wada and company.[53]

ferroelectric behavior (i.e., a spontaneous polarization in the presence on an electric field). In contrast, cubic barium titanate has no permanent dipole moment and undergoes induced polarization when placed in an electric field (paraelectric behavior). The profiles for ferroelectric and paraelectric behavior are also shown in Figure 1.8

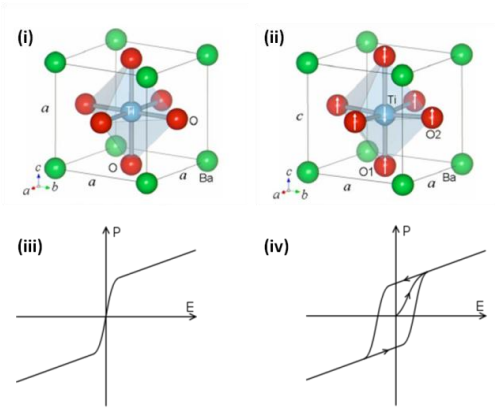

Figure 1.8 Crystal structures of (i) cubic [a = b = c] and (ii) tetragonal [a = b ≠ c] barium titanate. The green, blue, and red spheres denote Ba, Ti, and O atoms, respectively. The arrows in b show the direction of displacement for the Ti and O atoms with respect to the Ba atom. Reproduced from Yashima *et al.*[56] The polarization profiles for paraelectric (iii) and ferroelectric (iv) behavior are also shown. The polarization profiles were reproduced from Bigly.[57]

The cubic to tetragonal phase transition can also be induced by thermal agitation and the temperature at which the phase conversion takes place is referred to as the Curie Temperature (T_c). Since the exact value of T_c and, by extension, the crystal structure of BT under given conditions depends strongly on particle size,[58] the controlled synthesis of nanoparticles is critical for tuning the dielectric properties of $BaTiO_3$ (Figure 1.9).

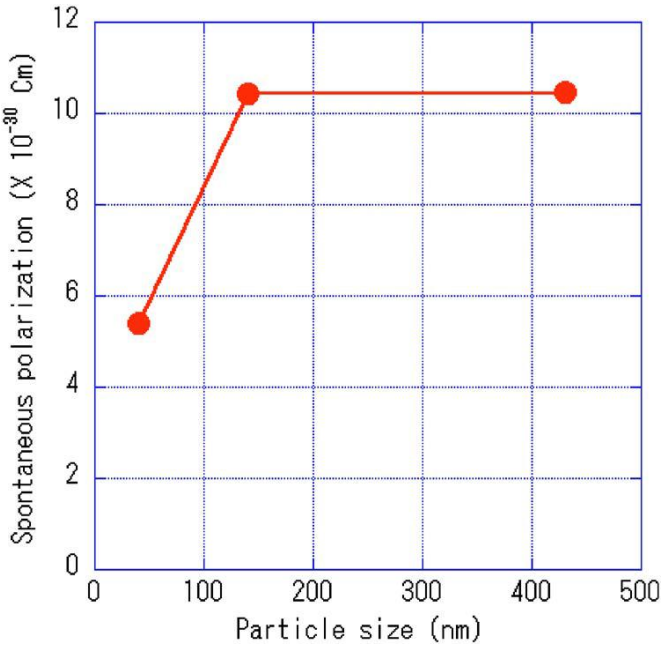

Figure 1.9 Size effect on the calculated spontaneous polarization of single domain tetragonal $BaTiO_3$ in the fine particles. Reproduced from Yashima *et al*.[56]

1.4 Use of monolayers to control the electronic and chemical properties of metal oxide surfaces

The electronic and chemical properties of metal oxide surfaces can be controlled via functionalization with molecular modifiers. To this end, surface modifiers have

proven to be a very effective chemical tool for tailoring interfaces in numerous organic electronic platforms. These molecules can be considered to comprise of three principal parts namely: (i) the anchoring/head group that binds to the substrate and determines the strength of the interaction at the surface; (ii) the linker/spacer that facilitates the stability and organization of the monolayer and acts as a physical barrier; and (iii) the tail group that acts to change the chemical functionality at the surface, alter the substrates electronic properties depending on it polarity and serve as sites for further chemistry.[58] A graphical representation is shown in Figure 1.10.

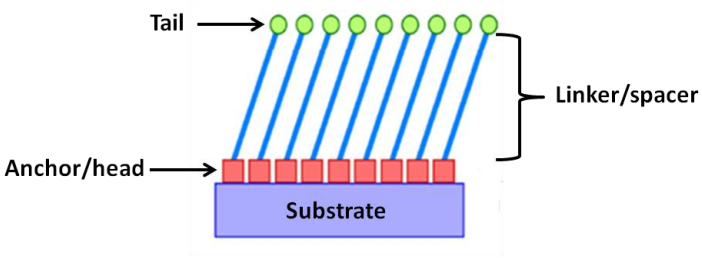

Figure 1.10 Schematic of a monolayer of surface modifiers attached to a substrate with the various constituents of the monolayer highlighted. Figure adapted from Love *et al*.[58]

Each constituent of the monolayer can be synthetically tuned independently of the other thereby making this a very attractive approach towards manipulating surfaces.

1.4.1 Modulating work function (Φ) with dipolar molecules

Generally, when two dissimilar materials are brought together an energy barrier is usually created that precludes the efficient transfer of charge across the interface. These

barriers can be reduced by tuning the work function (i.e. the energy difference between the Fermi and vacuum levels) of the electrode or the IP and EA levels of the adjacent active layer. [59],[60] The former is a very attractive approach since the work function of the electrodes can be moderated by surface modifying them with dipolar molecules. In this approach generally the work function will be reduced if the molecular dipole is pointing towards the surface and will increase if the dipole is directed away from the surface. An illustration of changes in the frontier orbital energy levels that can occur when a prototypical hole-transporting layer (HTL) is brought in contact with ITO is depicted in Figure 1.11. The initial energy levels in both the ITO and HTL are shown in (a) prior to contact. Since the Fermi level in the HTL is higher than that of the electrode, once the HTL is brought into contact with the ITO an electronic equilibrium is established (b) by the transfer of electrons from the HTL to the ITO. In this scenario, the local vacuum level at the interface changes and is accompanied with band bending. The Fermi level is shifted into the conduction band and in so doing increases the barrier to charge transfer. When a dipolar molecule is used to modify the ITO surface and the HTL subsequently brought into contact with the ITO (c) the local work function is increased, which is consistent with the dipole moment of the modifier pointing away from the surface and the consequent increase in the vacuum level at the surface. This results in a reduction in the barrier to charge transfer at the interface relative to both the pre-contact and the unmodified surface.

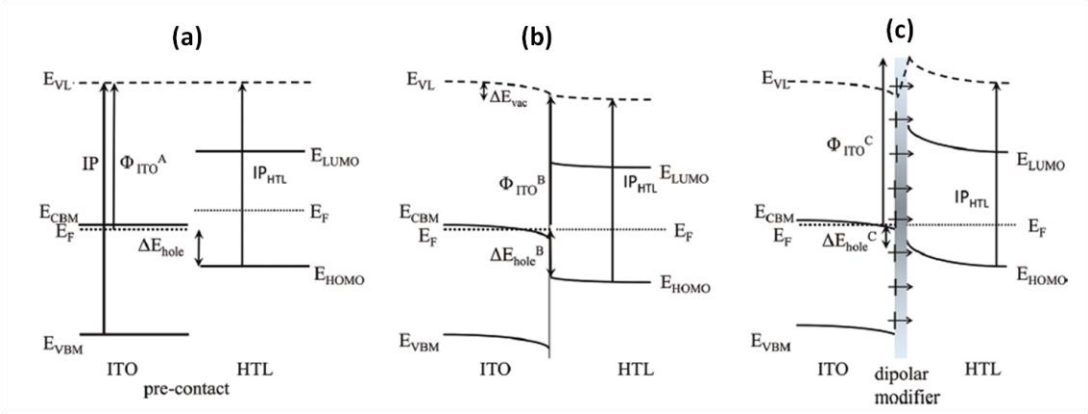

Figure 1.11 Schematic energy level diagrams representing three different heterojunctions: (A) an ITO electrode with prior to contact with a prototype HTL; (B) the heterojunction in (A) after electronic equilibrium has been achieved, (C) as in (B) but starting with an ITO electrode modified with a dipolar small molecule modifier, which increases the effective work function for ITO at the ITO/HTL interface. ΔE_{hole} is the energy barrier to hole transfer, E_{VL} is the vacuum level, IP is the ionization potential, E_{CBM} is the conduction band minimum, and E_{VBM} is the valence band maximum. All other symbols are as established in previous sections. Reproduced from Hotchkiss *et al*.[16]

In theory, the observed change in work function can be broken down into three components: (i) bond dipole (BD) that stems from the chemical attachment of the molecule to the surface; (ii) geometry rearrangement ($\Delta\Phi_M$) brought about by surface reconstruction and surface dipole ($\Delta\Phi_{SD}$), which is induced by the dipole moment of the molecule.[61] Of the three components, the surface dipole is often considered to be the largest contributor to the change in work function and is expressed mathematically as

$$\Delta\Phi_{SD} = \frac{N\mu_Z}{\varepsilon_{eff}\varepsilon_o} \qquad \text{(Equation 1.4)}$$

where N is the surface coverage, μ_z is the dipole moment of the modifier normal to the surface of the substrate, ε_o is the permittivity of free space and ε_{eff} is the effective dielectric constant.[61]

Hotchkiss *et al.*[62] examined, both experimentally and theoretically (DFT), the correlation between the calculated dipole moments for a series of benzylphosphonic acid modifiers and the observed change in work function relative to unmodified ITO. The molecules were chosen such that their relative degrees of fluorination would lead to significant changes in the magnitude of the induced surface dipole normal to the surface once the ITO was functionalized. The results for this study are presented in Figure 1.12. It is important to note that only one molecule had its dipole moment pointing towards the surface (i.e. positive μ_z) so all the other modifiers are expected to increase the work function relative to bare ITO; this is indeed the case. In this study the work function was tuned over a range of approximately 1.3 eV. This demonstrated that the work function of ITO can be systematically tuned by employing fluoroaryl molecules by varying the number and positions of fluorine substitutions.

Goh *et al.*[36] examined the effects of molecular surface modification in hybrid inorganic-organic photovoltaic cells and the results are presented in Figure 1.13. Here a systematic investigation of the effect of employing a series of dipolar, para-substituted benzoic acids with varying calculated dipole moments on the energy offset at the TiO_2-polymer interface and the open circuit voltage was investigated. Fluorine-doped indium tin oxide (FTO) was used as the electron selective contact electrode, TiO_2 as the electron transporting layer (ETL), a 160 nm thick poly(3-hexyl thiophene) as the HTL and

oxidized Ag as the hole selective contact (a). Voc and Jsc are plotted against the calculated dipole moments of the molecules (b).

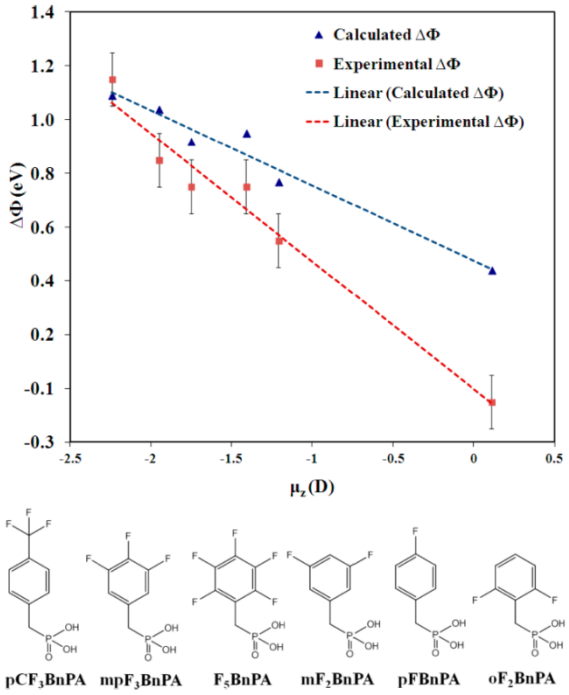

Figure 1.12 Plots comparing the changes in work function measured by UPS (red) and evaluated by DFT (blue) as a function of the calculated dipole moment normal to the surface, for the six PA molecules depicted at the bottom, listed from left to right in the same sequence as the data points. Reproduced from Hotchkiss *et al*.[62]

Relative to the unmodified titania, Voc increases and decreases depending on whether the dipole moment of the molecule is pointing away (i.e. negative μz) or towards (i.e. positive μz) the surface, respectively. Analogously, strong enhancements in the short circuit current (b and d) are observed when molecules having their dipoles directed towards the TiO_2 are used compared to those with their dipoles pointing away from the

metal oxide, relative to the unmodified surface. Even when there is no illumination (c) there is an offset in the J-V curves that can be correlated to the calculated dipole moments. These results indicate that the main effect of changing the dipole moment at the interface is modulation of the energy level offset at the titania/polymer interface. Further, this provides direct evidence that the efficiency of OPVs can be modulated via appropriate surface modification techniques.

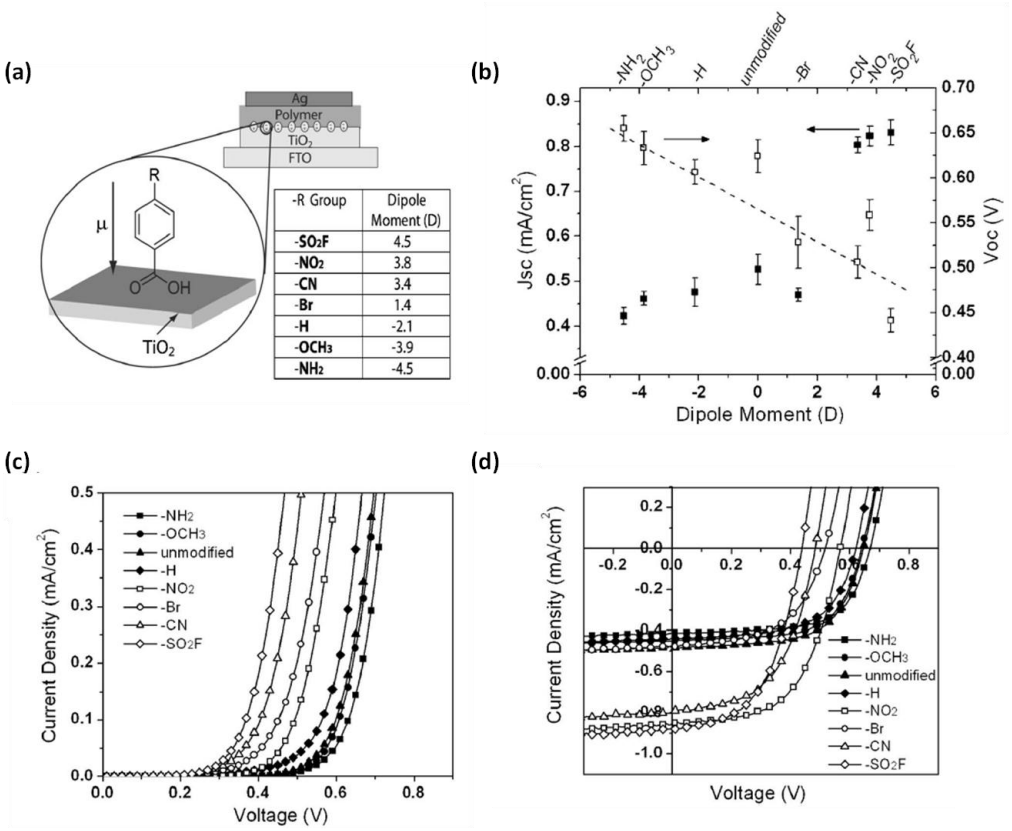

Figure 1.13 Schematic of bilayer TiO_2 /P3HT devices with dipolar modification of titania surface (a). The table lists the substituent −*R* group on the *para* position of the benzoic acid accompanied with calculated dipole moment. The V_{oc} and J_{sc} of devices shown in (b) are plotted against dipole moment of the modifiers *J-V* curves of the hybrid bilayer devices with and without interface modifications employing *para*-substituted benzoic acid derivatives (c) in dark and (d) under llumination. The dashed line is drawn as a guide to the eye. Reproduced from Goh *et al*.[36]

1.4.2 Surface energy matching in organic electronics

Surface energy (γ) is considered a measure of the intermolecular forces or free energy at an interface. In organic electronic devices the surface modification is not only important for manipulating the energy levels at the surface but also for controlling the physical interactions (Figure 1.14). Controlling the surface energies of both phases allows for the preparation of homogeneous films, minimizes pinholes, improves device lifetime, and increases the adhesion of the organic phase to the metal or metal oxide surface.[63, 64]

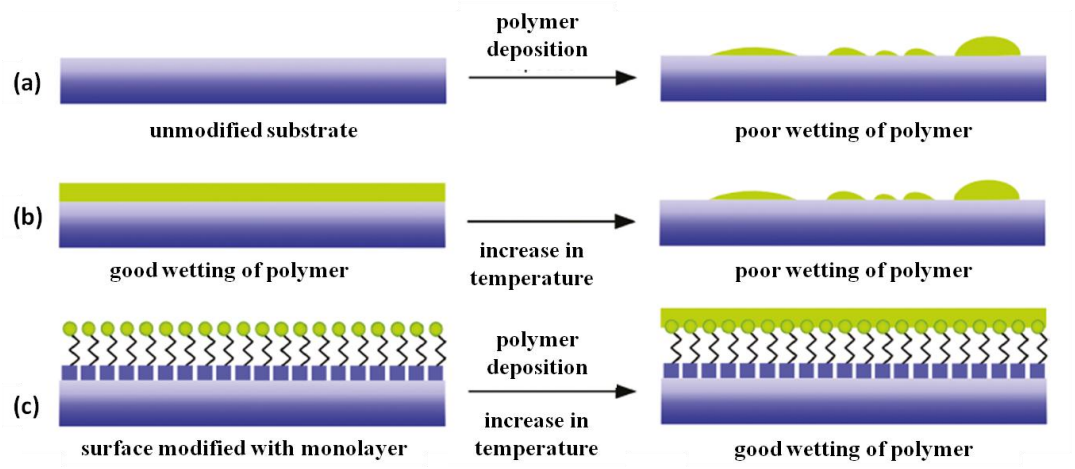

Figure 1.14 Illustration of the physical interactions between a substrate and deposited polymer. (a) Hydrophilic substrate that does not interact well with the deposited polymer, thereby causing inhomogeneous coating of the polymer on the surface. (b) Initial good wetting of the polymer which displays poor wetting after an increase in temperature and/or over time. (c) Substrate modified with a monolayer that changes the surface energy of the material in such a way as to interact more favorably with the polymer, resulting in lasting homogeneous film coverage. Reproduced from Hotchkiss *et al*.[16]

Improving the adhesion between the polymer and the inorganic phase increases the effective contact area and, consequently, provides for greater electronic contact between the two materials. This often results in reduced contact and sheet resistance. In OPVs, having greater electrical contact significantly impacts the charge transfer rates and densities across the hybrid interface.[65, 66] Analogously, it has been demonstrated that the modification of the filler particles with the appropriate ligand can result in improved breakdown strength and reduced loss in dielectric nanocomposites.[67-69]

The ability to wet a surface can be quantitatively explored using contact angle (θ) where smaller angles correspond to better matching of the surface energies and vice versa. Surface energy is comprised of a polar component (γ^p), which accounts for permanent and induced dipoles as well as hydrogen bonding, and a dispersive component (γ^d) due to instantaneous dipole moments. The sum of both components gives the surface energy. Using this approach, Paniagua *et al*.[70] were able to examine the surface energy of ITO modified with a series of phosphonic acid molecules (Figure 1.15). The results of this study showed that there is a marked reduction in the surface energy of the modified ITO surface relative to the untreated electrode. Most of the change appears to come from a diminution of the polar component due to the introduction of new terminal/tail groups at the surface.

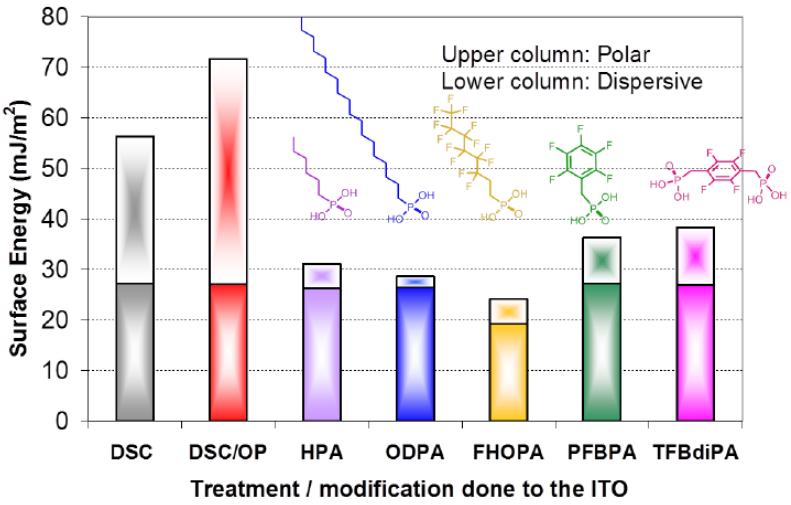

Figure 1.15 Harmonic mean-determined surface energies (γs) broken into their polar (γsp) and dispersion (γsd) components for ITO and after DSC/OP activation and modification with the phosphonic acids. Reproduced from Paniagua *et al.*[70]

1.4.3 Anchoring groups for the modification of metal oxide surfaces

Generally, organic surface modifiers are classified according to their anchoring group; several of which have been used to successfully modify the surface of metal oxides. Among the functional groups mostly investigated for this purpose are silanes, carboxylic acids, and phosphonic acids. Each of these head groups present a viable means of modulating the chemical, physical and electrical properties of interfaces, but they also pose unique challenges that must be taken into account when modifying surfaces.

Silanes are particularly attractive molecules for surface modification because, in addition to being able to functionalize metal oxide surfaces, a wide array of them is commercially available. The reactivity of these silicon-based molecules towards the surface of metal oxides is dependent on choice of hydrolysable group that is used as the anchoring moiety. The commonly used terminations include alkoxysilane and

chlorosilanes the latter being very reactive.[71] The mechanism of formation of monolayers on the surface of metal oxides is believed to commence with the hydrolysis of the terminating moiety to form silanol groups (Si-OH) followed by hetero-condensation with hydroxyl groups on the surface.[72, 73] Unfortunately, the silanol groups formed in the first step also have the propensity to hetero-condense with neighboring molecules, thereby forming a three-dimensional molecular network on the surface. The balance between homo and hetero-condensation is highly dependent on the amount of water present during the reaction and, as a consequence, so is the quality of the layer of the film formed on the surface (Figure 1.16).[73, 74]

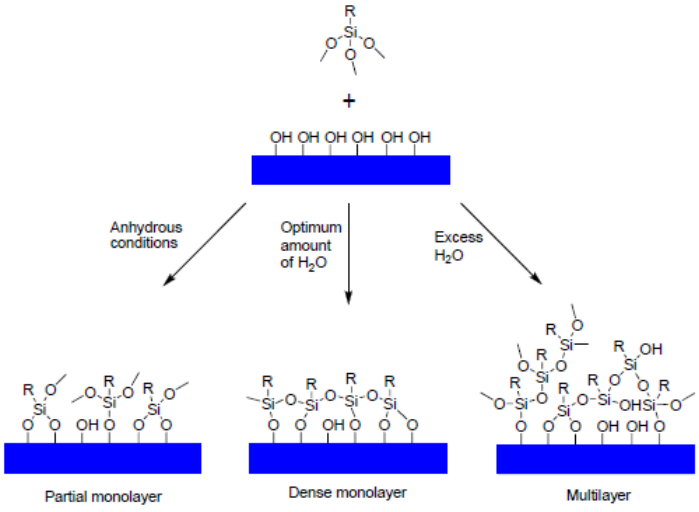

Figure 1.16 Schematic representation of the influence of water content on the surface modification of an oxide by a trimethoxysilane. Modified from Mutin *et al*.[73]

Additional factors such as deposition time, temperature and pH also affect the initial hydrolysis, which makes the deposition of a single monolayer of silane difficult. In the

event that one is able to successfully deposit a monolayer of silane on a surface, the fidelity of the layer can be easily compromised by further hydrolysis if the sample is stored under ambient conditions. It is also important to note that during the modification of metal oxides with silanes alcohols or acid (HCl) are generated as side products, which may also adversely affect the surface.

Another class of compounds used to prepare monolayers on surfaces is carboxylic acids. In this case the acid can participate in hydrogen bonding with the metal oxide surface or generate the carboxylate anion via acid-base chemistry, which subsequently interacts with one of the metal centers of the surface.[75, 76] The interactions that result from the latter scenario usually occurs through a variety of modes including: (i) as a monodentate ligand, (ii) a bridging chelate and (iii) a bidentate chelate.[77, 78] Regardless of the mode, the strength of the interaction is relatively weak, which predisposes carboxylic acid monolayer to be easily cleaved from the surface.[79] Despite these issues, carboxylic acids have been effectively used to tailor the interface properties in many organic electronic devices to improve their performance. In dye-sensitized solar cells, for example, carboxylic acid head groups are almost exclusively used to anchor the photoactive dyes to the electrode. Armstrong *et al*.[66],[80] have demonstrated the utility of carboxylic acids improving heterogeneous electron transfer at the ITO-HTL interface in both OPVs, due to an improvement in the electrical contact between the two layers.

Phosphonic acids have been found to form very robust monolayers on the surface of metal oxides. Unlike silanes, phosphonic acids do not readily undergo homo-condensation unless exposed to high temperatures and anhydrous conditions.[73] Therefore, surface modification with phosphonic acids usually result in the formation of a

single monolayer; additional physisorbed molecules that can be easily removed with rinsing. It is believed phosphonic acids can bind to the surfaces of metal oxides via either of the two different mechanisms shown in Figure (1.17). In the mechanism 1, the acid is first oriented at the surface of the metal oxide, via Lewis acid coordination of the phosphoryl oxygen, and then subsequently undergoes hetero-condensation with hydroxyl groups on the surface. In the second mechanism, a nucleophillic attack by the surface hydroxyl groups on the phosphorus center results in the cleavage of the P-OH bond and the formation of P-OM bonds.

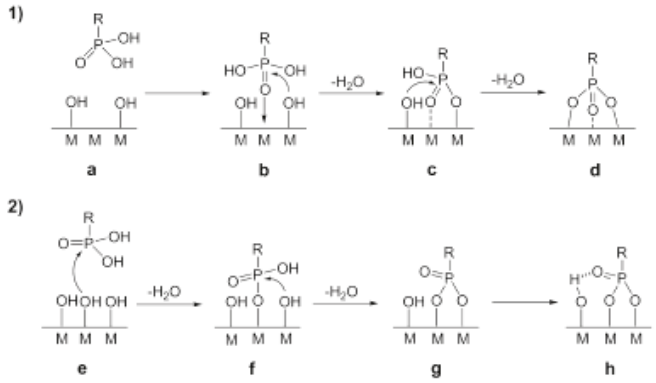

Figure 1.17 (1) Mechanism of phosphonic acid attachment to Lewis acidic metal oxides: (a) initial conditions, (b) coordination of the phosphoryl oxygen to a Lewis acidic site on the surface followed by heterocondensation with the now more electrophilic phosphorus, (c) additional heterocondensation, and (d) final tridentate binding state. (2) Mechanism of phosphonic acid attachment to poorly Lewis acidic metal oxides: (e) heterocondensation with a surface hydroxyl group, (f) second heterocondensation with the surface, (g) bidentate bound state, and (h) hydrogen bonding of phosphoryl group with surface hydroxyl. Reproduced from Hotchkiss *et al*.[16]

1.4.3.1 Mediating charge transfer by anchoring groups

While there are many studies demonstrating the use of organic molecules to control the chemistry at surfaces, much still remains to be understood about the role that the anchoring group plays in controlling the kinetics of charge transfer at the metal oxide-organic interface. Several studies have highlighted the dependence of the local interface electronic structure on the choice of tethering group.

Nilsing *et al.*[81] examined the electronic structure and adsorption of pyridine rings attached to an anatase (101) TiO_2 surface via phosphonic and carboxylic acid groups using density functional theory calculations. Their findings indicated that, while the phosphonic acid anchoring group bonded more strongly to the substrate than the carboxylic derivative, the latter reduced the injection time by half from 35 fs to 17 fs. owing to better electronic coupling between the π^* orbital of the adsorbate and the conduction band of the metal oxide.

Ernstorfer *et al.*[82] conducted transient absorption studies to investigated the heterogeneous electron transfer between a perylene chromophore anchored to TiO_2 anatase via two different anchoring groups namely: phosphonic and carboxylic acid. The time constants for the electron transfer process were 13 and 28 fs for carboxylic and phosphonic acid, respectively. This again shows that the carboxylic acid-anchored dye facilitates higher electron transfer.

In a similar study Hyun *et al.*[83] compared the rates of electron transfer from PbS to TiO_2 through a series of thiol-containing molecules with varying anchoring groups (4-mercaptobutryic acid, 4mercaptobutylphosphonic acid, 3-(mercaptopropyl)-trimethoxysilane and sodium 3-mercaptopropane-1sulfonate) by examining the

fluorescence decay. It is important to note that all the molecules investigated in this study had a three-carbon linker except for the phosphonic acid. The decay times based on an exponential fit of their experimental data for the silane, carboxylic acid, phosphonic and sulfonic acid groups were 77, 12, 5.8 and 2.5 ns, respectively. In this case the phosphonic acid performance was superior to the carboxylic acid but the sulfonic acid proved to be the most effective anchoring group. The authors attributed the differences in electron transfer rate to the variation in the degree of electronic coupling of the states in the molecule to the states in the metal oxide.

Martini *et al*.[84] examined zinc porphyrins coordinated to TiO_2 via pyridyl linkers with caboxylic, phosphonic, and hydroxamic acid groups using time-resolved tetrahertz spectroscopy. These efforts were geared towards the development of photoanodes for light-driven water oxidation, in which stability in an aqueous environment is as important as charge injection efficiency. The carboxylic acid was, again found to be more efficient but less robust than the phosphonic acid. The hydroxamic acid, however, was as stable and efficient as the phosphonic and carboxylic acids, respectively. Taken together, these studies show that the charge-transfer kinetics at the organic-inorganic interface can be mediated by the anchoring group, and its ability to couple into the electronic levels of the metal oxide.

1.4.3.2 Anchoring groups and their role in binding and molecular orientation at the surface

As discussed in section 1.4.1 dipolar molecules can be used to adjust the work function at the inorganic-organic interface thereby modulating the injection efficiency in various organic electronic devices. Recall that the change in work function brought about by modifying a surface can be described as the combination of three factors: (i) the surface dipole induced by the molecular dipole; (ii) the bond dipole that results from the covalent attachment of the molecule to the surface; and (iii) the surface reorganization due to the relaxation of the surface upon the binding of the molecule. Since the largest contributor to the work function change is often considered to be the induced surface dipole, which is derived from the molecular dipole normal to the surface, understanding the mode of binding to the surface of metal oxide is important for modulating frontier orbital energetic. The binding interaction vary among anchoring groups and leads to different molecular orientation as well as differences in the magnitude and direction dipole molecular moment relative to the surface of the metal oxide. All these factors will have a significant effect on our ability to modulate the work function; therefore, developing an understanding of binding and orientation is important for the advancement of organic electronics. A substantial amount of work has been devoted towards examining the binding of various surface modifiers, including thiols,[85] silanes,[86]carboxylics acids[87] and phosphonic acids[16, 62, 70] to metal oxides. Owing to their affinity for metal oxides and the robust nature of the bonds formed, the Marder group has examined the use of phosphonic acids to tune the interfacial energetics of

organic electronics. Most of what has been outlined regarding phosphonic acids suggests the formation of P-O-M bond (where M represents a metal center) to the substrate, which can take on any of the combination of binding configurations depicted in Figure 1.18

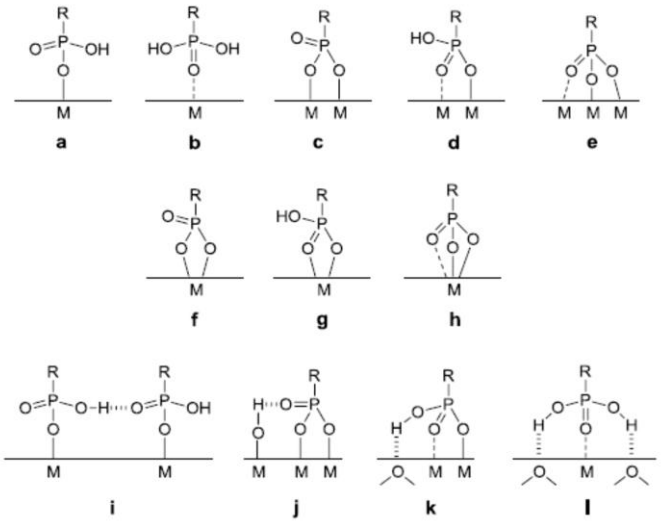

Figure 1.18 Some possible binding modes of phosphonic acids to a metal oxide surface, where M = metal: Monodentate (a and b), bridging bidentate (c and d), bridging tridentate (e), chelating bidentate (f and g), chelating tridentate (h), and some possible additional hydrogen bonding interactions (i-l).Reproduced from Hotchkiss *et al*.[16]

Gliboff *et al*.[88] examined the orientation of phenyl phosphonic acid on an indium zinc oxide (IZO) surface using polarization modulation infrared reflection absorption spectroscopy (PM-IRRAS) and near-edge X-ray absorption fine structure (NEXAFS) and compared to results of density functional theory (DFT) calculations. The experiments showed that the monolayer was well ordered with a tilt angle of 15 ± 4°, which was in good agreement in with the DFT data. In a later publication[89] the author examined the

effect of fluorination on binding and orientation for aryl (phenylphosphonic acid [PPA] and 3,4,5-trifluorophenylphosphonic acid [F_3PPA]) and alkyl (octylphosphonic acid [OPA] and 3,3,4,4,5,5,6,6,7,7,8,8,8-tridecafluorooctylphosphonic acid [F_{13}OPA]) monolayers on ITO using the same techniques. The fluorinated version of OPA had a smaller displacement angle from the surface normal of 30° ± 5, compared to 41° ± 8 for OPA. The smaller displacement observed in F_3OPA was attributed to steric effects. In contrast, fluorination of the PPA produced a less upright structure with a displacement from the surface normal of (27° ± 4) compared to (19° ± 4) observed for PPA. Here the differences between the aryl molecules were ascribed to the molecules having different binding modes on the surface.

1.5 Redox monolayers as a tool for probing the kinetics of charge injection at the metal oxide-organic interface

As outlined in the previous two sections, the local electronic coupling, and by extension, the charge-transfer properties at the organic-electrode interface can be mediated by the anchoring moiety of surface modifiers. These findings highlight the need to decipher the role of anchoring groups in mitigating charge-transfer kinetics at the TCO-organic interface. The combination of synthetic tunability and electroactivity makes redox monolayers an excellent means of investigating the kinetics of charge transfer at the hybrid interface. These molecules usually contain a terminal group that is capable of being oxidized and/or reduced in solution when an external potential is applied. While the rates of solution-based charge-transfer processes cannot be directly extrapolated to solid state device kinetics, the electrochemical template can serve as a guide for understanding

photo-induced electron transfer processes thereby facilitating a model that can be used to design suitable surface modifiers.

1.5.1 Ferrocene as a redox probe for the electrochemical determination of electron transfer rates

Ferrocene serves as a good prototypical probe for these studies because its electrochemical properties have been well characterized,[90, 91] it has been extensively used to study electron transfer rates from various electrodes, and it is also soluble in many organic solvents.[92] Also, the oxidation potential of ferrocene is comparable to some commonly used hole transporting materials such as poly(3-hexylthiophene) (+ 0.18 V *vs*. Fc/Fc^+)[93] and 4,4´-bis-(*m*-tolyphenylamino)biphenyl (TPD; 0.35 V *vs*. Fc/Fc^+).[94] Furthermore, it has been demonstrated that the integration of ferrocene dicarboxylic acid modifiers/interlayers into OPV cells resulted in lower contact resistance, and consequently, an improvement in the power conversion efficiency.[66] The improvement was mostly attributed to the ability of the modifier to provide accessible pathways to the electrically active domains of the heterogeneous electrode and simultaneously serve as an electroactive contact for the adjacent active layer.

1-Ferrocenyl-4-trichlorosilylbutane was synthesized by Li *et al*.[95] and used to characterize the electron transfer properties from a series on transparent conducting oxides including: commercial and ion-assisted deposited (IAD) indium tin oxide (ITO); metal-organic chemical vapor deposited (MOCVD) cadmium oxide (CdO); MOCVD zinc indium tin oxide (ZITO); and IAD In_2O_3. The results are summarized in Figure 1.19 and Table 1.1

Table 1.1 Relevant properties of various TCOs and cyclic voltammetry of self-assembled ferrocene-based monolayer films on various TCO surfaces at a scan rate of 0.1 V/s. Reproduced from Li *et al*.[95]

TCO	E_{pa}/E_{pc} (mV)	ΔE_p (mV)	$\Delta E_{p,1/2}$ (mV)	Coverage (mol/cm^2) $\times 10^{-10}$	Electron transfer rate (s^{-1})
as-received ITO	963/923	40	93 ± 2	6.6	6.65
MOCVD-CdO	1028/894	134	96 ± 1	8.1	0.42
MOCVD-ZITO	984/944	40	94 ± 3	7.6	7.12
IAD-ITO	994/942	52	90 ± 2	7.2	5.07
IAD-In_2O_3	1076/859	217	165 ± 2	6.7	0.03

E_{pa} and E_{pc} are the oxidation and reduction peak potentials of the electroactive molecule and ΔEp is the width at half height of the oxidation peak. All measurements were taken *vs*. a Ag reference electrode.

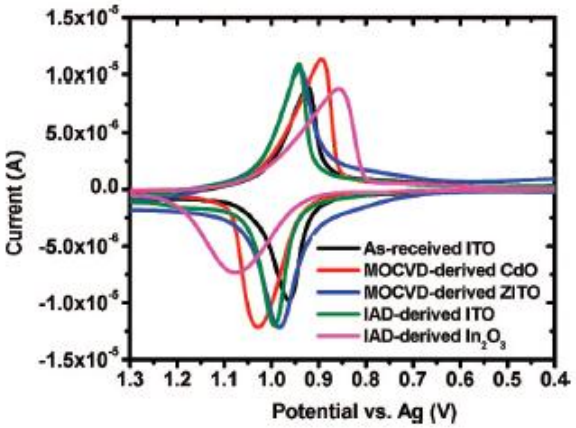

Figure 1.19 Cyclic voltammograms of ferrocene-based monolayers chemisorbed on various TCOs at 0.1 V/s scan rate.

From the voltammograms and Table 1.1 they concluded that the microstructure and electrochemical properties at the interface differ among the variously prepared TCOs as evident in the differences in the redox peak potentials (E_{pa} and E_{pc}) and peak separation (ΔE_p;) which was attributed in part to the heterogeneity of the chemisorptions sites

among the metal oxides. To a lesser extent, the differences in the observed redox behavior can partly be attributed to the lateral interactions between the ferrocene tail groups, which is qualitatively represented by the peak width at half height ($\Delta E_{p,1/2}$). In theory, surface confined redox molecules that exhibit ideal behavior according to the Nernst equation (*will be shown in the subsequent section*) should have a $\Delta E_{p,1/2}$ of 90.6/n mV. The greater the interaction between the redox sites the larger the deviation from the ideal value. They also found that ITO that treated with an oxygen plasma gave higher electron transfer rate (9.23 s^{-1}) and coverage (7.9×10^{-10} $mol.cm^2$) compared to the as received ITO that gave a rate of 6.65 s^{-1} and a coverage of 6.6×10^{-10} $mol.cm^2$.[95] Among the other metal oxides examined, the CdO and IZO that were prepared from metal-organic chemical vapor deposition gave the highest coverage (8.1×10^{-10} $mol.cm^2$) and rate (7.12 s^{-1}), respectively. Vercelli *et al*.[96] compared the coverage and stability of two separate 6-hexylferrocene molecules that were terminated by either a carboxylic or phosphonic acid anchoring group on ITO. The phosphonic acid formed a robust monolayer and gave coverage of 4.2×10^{-10} $mol.cm^{-2}$. The carboxylic acid was weakly tethered to the surface of the ITO and gave coverage of 1×10^{-10} $mol.cm^{-2}$, approximately four times lower than that of the phosphonic acid.

1.5.2 Electron transfer in an electrochemical cell

Electrochemistry can be used to investigate the processes occurring at the interface between an electrode (working electrode) and an electrolyte (i.e. an ionic conducting solution) containing a redox active species. Electron transfer processes of this kind are often referred to as being heterogeneous. The chemical process taking place in

an electrochemical cell can be considered to be two separate half-reactions : (i) the oxidation half and (ii) the reduction half. Both half-reactions depend on the potential difference applied between the working electrode and a reference electrode. Prior to immersion of the electrode into solution, the electrons occupy a range of energies according to the band models shown in section 1.3.1.1 and the electrode is considered to have a fixed chemical potential. When the electrode is placed in solution an equilibrium is reached between it and the electrolyte solution via the transfer of charge. If the potential of the working electrode is further driven towards increasingly negative potentials the electrons in the electrode will reach a sufficiently high level where they can be transferred to a vacant molecular orbital of any redox species in solution (reduction). Analogously, driving the electrode towards positive potentials will lower its level such that an electron can be transferred from an occupied state of the electroactive molecule to a vacant state in the electrode (oxidation). Both these scenarios are shown in Figure 1.20. The rate at which the electron transfer proceeds depends on how quickly the electroactive species can be supplied to the electrode from solution. The use of surface confined redox monolayer circumvents this issue as the molecules are already tethered to the surface of the electrode. As such, when surface confined molecules are used, electron transfer is primarily limited by the amount of the redox molecule present at the surface, the movement of the electron across the interface, and the inherent internal resistance of the electrode.

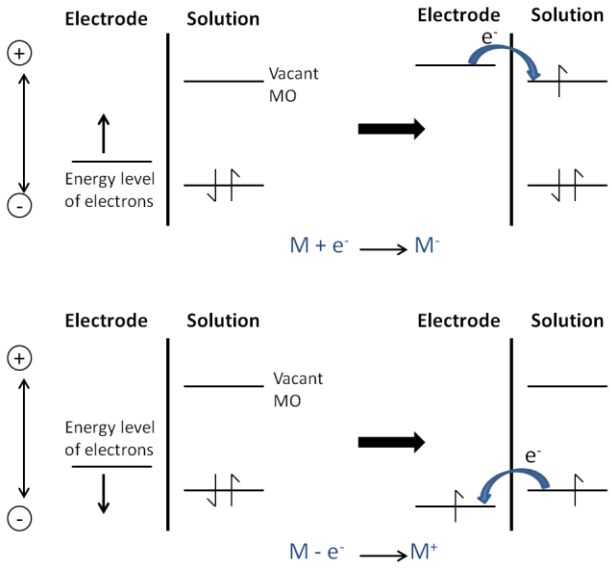

Figure 1.20 Illustration of the (top) reduction and (bottom) oxidation process of a species M in solution. The molecular orbitals (MO) shown are the highest occupied and lowest unoccupied/vacant orbitals.

The amount of redox molecule on the surface at equilibrium can be related to the potential of the electrochemical cell (E) by the Nernst equation shown below:

$$E = E^{o} - \frac{RT}{nF} \ln \frac{[Red]^{a}}{[Ox]^{b}} \qquad \text{(Equation 1.5)}$$

Where E^{o} is the formal potential, T is temperature, F is Faraday's constant, R is the molar gas constant, n is the number of electrons transferred, [Red] is the concentration of the reduced species, and [Ox] is the concentration of the oxidized species and a and b are the stochiometric coefficients of the redox species.[97],[15],[98]

Consider a simple one-electron transfer heterogeneous process where a species Ox receives an electron from the adjacent electrode to form Red

$$Ox + n\,e^- \underset{k_b}{\overset{k_f}{\rightleftharpoons}} Red$$

where, k_f and k_b represents the rate of the forward and reverse reactions, respectively. At equilibrium where the formal and applied potentials are the same the rate constants for both directions are equal. Under these conditions, a new rate constant called the standard rate constant can be defined k^o and k_s for solution and surface-confined species, respectively. Large standard rate constant values (k^o > 0.020 cm/s) indicate that the Ox and Red species achieve equilibrium quickly and that the electron-transfer process is fast, while slow values indicate slugglish electron transfer. Away from equilibrium (i.e. at potentials other E^o the rate of the electron transfer process in both the forward and reverse direction can be expressed according to equations 1.6 and 1.7.

$$k_f = k^o \exp\left[-\alpha n F(E - E^o)/RT\right] \qquad \text{(Equation 1.6)}$$

$$k_r = k^o \exp\left[(1 - \alpha) n (E - E^o)/RT\right] \qquad \text{(Equation 1.7)}$$

where alpha (α) is the dimensionless transfer coefficient and all other parameters are the same as before.[15],[97] Alpha defines the symmetry of the energy barrier between the Ox and Red; it is an indicator of whether the transition state for the electron-transfer process lies closer to the reactant or the product of the electrochemical reaction. This is shown graphically in Figure 1.20 for the oxidation of a species 'A' to form 'B'.

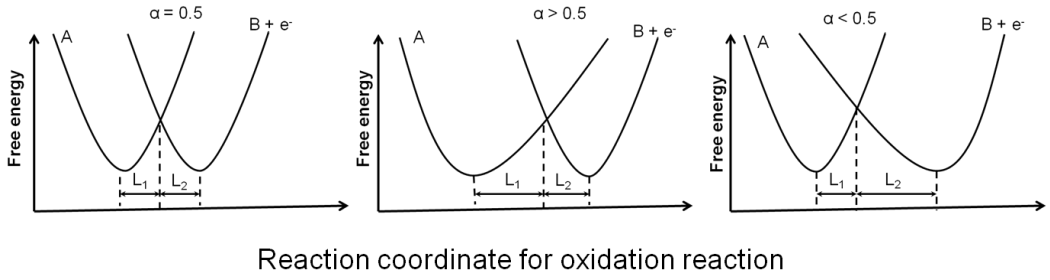

Figure 1.21 Transfer coefficient as an indicator of the symmetry of the barrier to the electrochemical reaction. Reproduced from Bond.[97]

The values of alpha range from 0 to 1, with ½ being a completely symmetric system. Values less than ½ indicate a transition state closer to the Red and values greater than ½ suggest a transition state closer to Ox.

1.6 The development of dielectric nanocomposites for energy storage applications

The development of dielectric materials for electronic applications has been advanced by the growing need for increasingly smaller energy storage platforms that are capable of accruing and efficiently delivering large amounts of charge per unit

volume.[42],[99],[100] While notable progress has been made, the storage and recoverable energy capacities of current dielectric materials severely lags behind the requirements of advanced applications. This necessitates a greater understanding of nanoscale dielectric properties and the role of permittivity and dielectric strength of materials at these length scales. Polymeric systems, for example, are often employed as dielectrics because of their high breakdown strength (> 300 V/μm); however, they generally suffer from low permittivity (< 15), which limits their achievable energy density.[101-105] In contrast, ceramic dielectrics possess high permittivity but they suffer from low breakdown strength, which limits their energy density.[100] The complementary nature of the dielectric properties of both polymers and ceramics makes a composite approach to dielectrics appealing.

In nanocomposites the underlying idea is that the combination of the high permittivity particles and large breakdown strength polymers could lead to dielectric materials with substantial energy storage capacity. However, a uniform dispersion of nanoparticles in the polymer matrix is crucial to the success of the approach in order to minimize both porosity and inhomogeneous electric fields that lead to premature failure.[106-109] In addition, the difference in permittivity between the two phases often results in early failure due to an uneven distribution of electric field between the constituents.[110] Therefore, high permittivity polymers that have dielectric constants relatively close to that of the inorganic phase are desirable. Optimization of the particle fraction in these matrices is also important in order to maximize the stored energy and simultaneously minimize porosity. Control of the chemical properties of the nanoparticle

surface through the appropriate surface modification protocol is a viable way of preparing low loss, high energy density dielectric nanocomposite materials.

1.6.1 The use of parallel plate capacitors in evaluating the dielectric properties of nanocomposite films.

In the simplest parallel plate capacitor a dielectric material is placed between two metal electrodes across which a voltage may be applied. When a voltage is applied opposite charges accumulate on each electrode, thereby creating a field across the dielectric material.[111] The amount of charge that accumulates on the electrodes (Q) is directly related to the applied voltage (V) via proportionality constant (C) that is referred to as the capacitance. The capacitance can be described as the charge per unit volt expressed in coulombs/volt or a Farad (F). The relationship is represented mathematically in equation 1.8 below.

$$Q = CV \qquad \text{(Equation 1.8)}$$

In general, the capacitance depends on the intrinsic properties of the dielectric material and the geometry/dimensions of the parallel plate capacitor as depicted in equation 1.9

$$C = \varepsilon_o \varepsilon_r \frac{A}{d} \qquad \text{(Equation 1.9)}$$

where ε_o is the permittivity of free space, ε_r is the relative permittivity of the dielectric material, A is the area of the electrode and d is the separation between the electrodes of

the device.[111] Based on the above equation, it is evident that the capacitance of a given device may be altered by changing the area of the electrode, the separation between the electrodes or the relative permittivity of the dielectric. For the purposes of this thesis, the focus will be on the dielectric material.

The charges that accumulate across the dielectric material represent stored energy. The maximum energy (E_{max}) that can be stored on a device prior to its catastrophic failure has a quadratic dependence on the maximum applied voltage (V_B). This is shown in equation 1.10. However, in the field of dielectric materials the storage capacity is often reported as the stored energy per unit volume (i.e. energy density, U_{max}), which is represented by equation 1.11 where E_B represents the breakdown field in V/m and all other variables are as defined before.

$$E_{max} = 0.5CV_B^2 \qquad \text{(Equation 1.10)}$$

$$U_{max} = \frac{E_{max}}{volume} = \frac{0.5CV_B^2}{A \times d} = 0.5\frac{\varepsilon_o \varepsilon_r (A/d) V_B^2}{A \times d} = 0.5\varepsilon_o \varepsilon_r E_B^2 \qquad \text{(Equation 1.11)}$$

1.6.2 Polarization in dielectric nancomposites

The permittivity of a material (ε*) can be expressed as a complex number with a real part (ε') and an imaginary part (ε") having the mathematical relationship described in equation 1.12 where j = √-1.

$$\varepsilon^* = \varepsilon' - j\varepsilon'' = \varepsilon_o\varepsilon_r - j\varepsilon'' \qquad \text{(Equation 1.12)}$$

The ratio of the imaginary part to the real part of permittivity (ε"/ ε') is considered the dissipation factor and is a measure of the loss experienced in the material. Under an applied electric field some of the field energy is dissipated through heat or conduction currents. Generally, materials exhibit four types of polarization mechanism depending on the frequency of the applied electric field (Figure1.22).

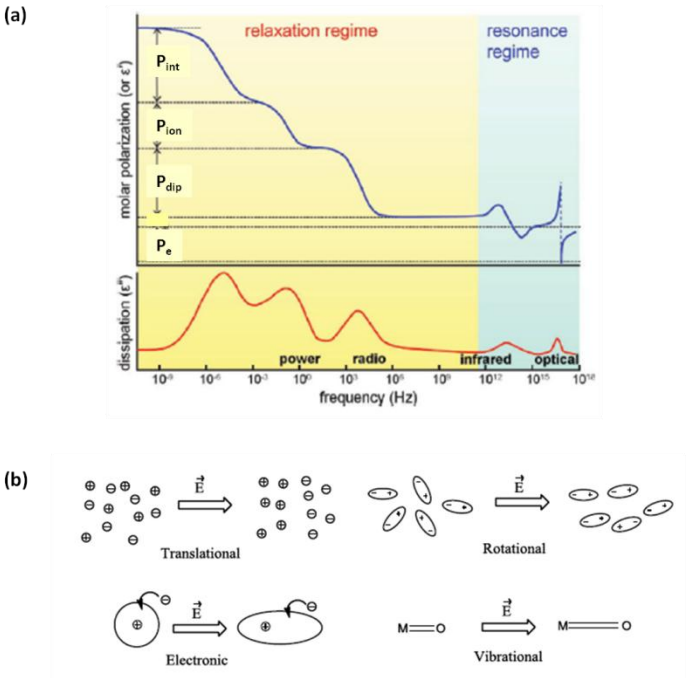

Figure 1.22 Different types of polarization as a function of frequency. P_e: electronic polarization; P_{at}: atomic/ vibrational polarization; P_{dip}: dipolar/rotational/orientational polarization; and P_{ion}: translational/interfacial polarization. (a) Reproduced from Zhu and Wang[104] (b) was adapted from MDITR the Wiki.[112]

Electronic and atomic polarizations originate from the respective displacement of the electron cloud and atoms from their equilibrium position when a material is exposed to an electric field. If the material has permanent dipoles they can rotate or orient in the presence of an electric field through rotational polarization. Translational or interfacial orientation occurs in materials that have ionic species that can migrate under the influence of an electric field

1.6.3 Methods of integrating nanoparticles into polymer matrices

In an effort to create nanocomposites with high storage capacity and low loss, a variety of chemical approaches have been developed. As mention before in section 1.2.2, one approach that have been utilized by the Marder and Perry groups at Georgia Tech, involves the functionalization of high permittivity (~ 80) barium titanate (BT) nanoparticles with a suitable phosphonic acid monolayer followed by subsequent integration into a polymer host (Figure 1.23).[107, 108]

This approach afforded films with a homogeneous dispersion of particles in the polymer matrix and a maximum permittivity of approximately 35 at 1 kHz and 50% v/v particle loading. Beyond 50% volume fraction of particle there is a rapid decline in permittivity that has been attributed to increase porosity in the matrix. The maximum energy density measured in obtained from this study was about 3.2 J/cm^3 also at 50% particle loading. Even though high relative permittivity and modest energy-density value was obtained, the breakdown field at 50% loading was about 210 V/μm. The breakdown behavior seemed to plummet around between 10% and 20% particle loading after which the decline is

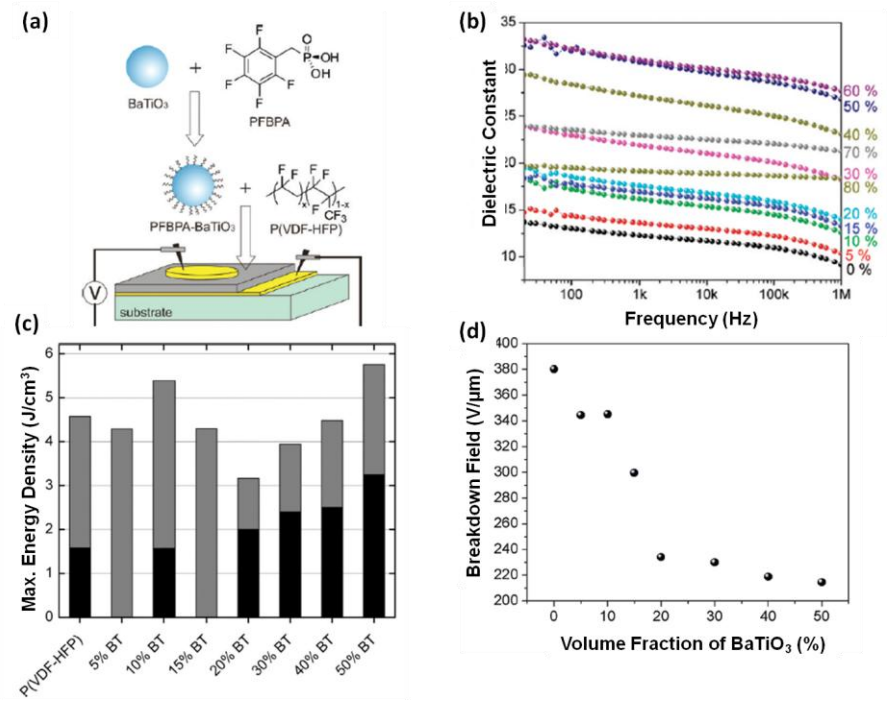

Figure 1.23 Dielectric characteristics of nanocomposites prepared from phosphonic acid functionalized barium titanate and poly(vinylidene fluoride-*co*-hexafluoro propylene) p(VDF-HFP). (a) Schematic illustrating the surface modification of BT, nanocomposite formation and the geometry of fabricated nanocomposite film capacitors. (b) Dielectric spectroscopy of nanocomposite films from 20 Hz to 1 MHz. (c) Calculated maximum energy density (gray) and measured energy density (black; at 164 V/μm). (d) Breakdown strengths at each volume fraction. Reproduced from Kim *et al.*[108]

more gradual. Li *et al.*[109] took a similar approach and functionalized barium titanate with ethylene diamines in order to promote a homogeneous dispersion of the nanoparticles in poly(vinylidene fluoride-*co*-trifluroethylene-co-chlorotrifluroethylene) p(VDF-TrFE-CTFE). The energy density measured at 150 MV/m was 7.0 J/cm3 for a 30% v/v loading of the nanoparticle, which constitutes a 120% improvement relative to the neat polymer.

An alternative approach towards developing high quality nanocomposites is the direct grafting of the polymer matrix to or from the surface of the particle. Xie *et al.*[113] demonstrated the effectiveness of this method by utilizing in situ atom transfer radical polymerization (ATRP) to graft polymethyl methacrylate (PMMA) from the surface of BT that was pre-functionalized with a brominated aminopropyl triethoxysilane (Figure 1.24). Using this approach composites with a well-defined core-shell (BT-PMMA) structure were prepared with up to ~77 wt% of particle loading. Also, a marked increase in the dielectric constant was observed (~14.6 at 1 kHz) relative to the neat polymer that had a value of ~3.5.

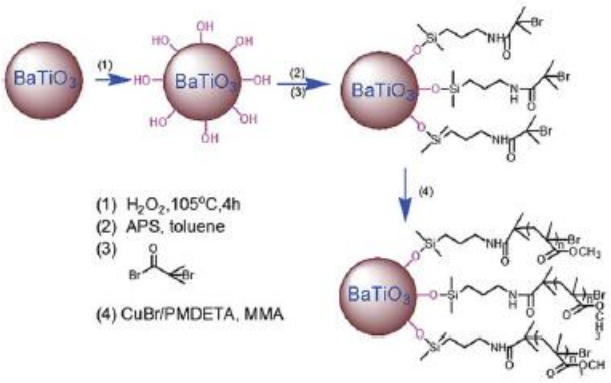

Figure 1.24 Schematic diagram illustrating the process of ATRP from the surface of BT. Reproduced from Xie *et al.*[113]

A similar approach was utilized by Li *et al.*[114] in which they prepared core-shell particles that had either a BT or zirconium oxide (ZrO_2) core and an aluminum oxide shell, from which polypropylene was subsequently polymerized. Their approach allowed

them to modulate the thickness of the aluminum shell and correlate it to the relative permittivity of the composites prepared. The results are presented in Table 1.2

Table 1.2 Dielectric properties data for metal oxide-polypropylene nanocomposites having different Al_2O_3 shell thickness on the nanofillers. Modifier from Li *et al*.[114]

Composite	Nanofiller vol (%)	Permittivity	Composite	Nanofiller vol (%)	Permittivity
$BaTiO_3$*	2	2.7 ± 0.5	$BaTiO_3$§	3	2.7 ± 0.2
	4	2.8 ± 0.3		5	2.9 ± 1.0
	13	6.0 ± 1.1		7	5.1 ± 1.7
	24	3.7 ± 0.6		14	2.7 ± 0.5
ZrO_2*	2	2.6 ± 0.9	ZrO_2§	2	1.7 ± 0.3
	4	2.6 ± 0.5		4	2.0 ± 0.4
	13	6.2 ± 0.7		8	4.8 ± 1.1
	25	4.0 ± 0.5		9	5.1 ± 1.3

§One deposition cycle of Al_2O_3
*Five deposition cycles of Al_2O_3

While only modest permittivity, only reaching 6.2, was obtained, there was also a suppression of the dielectric loss with increasing Al_2O_3 thickness.

1.7 Thesis Overview

The gradual shrinking architecture of devices coupled with the growing interest in flexible electronics amplifies the need to gain a molecular level understanding of interfaces and the role they play in modulating performance. The work presented in this dissertation focuses on the metal oxide-organic interface encountered in photovoltaic and dielectric nanocomposite capacitors; however, the knowledge garnered will be applicable to the wider organic electronics community.

Chapter 2 focuses on the synthesis and solution phase electrochemical characterization of ferrocene-based redox modifiers containing various anchoring group

(i.e. phosphonic, carboxylic, hydroxamic, and sulfonic acids) against an ITO working electrode. In order to isolate and evaluate the role of the tethering substituent on the redox potential, and the solution phase kinetics of electron transfer direct comparisons are made to ferrocene. The values of transfer coefficients and charge transfer mechanisms for the various molecules are also presented. Cyclic voltammetry (CV) and cyclic square wave voltammetry (CSWV) are the primary tools used in this study, so a comparison of the information garnered from the both techniques will be presented.

Chapter 3 examines the electron transfer kinetics between a self-assembled monolayer of the ferrocene-based redox probes synthesized in the previous chapter and ITO. Here too, electrochemical CV and CSWV studies will be used to examine the role of the various anchoring group in mediating the kinetics of charge transfer to the TCO. Characterization of the quality of monolayers formed and their impact on the electronic structure of the hybrid interface is presented based on results obtained from using X-ray photoelectron spectroscopy (XPS), ultraviolet photoelectron spectroscopy (UPS) and atomic force microscopy (AFM) measurements.

In Chapter 4 we investigate the binding of fluoroaryl acids, namely: pentaflurobenzyl phosphonic acid (PFBPA), and pentaflurobenzyl carboxylic (PFBCA) to metal oxide using XPS and infrared reflection absorption spectroscopy (IRRAS). Aryl fluorinated molecules were chosen owing to the relatively strong fluorine XPS cross-section as well as the strong C-F vibrational modes generally observed in vibrational spectroscopy. Studies were conducted using both ITO and indium zinc oxide (IZO) and the differences surface chemistry and binding mode are presented.

Chapter 5 examines the dielectric properties of composites prepared using PVDF based polymer derivatives, poly(vinylidene fluoride-co-hexafluro propylene) [P(VDF-HFP)] and poly(vinylidene fluoride-trifluoroethylene-chlorotrifluoroethylene) [P(VDF-TrFE-CTFE)], and phosphonic acid surface-functionalized barium titanate (BT) nanoparticles. In particular, the effects of processing conditions, dielectric contrast and nanoparticle loading are examined. The chapter concludes with a discussion of the role that the structure of the molecular modifiers plays in tuning the dielectric properties of the nanocomposite films

Chapter 6 presents a summary of the main results garnered throughout this thesis, their significance and broader impact. It concludes by putting forth a perspective on the field of surface science and some of the challenges that need to be met.

1.8 Literature cited

[1] U. Seifert, *Advances in Physics* **1997**, *46*, 13.

[2] R. Maget-Dana, *Biochimica Et Biophysica Acta-Biomembranes* **1999**, *1462*, 109.

[3] J. M. White, C. T. Campbell, *J. Chem. Educ.* **1980**, *57*, 471.

[4] Z. Ma, F. Zaera, *Surf. Sci. Rep.* **2006**, *61*, 229.

[5] F. Zaera, *Chem. Rec.* **2005**, *5*, 133.

[6] O. Kachurina, E. Knobbe, T. L. Metroke, J. W. Ostrander, N. A. Kotov, *Int. J. Nanotechnol* **2004**, *1*, 347.

[7] V. Kumar, *Corros. Rev.* **1998**, *16*, 317.

[8] M. Zebarjadi, K. Esfarjani, M. S. Dresselhaus, Z. F. Ren, G. Chen, *Energy Environ. Sci.* **2012**, *5*, 5147.

[9] J. H. Taphouse, O. N. L. Smith, S. R. Marder, B. A. Cola, *Adv. Funct. Mater.* **2014**, *24*, 465.

[10] B. Goswami, A. K. Ray, S. K. Sahay, *High Temp. Mater. Processes (London, U. K.)* **2004**, *23*, 73.

[11] A. J. McNamara, Y. Joshi, Z. M. Zhang, *Int. J. Therm. Sci.* **2012**, *62*, 2.

[12] A. M. Adham, N. Mohd-Ghazali, R. Ahmad, *Renew. Sus. Energ. Rev.* **2013**, *21*, 614.

[13] Q. Wang, X. H. Han, A. Sommers, Y. Park, C. T'Joen, A. Jacobi, *Int. J. Refrig.* **2012**, *35*, 7.

[14] A. J. Bard, M. Stratmann, *Semiconductor Electrodes and Photoelectrochemistry Vol. 6*, Wiley-VCH, Weinheim, **2002**.

[15] D. K. Gosser, *Cyclic Voltammetry: Simulation and Analysis of Reaction Mechanisms*, VCH Publishers, New York, **1993**.

[16] P. J. Hotchkiss, S. C. Jones, S. A. Paniagua, A. Sharma, B. Kippelen, N. R. Armstrong, S. R. Marder, *Acc. Chem. Res.* **2012**, *45*, 337.

[17] A. Sharma, B. Kippelen, P. J. Hotchkiss, S. R. Marder, *Appl. Phys. Lett.* **2008**, *93*, 163308.

[18] P. W. M. Blom, V. D. Mihailetchi, L. J. A. Koster, D. E. Markov, *Adv. Mater.* **2007**, *19*, 1551.

[19] G. Lanzani, R. Martinazzo, G. Materzanini, I. Pino, G. F. Tantardini, *Theor. Chem. Acc.* **2007**, *117*, 805.

[20] D. P. Woodruff, T. A. Delchar, *Modern Techniques of Surface Science*, Second ed., Cambridge University Press, **1994**.

[21] H. Klauk, *Organic Electronics: Materials, Manufacturing and Applications* Wiley-VCH, Weinheim, **2006**.

[22] S. R. Forrest, *Nature* **2004**, *428*, 911.

[23] S. B. Darling, F. You, *Rsc Advances* **2013**, *3*, 17633.

[24] A. Marrocchi, I. Tomasi, L. Vaccaro, *Isr. J. Chem.* **2012**, *52*, 41.

[25] J. B. H. Tok, Z. Bao, *Science China-Chemistry* **2012**, *55*, 718.

[26] A. Lodha, R. Singh, *IEEE. T. Semiconduct. M.* **2001**, *14*, 281.

[27] J. A. Rogers, T. Someya, Y. Huang, *Science* **2010**, *327*, 1603.

[28] A. Dodabalapur, *Mater. Today* **2006**, *9*, 24.

[29] T. Sekitani, T. Someya, *Adv. Mater.* **2010**, *22*, 2228.

[30] J. D. Tovar, *Acc. Chem. Res.* **2013**, *46*, 1527.

[31] V. Coropceanu, H. Li, P. Winget, L. Zhu, J.-L. Bredas, *Annu. Rev. Mater. Res.* **2013**, *43*, 63.

[32] B. Kippelen, J.-L. Bredas, *Energy Environ. Sci.* **2009**, *2*, 251.

[33] R. Steim, F. R. Kogler, C. J. Brabec, *J. Mater. Chem.* **2010**, *20*, 2499.

[34] H.-C. Lin, *Charge Transfer Processes Across Organic/Electrode Interfaces in Organic Photovoltaics*, Ph. D. Thesis, University of Arizona (Tucson), **2013**.

[35] C. J. Brabec, A. Cravino, D. Meissner, N. S. Sariciftci, T. Fromherz, M. T. Rispens, L. Sanchez, J. C. Hummelen, *Adv. Funct. Mater.* **2001**, *11*, 374.

[36] C. Goh, S. R. Scully, M. D. McGehee, *J. Appl. Phys.* **2007**, *101*.

[37] K. M. Knesting, H. Ju, C. W. Schlenker, A. J. Giordano, A. Garcia, O. N. L. Smith, D. C. Olson, S. R. Marder, D. S. Ginger, *J. Phys. Chem. Lett.* **2013**, *4*, 4038.

[38] E. L. Ratcliff, A. Garcia, S. A. Paniagua, S. R. Cowan, A. J. Giordano, D. S. Ginley, S. R. Marder, J. J. Berry, D. C. Olson, *Adv. Energy Mater.* **2013**, *3*, 647.

[39] H. T. Vo, F. G. Shi, *Microelectron. J.* **2002**, *33*, 409.

[40] S. Ramesh, B. A. Shutzberg, C. Huang, J. Gao, E. P. Giannelis, *IEEE. T. Adv. Pack.* **2003**, *26*, 17.

[41] E. L. Ratcliff, B. Zacher, N. R. Armstrong, *J. Phys. Chem. Lett.* **2011**, *2*, 1337.

[42] P. Barber, S. Balasubramanian, Y. Anguchamy, S. Gong, A. Wibowo, H. Gao, H. J. Ploehn, H. C. zur Loye, *Materials* **2009**, *2*, 1697.

[43] D. E. Ebbing, S. D. Gammon, *General Chemistry*, Houghton Mifflin New York, **2005**.

[44] S. M. Sze, K. K. Ng, *Physics of Semiconductors*, 3rd. ed. ed., Wiley Interscience, New Jersey, **2006**.

[45] H.-J. Butt, K. Graf, M. Kappl, *Physics and Chemistry of Interfaces*, 2nd ed., Wiley-VCH, Wienheim, **2006**.

[46] E. Fortunato, D. Ginley, H. Hosono, D. C. Paine, *Mrs Bulletin* **2007**, *32*, 242.

[47] H. Li, P. Winget, J.-L. Bredas, *Chem. Mater.* **2014**, *26*, 631.

[48] J. C. C. Fan, J. B. Goodenough, *J. Appl. Phys.* **1977**, *48*, 3524.

[49] B. Yaglioglu, Y.-J. Huang, H.-Y. Yeom, D. C. Paine, *Thin Solid Films* **2005**, *496*, 89.

[50] O. Warschkow, L. Miljacic, D. E. Ellis, G. B. Gonzalez, T. O. Mason, *J. Am. Ceram. Soc.* **2006**, *89*, 616.

[51] H. Gao, J. Cao, L. Liu, Y. Yang, *J. Mol. Struct.* **2011**, *1003*, 75.

[52] S. Wada, T. Hoshina, H. Yasuno, S.-M. Nam, H. Kakemoto, T. Tsurumi, M. Yashima, *Ceramic Transactions, Vol. 167*, American Ceramic Society, Westerville, OH, **2005**.

[53] S. Wada, H. Yasuno, T. Hoshina, S. M. Nam, H. Kakemoto, T. Tsurumi, *JPN J Appl. Phys. 1* **2003**, *42*, 6188.

[54] T. Tsurumi, T. Sekine, H. Kakemoto, T. Hoshina, S. M. Nam, H. Yasuno, S. Wada, in *Materials, Integration and Packaging Issues for High-Frequency Devices II, Vol. 833* (Eds.: Y. S. Cho, D. Shiffler, C. A. Randall, H. A. C. Tilmans, T. Tsurumi), **2005**, pp. 243.

[55] K. Suzuki, K. Kijima, *J. Alloys Compd.* **2006**, *419*, 234.

[56] M. Yashima, T. Hoshina, D. Ishimura, S. Kobayashi, W. Nakamura, T. Tsurumi, S. Wada, *J. Appl. Phys.* **2005**, *98*.

[57] Bigly, Wikipedia, en.wikipedia.org/wiki/Ferroelectricity, **2007**.

[58] J. C. Love, L. A. Estroff, J. K. Kriebel, R. G. Nuzzo, G. M. Whitesides, *Chem. Rev. (Washington, DC, U. S.)* **2005**, *105*, 1103.

[59] B. de Boer, A. Hadipour, M. M. Mandoc, T. van Woudenbergh, P. W. M. Blom, *Adv. Mater.* **2005**, *17*, 621.

[60] Y. Y. Liang, S. Q. Xiao, D. Q. Feng, L. P. Yu, *J. Phys. Chem. C.* **2008**, *112*, 7866.

[61] G. Heimel, L. Romaner, E. Zojer, J. L. Bredas, *Acc. Chem. Res.* **2008**, *41*, 721.

[62] P. J. Hotchkiss, H. Li, P. B. Paramonov, S. A. Paniagua, S. C. Jones, N. R. Armstrong, J.-L. Bredas, S. R. Marder, *Adv. Mater. (Weinheim, Ger.)* **2009**, *21*, 4496.

[63] Z. Y. Zhong, Y. X. Zhong, C. Liu, S. Yin, W. X. Zhang, D. F. Shi, *Phys. Status Solidi. A.* **2003**, *198*, 197.

[64] L.-W. Chong, Y.-L. Lee, T.-C. Wen, *Thin Solid Films* **2007**, *515*, 2833.

[65] H. L. Yip, S. K. Hau, N. S. Baek, A. K. Y. Jen, *Appl. Phys. Lett.* **2008**, *92*, 193313.

[66] N. R. Armstrong, C. Carter, C. Donley, A. Simmonds, P. Lee, M. Brumbach, B. Kippelen, B. Domercq, S. Y. Yoo, *Thin Solid Films* **2003**, *445*, 342.

[67] D. L. Ma, T. A. Hugener, R. W. Siegel, A. Christerson, E. Martensson, C. Onneby, L. S. Schadler, *Nanotechnology* **2005**, *16*, 724.

[68] D. L. Ma, R. W. Siegel, J. I. Hong, L. S. Schadler, E. Martensson, C. Onneby, *J. Mater. Res.* **2004**, *19*, 857.

[69] C. W. Beier, M. A. Cuevas, R. L. Brutchey, *Langmuir* **2010**, *26*, 5067.

[70] S. A. Paniagua, P. J. Hotchkiss, S. C. Jones, S. R. Marder, A. Mudalige, F. S. Marrikar, J. E. Pemberton, N. R. Armstrong, *J. Phys. Chem. C.* **2008**, *112*, 7809.

[71] M.-A. Neouze, U. Schubert, *Monatsh. Chem.* **2008**, *139*, 183.

[72] E. P. Plueddemann, *Silane Coupling Agents*, Plenum Press, New York, **1982**.

[73] P. H. Mutin, G. Guerrero, A. Vioux, *J. Mater. Chem.* **2005**, *15*, 3761.

[74] M. Hancer, *Prog. Org. Coat.* **2008**, *63*, 395.

[75] S. A. Jadhav, *Cent. Eur. J. Chem.* **2011**, *9*, 369.

[76] W. R. Thompson, J. E. Pemberton, *Langmuir* **1995**, *11*, 1720.

[77] S. Pawsey, K. Yach, J. Halla, L. Reven, *Langmuir* **2000**, *16*, 3294.

[78] S. Pawsey, K. Yach, L. Reven, *Langmuir* **2002**, *18*, 5205.

[79] C. E. Taylor, D. K. Schwartz, *Langmuir* **2003**, *19*, 2665.

[80] C. Carter, M. Brumbach, C. Donley, R. D. Hreha, S. R. Marder, B. Domercq, S. Yoo, B. Kippelen, N. R. Armstrong, *J. Phys. Chem. B* **2006**, *110*, 25191.

[81] M. Nilsing, P. Persson, L. Ojamae, *Chem. Phys. Lett.* **2005**, *415*, 375.

[82] R. Ernstorfer, L. Gundlach, S. Felber, W. Storck, R. Eichberger, F. Willig, *J. Phys. Chem. B* **2006**, *110*, 25383.

[83] B.-R. Hyun, A. C. Bartnik, L. Sun, T. Hanrath, F. W. Wise, *Nano Lett.* **2011**, *11*, 2126.

[84] L. A. Martini, G. F. Moore, R. L. Milot, L. Z. Cai, S. W. Sheehan, C. A. Schmuttenmaer, G. W. Brudvig, R. H. Crabtree, *J. Phys. Chem. C.* **2013**, *117*, 14526.

[85] C. Nogues, P. Lang, *Langmuir* **2007**, *23*, 8385.

[86] C. G. Allen, D. J. Baker, J. M. Albin, H. E. Oertli, D. T. Gillaspie, D. C. Olson, T. E. Furtak, R. T. Collins, *Langmuir* **2008**, *24*, 13393.

[87] N. H. Moreira, A. L. da Rosa, T. Frauenheim, *Appl. Phys. Lett.* **2009**, *94*.

[88] M. Gliboff, L. Z. Sang, K. M. Knesting, M. C. Schalnat, A. Mudalige, E. L. Ratcliff, H. Li, A. K. Sigdel, A. J. Giordano, J. J. Berry, D. Nordlund, G. T. Seidler, J. L. Bredas, S. R. Marder, J. E. Pemberton, D. S. Ginger, *Langmuir* **2013**, *29*, 2166.

[89] M. Gliboff, H. Li, K. M. Knesting, A. J. Giordano, D. Nordlund, G. T. Seidler, J. L. Bredas, S. R. Marder, D. S. Ginger, *J. Phys. Chem. C.* **2013**, *117*, 15139.

[90] T. J. Colacot, *Chem. Rev. (Washington, DC, U. S.)* **2003**, *103*, 3101.

[91] P. Zanello, *Electrochemical and X-ray Structural Aspects of Transition Metal Complexes Containing Redox-Active Ferrocene Ligands*, Wiley, New York, **1995**.

[92] E. Nakamura, *J. Organomet. Chem.* **2004**, *689*, 4630.

[93] J. Liu, R. Zhang, G. Sauve, T. Kowalewski, R. D. McCullough, *J. Am. Chem. Soc.* **2008**, *130*, 13167.

[94] J. D. Anderson, E. M. McDonald, P. A. Lee, M. L. Anderson, E. L. Ritchie, H. K. Hall, T. Hopkins, E. A. Mash, J. Wang, A. Padias, S. Thayumanavan, S. Barlow, S. R. Marder, G. E. Jabbour, S. Shaheen, B. Kippelen, N. Peyghambarian, R. M. Wightman, N. R. Armstrong, *J. Am. Chem. Soc.* **1998**, *120*, 9646.

[95] J. Li, L. Wang, J. Liu, G. Evmenenko, P. Dutta, T. J. Marks, *Langmuir* **2008**, *24*, 5755.

[96] B. Vercelli, G. Zotti, G. Schiavon, S. Zecchin, A. Berlin, *Langmuir* **2003**, *19*, 9351.

[97] A. M. Bond, *Broadening Electrochemical Horizons: Principles and Illustration of Voltammetric and Related Techniques*, Oxford university press, New York, **2002**.

[98] P. Monk, *Fundamentals of Electroanalytical Chemistry*, John Wiley and Sons Ltd, West Sussex, **2001**.

[99] H. S. Nalwa, *Handbook of Low and High Dielectric Constant Materials and Their Applications*, Academic Press, New York, **1999**.

[100] Q. Wang, L. Zhu, *J. Polm. Sci. Pol. Phys.* **2011**, *49*, 1421.

[101] W. J. Sarjeant, J. Zirnheld, F. W. MacDougall, *IEEE. T. Plasma Sci.* **1998**, *26*, 1368.

[102] W. J. Sarjeant, I. W. Clelland, R. A. Price, *Proc. IEEE.* **2001**, *89*, 846.

[103] H. W. Starkweather, P. Avakian, R. R. Matheson, J. J. Fontanella, M. C. Wintersgill, *Macromolecules* **1992**, *25*, 6871.

[104] L. Zhu, Q. Wang, *Macromolecules* **2012**, *45*, 2937.

[105] K. Yao, S. Chen, M. Rahimabady, M. S. Mirshekarloo, S. Yu, F. E. H. Tay, T. Sritharan, L. Lu, *IEEE. T. Ultrason. Ferro.* **2011**, *58*, 1968.

[106] S. Ogitani, S. A. Bidstrup-Allen, P. A. Kohl, *IEEE. T. Adv. Pack.* **2000**, *23*, 313.

[107] P. Kim, S. C. Jones, P. J. Hotchkiss, J. N. Haddock, B. Kippelen, S. R. Marder, J. W. Perry, *Adv. Mater.* **2007**, *19*, 1001.

[108] P. Kim, N. M. Doss, J. P. Tillotson, P. J. Hotchkiss, M.-J. Pan, S. R. Marder, J. Li, J. P. Calame, J. W. Perry, *ACS Nano* **2009**, *3*, 2581.

[109] J. Li, J. Claude, L. E. Norena-Franco, S. Il Seok, Q. Wang, *Chem. Mater.* **2008**, *20*, 6304.

[110] J. Y. Li, L. Zhang, S. Ducharme, *Appl. Phys. Lett.* **2007**, *90*.

[111] D. C. Giancoli, *Physics for Scientist and Engineers*, Prentice Hall, New Jersey, **2000**.

[112] MDITR, MDITR Wiki, photonicswiki.org/index.php?title=Polarization_and_Polarizability, **2008**.

[113] L. Xie, X. Huang, C. Wu, P. Jiang, *J. Mater. Chem.* **2011**, *21*, 5897.

[114] Z. Li, L. A. Fredin, P. Tewari, S. A. DiBenedetto, M. T. Lanagan, M. A. Ratner, T. J. Marks, *Chem. Mater.* **2010**, *22*, 5154.

CHAPTER 2 SOLUTION PHASE ELECTROCHEMICAL CHARACTERIZATION OF FERROCENE MODIFIERS CONTAINING VARIOUS ANCHORING GROUPS ON ITO

2.1 Ferrocene modifiers with various anchoring group

The merits of using ferrocene as an electroactive probe have been previously discussed in section 1.53. It has been shown that measurements of electron transfer rates between ferrocene molecules and metal oxide electrodes can provide insight into the kinetics of charge-transfer at the TCO-organic interface in solid state organic electronic devices.[1, 2] As such, there is merit to using ferrocene to understand the kinetics of charge transfer between redox molecules in solution and metal oxide electrodes. In particular, there is an interest in understanding how various anchoring groups, often utilized in surface modifiers, affect the molecules redox properties as well as the heterogeneous charge transfer kinetics at the solution-TCO interface. As such, this chapter focuses on the design and solution phase electrochemical characterization of ferrocene-based redox molecules that have different anchoring groups (Figure 2.1). Most of the studies reported in literature regarding electron-transfer processes across the metal oxide-organic interface have been done using dye molecules that utilize phosphonic acids ($pKa_1$1 – 4, pK_{a2} 5 – 9)[3] and carboxylic acid (pK_a 2 – 5) as the anchoring moiety.[4] However, other acids, such as sulfonic acids (pK_a -9 – -3)[5-7] and hydroxamic acids (pK_a 9),[8-11] have been shown to form ordered monolayers on metal oxides but much less is understood about the role that these anchoring groups play in mediating the kinetics of charge transfer across hybrid interfaces.

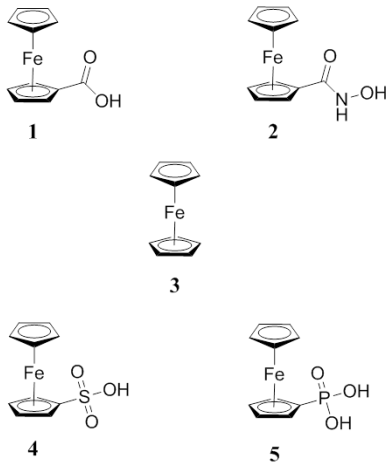

Figure 2.1 Structure of the redox surface modifiers and ferrocene. 1, Ferrocene carboxylic acid (FcCA) 2, ferrocene hydroxamic acid (FcHA), 3, ferrocene 4, ferrocene sulfonic acid (FcSA) and 5, ferrocene phosphonic acid (FcPA).

In order to isolate and evaluate the role of the tethering substituent on the redox properties of the molecules, ferrocene (the unsubstituted analog) was included for comparison.

Cyclic voltammetry (CV) and cyclic square wave voltammetry (CSWV) are the two techniques that were used to conduct the electrochemical analysis. CV is a technique that is often used to evaluate the kinetics and mechanisms of charge-transfer (CT) owing to its versatility, low cost instrumentation, and the wealth of theoretical background available to the experimentalist. However, the technique has limited detection at concentrations below 10 μM due to the predominance of background currents that flow because of changes in the structure of the electrode-solution interface that occur in the absence of charge-transfer (non-Faradaic currents). These changes result from accumulation of electrolyte ions at the electrode-solution interface. In such cases, an electrical double layer is created at the electrode-solution interface, which behaves as a

capacitor in series with the solution resistance. Background currents also rise from Faradaic reactions involving the solvent or trace levels of redox active solutes that may be present in solution. The resulting background current limits the detection limit of CV.[12],[13] In contrast, CSWV is able to measure sub-micromolar concentration with increased resolution due to the techniques inherent ability to discriminate against background currents.[14-16] The details of the techniques will be explained in section 2.2 and 2.3.

2.2 An overview of cyclic voltammetry

In CV the current is measured as a function of the potential applied between the working electrode and a reference electrode. The detailed characteristics of the signal obtained provide information on the kinetics and mechanisms involved in heterogeneous electron transfer. The potential on the working electrode (is applied relative to a reference electrode and a third auxiliary/counter electrode is incorporated in order to complete the circuit. Figure 2.2 shows a schematic setup for a cell used in CV studies. A triangular voltage waveform is used in CV such that the potential is varied linearly for a period of time (t) before the direction of scan is reversed and the potential is returned to its original value (Figure 2.3). The potential range is chosen such that the oxidation and/or the reduction of the electroactive species occurs prior to voltage at which the potential is reversed (i.e. the switching potential). The waveform can therefore be described in terms of the sweep/scan rate (ν), the initial potential (E_i), and the switching potential (E_s) as described in Equations 2.1 and 2.2.

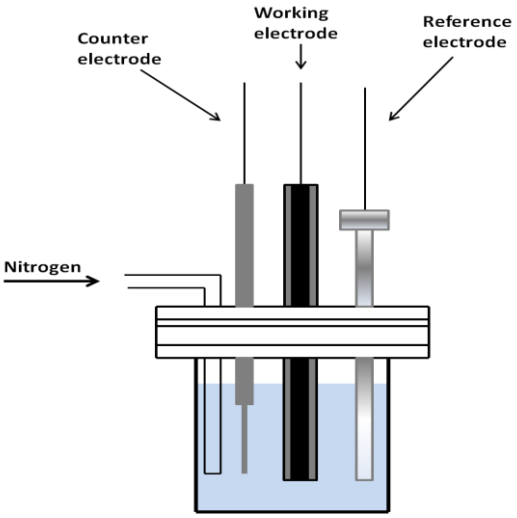

Figure 2.2 Typical electrochemical setup for voltammetric studies. The figure shows the three electrodes used in conducting measurements as well as a nitrogen inlet that is used to remove oxygen from the electrolyte solution. Reproduced from Gosser.[13]

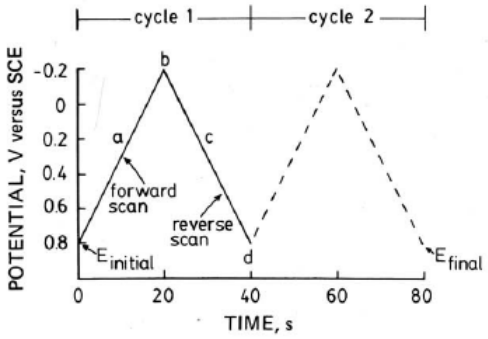

Figure 2.3 Two cycles of a typical signal for cyclic voltammetry-triangular potential waveform with initial potential at 0.8 V and switching potential at -0.2 V. The forward scan (a) and reverse scan (c) are also indicated. Reproduced from Kissinger and Heineman.[17]

$$E = E_i + \nu t \qquad \text{(Equation 2.1)}$$

$$E = E_s - \nu t \qquad \text{(Equation 2.2)}$$

An example cyclic voltammogram for a 6.0 mM solution of $K_3Fe(CN)_6$ in 1.0 M KNO_3 is shown in Figure 2.4 and the reaction is given below.

$$Fe(CN)_6^{3-} + e^- \rightleftharpoons Fe(CN)_6^{4-}$$

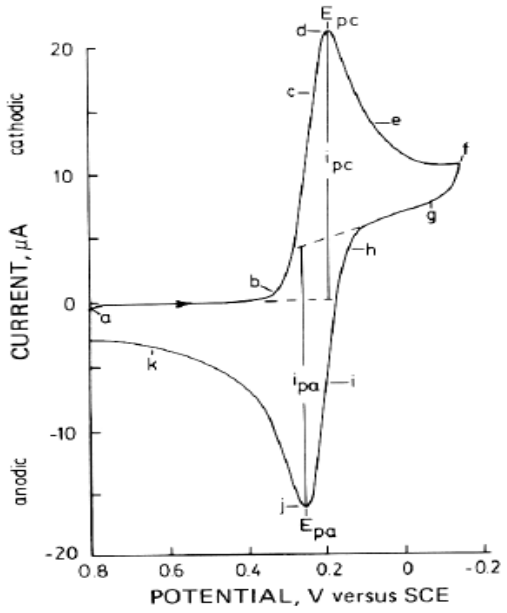

Figure 2.4 CV of 6 mM $K_3Fe(CN)_6$ in 1 M KNO_3. The scan was initiated at 0.8 V in the negative direction at a scan rate of 50 mV/s using a platinum working electrode. E_{pc}, i_{pc}, E_{pa} and i_{pa} represents the cathodic peak potential, the cathodic peak current, the anodic peak potential and the anodic peak current, respectively. Reproduced from Kissinger and Heineman.[17]

As the potential becomes increasingly negative the current observed remains at zero because there is no species present in solution that can be oxidized or reduced within this potential range. A point **b** is reached where the current begins to increase, which indicates the onset of the reduction of as the hexacyanoferrate (III) ion ($Fe(CN)_6^{3-}$) to hexcyanoferrate (II) ion ($Fe(CN)_6^{4-}$). Between **b** and **d** the current rapidly increases as more of the $Fe(CN)_6^{3-}$ is converted to $Fe(CN)_6^{4-}$ until the equilibrium Nernst conditions (section 1.5.2) are met at point **d**, which represents the cathodic peak potential (E_{pc})

Beyond this point the current decreases up to point **f** where the direction of scan is switched. The current remains positive between **f** and **g** since the applied potential within this range is still sufficient to continue reducing the ($Fe(CN)_6^{3-}$). This changes, however, at point **h**, which marks the onset of the oxidation of ($Fe(CN)_6^{4-}$) to regenerate ($Fe(CN)_6^{3-}$). The reaction rapidly approaches equilibrium conditions at point **j**, which represents the anodic peak potential (E_{pa}). Beyond this point the current is again reduced. The potential at midpoint between the anodic and cathodic peak potential (i.e., the half-wave potential, $E_{1/2}$) is related to the formal potential (E^o) via the relationship shown in Equation 2.3

$$E_{1/2} = E^o + \left(\frac{RT}{nF}\right)\ln(D_O/D_R)^{\frac{1}{2}} \qquad \text{(Equation 2.3)}$$

where D_O and D_R are the diffusion coefficients for the oxidized and reduced species, respectively n is the number of electrons transferred, F is Faraday's constant, R is the molar gas constant and T is temperature. If the diffusion coefficients are the same for the oxidized and reduced species then the formal potential is equal to the half-wave potential.

2.2.1 Evaluation of charge-transfer kinetics in solution using CV

The Nicholson formalism[18] can be used to determine the electron-transfer rate constant from the difference in the oxidation and reduction peak potentials (ΔE_p). In this approach, the theoretical Nicholson working curve (Figure 2.5) is used to relate the separation in the peak potential from the voltammogram to an electrokinetic parameter (Ψ^*) that is defined mathematically as shown in Equation 2.4

$$\Psi^* = \frac{\left(\frac{D_O}{D_R}\right)^{\alpha/2} k^o}{\left(\pi D_O \frac{nF}{RT}\nu\right)^{1/2}}$$ (Equation 2.4)

where α is the charge-transfer coefficient, k^o is the standard rate constant, and all other terms are as defined before. Details are provided in appendix B. By assuming $D_O = D_R$ and a symmetric energy barrier (α = 0.5) the standard rate constant for the electron transfer can be determined. Since CV determined alpha values in the range of 0.3 to 0.7 (typical for many redox couples) only reflect about 5% variation in ΔE_p[18] the assumption about alpha is reasonable.

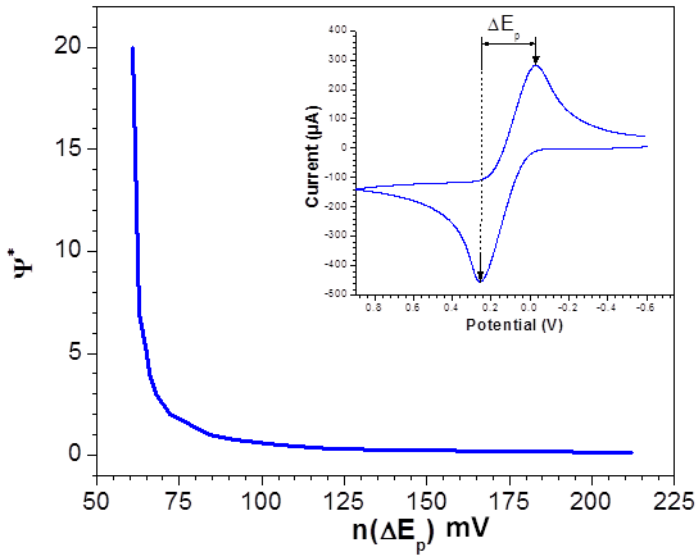

Figure 2.5 Nicholson working curve for deducing the electrokinetic parameter (Ψ*) from the separation in peak potentials (ΔE_p) of the voltammetric response of an electroactive species in solution. The inset shows an example voltammogram with ΔEp clearly illustrated. The working curve is adapted from the work of Nicholson for alpha of 0.5.[18]

2.2.2 Electrochemical reversibility in CV

Electrochemical reversibility is a measure of the rate at which charge transfer occurs between the working electrode and the redox species. In an electrochemically reversible system the charge transfer is fast such that equilibrium is achieved rapidly at each potential applied on the timescale of the experiment. Since the timescale of CV can be varied by varying the scan rate, the concept of electrochemical equilibrium is a practical term rather than an absolute. Therefore, a reaction may be electrochemically reversible at one scan rate and irreversible at another.[13] The Nernst equation (equation 1.15) applies to processes that are considered to be electrochemically reversible. Care should be taken not to confuse chemical and electrochemical reversibility; the former suggest that when the cell current is reversed the electrochemical reaction is also reversed without the introduction of any new species. Figure 2.6 shows a theoretical voltammogram for an electrochemically reversible one electron transfer process.

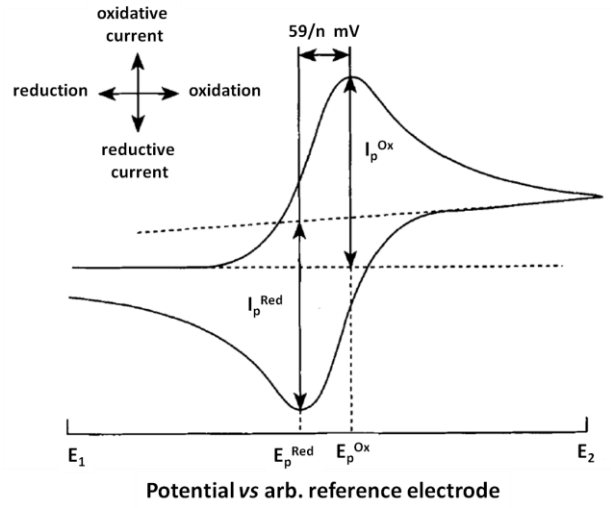

Figure 2.6 Typical cyclic voltammogram obtained for a reversible one electron redox process at 25 C. Modified from Eklund *et al*.[19]

The figure shows that in an ideal reversible electrochemical process, the peak potentials of the voltammograms are separated by 59 mV/n for an n-electron couple.[20] Furthermore, under conditions of electrochemical reversibility the relationship between the bulk concentration of the redox species and the peak currents can be expressed through the Randles-Sevcik relationship[12, 13] (equation 2.5)

$$I_p = (2.69 \times 10^5) n^{3/2} D^{1/2} \nu^{1/2} C^* A \qquad \text{(Equation 2.5)}$$

where I_p is the peak current, n is the number of electrons transferred during the process, C^* is the bulk concentration of the redox species, D, is the diffusion coefficient of the oxidized or reduced species, and A is the area of the electrode. Based on the Randles-Sevcik equation, in an electrochemically reversible process the peak current is limited by the rate at which the redox molecules can be supplied to the electrode (i.e., diffusion).

If the kinetics is extremely slow such that the exchange of charge between the redox species and the electrode is the rate limiting step (i.e., not diffusion) then the process is no longer governed by the Nernst equation and therefore not considered reversible. Figure 2.7 shows the cyclic voltammogram for a completely electrochemically irreversible one electron process. The voltammogram depicts a single peak for the forward electron transfer process because the reverse process does not occur at a measureable rate. Electron transfer rates that occur in between these two regions are said to be quasi-reversible. Table 2.1 shows diagnostic criteria for electrochemical reversibility of a redox couple.

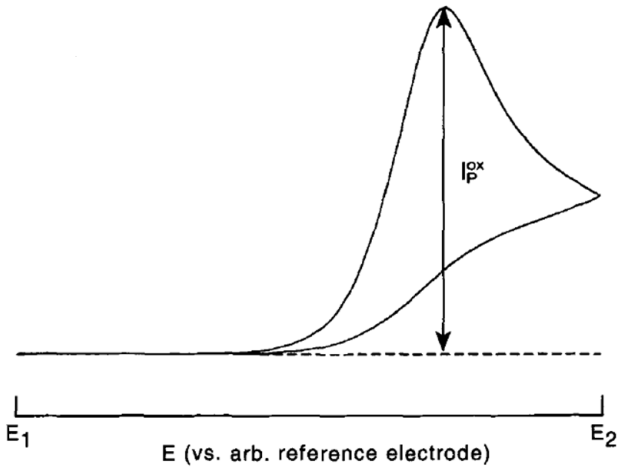

Figure 2.7 Typical cyclic voltammogram obtained for a electrochemically irreversible one electron redox process at 25 °C. Modified from Eklund *et al*.[19]

Table 2.1 Diagnostic criteria for assessing electrochemical reversibility. Reproduced from Monk[21] and Bond.[12]

I_p is proportional to square root of scan rate
ΔE_p = 57 mV/n
Reversibility $k^o > 0.3\ v^{1/2}$ cm/s
Quasi-reversible $k^o > 2 \times 10^{-5}\ v^{1/2}$ cm/s
Irreversible $k^o < 2 \times 10^{-5}\ v^{1/2}$ cm/s

2.3 An overview of cyclic square wave voltammetry (CSWV)

The potential signal used in cyclic square wave voltammetry can be considered as a superposition of a square wave on top of cyclic staircase voltammetry as depicted in the waveform shown in Figure 2.8a. Each step in the square wave component can be considered as two pulses: (i) the forward pulse and (ii) the reverse pulse. The current is

sampled at the end of each pulse and is designated as a forward pulse current (I_{pulse}) and reverse step current (I_{step}). In the output voltammogram, a net current is usually indicated, which is arrived at by taking the difference between the forward and reverse currents. The cyclic nature of the technique adds another tier to the analysis providing a forward sweep and a reverse sweep both of which will also have the previously mentioned currents. In total the technique has a total of six currents, namely: (i) forward sweep forward current, (ii) forward sweep reverse current, (iii) reverse sweep forward current, (iv) reverse sweep reverse current, (v) the net current on the forward sweep ($\Delta I_{p,f}$) and (vi) the net current on the reverse sweep ($\Delta I_{p,r}$). One peak potential is observed for each sweep and they are referred to as forward sweep peak potential (E_{pf}) and reverse sweep peak potential (E_{pr}). The only difference between CV and CSWV is the nature of the potential signal being applied; the instrument setup remains the same. Based on the waveform of CSWV the applied potential at any given odd numbered step can be calculated as

$$E = E_i + (m - 1)E_{step} + E_{sw} \qquad \text{(Equation 2.6)}$$

and the even-numbered potentials are calculated as

$$E = E_i + mE_{step} \qquad \text{(Equation 2.7)}$$

where m is the step number, E_i is the initial potential, E_{step} is the potential increment, and E is the applied potential.

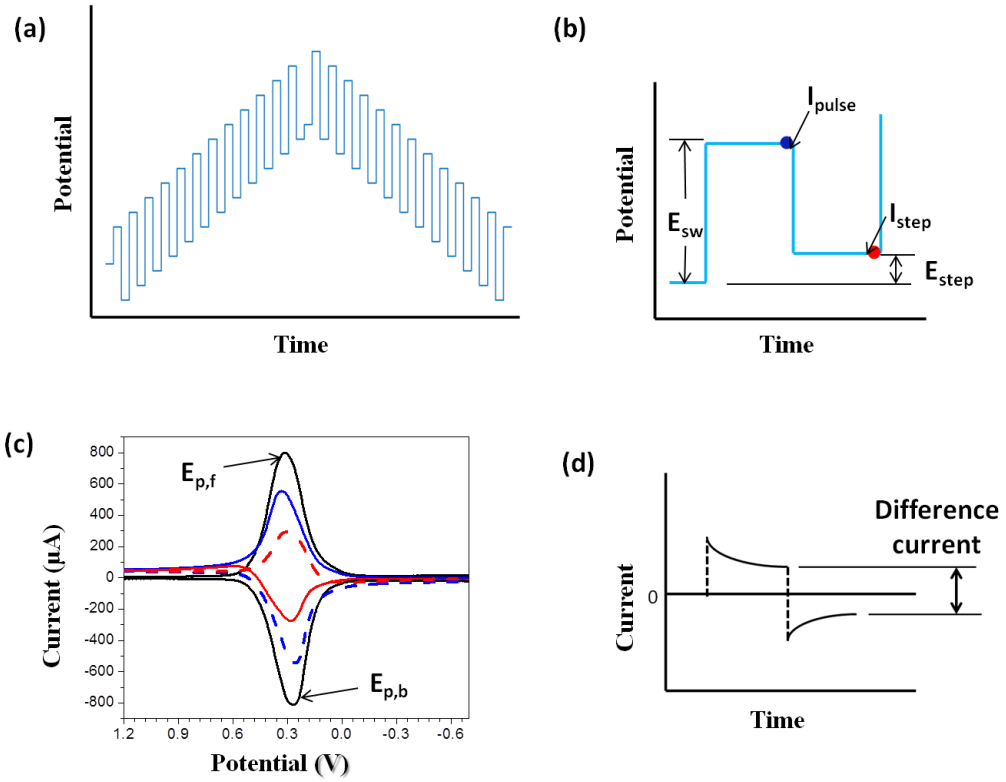

Figure 2.8 Schematic showing the various constituents of cyclic square wave voltammetry (CSWV). The figure shows the CSWV wave form (a) in which the backward potential step is a mirror image of the forward. An enlargement of a single step is shown (b) in which the amplitude (E_{sw}), the step or increment (E_{step}) and the sample point of the forward and reverse currents are shown. The current *vs.* time profile for a single step is depicted (d). An example of a CSWV voltammogram (c) with the forward (blue) and reverse (red) current shown for both the forward sweep (solid line) and reverse sweep (dashed line). Net currents are shown in solid black.

2.3.1 Evaluation of charge transfer kinetics in solution using CSWV

In order to evaluate the kinetics of charge transfer in solution using CSWV a method developed by O'Dea *et al*[22]. for square wave voltammetry and modified by the Bottomley Group at Georgia Tech[14, 15, 23, 24] was adapted. Recall from section 1.5.2, that the equilibrium forward and reverse rate of charge transfer can be represented by equations 1.6 and 1.7, respectively. By combining these equations with the diffusion

coefficients and step time (τ) a dimensionless rate constant (ktau) can be derived as shown in Equation 2.8

$$\mathrm{ktau} = \mathrm{k^o}\frac{\tau^{1/2}}{\mathrm{D_O^{\alpha/2}D_R^{(1-\alpha)/2}}} \qquad \text{(Equation 2.8)}$$

where τ is the step time (in seconds) and all other terms are as defined before in section 2.21.[22] Similar to the Nicholson approach,[18] a working curve can be generated that relates the separation in the peak potential of the voltammograms obtained from CSWV to the dimensionless rate constant as shown in Figure 2.9. However, before the working curve can be plotted, the transfer coefficient and formal potential must first be deduced. In their theoretical investigation of the effect of step height on the shape of the voltammogram the Bottomley Group predicted that α and the formal potential are related to the peak potentials by the equation 2.9.

$$\alpha\left(\mathrm{E_{p,f}} - \mathrm{E^o}\right) = (1-\alpha)\left(\mathrm{E_{p,r}} - \mathrm{E^o}\right) \qquad \text{(Equation 2.9)}$$

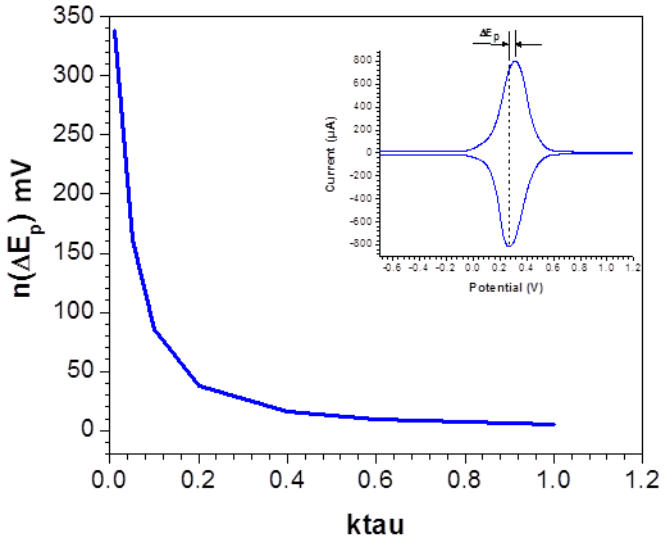

Figure 2.9 CSWV working curve for deducing the dimensionless rate constant (ktau) from the separation in peak potentials (ΔE_p) of the voltammetric response of a redox species in solution. The inset shows an example voltammogram with ΔE_p clearly illustrated.

In addition, they also found that when the experimental frequency is modulated the transfer coefficient can deduced from the slope of a plot of $E_{p,r}$ *vs* $E_{p,f}$ according to the relationship below

$$\text{slope} = \alpha/(1-\alpha)$$

Therefore, the transfer coefficient can be deduced and substituted into equation 2.9 in order to determine the formal potential. In turn, the working curve that relates ΔE_p to ktau can be generated using the predetermined alpha value. Once ktau is known equation 2.8 can be used to calculate the standard rate constant.

2.3.2 Electrochemical reversibility in CSWV

One major advantage of CSWV is that the various parameters of the waveform (amplitude, step height, and step time) can be used as diagnostic tools for deducing mechanisms involved in various electrochemical processes. Thorough theoretical and experimental investigations of the mechanistic criteria for CSWV have been performed by Helfrick [14, 15] and Mann.[24] In these studies the authors explored the changes in the current and potential of the voltammograms as a function of the input signal parameters. Equation 2.10 shows the relationship between current and step time for each pulse.

$$i(t) = \frac{\Delta\Psi(t) n F A D^{1/2} C^*}{(\pi t)^{1/2}} \qquad \text{(Equation 2.10)}$$

where i(t) is the current at a time t, and $\Delta\Psi(t)$ is the current function at time t. All other terms are as defined before. Recall from Figure 2.8b that the current is sampled at the end of each pulse; therefore as the period/step time is increased for a reversible process both the forward and reverse currents will be affected equally and their ratio will remain at unity. A scan rate can be defined for CSWV as the quotient of the step height in volts divided by step time (s). As was the case for CV, the peak potential for a reversible system is unaffected by changes in scan rate, and by extension, changes in step height and step time. In contrast, an irreversible system shows wide separation of the peak potentials around the formal potential and moderate separations of the potential indicate quasireversibility. The concept of reversibility is illustrated in Figure 2.10. Additionally,

the difference current is reduced as step height is increased for a reversible process because of a smaller voltage difference between the forward and reverse pulse potentials.

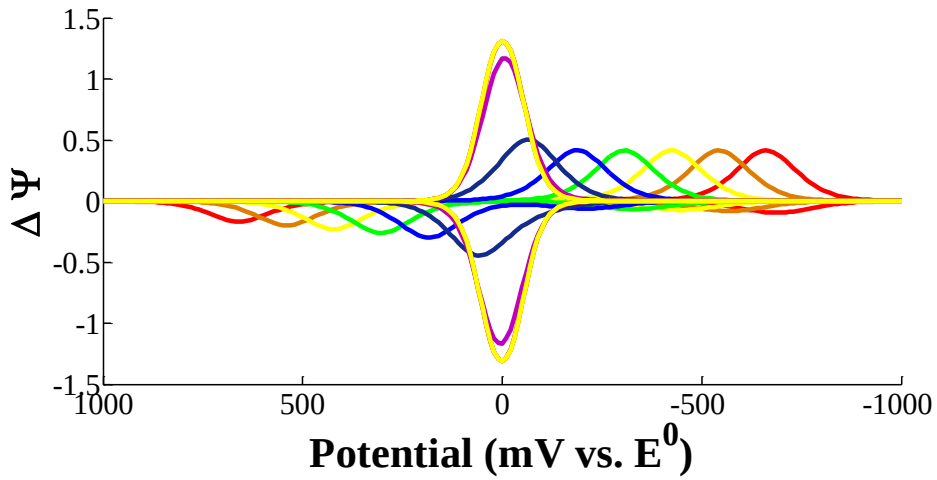

Figure 2.10 Theoretical CSW voltammograms showing varying degrees of reversibility. Red voltammogram represents an irreversible case while the other traces exhibit increasing reversibility towards the center yellow voltammogram that is considered completely reversible. Reproduced from Mann *et al*.[24]

However, if the step height is fixed and the amplitude of the signal is increased, the peak current increases. Peak potentials are again unaffected by changes in amplitude for a reversible process. Tables 2.2 and 2.3 summarize the diagnostic criteria for a reversible and quasireversible CSWV processes.

Table 2.2 Diagnostic criteria for a reversible CSWV mechanism. Reproduced from Helfrick.[14, 15]

Parameter	I_{pf}	I_{pr}	I_{pf}/I_{pr}	E_{pf}	E_{pr}	ΔE_p
Amplitude	+	+	=	=	=	=
Step time	-	-	=	=	=	=
Step height	-	-	=	=	=	=

All trends are for increasing value of parameter. A decrease is indicated by a -, an increase by a + and an = indicates that the value is constant.

Table 2.3 Diagnostic criteria for a quasireversible CSWV mechanism. Reproduced from Mann.[24]

Parameter	I_{pf}	I_{pr}	I_{pf}/I_{pr}	E_{pf}	E_{pr}	ΔE_p
Amplitude	+	+	=	=	=	=
Step time	-	-	+	-	-	-
Step height	+	+	-	-	+	+

All trends are for increasing value of parameter. A decrease is indicated by a -, an increase by a + and an = indicates that the value is constant.

2.4 Solution phase cyclic voltammetry characterization of redox modifiers.

The redox properties of ferrocene and its derivatives were evaluated against an ITO electrode using cyclic voltammetry. Solutions (1 mM) of the electroactive molecules in 0.1 M tetrabutylammonium perchlorate (TBAP) in acetonitrile (ACN) were used to conduct these studies. All the voltammograms show the anticipated one electron redox behavior that is well documented for ferrocene (Figure 2.11).

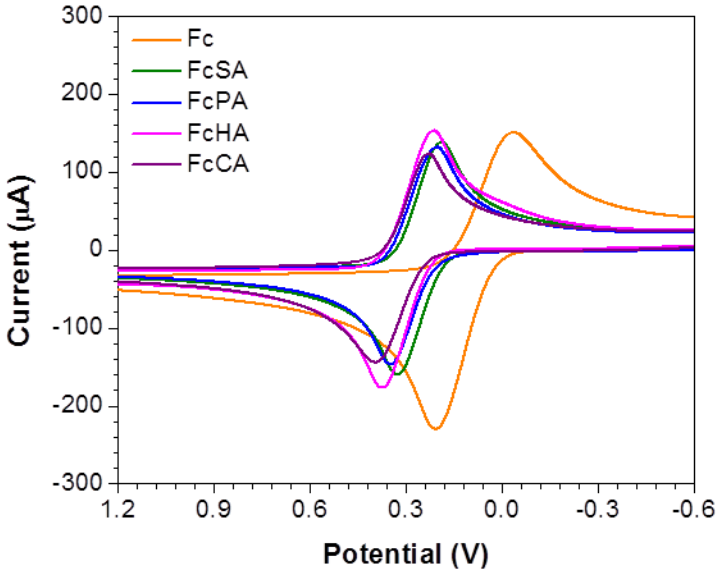

Figure 2.11 Solution phase cyclic voltammograms of ferrocene and ferrocene derivatives *vs* a Ag/Ag+ reference electrode. Measurements were taken at a scan rate of 0.1 V/s against an oxygen plasma treated working electrode.

Diffusion coefficients were first determined separately for each molecule by employing the Randles-Sevcik approach[12, 13] and these values are in turn used to calculate the outer-sphere electron transfer rate constants via the Nicholson formalism.[18] The results of these studies are summarized in Table 2.4.

Table 2.4 Solution phase redox properties of ferrocene and ferrocene derivatives. All measurements of potential and rate constants are reported for a scan rate of 0.1 V/s *vs* a Ag/Ag^{+} reference electrode using 1 mM solutions of the electroactive molecules. Hammett parameters for the various substituents are also included from the works of Hansch[25] and Imaizumi.[26]

	Fc	FcCA	FcPA	FcSA	FcHA
$E_{1/2}$ (mV)	91 ± 4	314 ± 1	276 ± 1	261 ± 1	294 ± 0.3
ΔE_p (mV)	238 ± 2	162 ± 8	144 ± 1	135 ± 2	159 ± 3
D_O (cm^2/s)	5.5×10^{-6}	1.76×10^{-6}	5.0×10^{-6}	4.5×10^{-6}	4.7×10^{-6}
$k^o \times 10^{-3}$(cm/s)	1.1 ± 0. 1	1.1 ± 0.1	2.2 ± 0.01	2.4 ± 0.06	1.7 ± 0.04
σ_p	0	0.45	0.42	0.64	N/A

Assuming $D_O = D_R$

The half-wave potential ($E_{1/2}$) is a measure of the ease with which the molecules of interest are oxidized under the conditions of the experiment and it is independent of scan rate and concentration. From the voltammograms in Figure 2.11, it can be seen that the modifiers experience a different chemical environment from ferrocene, which is reflected in their $E_{1/2}$ values. By comparing the $E_{1/2}$ of the modifiers to that of ferrocene, insight can be gained into the electronic effect of the tethering substituent on their redox properties. The larger the $E_{1/2,}$ the more difficult it is to oxidize the molecule; i.e., the order of increasing difficulty of oxidation for the molecules investigated is Fc < FcSA < FcPA < FcHA < FcCA. All the modifiers have an electron-withdrawing substituent, which leads to larger partial positive charge on the iron atom than in ferrocene itself resulting in a more positive $E_{1/2}$ being required for their oxidation relative to unsubstituted Fc/Fc^{+}. Hammett parameters (σ_p), which are based on the ionization constant of substituted benzoic acid, are a crude measure of the electron donating/withdrawing strength of substituent groups. Table 2.4 shows the Hammett parameters for the substituent groups with the exception of hydroxamic acid. Larger Hammett parameters values generally correlate to stronger electron withdrawing effect and greater potential requirements for oxidation. Based on the results, no reasonable correlation could be made between the Hammett parameter and $E_{1/2}$ values. This inconsistency could stem from a number of reasons including but not limited to: (i) the varying degree of solubility among the modifiers, (ii) poor extrapolation of data from the benzoic acid standards, (iii) the ability of the molecule to interact with the electrically active sites of the electrode, (iv) hydrogen bonding in solution and, (v) multiple

electrochemically unresolved processes occurring in solution simultaneously. Since the shift in $E_{1/2}$ can be considered to be a measure of the substituent group's ability to stabilize the ferrocenium cation formed upon oxidation, under the experimental conditions tested here the sulfonic and carboxylic acids seem to be the most and least effective in this regard, respectively. Of the two modifiers, the sulfonic acid would more readily facilitate the passage of holes from the active layer to the TCO electrode in OPVs due to its lower IP relative to the carboxylic acid.

Plots of peak current vs. the square root of scan rate (Figure 2.11) were constructed for the various molecules and the slopes used to calculate diffusion coefficients. The plots show a linear relationship between the current and the square root of scan rate suggesting a diffusion-limited mechanism is involved in the electrochemical process. Table 2.4 shows that Fc has the highest diffusion, which is consistent with it having the smallest Stokes-Einstein hydrodynamic radius (R_H, effective hydrated radius in solution) among the molecules. [27, 28]

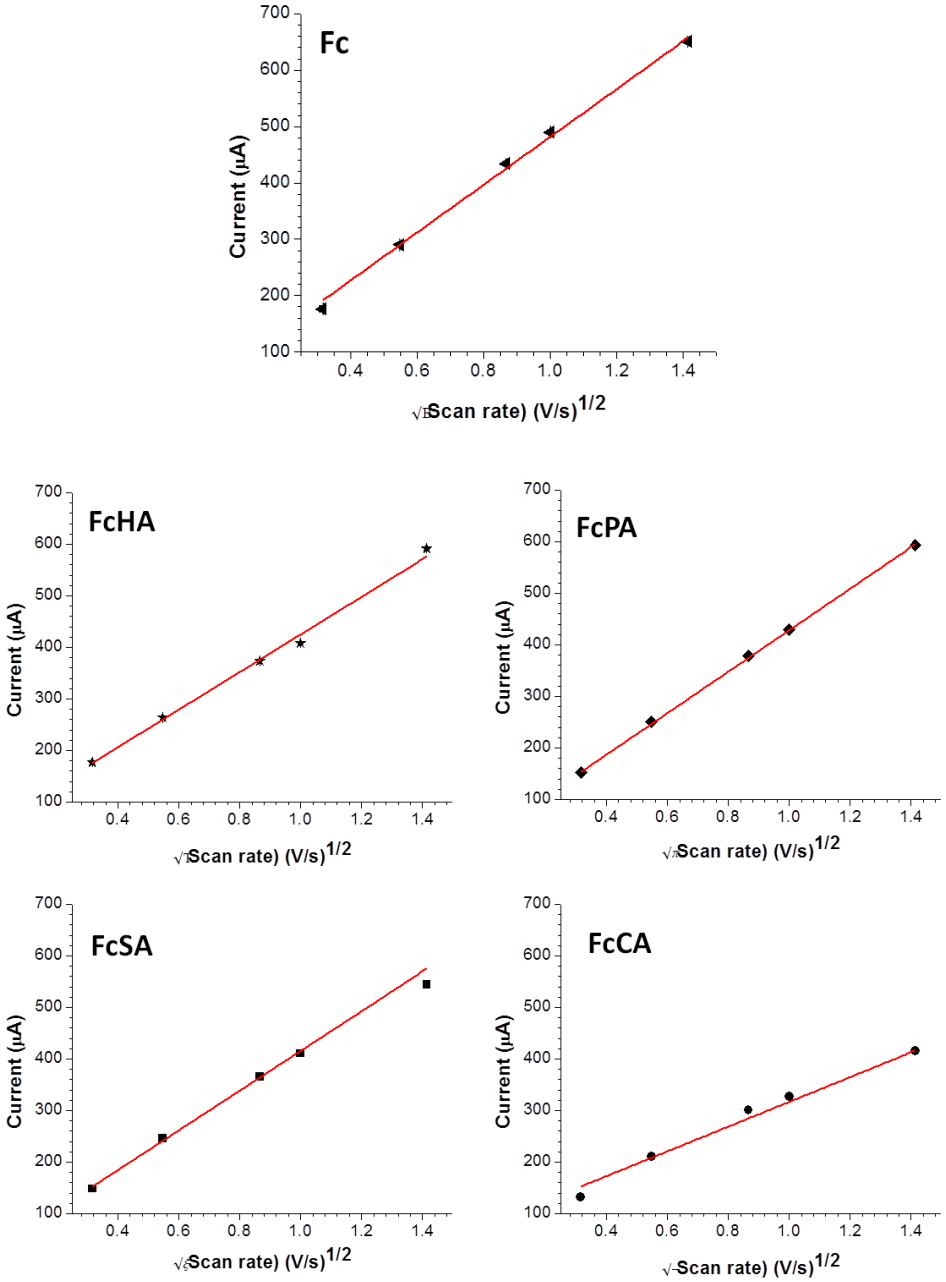

Figure 2.12 Plots of current *vs*. square root of scan rate for ferrocene, and the various modifiers. The linear fits to each plot is shown in red; all fits have a residual (R^2) > 0.992.

According to the Stokes-Einstein relationship, the differences in the diffusion coefficient of the molecules will be dependent on their hydrodynamic radii as shown in Equation 2.11

$$R_H = \frac{k_b T}{6\pi\eta D} \qquad \text{(Equation 2.11)}$$

where D is the diffusion coefficient, T is temperature, k_b is Boltzmann constant and η is the viscosity of the solvent. Based on the molecular structure of the other molecules, it is not expected that their hydrodynamic radii will be significantly different, so they should have similar diffusion coefficient. However, the results show that there are marked differences in the diffusion coefficient of the other molecules suggesting other interactions, such as hydrogen, bonding might be at play as well.

The electron-transfer rates were estimated using the Nicholson method and the diffusion coefficient values determined from the Randles-Sevcik analysis. From Table 2.4 the order of increasing rate constant is Fc ≈ FcCA < FcHA < FcPA < FcSA. The table shows that smaller peak separation (ΔE_p) affords higher electron-transfer rate constant, which is consistent with the concept of increasing electrochemical reversibility. Ferrocene, which has the highest diffusion coefficient and lowest thermodynamic barrier to charge transfer ($E_{1/2}$), show the largest peak separation and hence the lowest rate constant. This suggests that there is an additional barrier at the electrode-solution interface that prevents the probe molecule from interacting with the electroactive sites of the ITO. Interestingly, the carboxylic acid, which has a significantly lower diffusion coefficient and a greater half-wave potential, afforded a rate constant similar to that of the

ferrocene. This suggest that while the flux of the carboxylic acid to the surface is lower than that of the ferrocene the interaction between the former and the electrode is greater. Similar discrepancies are observed among the remaining molecules. One possible explanation for the discrepancies observed between the flux of the redox molecules to the surface and the observed electron transfer rates is the accessibility that the molecules have to the electrically active sites on the surface of ITO. Commercial ITO films are terminated with multiple forms of oxides, hydroxides and oxyhydroxides that create a highly electrically heterogeneous surface.[29] As a result, the surface is comprised of a mixture of electrically 'active' and 'inactive' sites, which affect the substrate ability to interact with adjacent molecules as well as conduct charges away from the surface.[29, 30] Cater *et al*.[1] have previously demonstrated that the adsorption of small acid modifiers, such as FcCA, on the surface of ITO can increase the exposed electrically active surface area due to etching. Based on these findings, the discrepancies in rate constants observed here could potentially stem from the varying degrees to which the redox molecules are able to etch the oxide surface and expose more electrically active sites. This would also explain why ferrocene, which has the smallest propensity for etching the surface and the highest diffusion coefficient among the molecules, has the lowest rate constant. In order to assess any potential etching of the ITO electrode by the modifiers, several 1″ × 1″ substrates were functionalized with the surface modifiers and the morphology of the surface examined by atomic force microscopy (AFM). The AFM results are presented in Figure 2.13.

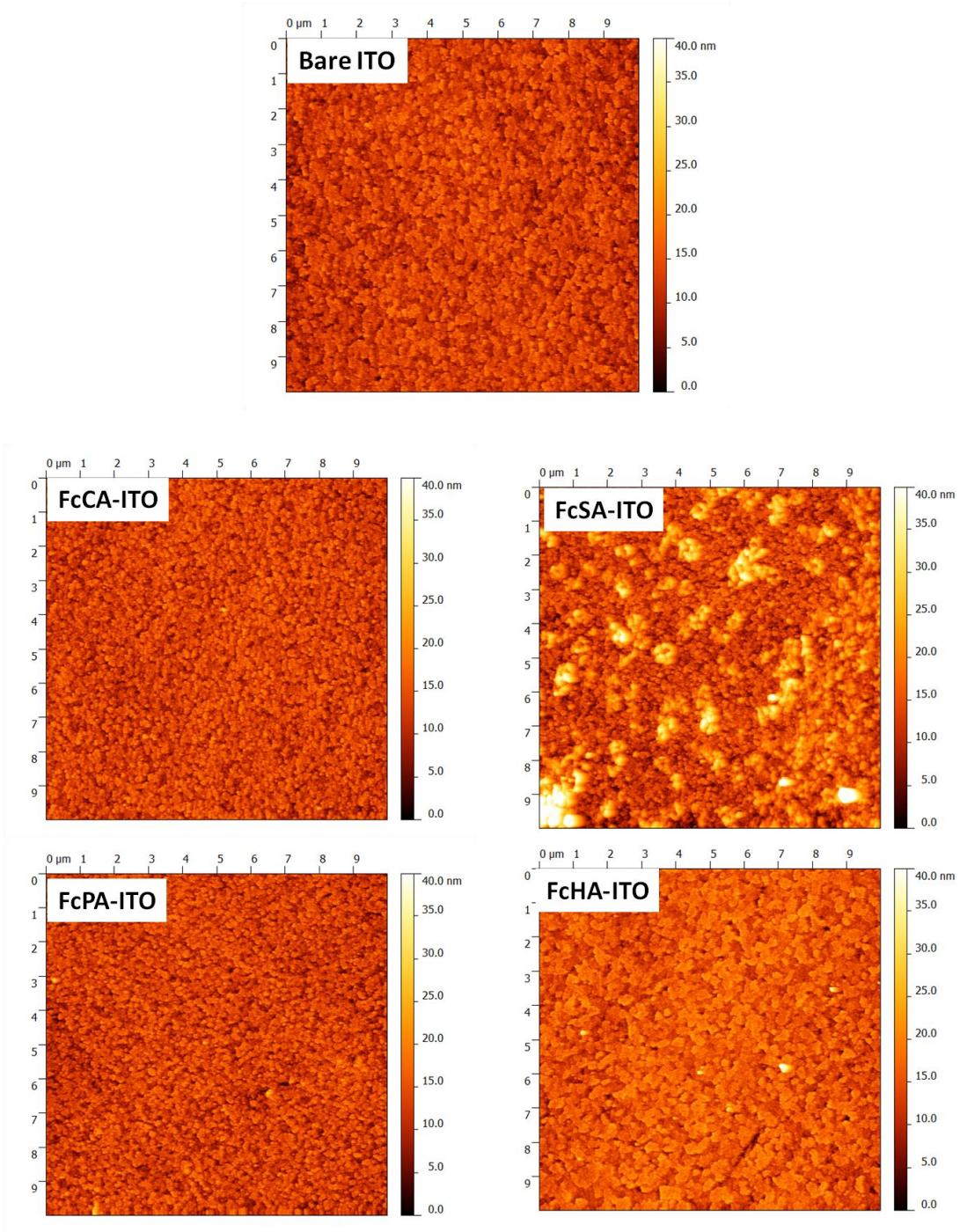

Figure 2.13 AFM images of bare and surface modified ITO. The RMS roughness as determined from 10 µm × 10 µm scans are: 3.06 ± 0.03 nm (bare ITO), 3.10 ± 0.02 nm (FcCA-ITO), 6.45 ± 0.08 nm (FcSA-ITO), 3.20 ± 0.02 nm (FcPA-ITO), and 3.33 ± 0.07 nm (FcHA-ITO).

The calculated RMS roughness over a 10 μm scan size indicates that there is very little difference between the bare and modified ITO with the exception of the sulfonic acid, which exhibited an approximately doubled roughness value. The significant increase in the roughness of the FcSA-modified ITO coupled with its high rate constant, relative to the other molecules, is consistent with the notion that the charge-transfer rates observed are intrinsically linked to the modifiers ability to increase the electrically active sites at the surface of the electrode. Additionally, these results also imply that if there is significant interaction between the molecules and the surface of the ITO then the charge-transfer kinetics is not completely diffusion-limited.

Given the propensity of the tethering groups to adsorb on the surface of ITO and the limitations of CV in resolving close lying redox potentials, plots of the logarithm of peak current *vs.* logarithm of scan rate were generated to investigate the possibility of a secondary contributions to the observed faradaic current from molecules adsorbed on the surface of the ITO. Theoretically, the slope of the plot will be 0.5 for diffusional mechanism, 1 for surface-absorbed mechanism (*vide infra*) and an intermediate number in the case of a mixture of both mechanisms.[13] The value of the slopes obtained for the molecules were 0.85 for Fc, 0.71 for FcCA, 0.80 for FcHA, 0.87 for FcSA and 0.91 for FcPA. The range of values indicates that all the molecules have a significant amount of interaction with ITO and further supports the argument put forth by Carter and coworkers.

2.5 Solution phase cyclic square wave voltammetry characterization of redox modifiers at ITO

Since the results obtained from CV suggest that all the molecules have a significant amount of interaction with the surface of ITO, CSWV was employed as an alternative potentiometric technique in order to deconvolute the processes taking place in solution. As mentioned in section 2.3, pulsed techniques such as CSWV have the capacity to resolve the electrochemical profiles of species that have successive redox processes at close potentials redox potentials and simultaneously provide mechanistic and kinetic information. This is in part due to the techniques ability to discriminate against background currents and partly because of the ease with which the various parameters of the applied potential waveform (i.e. amplitude, increment and step time) can be manipulated, thereby facilitating mechanistic diagnosis of the electrochemical processes taking place at the electrode-solution interface. Hence, the redox properties of ferrocene, and the derivatives described above were assessed in solution by CSWV using 1 mM solutions of the electroactive molecules in 0.1 M TBAP in acetonitrile.

2.5.1 CSWV of ferrocene (Fc) and ferrocene hydroxamic (FcHA) acid

Recall that in CSWV the current is sampled at the end of each pulse and the net response is plotted as a function of the applied potential. Since the electrochemical redox response of Fc and FcHA in solution is similar the results are presented together. Figure 2.14 shows the CSWV profiles of Fc and FcHA as well as the forward and reverse

currents for both sweeps. The voltammograms were obtained using 1 mM solutions of the redox molecules in the TBAP/CAN electrolyte. In both voltammograms the potential is first scanned positively up to the switching potential (E_s), as indicated by the arrow, before the direction of the potential scan is reversed. A scan rate of 0.1 V/s, as determined by the ratio of increment over step time, was used during the measurements.

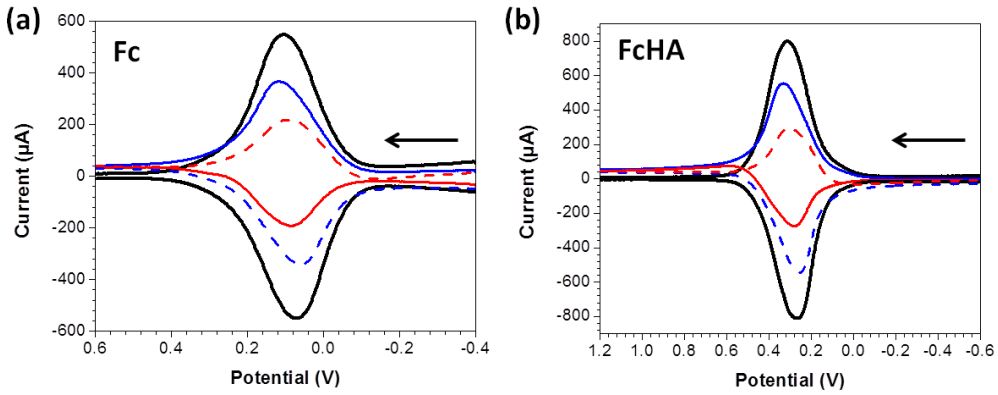

Figure 2.14 Cyclic square wave voltammograms of (a) ferrocene, and (b) ferrocene hydroxamic acid. Voltammograms were recorded *vs.* a Ag/Ag+ reference electrode with an increment of 2 mV, period of 20 ms, amplitude of 80 mV and sampling width of 1 ms. Net currents are shown in black, pulse currents in blue and step currents in red. With the exception of the net currents, solid lines indicate the currents on the forward sweep and dashed lines indicate the currents on the reverse sweep.

It is important to note that the half-wave potentials of Fc and FcHA as determined from CSWV are 92 ± 2 mV and 294 ± 4 mV, respectively, which is consistent with the values previously determined from CV at scan rates of 0.1 V/s. Also, higher net currents are again observed with the hydroxamic acid compared to ferrocene suggesting a poorer interaction between the latter and the ITO working electrode. Under these experimental

conditions both molecules have relatively fast charge-transfer kinetics as indicated by the comparable magnitude of the net currents on the forward and reverse sweeps ($|\Delta I_{p,r}/\Delta I_{p,f}| =1$) as well as the relatively small separation between the peak potentials (ΔE_p). Additionally, the step and pulse current traces show no evidence of a second peak suggesting that only the diffusional species is present in solution. Interestingly, the reverse components of the current on both sweeps are smaller in magnitude than that of the forward component, which indicates that the electrochemical process at the electrode surface is not completely reversible or that the alpha is not 0.5. In order to explore the reversibility of the reactions further their electrochemical behavior were assessed according to the diagnostic criteria outlined in Tables 2.2 and 2.3.

2.5.1.1 Effect of amplitude, step height/increment and step time on the CSWV profiles of Fc and FcHA

Figure 2.15 show the voltammograms for Fc and FcHA in which the amplitude is varied. The CSWV profiles show an increase in the net peak currents as the amplitude gets larger. The net current increases because as the amplitude gets larger, as does the difference between the pulse and step currents. Increasing amplitudes also result in a broadening of the voltammogram profiles. Based on these results, it can be concluded that while larger amplitudes afford easier detection of net currents they diminish the capacity to resolve peaks that have close lying potential due to peak broadening as was predicted by Helfrick *et al*.[14] Amplitude analysis, however, cannot be used to distinguish between reversible and quasireversible mechanisms since the trends in both cases are the

same (see Table 2.2 and 2.3), but it can confirm that the electrochemical reaction at the electrode-solvent interface is a single electron-transfer process void of any secondary processess.[15, 16]

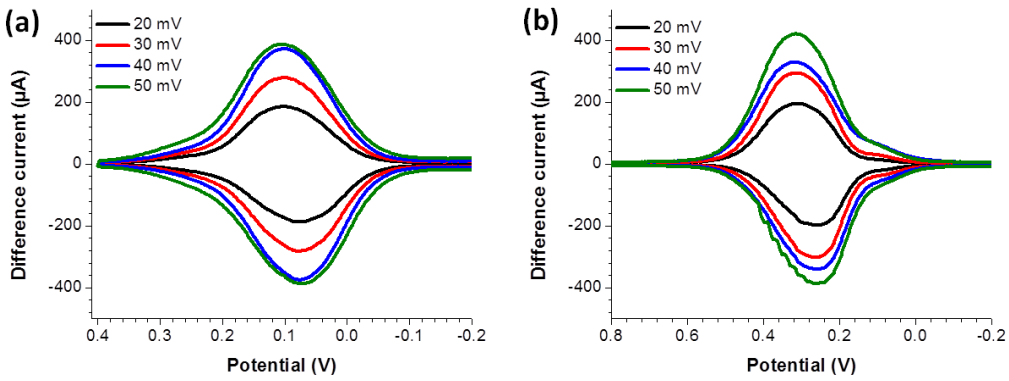

Figure 2.15 The effect of amplitude on the shape of the cyclic square wave voltammogram of (a) ferrocene, and (b) ferrocene hydroxamic acid. Voltammograms were recorded *vs.* an Ag/Ag+ reference electrode with an increment of 2 mV, period of 20 ms, and sampling width of 1 ms. Voltammograms were obtained using 1 mM solutions of the redox molecules in a TBAP/ACN electrolyte. The figure legend indicates the different amplitudes used.

Reversibility is better assessed by evaluating the impact of step height and step time on the shape of the voltammograms.

The impact of step height on the CSWV profiles of Fc, and FcHA are presented graphically in Figure 2.16. As the step height or increment is increased the peak potential of the forward sweep becomes more positive and the peak potential of the reverse sweep becomes more negative. In addition to the shifting of the peak potentials, the net current

of both the forward and reverse sweep also increases. Increasing the step time or increment in CSWV is synonymous to increasing the scan rate in CV.

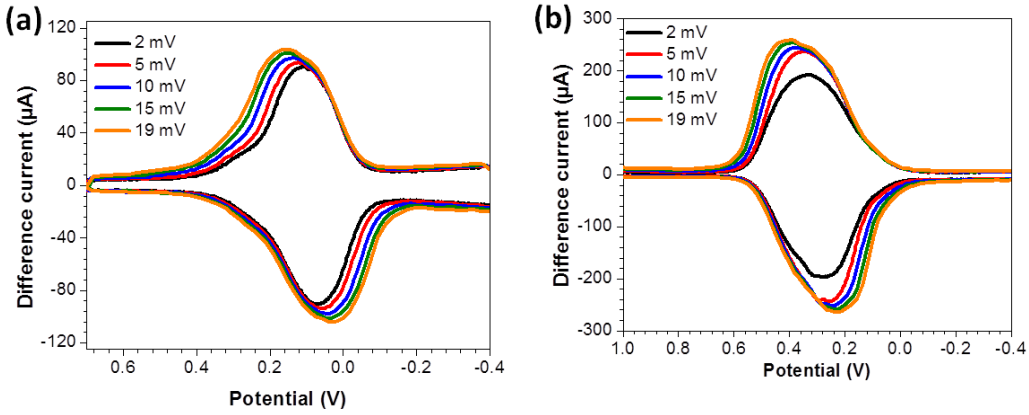

Figure 2.16 The effect of increment on the shape of the cyclic square wave voltammogram of (a) ferrocene, and (b) ferrocene hydroxamic acid. Voltammograms were recorded *vs*. an Ag/Ag+ reference electrode with an amplitude of 20 mV, period of 20 ms, and sampling width of 1 ms. Voltammograms were obtained using 1 mM solutions of the redox molecules in a TBAP/ACN electrolyte The figure legend indicates the different step heights used.

As a result, the peak potentials shift away from the formal potential. The evolution of the voltammograms as a function of step height indicates that both ferrocene, and the hydroxamic acid derivative exhibit quasireversible behavior in solution. For a completely reversible mechanism it is expected that the net current will decrease and the peak potential remain constant based on the theoretical work of Helfrick[14, 15] and Mann.[24] outlined in Tables 2.2 and 2.4 Figure 2.17 shows the effect of step time/period on the peak potential and net current of the voltammograms. As the period is increased the net peak currents decrease and the peak potentials converge around the formal potential (i.e., increase in reversibility).

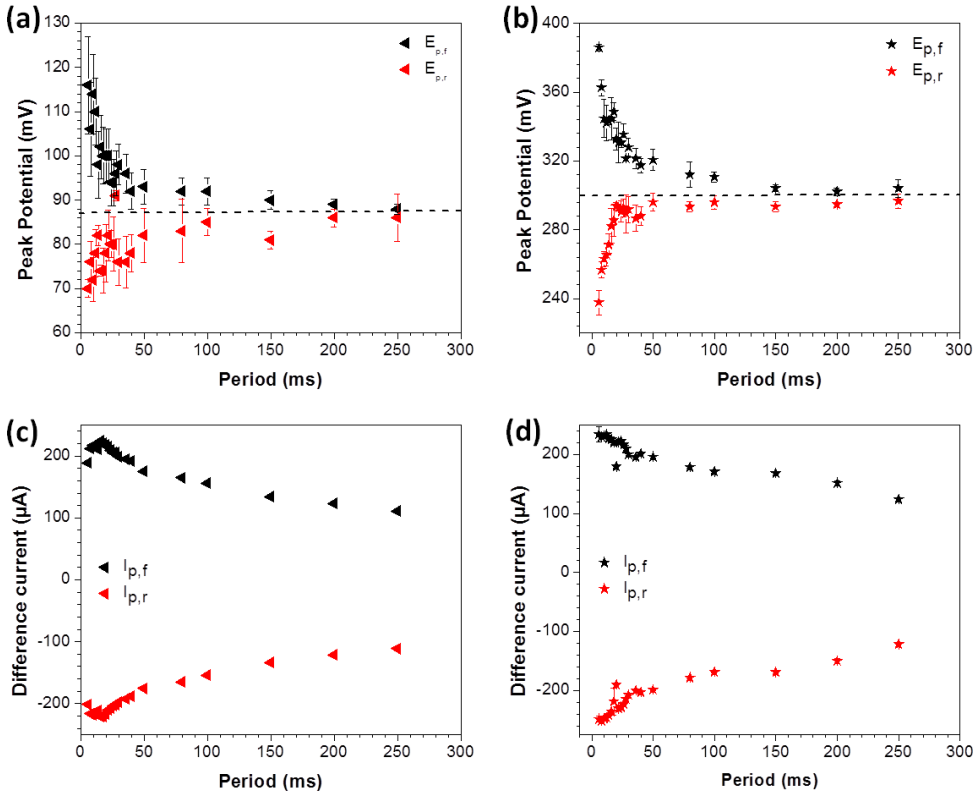

Figure 2.17 The effect of step time/period on the peak potentials and net current of the cyclic square wave voltammograms of (a and c) ferrocene, and (b and d) ferrocene hydroxamic acid. Voltammograms were recorded *vs.* Ag/Ag+ reference electrode with an amplitude of 20 mV, increment of 2 mV, and sampling width of 1 ms. Dashed lines serve as a guide to illustrate the convergence of the peak potentials around the formal potential. Voltammograms were obtained using 1 mM solutions of the redox molecules in a TBAP/ACN electrolyte.

Based on Equation 2.9 the net current is inversely related to $t^{1/2}$; therefore as the period or step time increases the difference current is reduced. While the behavior of the net current in the reversible case is similar to that of the irreversible scenario, the peak potentials in the former remain constant as the period is increase. These results indicate that ferrocene and ferrocene hydroxamic acid exhibit quasireversible behavior.

2.5.2 CSWV of ferrocenesulfonic acid (FcSA) and ferrocenephosphonic acid (FcPA).

The solution phase CSWV profiles for FcSA and FcPA are presented in Figure 2.18 along with their corresponding pulse and step currents.

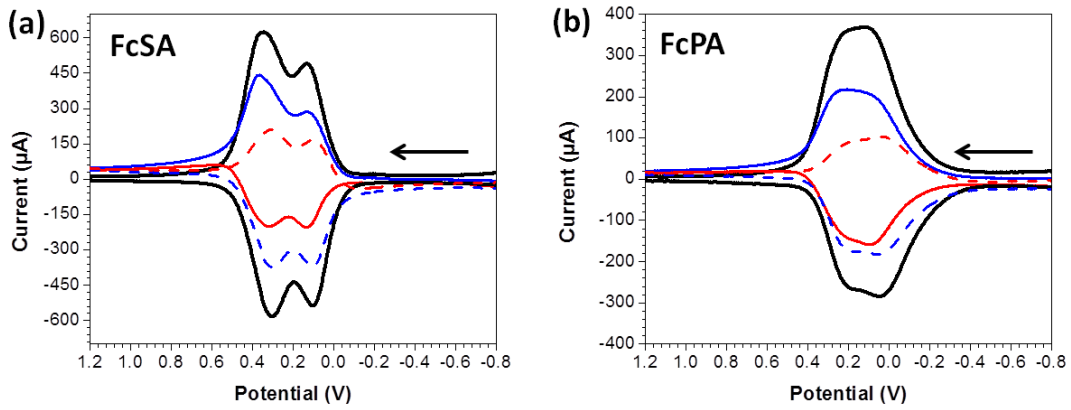

Figure 2.18 Cyclic square wave voltammograms of (a) ferrocene sulfonic, and (b) ferrocene phosphonic acids. Voltammograms were recorded *vs.* a Ag/Ag+ reference electrode with an increment of 2 mV, period of 20 ms, amplitude of 80 mV and sampling width of 1 ms. Net currents are shown in black, pulse currents in blue and step currents in red. With the exception of the net currents, solid lines indicate the currents on the forward sweep and dashed lines represent the currents on the reverse sweep. Voltammograms were obtained using 1 mM solutions of the redox molecules in a TBAP/ACN electrolyte

Surprisingly, the voltammograms of FcSA and FcPA show the presence of two oxidative and reductive peaks for molecules that were anticipated to undergo a single-electron transfer process similar to that seen for Fc and FcHA. Closer examination of the step and pulse currents confirms that indeed these are two independent species each making their own contribution to the final CSWV profile. In cases such as this, careful analysis of the step and pulse currents is important since a potential offset of the two currents could just as easily present itself as two peaks in the net current. Of the two molecules, the components of the FcSA voltammograms were better resolved than that of the FcPA

indicating that the constituents of the latter have significant overlapping potentials. Given the propensity of these molecules to adsorb on the surface of ITO and the previous results of CV we hypothesized that the two peaks represent a diffusional and a surface-confined species.

In order to verify the origin of the two species in the CSW voltammogarams concentration dependent studies were performed and the results are presented in Figure 2.19.

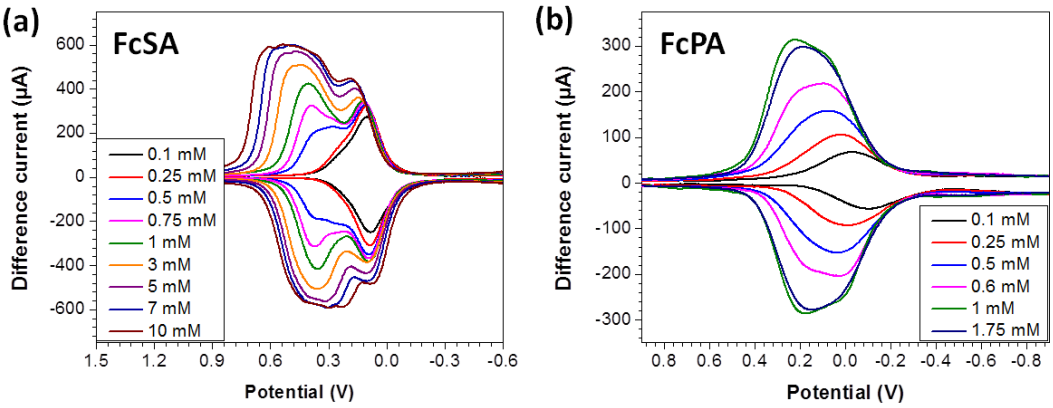

Figure 2.19 Cyclic square wave voltammograms of (a) ferrocene sulfonic, and (b) ferrocene phosphonic acids at various concentrations. Voltammograms were recorded *vs*. a Ag/Ag+ reference electrode with an increment of 2 mV, period of 20 ms, amplitude of 50 mV and sampling width of 1 ms.

Given the variation in the solubility of the two molecules, the maximum concentrations used in the study were different for the two molecules. At concentrations of 0.25 mM and lower, the sulfonic acid exhibits a single peak (peak 1); however, as the concentration is increased beyond this point a shoulder begins to grow in at higher potential. At around 1 mM the shoulder is transformed into a fully grown, dominant peak (peak 2), which

eventually broadens and saturates at a concentration of approximately 7 mM. The evolution of the voltammograms of FcSA with concentration suggests that peak 1 is due to surface-confined Fc groups and peak 2 to diffusionally free molecules in solution. The early saturation of the first peak at around 3 mM is indicative of having reached the maximum limit of surface coverage. Any further apparent increase in the intensity of the peak beyond this point is attributed to the overlapping contribution from the diffusional species (Figure 2.20). The saturation of the diffusional component at high concentrations is believed to be the result of the limitations of the detector of the instrument. Lovric developed a theoretical model that examined the effect of concentration on the shape of the voltammograms in systems that comprise both diffusional and surface-adsorbed species.[31] The calculations predicted that in systems where a diffusional response is complicated by adsorption systems, an increase in concentration will lead to a positive shift in the diffusional peak, which is consistent with our observations. In order to further verify the identities of the species in solution various equivalence of tetrabutylammonium hydroxide (TBAOH) base was titrated into a 4 mM solution of FcSA and the CSW voltammograms recorded (Figure 2.20).

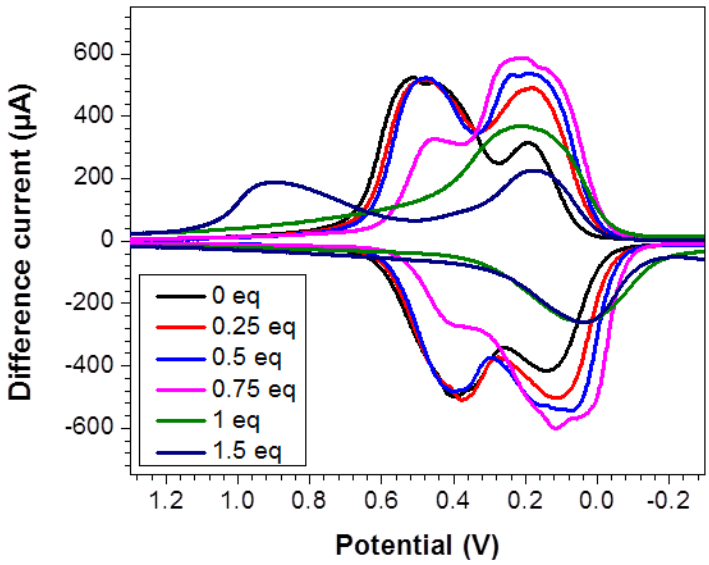

Figure 2.20. Cyclic square wave voltammetry titration studies of ferrocene sulfonic using tetrabutylammonium hydroxide (0.01 M solution). Voltammograms were recorded vs. a Ag/Ag+ reference electrode with an increment of 2 mV, period of 20 ms, amplitude of 50 mV and sampling width of 1 ms. Legend depicts the equivalence of the base added to the FcSA solution.

The results show that as the equivalence of base is increased peak 2 decreases and completely disappears at 1 eq. This directly shows that the second peak represents the protonated form of the acid. At 1.5 eq. a new species directly related to the oxidation of the base is observed at ~ 0.9 mV. The second peak is always present regardless on the amount of base added; however, its intensity diminishes with increasing TBAOH. The reduction in intensity is attributed to the competition between the base and the deprotonated molecule for the electroactive sites on the surface of the electrode. Based on these results it is believed that the deprotonated molecule readily adsorbs to the surface of the ITO and gives rise to peak 1.

Even though the peaks of the phosphonic acid are poorly resolved, upon peak fitting (Figure 2.21b) some similar trends to that of the sulfonic acid emerge. For

example, the higher potential diffusional peak (peak 2) shifts to more positive potentials as the concentration of the solution is increased. However, there is no clear evidence of saturation of either peak 2 or the peak at lower potential (peak 1) over the concentration range investigated. Also, unlike FcSA, the FcPA peaks remain unresolved at all concentrations. Lovric's model predicts that poor resolution of peaks at various concentrations is likely due to strong adsorption influenced by repulsion.[31] The peak fitting shown in Figure 2.21 indicate that while the diffusional species is the dominant constituent in the CSWV of FcSA at a concentration of 1 mM, it is the surface-confined component that dominates in the electrochemistry of FcPA. This confirms that FcPA interacts strongly to the surface of ITO as was deduced from CV.

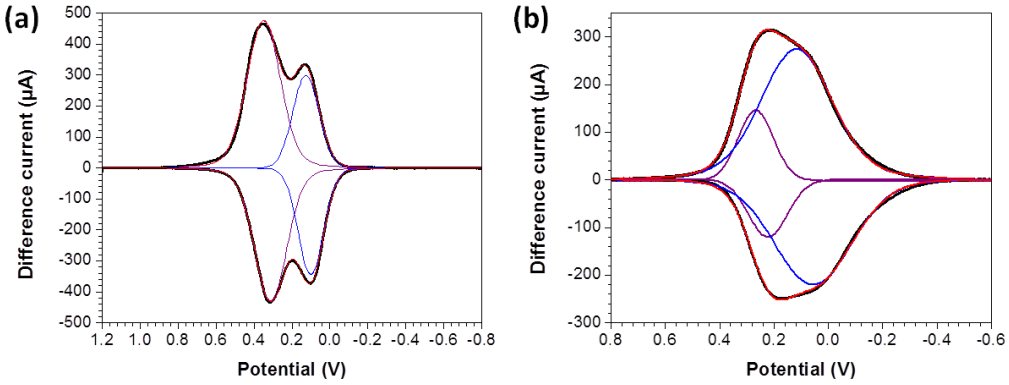

Figure 2.21 Deconvolution of cyclic square wave voltammograms of (a) ferrocene sulfonic, and (b) ferrocene phosphonic acids. Voltammograms were recorded *vs*.a Ag/Ag+ reference electrode with an increment of 2 mV, period of 20 ms, amplitude of 60 mV and sampling width of 1 ms. Net currents are shown in black, and the component indicated in purple and blue. Voltammograms were obtained using 1 mM solutions of the redox molecules in a TBAP/ACN electrolyte. Voigt curves, which accounts for both Gaussian and Lorentzian type broadening, were used to fit the CSWV data.

From the Randle-Sevcik relationship expressed by Equation 2.5 there is a linear relationship between the peak current obtained from CV and the square root of the scan rate. Analogously, the relationship between peak current and the scan rate for a surface-confined species in CV can be expressed according to Equation 2.12

$$I_p = \left(\frac{n^2F^2}{4RT}\right)\nu A\Gamma_{surf} \qquad \text{(Equation 2.12)}$$

where A is the area of the electrode Γ_{surf} and is the coverage of the redox molecules on the surface. Based on these two relationships and the trends observed in the CSWV concentration studies we hypothesized that at low concentrations (~ 0.25 mM) the surface-confined species should dominate, which can be verified by examination of the slopes of a plot of the log of current *vs*. log of scan rate as was done earlier. As such, the cyclic voltammograms of FcSA and FcPA were examined at low concentrations and the results are summarized graphically in Figures 2.22 and 2.23. Interestingly, at a concentration of 0.25 mM of FcSA the CV is able to resolve both peaks, which was not the case when the measurements were done using 1 mM solutions. In contrast, at the lower concentration only one peak was observed in the CSW voltammogram compared to the two that were seen before at 1mM. A log-log plot analysis of the peaks yielded gradients of 0.65 and 0.50 for peaks 1 and 2, respectively. This result confirms that the peak at higher potential (peak 2) is the result of a diffusional species in solution. The gradient of peak 1, however, suggests that there is a mixture of diffusional and surface-confined species with a predominance of the latter.

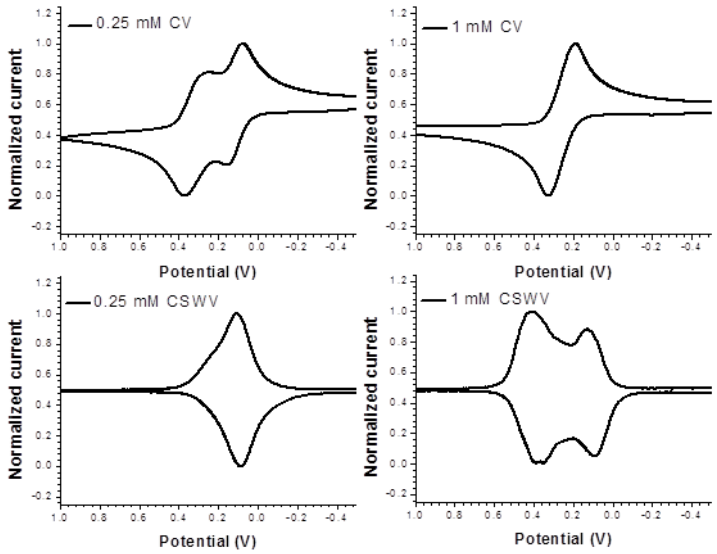

Figure 2.22 Graphical summary of CV and CSWV results of FcSA for experiments conducted using 0.25 mM and 1 mM solutions. CV were acquired at 0.1 V/s and CSWV data were acquired using an amplitude of 50 mV, step height of 2 mV period of 20 ms and sampling width of 2 ms.

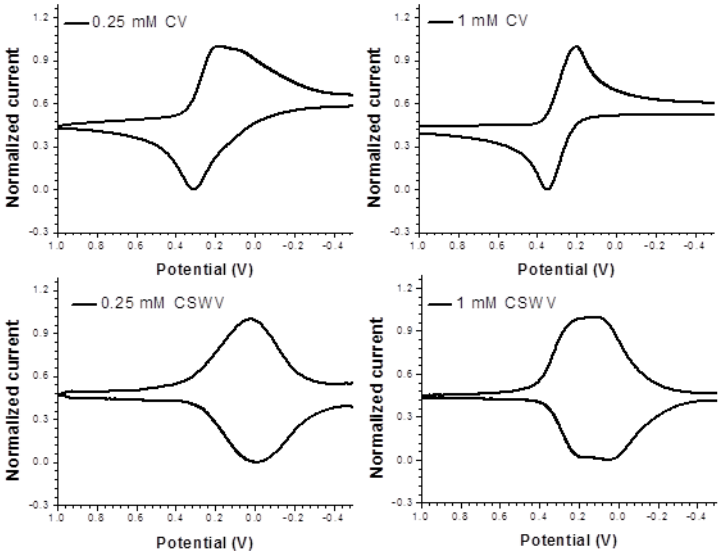

Figure 2.23 Graphical summary of CV and CSWV results of FcPA for experiments conducted using 0.25 mM and 1 mM solutions. CV were acquired at 0.1 V/s and CSWV data were acquired using an amplitude of 50 mV, step height of 2 mV period of 20 ms and sampling width of 2 ms.

The CV of FcPA acquired at 0.25 mM revealed a shoulder on the lower potential side of the oxidative peak current. While the resolution was still poor, it at least confirms that there is a second species present in solution as observed before from CSWV. As was the case with FcSA, the ability of CSWV to resolve the peaks of the FcPA species in solution is diminished at 0.25 mM. A gradient of 0.73 was obtained from log-log analysis of the the main cathodic peak of the 0.25 mM solution, which again indicates a mixed system with a predominance of surface-confined species.

2.5.2.1 Effect of amplitude, step height/increment and step time on the CSWV profiles of FcSA and FcPA

The effect of amplitude on the shape of the voltammograms of FcSA and FcPA are shown in Figure 2.24. As was the case for Fc and FcHA, as the amplitude is increased so does the net current and peak width of the voltammograms. As expected, the resolution of the peaks in FcPA is impaired by increasing amplitude due to the concomitant broadening of the peaks. However, the peaks in the FcSA voltammograms are sufficiently far apart on the potential axis such that the increase in the amplitude has minimal impact on their resolution.

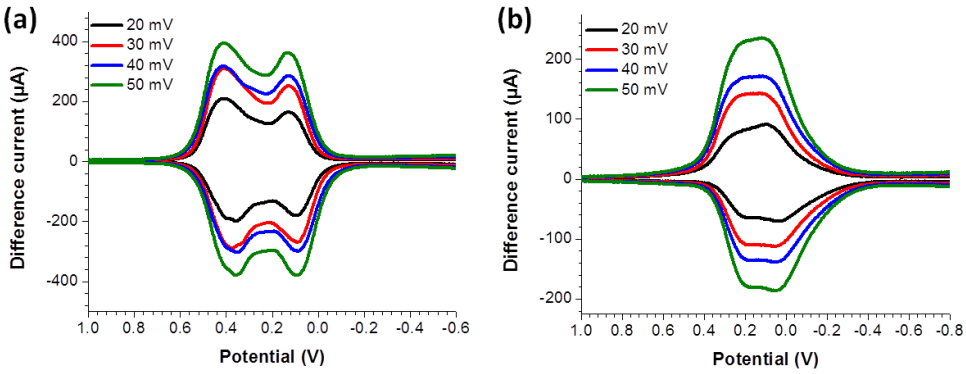

Figure 2.24 The effect of amplitude on the shape of the cyclic square wave voltammogram of (a) ferrocene sulfonic acid, and (b) ferrocene phosphonic acid. Voltammograms were recorded *vs*. a Ag/Ag+ reference electrode with an increment of 2 mV, period of 20 ms, and sampling width of 1 ms. Voltammograms were obtained using 1 mM solutions of the redox molecules in a TBAP/ACN electrolyte The figure legend indicates the different amplitudes used.

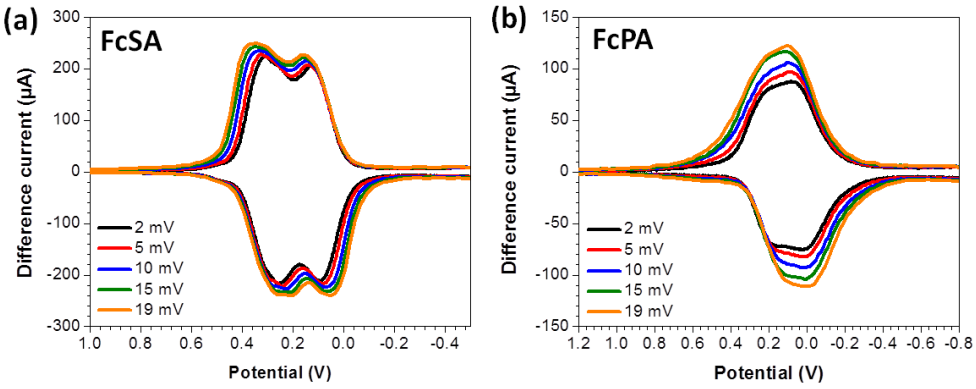

Figure 2.25 The effect of increment on the shape of the cyclic square wave voltammogram of (a) FcSA, and (b) FcPA. Voltammograms were recorded *vs*. a Ag/Ag+ reference electrode with an amplitude of 20 mV, period of 20 ms, and sampling width of 1 ms. Voltammograms were obtained using 1 mM solutions of the redox molecules in a TBAP/ACN electrolyte. The figure legend indicates the different step heights used.

Figure 2.25 illustrates the impact of increasing the step height on the shape of the voltammograms of FcSA and FcPA. In both cases, as step height is increased the peak

potentials shift away from the formal potential and the net current increase. This is similar to what was previously observed for Fc and FcHA. Based on the diagnostic criteria of CSWV both these molecules exhibit quasireversible behavior whether or not they are surface-confined or diffusion-limited. The reversibility of these molecules is further confirmed in Figure 2.26 in which the behavior of the peak potential and peak currents are plotted as a function of period. The figure shows that as the period is increased, the peak potentials converge and the current is reduced indicating a quasireversible process for both the diffusional and surface-confined species.

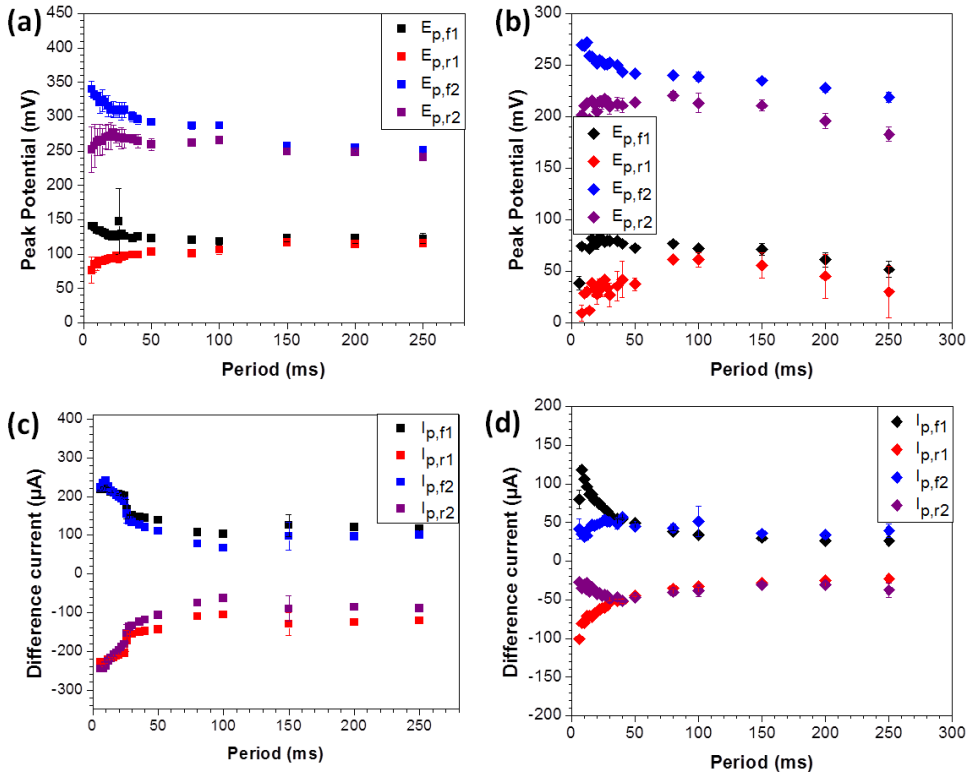

Figure 2.26 The effect of step time/period on the peak potentials and net current of the cyclic square wave voltammograms of (a, and c) FcSA, and (b and d) FcPA. Voltammograms were recorded *vs.* an Ag/Ag+ reference electrode with an amplitude of 20 mV, increment of 2 mV, and sampling width of 1 ms. Voltammograms were obtained using 1 mM solutions of the redox molecules in a TBAP/ACN electrolyte.

2.6 Cyclic square wave voltammetry of ferrocene carboxylic acid

The CSW voltammogram of FcCA presents electrochemical profile that is strikingly different from the previous molecules (Figure 2.27). The net response of the initial scan in the positive direction presents two peaks at approximately 257 mV and 808 mV. On the reverse sweep only one peak of significantly greater magnitude is observed at approximately 94 mV.

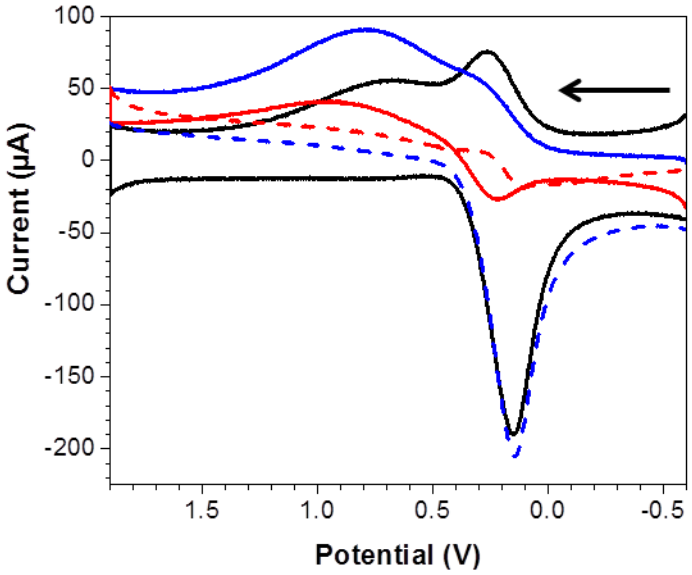

Figure 2.27 Cyclic square wave voltammogram of ferrocenecarboxylic acid. Voltammograms were recorded *vs*. an Ag/Ag+ reference electrode with an increment of 2 mV, period of 20 ms, amplitude of 80 mV and sampling width of 1 ms. Net currents are shown in black, pulse currents in blue and step currents in red. With the exception of the net currents, solid lines indicate the currents on the forward sweep and dashed lines represent the currents on the reverse sweep. Voltammograms were obtained using 1 mM solutions of the redox molecules in a TBAP/ACN electrolyte.

In order to deduce the origin of these peaks concentration studies were performed and the results presented in Figure 2.28. A small, peak is observed in these studies at higher potential on the reverse sweep, which signifies that some amount of the diffusional

species is still present. As the concentration is increased, the peak at higher potential on the forward scan rapidly grows in and eventually becomes dominant. Using the same treatment that was previously applied to FcSA and FcPA, this implies that the peak at lower potential (peak 1) can be assigned to a surface-confined species and the peak at higher potential (peak 2) is attributed to the diffusional species. Since the corresponding reductive current is not observed for the diffusional species on the reverse scan, it is postulated that majority of the oxidized form of the molecule has a strong affinity for the ITO electrode and assumes a surface-confined configuration upon oxidation. This is postulated to be a result of a strong equilibrium constant that favors deprotonation and subsequent adsorption of the oxidized solution-phase species.

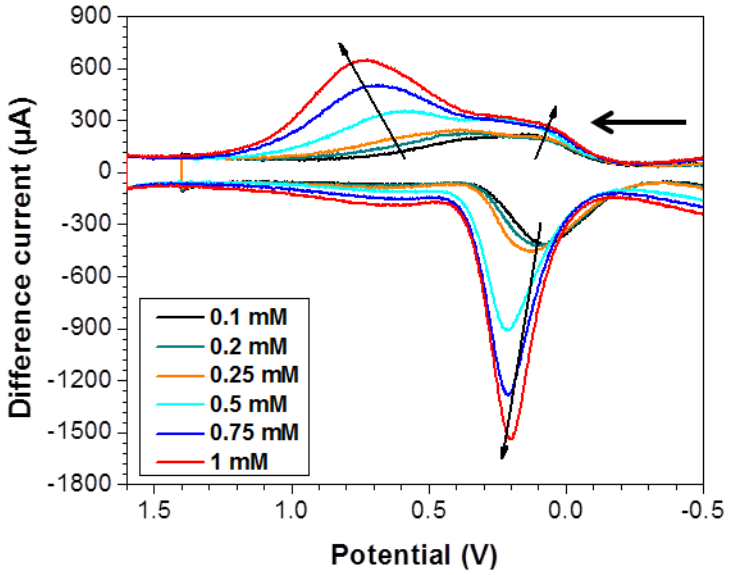

Figure 2.28 Cyclic square wave voltammograms of (a) ferrocene carboxylic acid at various concentrations. Voltammograms were recorded *vs*. a Ag/Ag+ reference electrode with an increment of 2 mV, period of 20 ms, amplitude of 50 mV and sampling width of 1 ms. The arrow indicates the direction of the forward scan.

This is supported by the dominant reductive peak observed in the reverse scan in the region where the redox potential for the surface-confined molecule is observed. This is also why the magnitude of the reductive current is so much greater than that observed for the oxidative peaks. The marked increase in the magnitude of the reductive current with concentration suggests that we could be forming multilayers on the surface of the ITO electrode.

2.6.1.1 Effect of amplitude, step height/increment and step time on the CSWV profiles of FcCA

The effect of amplitude on the CSWV profile of FcCA is shown in Figure 2.29. As was the case with the other molecules, the net current and peak width increases with amplitude. The reversibility of FcCA was assessed by examining the change in the shape of the voltammogram as a function of step height/increment (Figure 2.30). The results show that the electrochemical reaction approached irreversibility with increasing step height as the peak potentials shifted further away from the formal potential. This suggests that the electrochemical process taking place at the surface of the electrode is quasireversible.

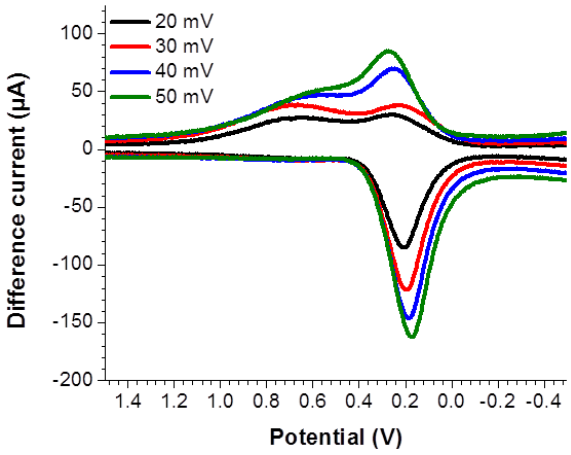

Figure 2.29 The effect of amplitude on the shape of the cyclic square wave voltammogram of ferrocenecarboxylic acid. Voltammograms were recorded *vs*. a Ag/Ag^{+} reference electrode with an increment of 2 mV, period of 20 ms, and sampling width of 1 ms. Voltammograms were obtained using 1 mM solutions of the redox molecules in a TBAP/ACN electrolyte The figure legend indicates the different amplitudes used.

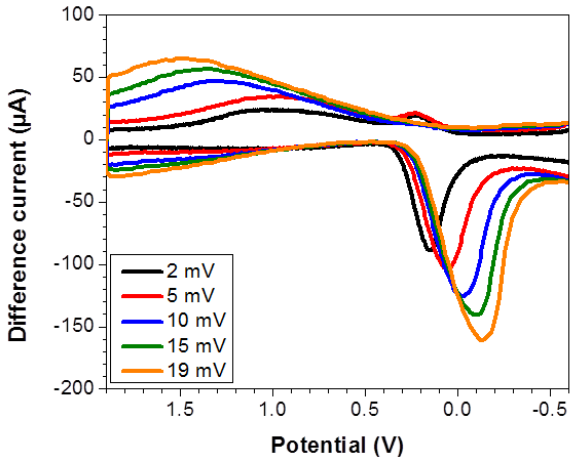

Figure 2.30 The effect of increment on the shape of the cyclic square wave voltammogram of ferrocenecarboxylic acid. Voltammograms were recorded *vs.* a Ag/Ag+ reference electrode with an amplitude of 20 mV, period of 20 ms, and sampling width of 1 ms. Voltammograms were obtained using 1 mM solutions of the redox molecules in a TBAP/ACN electrolyte The figure legend indicates the different step heights used.

However, examination of the change in the peak current and potential as a function of period contradicts these results due to the divergence of the peak potential with increasing period (Figure 2.31).

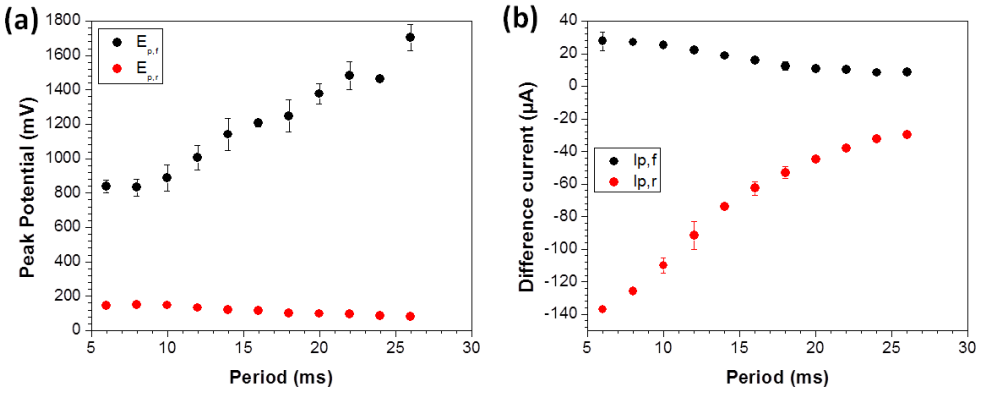

Figure 2.31 The effect of step time/period on the peak potentials (a) and net current (b) of the cyclic square wave voltammograms of FcCA. Voltammograms were recorded *vs*. Ag/Ag^{+} reference electrode with an amplitude of 20 mV, increment of 2 mV, and pulse width of 1 ms. Voltammograms were obtained using 1 mM solutions of the redox molecules in a TBAP/ACN electrolyte.

The divergence of the peak potential from the conventional behavior is believed to be due to the fact that the diffusional neutral molecule is not regenerated on the reverse sweep thereby making the process chemically irreversible.

2.7 Evaluation of the kinetics of charge transfer from CSWV data

The method developed by the Bottomley Group, and discussed in section 2.3.1, was used to evaluate the kinetic parameters of charge transfer and the results are presented in Table 2.5 The rates were determined for the solution species by using equation 2.8 and the diffusion coefficients determined from the CV measurements.

Table 2.5 Solution phase CSWV redox properties of ferrocene and ferrocene derivatives. All measurements were done *vs*. a Ag/Ag^+ reference electrode.

	Fc	FcCA	FcPA	FcSA	FcHA
E^o	83 ± 2	—	219 ± 3	281 ± 3	304 ± 4
E^o_{surf}	—	234 ± 8	51 ± 2	119 ± 4	—
α	0.40	—	0.56	0.46	0.45
α*	—	0.40	0.57	0.45	—
k^o ($\times 10^{-3}$cm/s)	2.8 ± 0.4	—	5.3 ± 1	3.2 ± 0.5	2.9 ± 0.6
k_s (s^{-1})	—	3.0 ± 1.5	3.0 ± 2.0	5.0 ± 3.6	—

*surface confined alpha values
k_s surface-confined charge transfer rate constant

The rate constant for FcCA could not be determined by CSWV since the reduced species was not observed on the reverse sweep. CSWV analysis of the phosphonic acid diffusional component afforded the highest charge-transfer kinetics and the largest transfer coefficient. However, these values must be interpreted with caution since a significant amount of the molecule is adsorbed on the surface of ITO and presents as a strongly overlapping peak with the diffusional peak. Similar to the PA, FcSA also adsorbs to the surface of the ITO, but with a significantly smaller overlap between the surface-confined and diffusional species. The diffusional component of FcSA had a modest rate and an alpha value slightly lower than 0.5. Neither the hydroxamic acid, nor

the ferrocene showed any evidence of surface adsorption and both molecules had comparable rates. Interestingly, Fc and FcHA demonstrated the smallest and largest driving force for the electron transfer process (based on their half wave potential) in solution among the various molecules, respectively. Transfer coefficients were also determined for the surface-confined species by employing the same method used for the diffusional molecules. The results show that the alpha values obtained for surface-bound FcSA and FcPA were comparable with those determined for the diffusional species, which suggest that α values determined from solution can be extrapolated to surface-confined molecules. Standard rate constants for the surface-confined species were determined using a method that will be the subject of the next chapter. However, the results presented in Table 2.5 show that the rate constant for the surface-confined molecules are comparable for the various anchoring groups used.

2.8 Experimental

Ferrocene and ferrocene carboxylic acid were obtained from Sigma-Aldrich and Alfa Aesar, respectively. All other molecules were synthesized as outlined below.

2.8.1 Synthesis of ferrocenehydroxamic acid

This molecule was synthesized using a combination of two previously reported procedures.[32, 33] Benzene (80 mL) was poured into a 250 mL round bottomed flask to which ferrocenecarboxylic acid (1.0 g, 4.0 mmol) was subsequently added under nitrogen with stirring. Oxalyl chloride (2.1 g, 17.0 mmol) was added dropwise *via* syringe followed by four drops of dimethylformamide (DMF). The mixture was allowed to stir for 2 h at room temperature before the volatiles were removed under reduced pressure to

give an orange-red solid that was dried under high vacuum (ca. 20 mTorr) for an hour. The orange-red solid was dissolved in ethyl ether (20 mL) and added dropwise to a solution of hydroxylamine hydrochloride (300 mg, 4.0 mmol) and sodium bicarbonate (500 mg, 6.0 mmol) in DI water in 0 °C ice bath. The resulting mixture was stirred for 30 min and DI water (50 mL) was added to give an orange precipitate. The orange solid was consecutively washed with water, ethanol, ether, and then placed under high vacuum for drying (460 mg, 42%). ^{1}H NMR (300 MHz, DMSO-d_6) δ 10.50 (s, 1H), 4.73 (s, 2H), 4.33 (s, 2H), 4.17 (s, 5H). ^{13}C {^{1}H}Material NMR (300 MHz, DMSO-d_6) δ 167.58, 75.06, 70.14, 69.76, 68.20. EI-MS calcd for $C_{11}H_{11}FeNO_2$ (M^+): 245.0139, found: 245.0132. Anal. Calcd for $C_{11}H_{11}FeNO_2$: C, 53.91; H, 4.52. Found : C, 53.91; H, 4.29.

2.8.2 Synthesis of ferrocenephosphonic acid

The phosphonic acid was synthesized by modifying a protocol previously reported by Oms *et al*.[34] Dry tetrahydrofuran (THF, 100 mL) was placed in a 500 mL round bottom flask and purged with nitrogen under stirring. Ferrocene (5.0 g, 27 mmol) was then added to the THF followed by potassium *tert*-butoxide (0.52 g, 4.6 mmol) and the mixture allowed to stir for 20 min at room temperature. The flask was placed in a -78 °C acetone/dry ice bath and the temperature allowed to equilibrate for a period of 10 min. *tert*-Butyllithium (12 mL of a 1.7 M solution in pentane, 20 mmol) was added dropwise to the reaction mixture and the contents of the flask allowed to stir for 30 min. Diethyl chlorophosphate (8.7 g, 27 mmol) was dissolved in dry 50 ml THF and then added dropwise to the reaction and the mixture allowed to stir for 40 min. The acetone bath was removed and the reaction mixture was allowed to gradually warm up to room temperature. The reaction mixture was then washed with a 1 M NaOH solution (200 mL)

and then the aqueous layer extracted with dichloromethane (DCM, 100 mL). The organic layer was collected and dried over $MgSO_4$. Column chromatography was performed on silica gel on the resulting material using a DCM:THF (70:30) solvent system. The sample was then dried under vacuum to obtain the pure phosphonate as a dark brown oil (3.5 g, 40%). ^{1}H NMR (300 MHz, $CDCl_3$) δ 1.34 (t, J = 7.5, 6H), 4.12 (m, 4H), 4.30 (s, 5H), 4.39 (m, 2H), 4.50 (m, 2H). A Schlenk flask containing a magnetic stir bar was evacuated to 20 mTorr and back-filled with nitrogen three times and then was purged under nitrogen for an additional 10 min. The previously prepared phosphonate was transferred to the schlenk flask *via* syringe and a second syringe was used to add dry dichloromethane (20 mL) to the phosphonate and the flask and its contents allowed to purge under nitrogen and stiring for another 10 min. Bromotrimethylsilane (2 mL, 15 mmol) was added dropwise to the contents of the flask and the mixture stirred overnight (~16 h). The contents of the flask were concentrated on a rotary evaporator to give a brown oil, which was dissolved in acetonitrile (30 mL) and stirred for 5 minute. A pipet was then used to add DI water dropwise until a yellow precipitate was formed. The precipitate was filtered and successively washed with DCM and then ethyl ether. The solid was then dried under vacuum to give the desired product as a yellow solid (1.2 g, 75% yield). ^{1}H NMR (300 MHz, CD_3OD) δ 4.48 (m, 2H), δ 4.41 (s, 2H), δ 4.30 (s, 5H). ^{31}P (161.9 MHz, CD_3OD) 24.32.

2.8.3 Synthesis of ferrocenesulfonic acid

An oven dried 1000 mL three-necked round bottom flask containing a stir bar was purged under nitrogen for 10 minutes. A thermometer was placed in one port to monitor

the reaction temperature in order to ensure that it does not exceed 50 °C. Acetic anhydride (70 mL) was added to the flask followed by ferrocene (8.0 g, 43 mmol) and the mixture stirred under nitrogen for 2 min. Dichloromethane (70 mL) was added to the contents of the flask and nitrogen purging continued for an additional 10 min. Chlorosulfonic acid (3.0 mL, 43 mmol) was slowly added to the contents of the flask over a period of 10 min and the mixture allowed to stir at room temperature overnight. The reaction was quenched by pouring the contents of the flask over ice and stirring for an hour. The water was then removed under reduced pressure and heating (taking care to not exceed 50 °C) to yield a dark green solid. A mortar and pestle was used to crush the solid and the powder extracted with boiling ether multiple times until the extracted fractions were colorless. The fractions were collected and concentrated on the rotary evaporator to give a brown liquid. The liquid was added to toluene to immediately precipitate crystals. A second recrystallization from toluene afforded the pure product (4.6 g, 40% yield). ^{1}H NMR (400 MHz, DMSO) δ 4.35 (s, 2H), 4.20 (s, 5H), 4.13 (s, 2H). ^{13}C NMR (100.58 MHz, DMSO) δ 69.62 (s, 5C), 67.87 (s, 2C), 67.20 (s, 2C). The quaternary carbon was not observed. EI-MS Calcd for $C_{10}H_{10}FeO_3S$ (M^+): 265.9700, found: 265.9705. Anal. Calcd for $C_{10}H_{10}FeO_3S•2H_2O$: C, 42.27; H, 4.26. Found: C, 42.04; H, 4.35.

2.8.4 Electrochemistry

Cyclic voltammetry (CV) and cyclic square wave voltammetry (CSWV) were performed using a CH1030A (CH Instruments) and Pine Instrument potentiostats, respectively. Using the conventional three electrode configuration. ITO served as the

working electrode, a Pt wire as the counter electrode, and an Ag/Ag^{+} as the reference electrode (10mM $AgNO_3$ in 0.1 M tetrabutylammonium perchlorate (TBAP) in acetonitrile electrolyte). ITO substrates were cut into 1″ × 1″ pieces and then subject to detergent solvent cleaning (DSC). This involves several steps: (1) scrubbing the substrates with dilute Triton X-100 solution with the aid of a lint-free cloth, (2) sonicating in Triton X-100 solution for 10 min then rinsing with distilled water, (3) sonicating in distilled water for 10 min, (4) sonicating in ethanol for 10 min, and (5) drying under nitrogen. The detergent solvent cleaned substrates were then Oxygen plasma treated (Plasma Etch, PE50) for 10 minutes after which they are immediately used to conduct studies. All CV measurements were performed at a scan rate of 0.1 V/s unless otherwise stated.

2.8.5 Modification of ITO for atomic force microscopy (AFM) studies

To assess the potential of the redox modifier to etch the surface of ITO self-assembled monolayers of the molecules were prepared on the surface of the metal oxide. Owing to differences in solubility and coverages observed in preliminary studies the solvent system used for modification varied depending on the redox modifier. The phosphonic and carboxylic acid experiments were done in ethanol, the sulfonic acid in chloroform, and the hydroxamic acid in tetrahydrofuran. Prior to modification the ITO was prepared by using the cleaning protocol detailed in the previous section. The substrates were modified in 1 mM solutions of the acids for approximately 16 h after which they were sonicated (5 min) in pure solvent (same solvent used during modification) and dried under N_2. AFM was then performed on the samples using an agilent N9524B microscope.

2.9 Conclusions

The studies undertaken in this chapter demonstrate that the solution-based electrochemical properties of the ferrocene modifiers can be complex and involve multiple mechanisms. We were able to show that Fc and FcHA exhibited a diffusion-limited quasireversible electrochemical response under both CV and CSWV conditions. In contrast, FcSA and FcPA undergo a quasireversible mechanisim that we were initially only able to deduce by employing CSWV techniques. These solution phase studies revealed that the use of CV to extract rate constants may lead to superficial analysis due to the techniques inability to resolve solution phase and surface-confined species whose formal potential are close. CSWV may be a better tool in this regard. While we were able to better identify the presence of two different populations in the solution-phase CSWV of FcPA, we were unable to completely resolve the peaks of the diffusional and surface-confined species for FcPA due to the significant ovelap of their redox potentials. Peak fitting was used to deconvolute the two species. FcCA proved to be another interesting case of a mixed system. The electrochemical response of FcCA under CSWV analysis shows both a surface-confined and a diffusional species on the forward scan but only the former on the reverse scan. Concentration dependent studies revealed that under the experimental conditions used the oxidized form of the molecule has a greater affinity for the ITO relative to the neutral form. It is interesting to note that while CV-based log-log plots of current *vs*. scan rate provided evidence that the molecules strongly interacted with the ITO surface, all the voltammograms only showed a single oxidation and reduction potential at 1 mM.

Using electrochemical techniques we were able to determine rate constants for the heterogeneous charge transfer. FcCA had the largest formal potentials and exhibited the slowest electron transfer kinetics as determined both from CV and CSWV. The latter also allowed us to determine a charge transfer coefficient value of 0.26 for the molecule, which suggest that the energy barrier for electron transfer is skewed toward the reactant. The surface confined and diffusional species in FcPA had comparable transfer coefficients that were both skewed toward the product side of the energy barrier. Similar observations were made for FcSA with the barriers going in the opposite direction. Relatively speaking, FcPA exhibited fast kinetics (5.3 ± 1) while the rate constant for FcSA were mostly modest (3.2 ± 0.5) under CSWV conditions in the diffusion-limited case.

2.10 Literature cited

[1] C. Carter, M. Brumbach, C. Donley, R. D. Hreha, S. R. Marder, B. Domercq, S. Yoo, B. Kippelen, N. R. Armstrong, *J. Phys. Chem. B* **2006**, *110*, 25191.

[2] N. R. Armstrong, C. Carter, C. Donley, A. Simmonds, P. Lee, M. Brumbach, B. Kippelen, B. Domercq, S. Y. Yoo, *Thin Solid Films* **2003**, *445*, 342.

[3] L. D. Freedman, G. O. Doak, *Chem. Rev. (Washington, DC, U. S.)* **1957**, *57*, 479.

[4] A. L. Bacarella, E. Grunwald, H. P. Marshall, E. L. Purlee, *J. Org. Chem.* **1955**, *20*, 747.

[5] J. P. Guthrie, *Can. J. Chem.* **1978**, *56*, 2342.

[6] C. Yee, G. Kataby, A. Ulman, T. Prozorov, H. White, A. King, M. Rafailovich, J. Sokolov, A. Gedanken, *Langmuir* **1999**, *15*, 7111.

[7] A. Raman, R. Quinones, L. Barriger, R. Eastman, A. Parsi, E. S. Gawalt, *Langmuir* **2010**, *26*, 1747.

[8] F. G. Bordwell, H. E. Fried, D. L. Hughes, T. Y. Lynch, A. V. Satish, Y. E. Whang, *J. Org. Chem.* **1990**, *55*, 3330.

[9] S. Bohm, O. Exner, *Org. Biomol. Chem.* **2003**, *1*, 1176.

[10] W. R. McNamara, R. L. Milot, H.-e. Song, R. C. Snoeberger, III, V. S. Batista, C. A. Schmuttenmaer, G. W. Brudvig, R. H. Crabtree, *Energy Environ. Sci.* **2010**, *3*, 917.

[11] W. R. McNamara, R. C. Snoeberger, III, G. Li, C. Richter, L. J. Allen, R. L. Milot, C. A. Schmuttenmaer, R. H. Crabtree, G. W. Brudvig, V. S. Batista, *Energy Environ. Sci.* **2009**, *2*, 1173.

[12] A. M. Bond, *Broadening Electrochemical Horizons: Principles and Illustration of Voltammetric and Related Techniques*, Oxford university press, New York, **2002**.

[13] D. K. Gosser, *Cyclic Voltammetry: Simulation and Analysis of Reaction Mechanisms*, VCH Publishers, New York, **1993**.

[14] J. C. Helfrick, L. A. Bottomley, *Anal. Chem.* **2009**, *81*, 9041.

[15] L. A. Bottomley, J. C. Helfrick, *Abstr. Pap. Am. Chem. Soc.* **1988**, *196*, 424.

[16] V. Mirčeski, Š. Komorsky-Lovrić, M. Lovrić, *Square wave voltammetry: theory and application*, Springer-Verlag, Berlin, **2007**.

[17] P. T. Kissinger, W. R. Heineman, *J. Chem. Educ.* **1983**, *60*, 702.

[18] R. S. Nicholson, *Anal. Chem.* **1965**, *37*, 1351.

[19] J. C. Eklund, A. M. Bond, J. A. Alden, R. G. Compton, *Adv. Phys. Org. Chem.* **1999**, *32*, 1.

[20] R. S. Nicholson, I. Shain, *Anal. Chem.* **1964**, *36*, 706.

[21] P. Monk, *Fundamentals of Electroanalytical Chemistry*, John Wiley and Sons Ltd, West Sussex, **2001**.

[22] J. J. Odea, J. Osteryoung, R. A. Osteryoung, *Anal. Chem.* **1981**, *53*, 695.

[23] L. A. Bottomley, J. C. Helfrick, *Abstr. Pap. Am. Chem. Soc.* **1991**, *201*, 116.

[24] M. A. Mann, *Thesis in preparation,* Ph. D., Georgia Institute of Technology **2014**.

[25] C. Hansch, A. Leo, R. W. Taft, *Chem. Rev. (Washington, DC, U. S.)* **1991**, *91*, 165.

[26] H. Imaizumi, T. Koyanagi, D. Zhao, *J. Radioanal. Nucl. Chem.* **2002**, *252*, 467.

[27] A. Harada, K. Kataoka, *Macromolecules* **1995**, *28*, 5294.

[28] E. M. Johnson, D. A. Berk, R. K. Jain, W. M. Deen, *Biophys. J.* **1996**, *70*, 1017.

[29] C. Donley, D. Dunphy, D. Paine, C. Carter, K. Nebesny, P. Lee, D. Alloway, N. R. Armstrong, *Langmuir* **2002**, *18*, 450.

[30] N. R. Armstrong, P. A. Veneman, E. Ratcliff, D. Placencia, M. Brumbach, *Acc. Chem. Res.* **2009**, *42*, 1748.

[31] M. Lovric, *Electroanalysis* **2002**, *14*, 405.

[32] W. Zhang, F. Si, F. Li, *Huaxue Shiji* **1995**, *17*, 293.

[33] M. Tanaka, T. Sawaguchi, Y. Sato, K. Yoshioka, O. Niwa, *Langmuir* **2011**, *27*, 170.

[34] O. Oms, F. Maurel, F. Carre, J. Le Bideau, A. Vioux, D. Leclercq, *J. Organomet. Chem.* **2004**, *689*, 2654.

CHAPTER 3 PROBING THE KINETICS OF CHARGE-TRANSFER FROM SURFACE-CONFINED REDOX FERROCENE MOLECULES CONTAINING VARIABLE ANCHORING GROUPS

3.1 Introduction

This chapter examines the charge-transfer kinetics between the chemically bound (i.e., surface-confined) ferrocene modifiers and ITO. Here, the ITO surface is pre-functionalized with the ferrocene molecules and the modified electrode subsequently used to study charge- transfer kinetics between the redox molecule and the TCO. These mechanisms are again investigated using CV and CSWV.

3.2 Evaluation of charge-transfer kinetics and coverage of surface-confined species using CV

In order to evaluate the kinetics of charge transfer by CV the Laviron mathematical treatment[1] was be used. As was the case for the Nicholson[2] and Bottomley[3, 4] methods used to study solution-phase kinetics, here a relationship is developed that relates the separation in peak potential (ΔE_p) to a dimensionless electrokinetic parameter (m) from which the rate constant can be determined. In this approach the current measured is represented by Equation 3.1

$$\frac{i}{(F^2/RT)n^2\Gamma_T A} = m(\Gamma_O/\Gamma_T)\eta^{-\alpha} - (\Gamma_R/\Gamma_T)\eta^{1-\alpha} \qquad \text{(Equation 3.1)}$$

$$\eta = \exp(nF/RT)\,(E - E^{o}) \qquad \text{(Equation 3.2)}$$

$$m = \frac{(RT/F)}{k_s/n\nu} \qquad \text{(Equation 3.3)}$$

where η and m are describe mathematically by equations 3.2 and 3.3, respectively, k_s is the surface-confined rate constant for charge transfer, Γ_T represent the total monolayer coverage on the surface, Γ_O is the coverage of oxidized species and Γ_R is the coverage of reduced species. All other terms are as defined previously. Assuming a symmetric barrier for charge transfer, a working curve (Figure 3.1) can be generated that relates the separation in the peak potential from the voltammogram to the electrokinetic parameter (m). Once m is determined equation 3.3 can be used to solve for the rate constant.

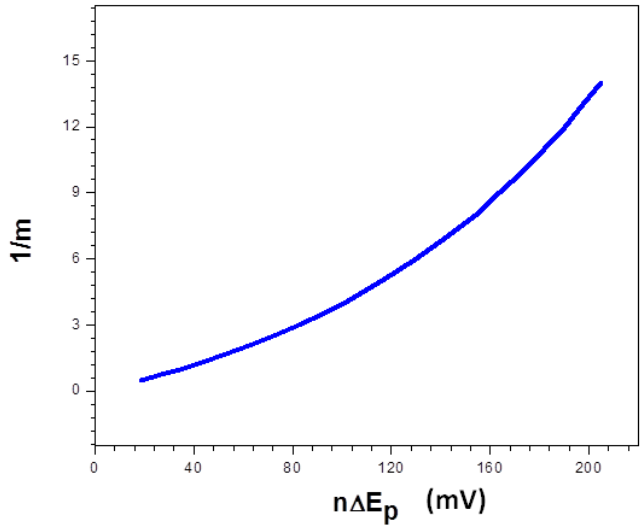

Figure 3.1 Laviron working curve for deducing the electrokinetic parameter (m) from the separation in peak potentials (ΔE_p) of the voltammetric response of a surface-confined electroactive species. Working curve adapted from the work of Laviron.[1]

The coverage of redox modifier on the surface is related to the amount of charge (Q) passed during the oxidation of the surface-confined molecule and is expressed mathematically by Equation 3.4.

$$Q = nFA\Gamma_T \qquad \text{(Equation 3.4)}$$

Q can be determined by integrating the background-subtracted peaks in the cyclic voltammogram. A percent monolayer coverage can be determined based on a theoretical close packed model of electroactive ferrocene groups having coverage of ~ 4×10^{-10} mol/cm^2.[5]

3.3 Evaluation of charge-transfer kinetics of surface-confined species using CSWV

To determine the rate constant of charge transfer using CSWV an approach similar to the one described in chapter 2 is used. Here, working curves are generated that relate the separation in peak potentials to the log of period (ms) for different rate constants. The rate constants can subsequently be deduced from an overlay of the experimental data on top of the working curves. An example is shown in Figure 3.2 for the surface-confined component of the FcSA discussed in the previous chapter.

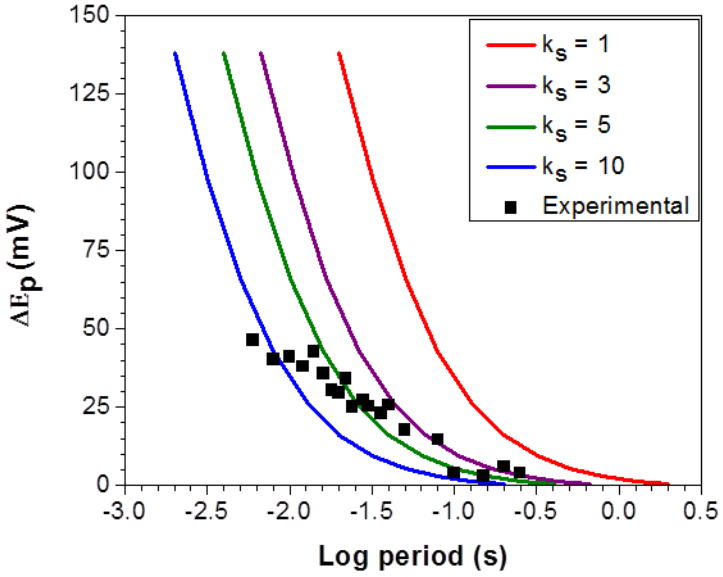

Figure 3.2 CSWV working curves for determining the rate constant of charge transfer for surface-confined species from CSWV. The legend depicts different rate constant for which the theoretical curves were generated. The experimental data is for the surface-confined FcSA component discussed in the previous chapter. The method was adopted from the Bottomley Group.[6]

3.4 Characterization of ferrocene-based monolayers on ITO by X-ray photoelectron spectroscopy

A prerequisite to understanding the kinetics of charge injection between ITO and the redox moieties is a method for depositing the molecules of interest on the surface of the metal oxide. To validate coverage, surface-sensitive techniques such as x-ray photoelectron spectroscopy (XPS) are required. XPS is a photoelectric effect-based technique that provides molecular composition information at interfaces down to the parts per thousands. In XPS, core-level electrons within the first 10 nm of the surface are excited by monochromatic x-ray radiation, and consequently ejected to vacuum where

their kinetic energy is analyzed by a suitable detector (Figure 3.3). The kinetic energy of the ejected electrons can, in turn, be correlated to a unique set of elemental core level thereby providing information on the chemical identity and environment of the molecules and/or atoms. The relative composition of the various constituents at the interface can be determined from the intensities of the various elemental peaks down to approximately 0.1%

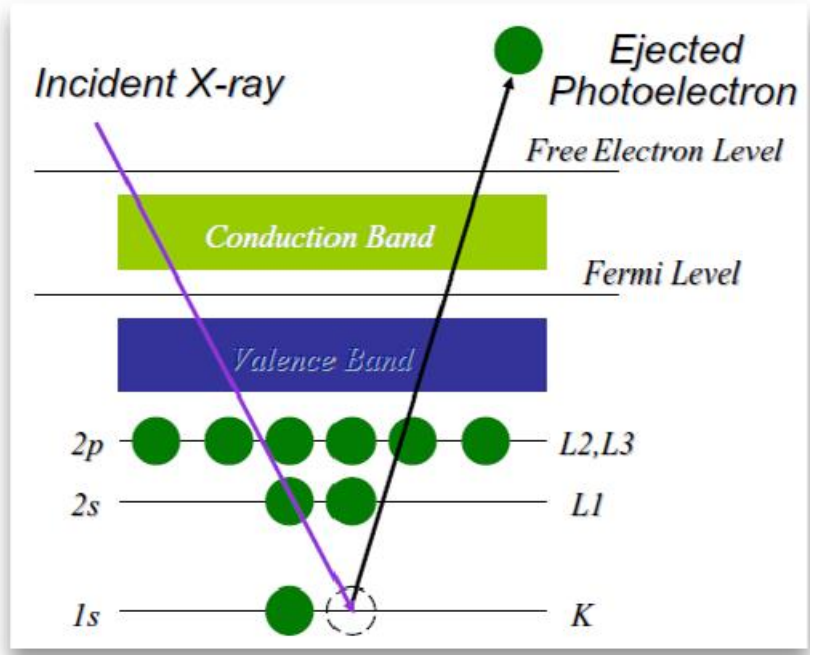

Figure 3.3 Schematic showing the process of x-ray photoelectron spectroscopy. Reproduced from UTEP.[7]

Several solvents were used in the preparation of samples for XPS analysis; the selection for a particular modifier was based on which solvent afforded maximum coverage on the metal oxide surface.[8] The details for cleaning and modifying ITO were previously outlined in section 2.8.5. Briefly, A piece of 1″ × 1″ ITO was placed in 1 mM solutions of the various modifiers overnight (~14 h) at room temperature. The samples

were then removed from their modification solutions, sonicated in fresh solvent for five minutes to remove any physisorbed molecules, and then dried under a stream of N_2. Figure 3.4 shows the result of the XPS studies that confirms the successful modification of the ITO substrate with the ferrocene modifiers. The measurements were done at an angle of 70° in order to increase the surface sensitivity of the technique. In addition to the characteristic lines of the ITO substrate, the surveys show clear differences in the photoemission spectra among the substrates functionalized with the different modifiers (Figure. 3.4a). All survey spectra show an increase in the C 1s signal upon modification of the ITO film with the ferrocene modifiers, which is consistent with introducing a carbon-based overlayer at the surface. The region of the spectrum in which the Fe (2p) photoelectron line is observed (~ 713 eV) is not shown because overlap of the signal with that of the In (3p) line. The high resolution spectra (Figure 3.4 b-d) show the P (2p), N (1s), and S (2p) lines that are unique to the FcPA, FcHA, and FcSA modifiers, respectively. Unfortunately, FcCA had no unique molecular marker that could be used to identify it by XPS, so the increased carbon content on the surface was taken as evidence of successful modification.

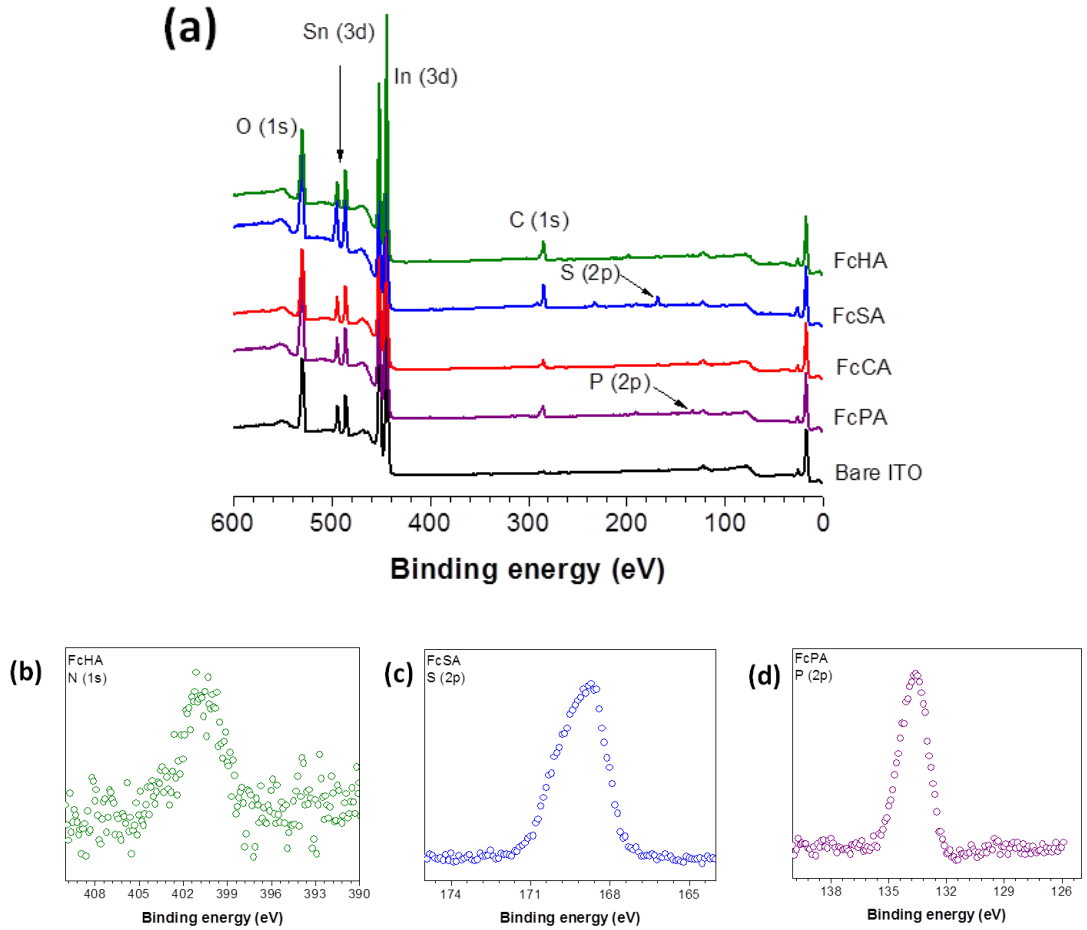

Figure 3.4 Low and high resolution XPS spectra of surface modified ITO. (a) Survey spectra of bare and modified ITO depicting the various photoemission lines. (b) High resolution N (1s) line from FcHA-modified ITO, (c) S (2p) line from FSA modified ITO and (d) P (2p) line from FcPA-modified ITO. All spectra were obtained at an angle of 70°.

3.5 Monolayer formation kinetics on ITO

The time required to form a full monolayer of the molecules on the ITO surface was evaluated by CV and coverage calculated by using equation 3.4. The results are shown graphically in Figure 3.5.

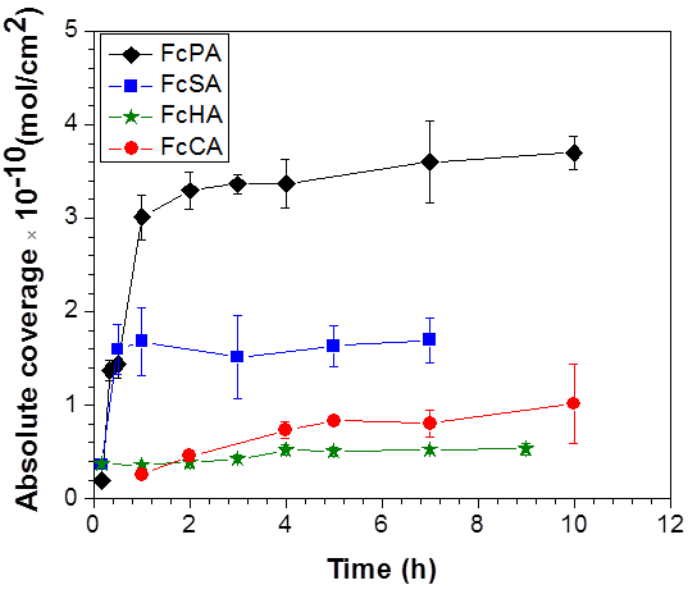

Figure 3.5 Surface coverage of ferrocene-based monolayers on ITO as a function of deposition time. Measurements were taken at a scan rate of 0.1 V/s against an Ag/Ag^{+} reference electrode.

It was found that the sulfonic acid reached maximum coverage after ~ 1 h, while the carboxylic, phosphonic, and hydroxamic acids took 4 h. The data shows that the order of maximum coverage is FcPA (93%) > FcSA (39%) >FcCA (25%) and FcHA (12%) where the percent coverage is based on a theoretical monolayer (4×10^{-10} mol/cm^2). The difference in coverage is believed to be a result of variations in the binding affinity of the anchoring group for the surface of the ITO, the ordering/packing of the molecules on the surface and their relative stability.

The adsorption kinetics of ferrocene-based monolayer on ITO has been previously shown to follow Langmuir isotherm profile.[9, 10] In this model the relative coverage ($\Theta = \Gamma/\Gamma_{mono}$) of molecules on the surface of the substrate is related to the bulk concentration (C*) of molecules in solution (i.e. the solution system used to prepare the functionalized substrates) by Equation 3.5

$$\theta = (K_L C^*)/(1 + K_L C^*) \quad \text{(Equation 3.5)}$$

where K_L is the Langmuir adsorption constant, Γ is the absolute coverage of molecules on the surface and Γ_{mono} is the maximum theoretical coverage.[11] Assuming that all adsorption sites on the surface of ITO are equivalent and that there is minimal interaction between the molecules on the surface, a series of experiments were conducted to examine the dependence of coverage of the concentration of the modification solutions and the results fitted to a Langmuir isotherm (Figure 3.6). Concentrations representative of those often reported in literature were used to conduct these studies. The results show that the phosphonic and carboxylic acid have the highest and lowest affinity for the ITO surface, respectively. On average, the hydroxamic acid has a larger binding constant than the sulfonic acid but given the error bars their affinity for the ITO surface can be considered comparable. The fact that the trends in the binding constant show no direct correlation to coverage obtained over time serves as an indication that molecular stability and packing may play a significant role in the adsorption kinetics.

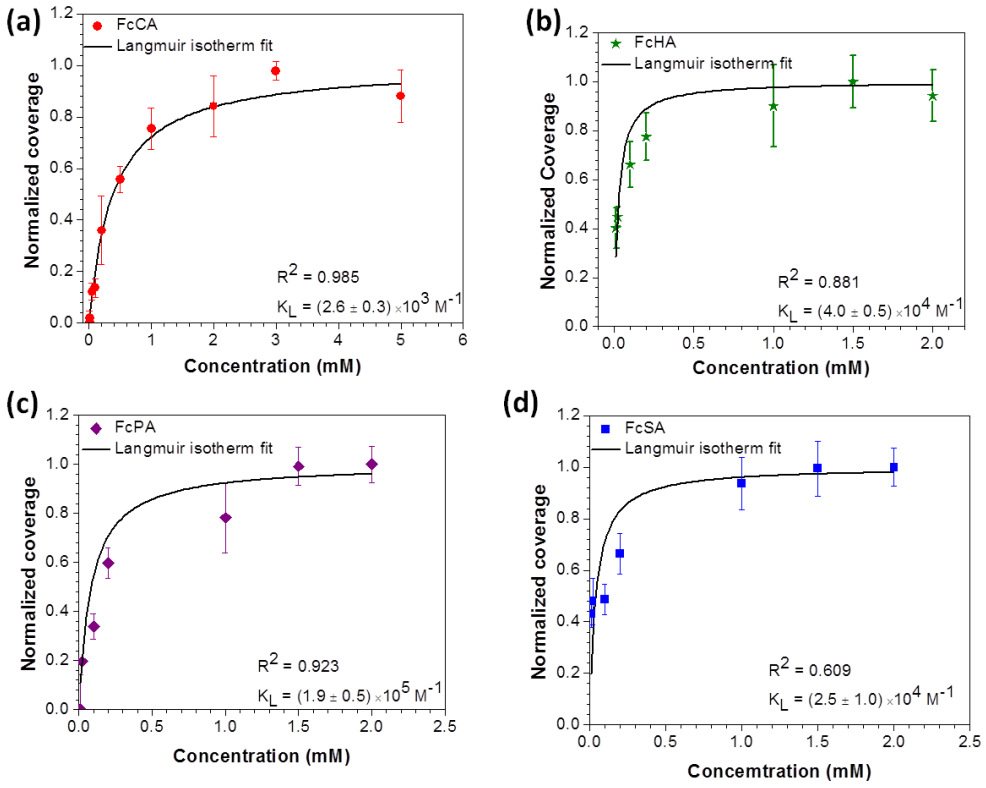

Figure 3.6 Electrochemically determined Langmuir isotherm for the adsorption of the ferrocene redox molecules on ITO. The CVs used to determine coverage were obtained vs an Ag/Ag^{+} reference electrode.

The molecular footprint of the molecules used in this study was previously visualized by Park *et al.*[8] using Hartree-Fock optimized geometry (basis set 6-31 G). In this study, the maximum and minimum projection areas for molecules having various binding configuration on the surface were determined using a close-packed monolayer model. The range of projection areas in angstroms for the molecules are: (i) FcPA, 24-27 Å (ii) FcSA, 25-48 Å (iii) FcHA, 20-41 Å and (iv) FcCA, 19-33 Å. These results indicate that there is significant variability in the degree of coverage that can be obtained for any one of these molecules, which was not observed experimentally. More sophisticated and refined modeling may be required to fully understand molecular packing on the surface.

In any organic electronic application, the long-term stability of the surface modifiers is crucial for the efficient performance of the device. As such, the electrochemical stability of the modifiers on the surface was evaluated by subjecting the surface-modified ITO samples to 10 consecutive voltammetric cycles and coverage monitored. These electrochemical experiments were conducted using a scan rate of 0.1 V/s against a Ag/Ag+ reference electrode. The observed reduction in coverage after 10 cycles was: 6% , 43%, 44% and 45% for FcPA, FcSA, FcHA and FcCA; respectively. These results highlight the superior stability of phosphonic acids on the surface of ITO.

3.5.1 Evolution of electron-transfer rate constant as a function of coverage using CV

The Laviron formalism was used to track the electron-transfer rate constant as a function of coverage (i.e., increasing modification time). In these experiments, the pre-modified samples were prepared in 1 mM solutions and the rate constant determined from the separation of the peak potentials. The results of these studies are presented in Figure 3.7.

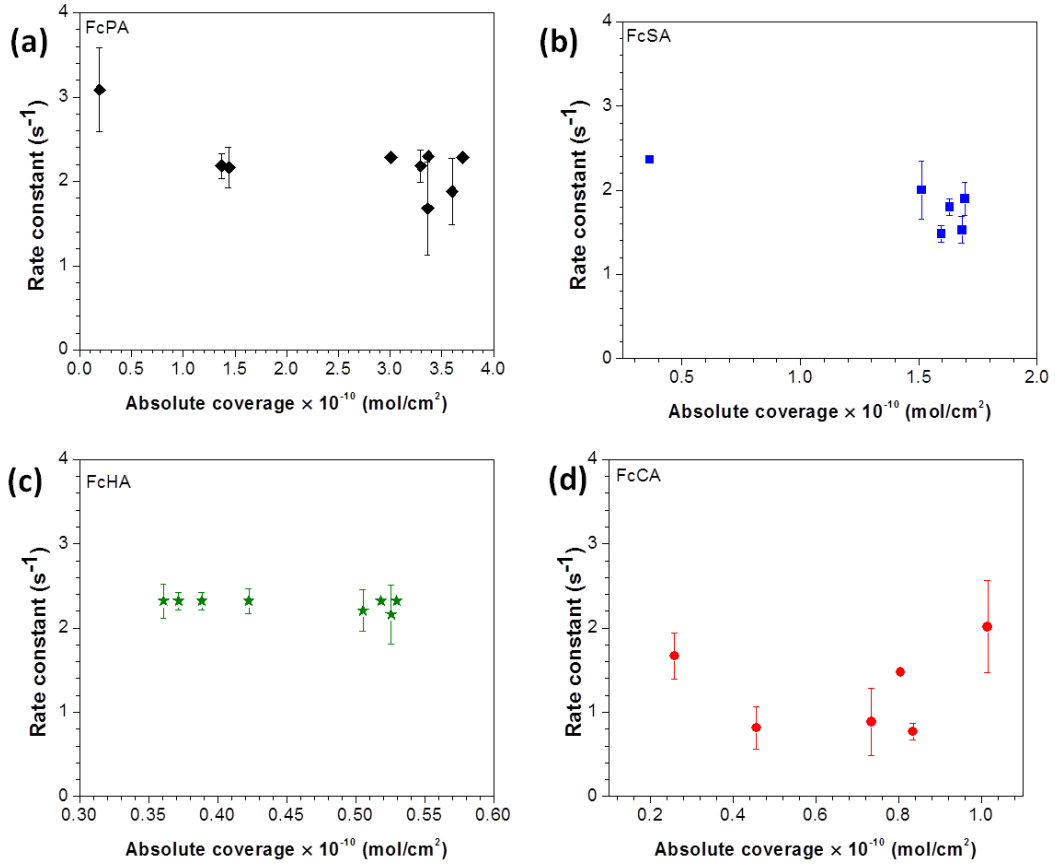

Figure 3.7 Illustration of the evolution in rate constant as a function of coverage for (a) FcPA, (b) FcSA, (c) FcHA and (d) FcCA. Dashed lines serve as a guide for the eye. All measurements were done at a scan rate of 0.1 V/s using an Ag/Ag^{+} reference electrode.

At the onset of modification with FcPA and FcSA higher values of charge transfer are observed, which rapidly falls off at loading levels of approximately 1.5 $\times 10^{-10}$ mols/cm^2. Beyond this point, the rate constant undergoes moderate fluctuations around 2.1 s^{-1} and 1.8 s^{-1} for FcPA and FcSA, respectively. The initial high rate constant observed for these two molecules is believed to be due to the rapid adsorption of independently anchored redox molecules on the electroactive sites of the ITO surface. With prolonged exposure to the modification solution more molecules begin to adsorb onto the surface resulting in significant lateral interaction between the molecules, which reduces the rate of

heterogeneous charge-transfer to an approximate constant level with further increases in coverage.[12, 13] FcHA rapidly achieves an invariable level of electron-transfer at low concentrations, which suggest that the lateral interaction of the molecules plateaus early in the adsorption process. Given the small difference in coverage of FcHA on the surface of ITO at the onset and end (i.e., when saturated coverage is achieved) we postulate that the molecular footprint of the adsorbed molecule limits the coverage and simultaneously the observed rates of charge transfer. FcCA shows a great deal of variability in the rate constant as a function of coverage. This is believed to be a result of the formation of unstable monolayers on ITO due to its relatively low binding constant. Under the condition of CV, the microstructure of the FcCA layer is constantly changing as molecules rearrange on or desorb from the surface.

3.6 Evaluation of the redox properties of the surface-confined ferrocene modifiers on ITO using CV

The redox properties of the surface-anchored ferrocene derivatives were evaluated using cyclic voltammetry. Voltammograms were obtained for saturated coverage of the redox molecules on oxygen plasma treated ITO. The experiments were conducted using 0.1 M tetrabutylammonium perchlorate (TBAP) in acetonitrile (ACN). The voltammogram of FcPA-modified ITO is shown in Figure 3.8 as an example; all the other molecules exhibit similar behavior. All the voltammograms show the anticipated one-electron redox behavior that is well documented for ferrocene. At low scan rate (~0.1 V/s) the separation between oxidation and reduction peaks are minimal and the voltammogram has a nearly symmetric profile. As was the case with solution phase

voltammetry, this indicates a high degree of reversibility and fast charge-transfer rates on the timescale of the experiment.

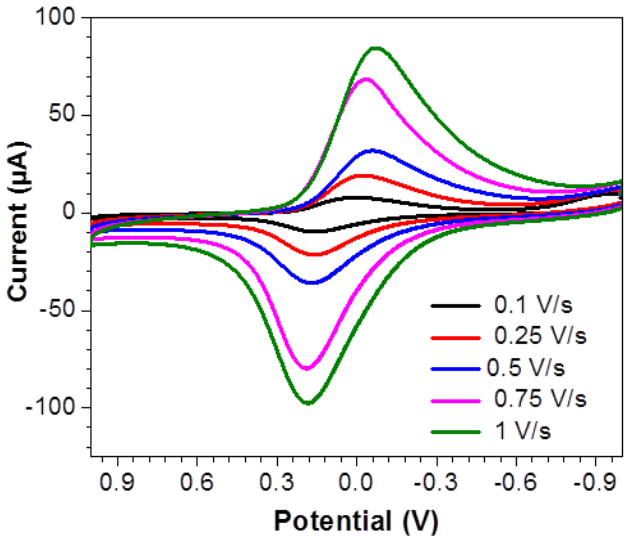

Figure 3.8 Cyclic voltammograms of saturated FcPA modifier on ITO at scan rates ranging from 0.1-1V/s. Measurements were taken *vs*. a Ag/Ag^{+} reference electrode.

However, as the scan rate is increased the peak separation and current increases and the peak shapes becomes broader indicating a more sluggish charge-transfer process. Recall from equation 2.21 that there should be a linear relationship between the current and scan rate for surface-confined species in CV. The relationship between current and scan rate is depicted in Figure 3.9. The plots show that most of the molecules did not follow the predicted linear trend. It is postulated that the observed scattering in the data is due in part to the fact that the molecules are being ejected from the surface as the potential is scanned, which creates an additional diffusional component in the observed current. Further, the deviation can also be partly attributed to the structural changes in the

monolayer, and the associated fluctuations in the lateral interactions, that occur under the influence of the potential scan.

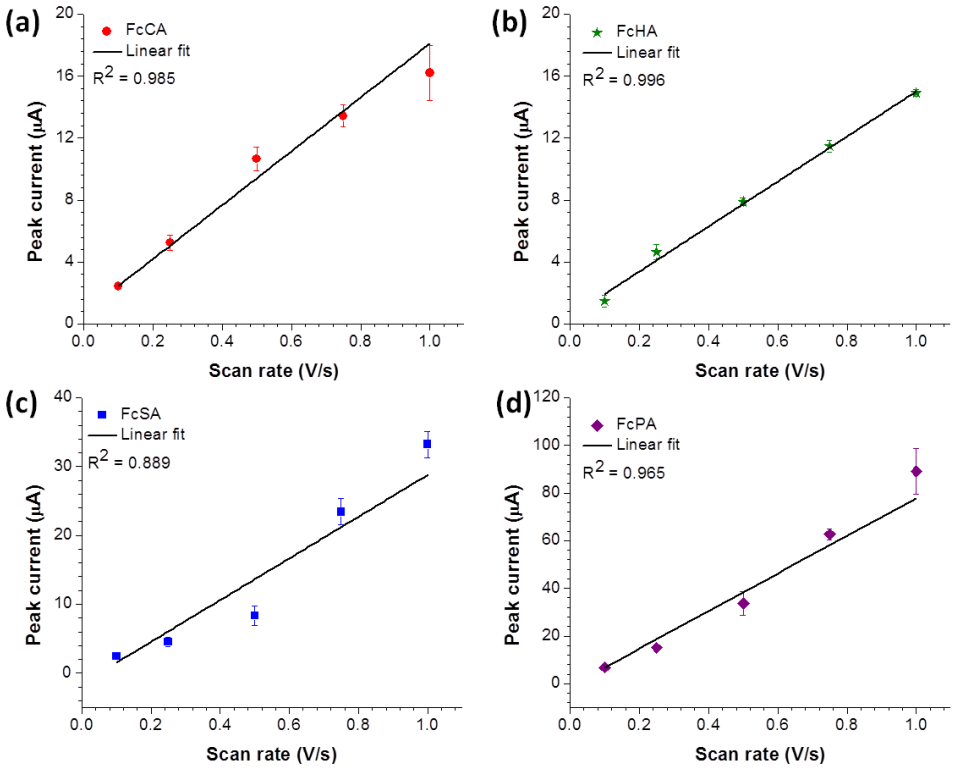

Figure 3.9 Plots of current *vs.* of scan rate for the various modifiers. The linear fits to each plot is shown in black.

Table 3.1 and Figure 3.10 summarize the electrochemical response for saturated monolayers of the redox modifiers on oxygen plasma treated ITO obtained at a scan rate of 0.1 V/s. The voltammograms in Figure 3.10 show that the modifiers experience vastly different microstructure and consequently, exhibit different electrochemical properties on the surface of ITO. The differences in the peak currents reflect the variations in the

coverage of the molecules on the metal oxide surface, while the broad voltammetric profiles (FWHM) suggest a heterogeneous surface environment. In theory, the peak width at half max (FWHM) in an ideal monolayer is 90.6 mV for a one-electron transfer reaction at 25 °C.[14] Deviations from this value are generally attributed to site-to-site heterogeneity, intermolecular interactions, multiple populations of redox molecules on the electrode surface or any combination of the aforementioned issues. On average, the experimentally determined FWHM values ranged from 161mV to 342 mV thereby, emphasizing the heterogeneous nature of the films formed on the electrode surface. Based on the half-wave potential values, it can be deduce that the order of increasing difficulty of oxidation for the surface-confined molecules investigated is FcCA < FcPA < FcSA < FcHA. Interestingly, the order is very different from that previously obtained from the solution phase CV studies, which was FcSA < FcPA < FcHA < FcCA.

Table 3.1 Electrochemical response of the various surface-confined ferrocene modifiers on ITO All measurements of potential and rate constants are reported for a scan rate of 0.1 V/s vs Ag/Ag^{+} reference electrode.

	FcPA	FcHA	FcSA	FcCA
$E_{1/2}$ (mV)	209 ± 20	340 ± 11	260 ± 14	31 ± 70
ΔE_p (mV)	55 ± 3	52 ± 8	64 ± 5	66 ± 13
FWHM (mV)	342 ± 24	166 ± 7	161 ± 2	282 ± 12
k_s (s^{-1})	2.2 ± 0.2	2.4 ± 0.5	1.8 ± 0.2	2.0 ± 0.5

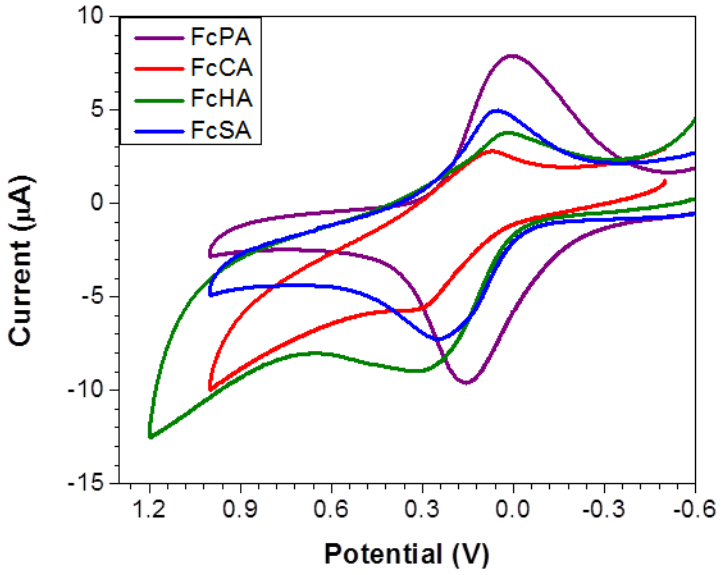

Figure 3.10 Cyclic voltammograms of surface-confined ferrocene-based modifiers *vs.* a Ag/Ag^{+} reference electrode. Measurements were taken at a scan rate of 0.1 V/s against an oxygen plasma treated working ITO electrode

This difference in $E_{1/2}$ values for the solution-phase and pre-modified electrode studies show that the barrier to charge-transfer is significantly altered by the adsorption of the molecules on the surface of ITO. This is particularly obvious in the case of the FcCA which proved to be the most difficult molecule to oxidize in solution and the easiest once it was tethered to the surface of the ITO.

The Laviron formalism[1] was used to calculate the rate constant for electron transfer for the surface-confined molecules on ITO and the results are presented in Table 3.1. The values for the rate constant are significantly greater than those obtained from the solution experiments discussed in the previous chapter. This is an expected result since the measured rated are no longer limited by diffusion as well as the fact that the molecules are now in greater electrical contact with the electrode. As was observed in chapter 2, the rate constants for the surface-confined molecules are comparable, which

suggest that the molecules experience a similar barrier to charge transfer. This seems to be the case whether or not the molecules are absorbed from solution or pre-modified on the electrode. The implication here is that in an OPV device the choice of the tethering group does not play a significant role in the rate of charge-transfer across the inorganic-organic interface. However, recall from the introductory chapter that the work function of the metal oxide electrode depends significantly on the number density of molecules on the surface, which suggest that the phosphonic acid is the tethering group of choice among this class of molecules.

3.7 The effect of surface pretreatment on the redox response of ITO electrochemical

It has been demonstrated that the surface composition of ITO affects the electrochemical kinetics of charge transfer between redox molecules and the TCO.[15-17] As such, in this section we set out to examine the influence of various surface pretreatments on the kinetics of charge transfer. Recall from chapter one that the surface hydroxides play a key role in tethering the anchoring group of the acids to the surface of metal oxides. Based on this premise, the hydroxyl content of the surface was altered by using an acid (HI) and a base (KOH) to etch the surface of the ITO. Detergent solvent cleaned (DSC) and oxygen plasma (OP) treated ITO was also examined. In order to assess the changes in the surface composition as a function of pretreatment XPS analysis was conducted.

3.7.1 XPS assessment of the surface composition of ITO as a function of different pretreatments

XPS was utilized to gain insight into the compositional changes that occur when ITO is subjected to the aforementioned pretreatments. The results of the study are shown in table

Table 3.2 Pretreatment-dependent surface atomic concentrations of the ITO.

	Atomic concentrations (%)			
	DSC	**OP**	**HI**	**KOH**
In (3d)	36.1	28.0	29.0	36.8
Sn (3d)	6.4	4.1	5.0	6.5
O (1s)	57.5	67.9	66	56.7

Relative to the DSC treated substrate, the KOH treated surface showed marginal increases in In and Sn and a slight reduction in the oxygen content. However, the OP and HI treated ITO substrates showed a significant reduction in Sn and In and a substantial increase in the oxygen. In order to gain additional insight into the changes occurring at the surface, high resolution spectra were obtained and analyzed.

Since the O (1s) core-level photoemission line showed the most significant changes in its shape and composition after pretreatment relative to those of the metals lines, it was used to conduct the analysis.[15] Peak fitting analysis of the O (1s) line has

been shown before to be a suitable means of assess hydroxyl content on the surface of ITO; this approach was employed here. [15, 18] Figure 3.11 presents the high resolution O (1s) lines for the ITO that have been subjected to the aforementioned surface pretreatment. In order to increase the surface sensitivity of the technique, the measurements were done at an angle of 70°.

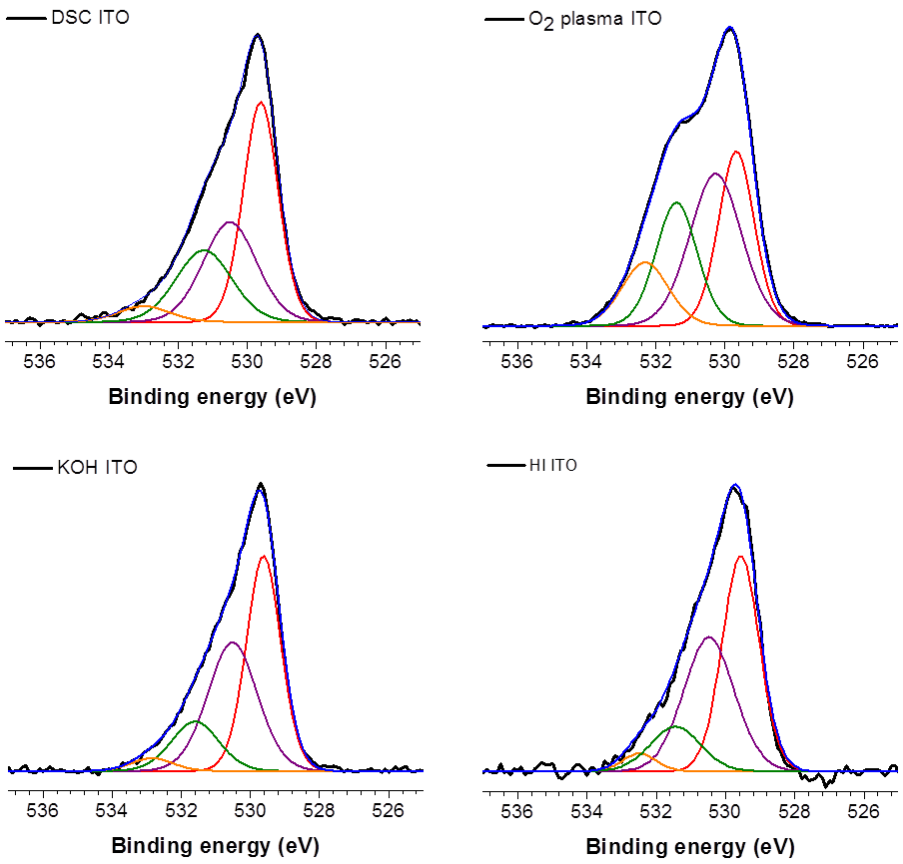

Figure 3.11 High resolution XPS O (1s) spectra of differently pretreated ITO. The spectra shows four components: (i) fully coordinated In_2O_2 oxygen (red trace), (ii) oxygen species close to vacancy sites and at the surface (purple trace), (iii) hydroxyl oxygen $In(OH)_3$ (green trace) and (iv) adventitious carbon (orange trace).

All the peaks were fitted to with a model that that was previously developed in the Armstrong Group at the University of Arizona for ITO surfaces; the details of the model will be provided in the next chapter.[15, 19] All peaks were fit with the minimum number of components using a 70% Gaussian, 30% Lorenzian profile to provide reasonable fit to the experimental data. The binding energy and full width at half maximum (FWHM) of the peaks were fixed such that only the height of the components were allowed to vary. Based on the Armstrong model, four different oxygen species were observed on the surface of the ITO. From low to high binding energy these species were determined to be: (i) fully coordinated In_2O_2 oxygen (red trace), (ii) oxygen species close to vacancy sites and at the surface (purple trace), (iii) hydroxyl oxygen $In(OH)_3$ (green trace) and (iv) adventitious carbon (orange trace), which is consistent with what is reported in literature.[15, 19]. The results indicate that the hydroxyl content of the HI and KOH etched surface were (8%) and (11.5%), respectively, which was much lower much lower than that of the DSC treated surface (15.4%). However OP etching provided a surface on which the hydroxyl content was significantly increased to 24.5%.

3.7.2 Assessing the kinetics of charge transfer for differently pretreated ITO surfaces.

The Laviron formalism[1] was used to assess the kinetics of charge transfer between the surface-confined ferrocene redox modifiers and ITO that has been pretreated using the various protocols mentioned in the preceding section. Table 3.3 summarizes the results from these studies.

Table 3.3 Rate constant and coverage for surface-bound ferrocene modifiers on ITO pretreated with KOH, HI, OP, and DSC.

	Rate constant (s^{-1}) [% monolayer]			
	FcPA	**FcCA**	**FcSA**	**FcHA**
DSC	1.3 ± 0.2 [56%]	1.6 ± 0.2 [8%]	1.2 ± 0.2 [26%]	1.4 ± 0.1 [8%]
KOH etch	1.7 ± 0.2 [48%]	1.92 ± 0.1 [28%]	1.5 ± 0.4 [28%]	2.3 ± 0.2 [15%]
O_2 plasma	2.2 ± 0.2 [89%]	2.0 ± 0.5 [25%]	1.8 ± 0.2 [39%]	2.4 ± 0.5 [12%]
HI etch	1.4 ± 0.2 [65%]	2.0 ± 0.6 [18%]	1.6 ± 0.3 [20%]	2.2 ± 0.2 [18%]

The results depicted in Table 3.3 shows that surface pretreatment significantly impacts the coverage of the molecules on the surface of the ITO. From the table it can be seen that the pretreatment protocol that affords the highest coverage on the ITO surface varies among the different molecules. This observation is significant because it reinforces the notion that pretreatment protocols should be treated as being system specific unless experimental evidence suggest otherwise. This is important for the development of OPVs where monolayers are often deposited on the TCO electrode to modulate the work function. In the case of the phosphonic acid, the highest coverage (89%) and rate constant (2.2 ± 0.2) were obtained using OP treated ITO. It is not surprising that the DSC treated ITO consistently gave the lowest rate constant for FcPA as it is generally understood that substrates prepared in this manner have a thin, tightly bound carbonaceous layer that diminishes the electrical and electrochemical properties at the interface.[15] It is for this reason why DSC surfaces a usually referred to as being “un-activated.” Etching with

KOH afforded the highest coverage (28%) for FcCA but the rate constant was independent of the pretreatment protocol, not considering DSC. Similarly, the rate constants obtained for FcSA on activated ITO also appeared to be independent of pretreatment and the highest coverage (39%) was obtained from OP etched TCO. FcHA achieved its highest coverage (18%) from HI etching but, here too, the rate constants were almost comparable. Given the standard deviations associated with the CV derived rate constants it can be concluded that the anchoring group has very minimal effect on the electron transfer rate regardless of the pretreatment used. Furthermore no correlation could be made between the hydroxyl concentration on the surface and the coverage observed. One possible rationale for the observed discrepancy between the hydroxyl concentration and the observed coverage is that the redox molecules may bind to sites on the ITO surface that are not in good electrical contact with the remainder of the lattice as was observed before by Donley[15] and Carter[19]. Under these conditions, a high surface hydroxyl concentration may lead to high coverage of the redox molecules on the surface; however; because of the abundance of electrically inactive sites the measured apparent degree of coverage is low. Collectively, the CV studies suggest that the barrier to charge transfer is approximately the same for all the molecules.

3.7.3 Electronic structure of the metal oxide-redox molecule interface.

To examine the effect of the various anchoring group on the electronic structure at the ITO-molecule interface, ultra-violet photoelectron spectroscopy (UPS) measurements were performed on modified, oxygen plasma treated ITO samples. Briefly, UPS is surface sensitive technique (~2-10 nm probing depth) that can be used to determine the

electronic structure at interfaces. An example, band structure of indium tin oxide and its corresponding ultraviolet photoelectron spectroscopy (UPS) spectrum is shown in Figure 3.10. The spectrum is calibrated with the Fermi level (E_F) at zero since it separates the occupied and unoccupied states. Another point of demarcation below the Fermi level at low binding energy is the maximum valence band energy (E_{VBM}), which marks the onset of occupied levels.

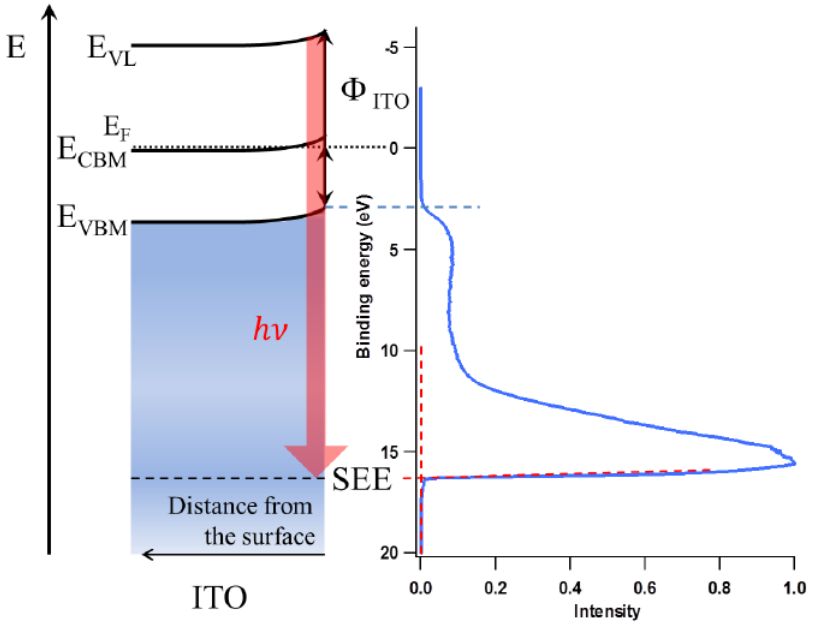

Figure 3.12 Schematic illustrating the electronic structure of ITO (left) and its corresponding UPS spectrum (right). VBM represents valence band maximum, and CBM the conduction band maximum. The work function (Φ), vacuum level (E_L) and secondary electron edge (SEE) are also indicated. Adapted from Paniagua thesis.

Analogously, the high binding energy cut-off feature or secondary electron edge (SEE) signifies the maximum depth from which electrons can be ejected and electrons at this level have approximately zero kinetic energy. The absolute difference between the SEE

and the energy of the radiation source is the work function (Φ) of the material. Therefore, by knowing all these features of a prototypical UPS spectrum one is able to construct energy level diagrams that convey the interface electronic structure. The results of the UPS measurements for the various ferrocene modifiers on ITO are presented graphically in Figure 3.13.

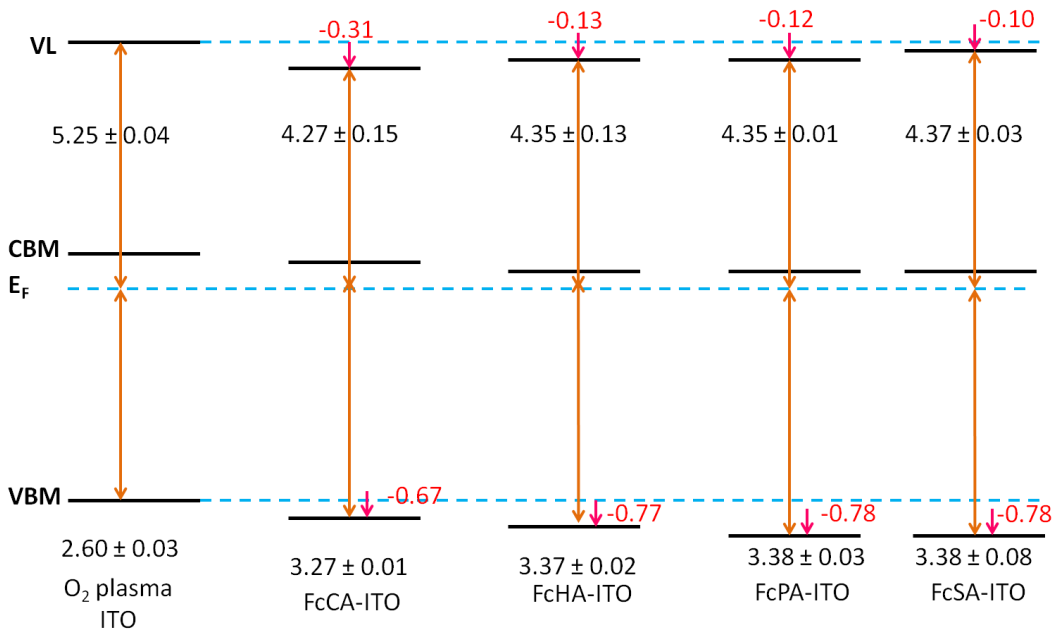

Figure 3.13 Energy level diagrams constructed from UPS for bare OP (far left) and ferrocene-modified oxygen plasma treated ITO. Significant changes in the valence band maximum and surface dipole are shown in red. A band gap of 3.6 eV was assumed and maintained throughout.

The UPS data reveal that the modified ITOs have comparable work functions thereby confirming that the barriers to electron transfer are the similar. All the molecules reduce the work function relative to the oxygen and concomitantly cause an increase in the valence band maximum.

3.8 Evaluation of the kinetics of charge-transfer using CSWV: a brief summary

In this study we investigated the kinetics of charge transfer with the aid of CSWV using the method developed by the Bottomley group. As was the case for CV, ITO electrodes with saturated coverage of the molecules were measured using a Ag/Ag^{+} electrode as reference. Given the greater sensitivity of the technique relative to CV, we hypothesized that CSWV would provide insight into any potential secondary processes occurring during the measurement that were not observed during CV. Also, the voltammograms should be better resolved due to the intrinsic nature of the technique to discriminate against background currents. Unfortunately, the results obtained from CSWV proved to be unreliable as there was significant fluctuation in the experimental result, specifically the peak potentials. Figure 3.14 shows the experimental plot of the separation of peak potentials *vs.* period for the four molecules. As was the case for the CV, the scattering of the peak potentials is indicative of heterogeneity in the monolayer. This heterogeneity is further compounded by the ejection of the molecules from the surface of the ITO during the experiment. These perturbations change the local structure of the monolayer resulting in random shifting of the peak potential position. Additionally, each data point collected in the CSWV experiments were done with a different piece of ITO; this changes the effective electroactive area exposed to the electrolyte and consequently introduces more errors. For each ITO the packing of the monolayer will vary, and these structural differences can give very different results. While similar issues

arise during the CV measurements we postulate that they are less pronounced due to the reduced sensitivity of the technique.

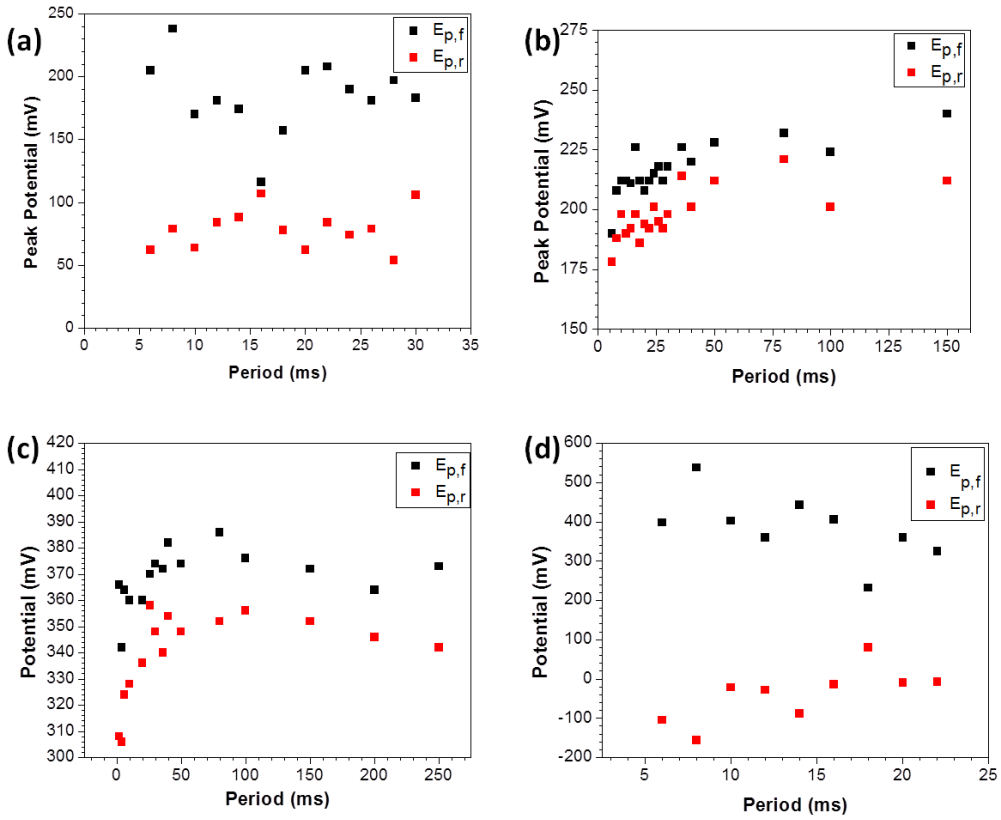

Figure 3.14 CSWV plots of peak potentials *vs.* period. The experimental data represents the surface-confined (a) FcSA (b) FcPA, (c) FcHA, and (d) FcCA. The potentials are plotted on different scales to highlight the regions of interest while the maximum value on the x-axis reflect the highest period at which a current could be measured.

3.9 Experimental Section

3.9.1 Surface pretreatment of ITO

ITO substrates were cut into 1″ × 1″ pieces and then subject to detergent solvent cleaning (DSC). This involves several steps (1) scrubbing the substrates with dilute Triton X-100 solution with the aid of a lint-free cloth, (2) sonicating in Triton X-100 solution for 10 min then rinsing with distilled water, (3) sonicating in distilled water for 10 min, (4) sonicating in ethanol for 10 min, and then (5) drying under nitrogen. All substrates were subjected to DSC treatment prior to any subsequent activation. Oxygen plasma treated ITO were treated with and O_2 plasma (Plasma Etch, PE50) for a total of 5 min prior to being used for modification and or measurement. In the case of the HI activated substrates, the TCOs were exposed to 57% hydriodic acid (Sigma Aldrich) for 10 seconds, followed by rinsing with distilled water then ethanol and then drying under a stream of nitrogen. In the KOH etch pretreatment the ITO was exposed to a 6 M aqueous solution of potassium hydroxide prior to subjecting them to the same rinsing and drying procedure used for the HI etched substrates.

3.9.2 Monolayer formation

In order to analyze the surface-confined species slightly different protocols were used depending on the objective of the experiment. The solvent system used for modification varied depending on the redox modifier; the phosphonic and carboxylic acids were done in ethanol, the sulfonic acid in chloroform, and the hydroxamic acid in THF. In the case of the absorption kinetics experiments, O_2 plasma treated ITO substrates were removed at different time points from 1mM solutions of the various acids, sonicated in the modification solvent, dried with a stream of nitrogen, and immeadiately used for

electrochemical measurements. The adsorption isotherm studies differed in two ways from the adsorption kinetic experiments: (1) the modification time was 4 h in each case and (2) various concentrations of acid solutions were used to modify the electrode. For all other experiments, 1 mM solutions were used to do the modification with a modification time that exceed the minimum saturation time as determined from the kinetic curves.

3.9.3 Electrochemical measurements

Cyclic voltammetry was performed using a CH1030A potentiostat (CH Instruments) in the conventional three electrode configuration. Cyclic square wave voltammetry was done using a Pine Instrument potentiostat. ITO served as the working electrode, a Pt wire as the counter electrode, and an Ag/Ag^{+} as the reference electrode (10mM AgNO3 in 0.1M tetrabutylammoniumperchlorate (TBAP) in acetonitrile electrolyte). All measurements were performed at a scan rate of 0.1 V/s. Measurements were performed immediately after the electrodes were pretreated as outlined in the previous section.

3.9.4 XPS Studies

All XPS measurements were carried out on a Kratos Axis Ultra^{DLD} spectrometer using a monochromatic Al(Kα) source. All the measurements were acquired at take-off angle of 70º relative to the surface normal at pass energies of 160 eV and 20 eV for surveys and high resolution data, respectively.

3.10 Conclusion

The studies outlined in this work are geared towards understanding charge transfer at the organic-TCO interface using an ITO electrode and four ferrocene based

probes containing variable anchoring groups. Binding constants for the surface-confined species on O_2 plasma ITO substrates were determined by conducting concentration dependent coverage studies and fitting the experimental data to a Langmuir adsorption isotherms model. The order of decreasing binding strength was found to be FcPA > FcSA > FcHA > FcCA, which showed a direct correlation with the electrochemically determined stability of the molecules on the surface. Different surface pretreatments were found to affect the surface composition of the ITO, and consequently the coverage of the molecules on the surface. However, no direct correlation could be made between the surface hydroxyl content and the coverage obtained. We postulate that this is due to the heterogeneity of the ITO surface, which presents as a mixture of electrically conductive and insulating regions at the surface. The CV determined rate constants on activate ITO were comparable for all the molecules, which suggest that they all experience a similar thermodynamic barrier during the charge-transfer process. A similar observation was made in chapter 2 for the surface-confined redox species. A comparison of the kinetics observed from the pre-modified ITO samples and the surface-confined species in the solution-phase experiments reveal that the rate constants are the same given the error associated with the measurements. This suggests that the anchoring group plays a minimal role in mediating the kinetics of charge transfer.

3.11 Literature cited

[1] E. Laviron, *J. Electroanal. Chem.* **1979**, *101*, 19.

[2] R. S. Nicholson, *Anal. Chem.* **1965**, *37*, 1351.

[3] L. A. Bottomley, J. C. Helfrick, *Abstr. Pap. Am. Chem. Soc.* **1988**, *196*, 424.

[4] J. C. Helfrick, L. A. Bottomley, *Anal. Chem.* **2009**, *81*, 9041.

[5] C. E. D. Chidsey, C. R. Bertozzi, T. M. Putvinski, A. M. Mujsce, *J. Am. Chem. Soc.* **1990**, *112*, 4301.

[6] M. A. Mann, *Thesis in preparation,* Ph. D., Georgia Institute of Technology **2014**.

[7] U. Wiki, http://wiki.utep.edu/download/attachments/39191737/Ch-4-Students.pdf?version=1.

[8] S. Park, *Electrochemical Evaluation of TCO Modification Using Substituted Ferrocenes,* Masters, University of Arizona **2012**.

[9] G. Zotti, G. Schiavon, S. Zecchin, A. Berlin, G. Pagani, *Langmuir* **1998**, *14*, 1728.

[10] T. Kondo, M. Takechi, Y. Sato, K. Uosaki, *J. Electroanal. Chem.* **1995**, *381*, 203.

[11] H.-J. Butt, K. Graf, M. Kappl, *Physics and Chemistry of Interfaces*, 2nd ed., Wiley-VCH, Wienheim, **2006**.

[12] R. C. Sabapathy, S. Bhattacharyya, M. C. Leavy, W. E. Cleland, C. L. Hussey, *Langmuir* **1998**, *14*, 124.

[13] S.-H. Hsu, D. N. Reinhoudt, J. Huskens, A. H. Velders, *J. Mater. Chem.* **2011**, *21*, 2428.

[14] A. M. Bond, *Broadening Electrochemical Horizons: Principles and Illustration of Voltammetric and Related Techniques*, Oxford university press, New York, **2002**.

[15] C. Donley, D. Dunphy, D. Paine, C. Carter, K. Nebesny, P. Lee, D. Alloway, N. R. Armstrong, *Langmuir* **2002**, *18*, 450.

[16] D. J. Milliron, I. G. Hill, C. Shen, A. Kahn, J. Schwartz, *J. Appl. Phys.* **2000**, *87*, 572.

[17] J. Li, L. Wang, J. Liu, G. Evmenenko, P. Dutta, T. J. Marks, *Langmuir* **2008**, *24*, 5755.

[18] E. L. Ratcliff, A. K. Sigdel, M. R. Macech, K. Nebesny, P. A. Lee, D. S. Ginley, N. R. Armstrong, J. J. Berry, *Thin Solid Films* **2012**, *520*, 5652.

[19] C. Carter, M. Brumbach, C. Donley, R. D. Hreha, S. R. Marder, B. Domercq, S. Yoo, B. Kippelen, N. R. Armstrong, *J. Phys. Chem. B* **2006**, *110*, 25191.

CHAPTER 4 BINDING OF FLUOROARYL MODIFIERS TO INDIUM ZINC OXIDE SURFACE:

4.1 Introduction

As detailed in section 1.4 of the introductory chapter, the binding interaction between small molecule surface modifiers and metal oxides determines molecular orientation of the molecules on the surface, and consequently, the magnitude and direction of the surface dipole. Therefore, in order to reliably and reproducibly tune the surface properties and energy levels at the organic-inorganic interface it is important to have a clear understanding of the mode of binding of molecular modifiers to metal oxides. As such, this chapter focuses on the binding of fluoroaryl acids, namely: pentaflurobenzyl phosphonic acid (PFBPA), and pentaflurobenzyl carboxylic (PFBCA), on the surface of indium zinc oxide (IZO). Indium tin oxide is found ubiquitously throughout the organic electronics society due to its use in solar cells, flat panel displays, electrochromic windows and so on.[1] However, owing to the rising cost of indium and the simultaneous need for transparent conducting oxide with superior electrical, optical and chemical properties there is a push toward alternative metal oxides. Indium zinc oxide (IZO) is one alternative metal oxide that is being aggressively explored as a replacement for ITO and is reported to have greater stability, comparable sheet resistance, and wide band gap.[2, 3]. The structures of the molecules are depicted in Figure 4.1. Aryl fluorinated molecules were chosen because of their relatively strong fluorine XPS cross-

section as well as the strong C-F vibration modes generally observed in infrared spectroscopy.

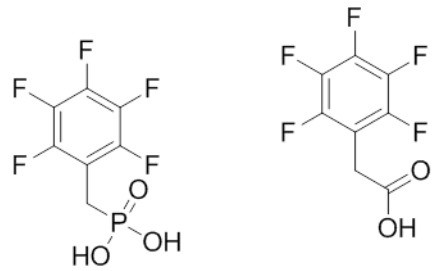

Figure 4.1 Structure of fluroaryl acids used to investigate binding on the surface of IZO

4.2 Characterization of the IZO surface

Before the binding mode of the fluoroaryl modifiers can be assessed the surface composition of the metal oxide must first be determined. As such, XPS peak fitting analysis was conducted on the oxygen plasma treated IZO. Indium oxide, indium hydroxide, zinc oxide were utilized as controls to aid in peak assignment. All the peaks were fitted to with a model that that was previously developed in the Armstrong Group at the University of Arizona for ITO surfaces.[4, 5] In the Armstrong method, peak fitting of the high resolution photoemission lines with a 70% Gaussian, 30% Lorenzian curve was found to provide reasonable fit to ITO profile. In addition, the binding energy and full width at half maximum (FWHM) of the peaks were fixed such that only the height of the components were allowed to vary. Each peak was fitted with the minimum amount of components that were needed to provide reasonable agreement with the experimental data. Table 4.1 and Figure 4.2 summarize the results from the peak fitting analysis of

IZO. In order to increase the surface sensitivity of the technique, the data was acquired using angle resolve XPS (AR-XPS) at 70°.

Table 4.1 Summary of binding energy and full width at half maximum values for IZO and related indium hydroxide/indium oxide controls.

	O (1S) [FWHM] (eV)	In (3d) [FWHM] (eV)		Zn (2p) [FWHM] (eV)	
		$3d_{3/2}$	$3d_{5/2}$	$2p_{1/2}$	$2p_{3/2}$
In_2O_3	529.5 [1.1]	451.6 [1.2]	444.1 [1.2]		
	531.2 [2.0]	452.6 [1.4]	444.9 [1.3]		
$In(OH)_3$	531.2 [1.4]	452.1 [1.2]	444.7 [1.3]		
	532.6 [1.9]	453.3 [1.7]	446.1 [1.2]		
ZnO	529.8 [1.1]			1044 [1.4]	1020.9 [1.4]
	531.3 [1.7]			1045.1 [1.7]	1022.1 [1.7]
IZO	529.5 [1.2]	451.5 [1.2]	443.5 [1.2]		
	530.3 [1.8]	452.5 [1.2]	445 [1.4]		
	531.2 [1.9]				
	532.7 [1.7]				

The atomic concentration at the surface was determined to be 3%, 27% and 70% for zinc, indium and oxygen, respectively. The results show that the O (1s) photoemission line can be fitted with four different components. The component at low binding energy (O_I) is attributed to the fully coordinated In_2O_3 oxygen species of the indium lattice. The adjacent component (O_{II}) is assigned to oxygen near defect sites of at the surface of the metal oxide (i.e., In-O-In), which contribute to the conductivity of the TCO.[4, 6] It is reported that these oxygen species show up at higher binding energies (BE) because they donate a fraction of their electron densities to under-coordinated indium sites.[7] The binding energy of the third component (O_{III}) correlated well with the main component of In(OH) and was assigned to hydroxide surface species.[4, 6, 7] Component O_{IV} was

attributed to adventitious contaminants such as CO and CO_2 on the surface of the metal oxide.[4, 8]

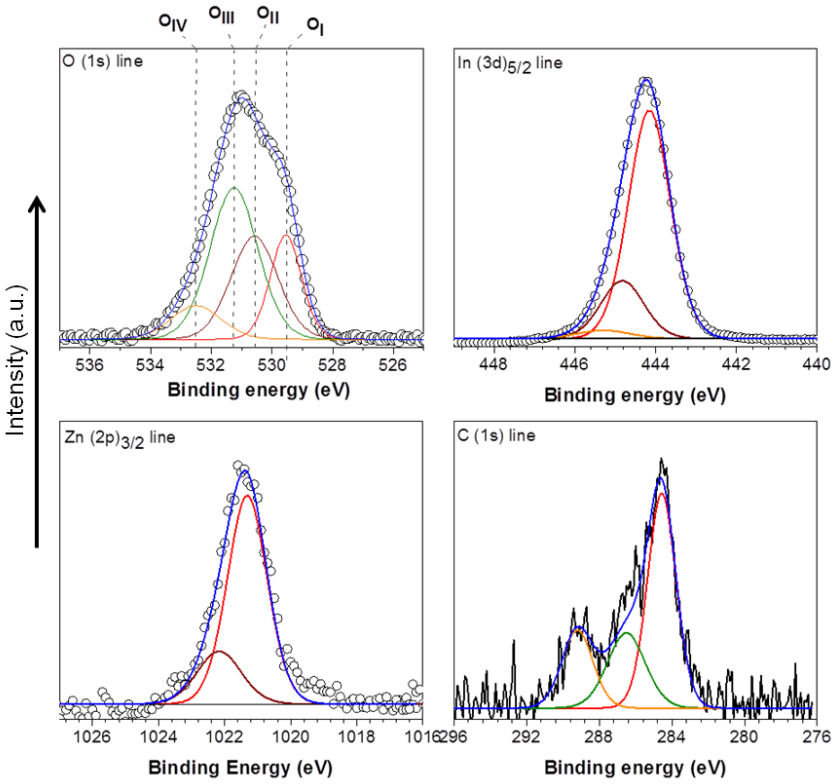

Figure 4.2 High resolution XPS spectra of the O (1s), In (3d), Zn (2p), and C (1s) lines of oxygen plasma treated IZO. Data was collected at an angle of 70°.

The atomic composition of the oxygen species of ITO was determined to be 19.0%, 21.9%, 52.5% and 6.6% in order of increasing binding energy. Both the indium and zinc lines show two main species; that can be assigned to (i) the fully coordinated metal oxide, and (ii) metal hydroxides. A third component is observed in the In (3d) line that is attributed to surface contamination.[4, 6, 7] Further evidence of surface contaminants can be

seen from the C (1s) spectrum, which shows the presences of at least three different carbonaceous species.

4.3 PFBPA modification of IZO: towards optimal coverage

An important part of surface modification is choosing conditions that will afford optimal coverage and high quality monolayers on the surface of the metal oxide. In this study we examine the modification of IZO under three different experimental conditions, namely: (i) room temperature (RT) modification for 24 hours, (ii) room temperature modification for a week (1 wk) and (iii) high temperature deposition for 24 hours. Figure 4.3 shows the evolution of the O (1s) peak as a function of the modification condition.

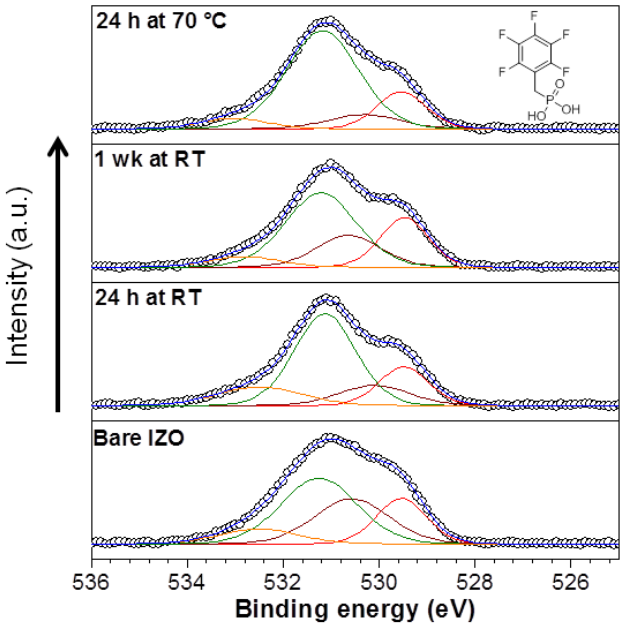

Figure 4.3 O (1s) core level spectra of PFBPA-modified ITO depicting the impact of various modification conditions on the shape and constituent of the spectra. The structure of the molecule used in this experiment is shown in the top panel.

The modification was done in ethanol because this solvent system the highest coverage on IZO. As previously mentioned in chapter 3, the shape and constituent of the O (1s) photoemission line is very sensitive to any chemical changes that take place at the surface of the metal oxide. The results depicted in Figure 4.3, for example, show differences in the profile and composition of the O (1s) line for the various modification conditions. Generally, a relative decrease in the intensity of the components associated with the fully coordinated metal oxides is observed after modification, which is consistent with the formation of a monolayer on the surface that attenuates the photoelectrons from the metal oxide. Concomitantly, the component in the hydroxyl region increases in its relative intensity further substantiating the formation of a monolayer. Figure 4.4 shows a comparison between the P (2p) photoemission line of the PFBPA-modified IZO and the free phosphonic acid. The spectra were calibrated to the C (1s) photoemission line at 284.6 eV. Upon binding to the surface of the metal oxide the P (2p) emission gets shifted to lower binding energy, which is indicative of a greater electron density being placed on the phosphorus atom.

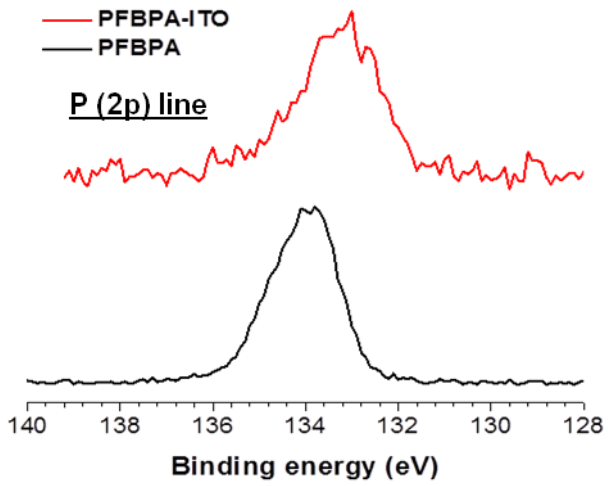

Figure 4.4 High resolution XPS spectra of the p (2p) peaks of free (bottom) and IZO-bound (top) PFBPA. All binding energies were calibrated to the C (1s) peak at 284.6 eV.

Figure 4.5 depicts the F/In and F/C ratios for PFBPA-modified IZO samples prepared using the aforementioned modification conditions. All ratios were determined from the high resolution F (1s), C (1s) and In (3d) spectra (Figure 4.6) after correcting for instrumental and sensitivity factors.

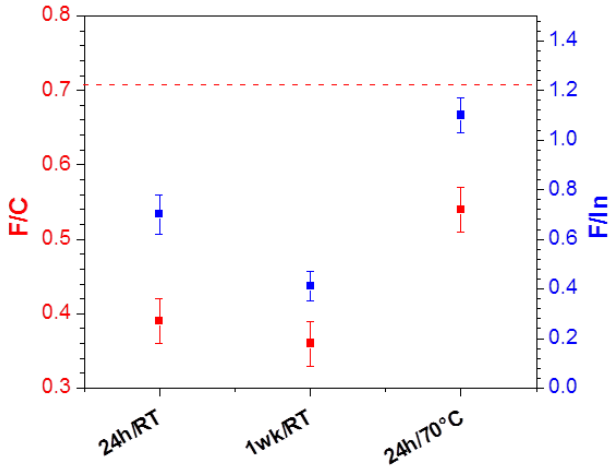

Figure 4.5 XPS-determined F/C and F/In ratios for PFBPA-IZO samples prepared using different modification protocols. Dashed line indicates the theoretical F/C ratio for a pristine monolayer.

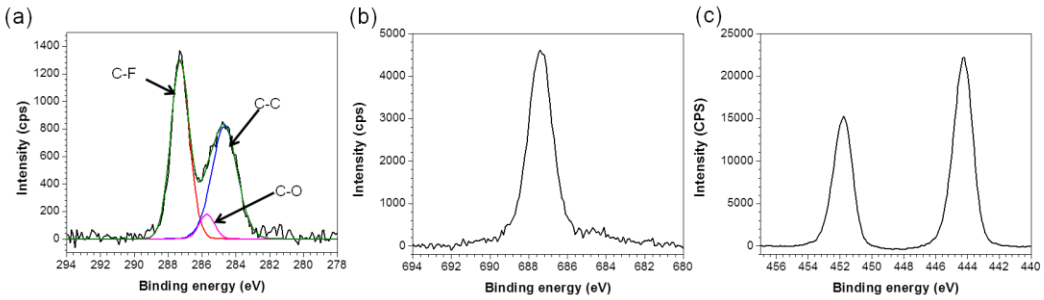

Figure 4.6 High resolution XPS photoemission spectra for a PFBPA-modified IZO substrate showing the (a) C (1s), (b) F (1s) and (c) In (3d) lines. The carbon spectrum shows the fits to the different carbon species.

The F/C ratio can be considered as a measure of the quality of the monolayer on the surface of the metal oxide. Since the only source of carbon and fluorine on the modified IZO should be from the surface modifier, ratios lower than the theoretical value suggest that there are contaminants on the metal oxide surface. Analogously, the F/In provides a means of assessing the relative coverage of the molecules on the surface. The results indicate that high temperature modification of IZO afforded the highest quality and coverage of a monolayer on the surface of IZO. Water contact angle measurements were acquired over four spots on the surface of PFBPA-modified IZO and a value 84° ± 1 was obtained, which is consistent with values reported for perfluroterphenyl thiols on gold.[9] The surface morphology was visualized by AFM and the results are presented in Figure 4.7 below.

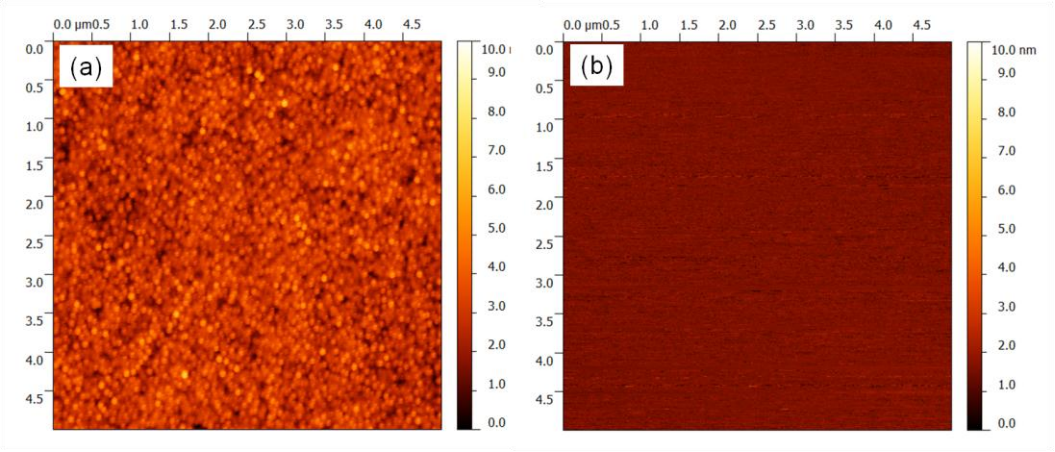

Figure 4.7 Topographical AFM images of bare oxygen plasma treated IZO (a) and PFBPA-modified IZO (b). The rms surface roughness determined over a 5 × 5 µm scan was measured to be 0.73 nm and 0.21 nm for a and b, respectively.

The AFM data shows that the modified surface had a lower surface roughness than the bare substrate, which indicates some degree of planarization of the IZO substrate.

4.3.1 Quantification of surface coverage using XPS

Usually fractional monlayer coverage (f) can be determined from contact angle measurement by employing the Cassie equation shown below

$$\cos\Theta = f\cos\Theta_{ref} + (1 - f)\cos\Theta_{bare} \qquad \text{(Equation 4.1)}$$

where Θ is the contact angle of the modified substrate, Θ_{bare} is the contact angle of the bare substrate and Θ_{ref} is the contact angle of a reference film. The reference film is usually a thiol analog of the molecule of interest that is usually deposited and measured on gold. Unfortunately, no suitable analog could be found for the molecules used in this

study so an alternate XPS-based method developed in the Marder group[10] for calculating coverages on ITO was used. This approach relies on having an accurate model of the structure of the metal oxide. To the best of our knowledge, no models have been developed for polycrystalline IZO so the crystal structure is used ITO is used instead to approximate coverage. The method relies on comparing the F/In ratio from XPS to theoretical values for a close packed monolayer of the acid on the surface of ITO

A model of polycrystalline ITO developed by the Brédas group is shown in Figure 4.8. The unit cell of the metal oxide comprise of 28 In and 4 Sn per layer with each layer being separated by 3.32 Å.

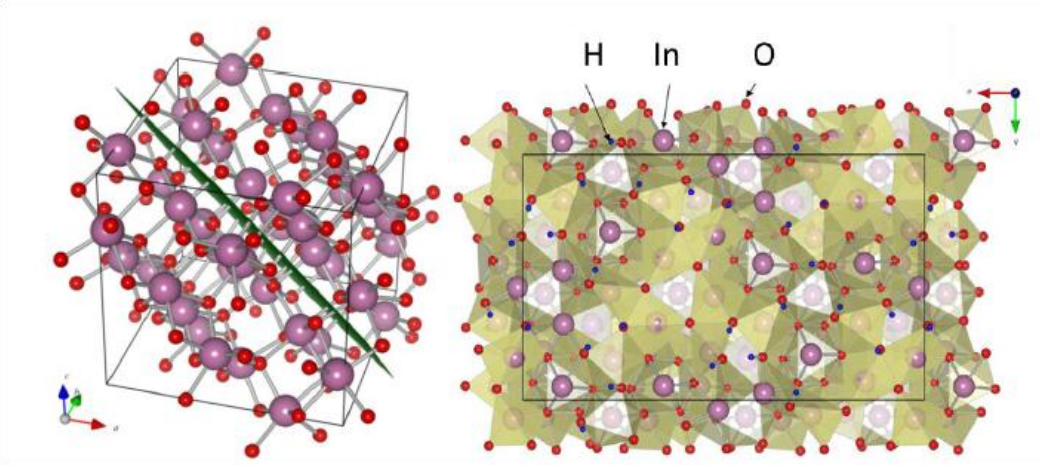

Figure 4.8 Bulk In2O3 unit cell (cubic) with the (222) lattice plane highlighted in green. Right: Top view of a rectangular, OH-terminated ITO (222) surface slab, optimized at the DFT level. The periodic rectangular supercell is indicated. Sn-substitutions are randomly distributed over the cationic positions throughout the slab.Reproduced from Paramonov and company.[6]

The intensity (I) of the XPS signal can be represented mathematically by Equation 4.2

$$I = I_s(-d/\lambda cos\Theta) \qquad \text{(Equation 4.2)}$$

where I_s is the unscattered intensity and Θ is the angle of detection relative to the surface normal and d is the sampling depth (i.e., the distance from which the detected photoelectrons originate) and λ represents the distance that the ejected electrons will travel before the inelatically scatter (i.e., inelastic mean free path). The decay profile for the signal intensity as a function of λ is shown graphically in Figure 4.9.

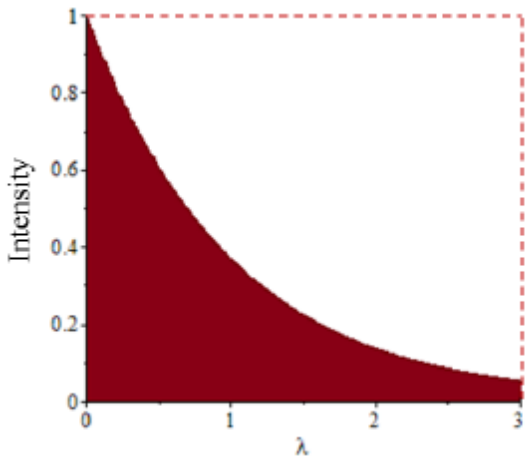

Figure 4.9 Signal intensity as a function of distance from surface in units of λ for normal angle detection.

The total intensity for the electrons detected can be determined from the integration of Equation 4.2 between 0 and 3λ, which is the range over which 95% of the signal originates. Since in the absence of attenuation the signal detected would be equivalent to the complete rectangular area shown in Figure 4.3, then we can correct for the attenuation by dividing the experimental F/In ration by a correction factor of 3λ/0.95λ. The In ($3p_{3/2}$) photoemission line has a 3λ value of 8.2 nm,[11] which based on the model put forward by the Brédas group is equivalent to ~ 25 layers of ITO. This translates into 44 total indium

atoms within 3λ of the surface. Given the footprint of PFBPA (22.62 Å^2),[12] the ITO surface can accommodate 4.4×14 molecules cm^{-2}. This gives a F/In ratio of 0.11, which becomes 0.36 after attenuation is accounted for. Using this approach the approximate coverage of PFBPA on the surface was found to be 72% of a theoretical monolayer (i.e., 3.2×10^{14} molecules cm^{-2}).

4.3.2 Evaluating the interaction between the PFBPA modifier and IZO by XPS analysis

XPS analysis was used to provide insight into the local environment at the interface and the interaction between the surface modifier and IZO. Figure 4.10 shows the O (1s) spectrum of the isolated PFBPA powder and a PFBPA-modified IZO surface. The PFBPA-modified IZO was prepared using the high temperature protocol and both spectra were calibrated to the C (1s) photoemission line at 284.6 eV.

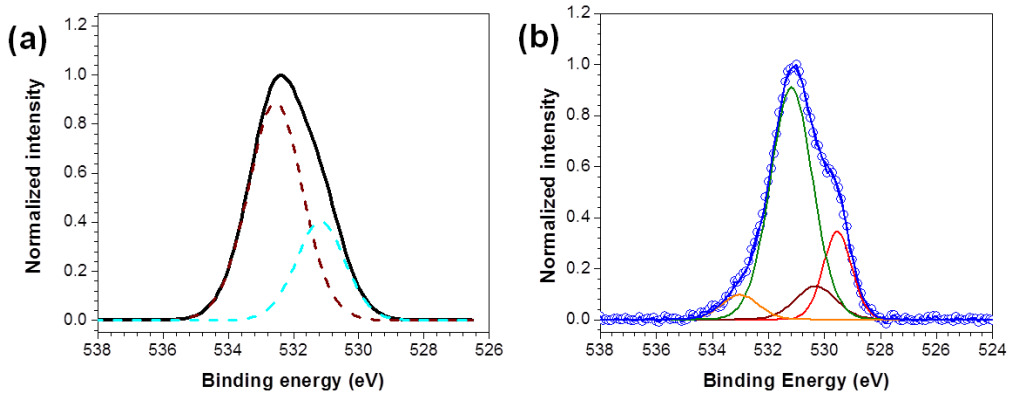

Figure 4.10 High resolution O (1s) XPS spectra for (a) neat PFBPA and (b) PFBPA-modified IZO substrate. The dashed lines represent the components of the powder and the solid lines are indicative of the components of the modified.IZO substrate. The measurements were done at normal angle and 70° for the powder and modified IZO, respectively.

As expected, the photoemission line of the powder shows the presence of two different oxygen environment, which can be assigned to the phosphoryl oxygen at 532.1 eV and the oxygen atoms in the P-OH groups at 532.5 eV. The ratio of the area of the peak was 2:1 (P-OH : P=O), which is consistent with the structure of the molecule. The O (1s) spectrum for the modified surface is shifted negatively relative to the neat powder; this is consistent with what was observed before for the P (2p) peak (Figure 4.4). The spectrum of the modified IZO shows four components at similar binding energies to those reported for bare oxygen plasma etched IZO. In order to deduce the nature of the local interface environment an overlay of both spectra is presented in Figure 4.11.

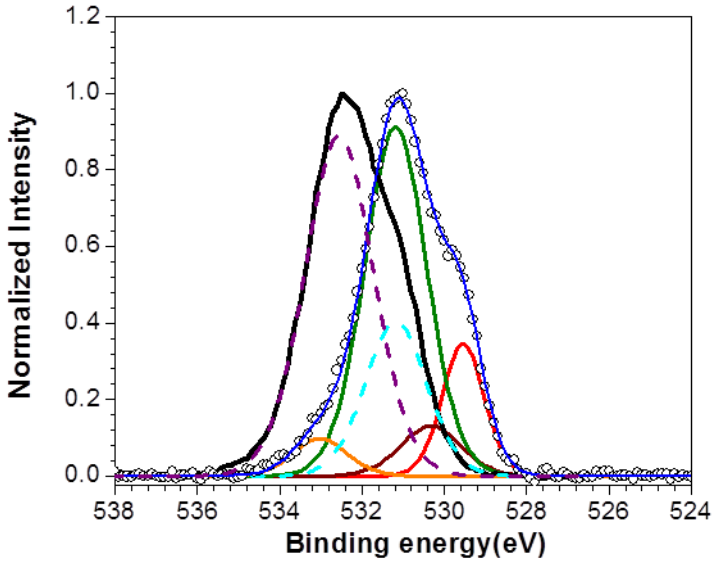

Figure 4.11 Overlay of the high resolution O (1s) spectra of neat PFBPA powder and PFBPA-modified IZO

The overlay of the powder and the modified substrate show complete overlap between the phosphoryl group in the neat powder and the hydroxyl region of the substrate. In

addition, there is also significant overlap between a fraction of the hydroxyl groups in the powder and the OH region associated with surface hydroxyls. Similar observations were made by Paramonov and company[6] who used a combination of density functional theory (DFT) calculations and experimental data to deduce the binding mode of phosphonic acids on indium tin oxide. In their calculations they examined the three different binding modes that were most common upon structural optimization for phosphonic acids adsorption on the surface of ITO. The modes include:

(i) Bidentate binding to two In sites with a free phosphoryl group. Here, the oxygens participating in the bonding are expected to have a binding energy of approximately 530.3 eV.

(ii) A bidentate mode that involve the formation of a bond between the phosphoryl group and In with additional hydrogen bonding interactions (P-O⋯H). The relative binding energies of the oxygen species were predicted to be approximately 530.7 eV.

(iii) Tridendate binding with an approximate binding energy of 530.6 eV.

Based on these theoretical predictions and our experimental data it is clear that the region assigned to the surface hydroxyls for the bare substrate gets increasingly complex upon modification with the phosphonic acid owing to the large extent of component overlap. As such, it is difficult to deduce the mode of binding from the overlay of the XPS data.

4.3.3 Evaluating the interaction between the PFBPA modifier and IZO by vibrational spectroscopy

Infrared reflection absorption spectroscopy (IRRAS) is a very useful tool for the determination of molecular structural information on thin films.[13, 14] In this technique, an IR beam reflected off a reflective surface at a grazing angle of incidence and the vibrational modes of the molecules on the surface examined. As such, the vibrational spectroscopy technique was utilized in this study to deduce the binding mode of PHBPA on the surface of IZO. The studies were conducted using samples that had saturated coverage of the acid on the surface. In order to facilitate accurate peak assignment the monobasic and dibasic potassium salts of the acid were prepared by titrating PFBPA with potassium hydroxide (see experimental) and their Fourier transform infrared radiation (FT-IR) spectra acquired. An example of a titration curve for PFBPA is shown in Figure 4.12.

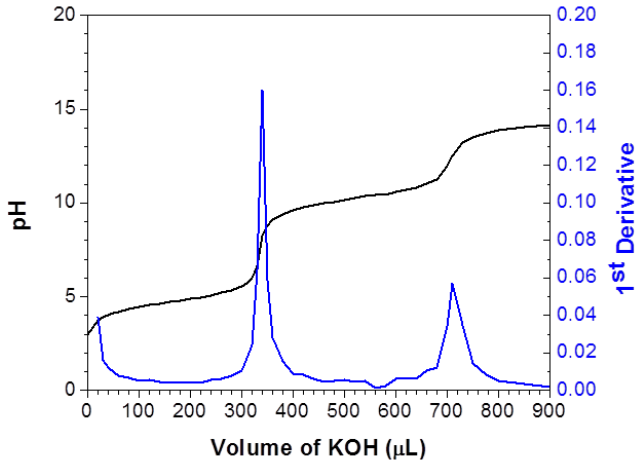

Figure 4.12 Titration and first derivative curves for PFBPA Courtesy of Zachary Lachance (Pemberton Group, Univ. of Arizona).

In addition, the FT-IR spectra of benzyl phoshonic acid (BPA) was also obtained as control. The results of the study are shown in Figure 4.13.

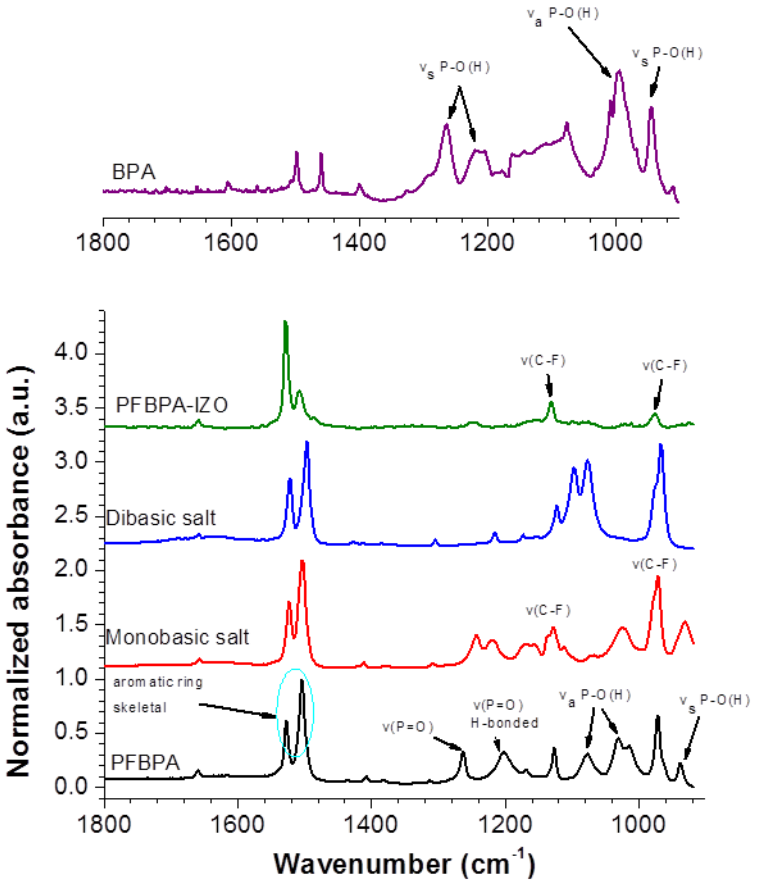

Figure 4.13 FT-IR vibrational spectroscopy data of isolated PFBPA (black) and its corresponding monobasic (red) and dibasic (blue) salts. The FT-IR spectra of the un-fluorinated BPA is also shown (purple). The IRRAS of PFBPA-modified IZO is presented in green. The main vibrational modes used in the analysis are labeled. With Zachary Lachance (Pemberton Group, Univ. of Arizona)

The use of the salts helps us to predict the kinds of changes that are expected in the vibrational spectrum of the pristine acid once it is tethered to the TCO; this will help to

identify the mode of binding. The inclusion of BPA as a control experiment helps in the identification of the C-F stretch. The figure shows that the C-F stretching modes are preserved after modification and are observed at 975cm^{-1} and 1131cm^{-1}.[12, 15] The symmetric P-O(H) stretch (937 cm^{-1})[12, 15-17] is not observed in the IRRAS spectrum thereby indicating that both P-O(H) are tethered to the surface of the IZO. The phosphoryl stretch at approximately 1260cm^{-1} is visible in the IRRAS spectrum, which suggest that there is still some free phosphoryl groups on the surface of IZO.[12, 16] Taken together, these results suggest that PFBPA binds to the surface of IZO in a predominantly bidentate manner.

4.4 PFBCA modification of IZO: towards optimal coverage

As was the case with the phosphonic acid, the conditions required for optimal deposition of PFBCA were explored. Figure 4.11 presents the F/In and F/C ratios for PFBCA-modified IZO samples prepared as a function of the different modification conditions. Similarly to the PFBPA, the surface modification was done in ethanol.

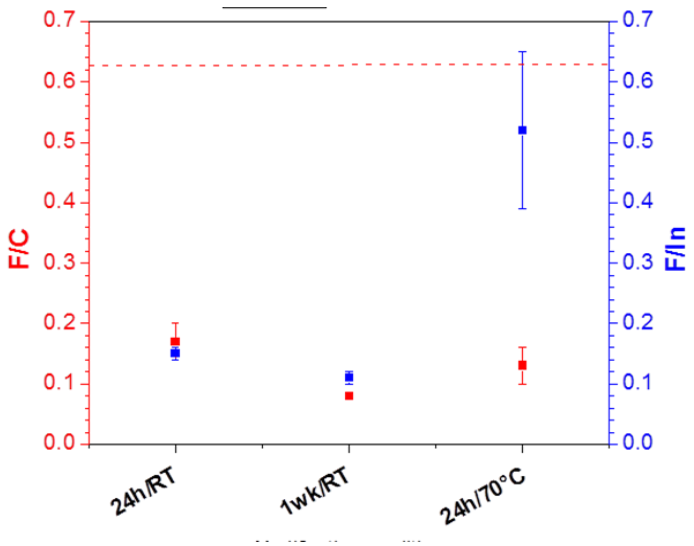

Figure 4.14 XPS-determined F/C and F/In ratios for PFBCA-IZO samples prepared using different modification protocols. Dashed line indicates the theoretical F/C ratio for a pristine monolayer.

As done previously, the ratios were determined from the high resolution F (1s), C (1s) and In (3d) spectra after correcting for instrumental and sensitivity factors. The results depicted in Figure 4.11 shows that highest coverage was obtained with high temperature deposition; however, the uncertainty in coverage was much greater at these elevated temperatures. Interestingly, the quality of the monolayer formed, as depicted by the F/C ratio, seems to be independent of the modification protocol used. The evolution of the shape and constituents of the O (1s) photoemission (Figure 4.15) is similar to that observed with FCPA-modified IZO. Here too, a significant increase is observed in the hydroxyl component at high temperatures, which is paralleled with a reduction in the IZO bulk oxygen species, which is consistent with the deposition of an overlayer on the surface of IZO.

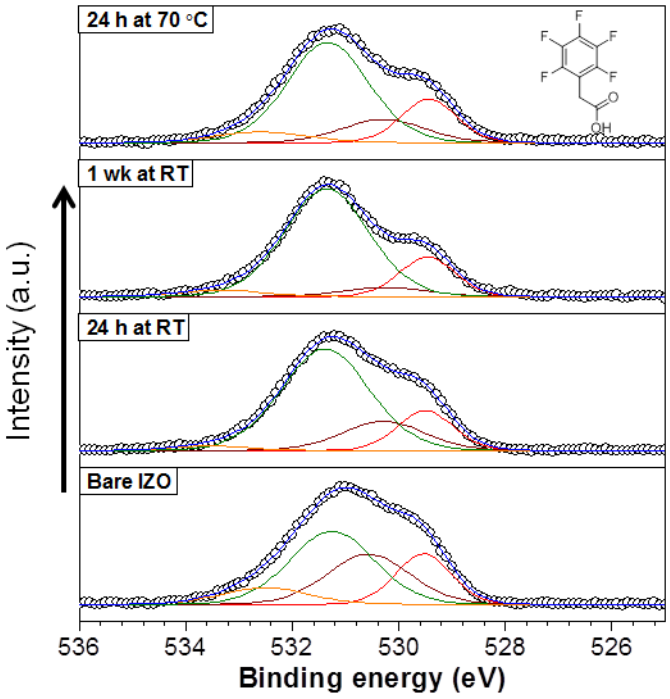

Figure 4.15 O (1s) core level spectra of PFBCA-modified ITO depicting the impact of various modification conditions on the shape and constituent of the spectra. The structure of the molecule used in this experiment is shown in the top panel.

Contact angle measurements on the PFBCA-substrate provided an angle of 59 ± 5, which suggest that the monolayer was not as densely packed on the surface as the phosphonic acid. AFM was used to examine the morphology of the PFBCA-modified substrate and the results are presented in Figure 4.16.

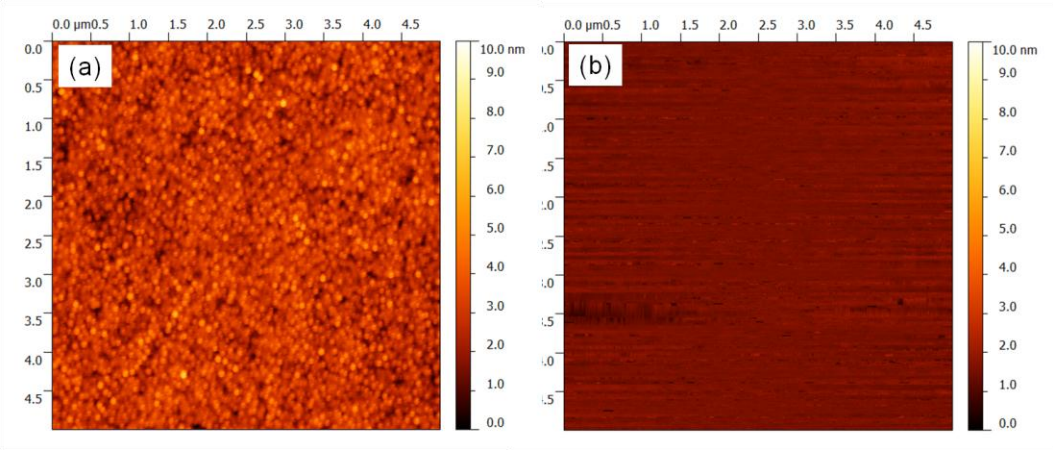

Figure 4.16 Topographical AFM images of bare oxygen plasma treated IZO (a) and PFBCA-modified IZO (b). The rms surface roughness determined over a 5 × 5 µm scan was measured to be 0.73 nm and 0.16 nm for a and b, respectively.

The surface roughness of the modified substrate was reduced relative the unmodified IZO surface. Using the XPS method previously discussed and a molecular footprint for carboxylic acids (21Å^2) the coverage was determined to be 42% of a monolayer. This is consistent with having a less densely packed layer compared to PFBPA as was indicated by the results of the contact angle.

4.4.1 Evaluating the interaction between the PFBCA modifier and IZO by XPS analysis

The O (1s) spectrum of the isolated PFBCA powder and a PFBCA-modified IZO surface is shown in Figure 4.17. As was the case with the PFBPA, the PFBCA-modified

IZO sample was prepared using the high temperature protocol and both spectra were calibrated to the C (1s) photoemission line at 284.6 eV.

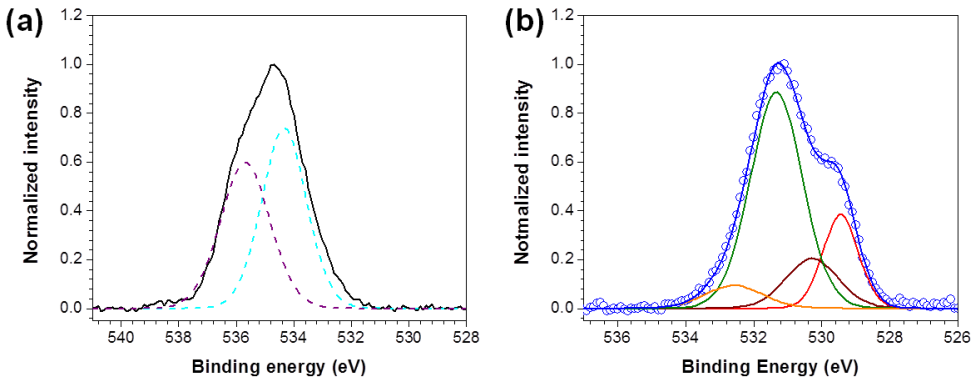

Figure 4.17 High resolution O (1s) XPS spectra for (a) neat PFBCA and (b) PFBCA-modified IZO substrate. The dashed lines represent the components of the powder and the solid lines are indicative of the components of the modified.IZO substrate. The measurements were done at normal angle and 70° for the powder and modified IZO, respectively.

The photoemission spectra of the powder shows two distinct oxygen environment, which we attribute to the carbonyl and the oxygen in the C-OH functional group at 534.3 and 537.5 eV, respectively. The ratio of the area of the oxygen components was 1:1, which is in agreement with the structure of the molecule. Similarly to the phosphonic acid, the O (1s) spectrum for the modified surface is shifted negatively relative to the neat powder. In addition, the spectrum of the PFBCA-modified IZO shows four components at similar binding energies to those reported for bare oxygen plasma etched IZO. An overlay of the spectra of the powder and the bare IZO is presented in Figure 4.18.

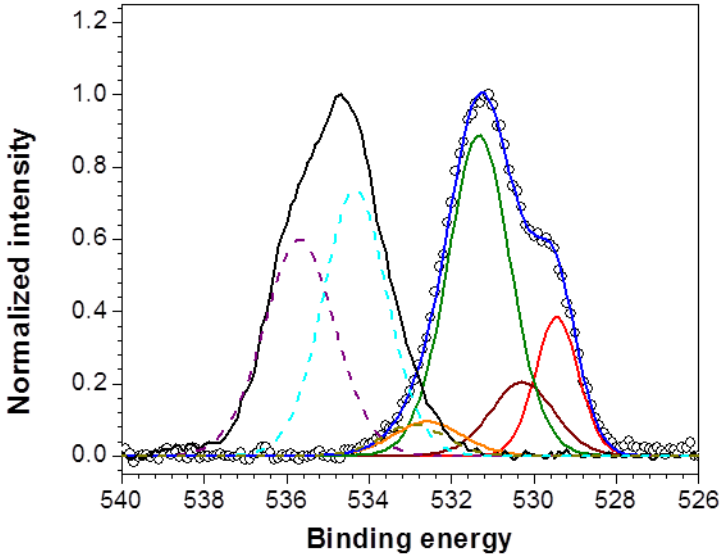

Figure 4.18 Overlay of the high resolution O (1s) spectra of neat PFBCA powder and PFBCA-modified IZO

Greater separation is observed between the isolated powder and the modified IZO O (1s) spectra. There is almost no overlap between the C-O(H) oxygen component and the O 1(s) line of the IZO. This suggests that all the hydroxyl group from PFBCA is tethered to the surface. A more significant overlap occurs between the carbonyl group of the acid and the oxygen line of the substrate is observed. Based on this result, it is likely that there are still unbounded carbonyl groups on the surface of the IZO.

4.4.2 Evaluating the interaction between the PFBCA modifier and IZO by vibrational spectroscopy

In order more definitively determine the mode of binding of the carboxylic acid on surface of IZO, vibrational spectroscopy measurements were performed and the results are presented in Figure 4.19. The spectra of benzyl carboxylic acid (BPA) and the monobasic salt are included for comparison. The salt was prepared by titrating with KOH; the titration curve is shown in Figure 4.20.

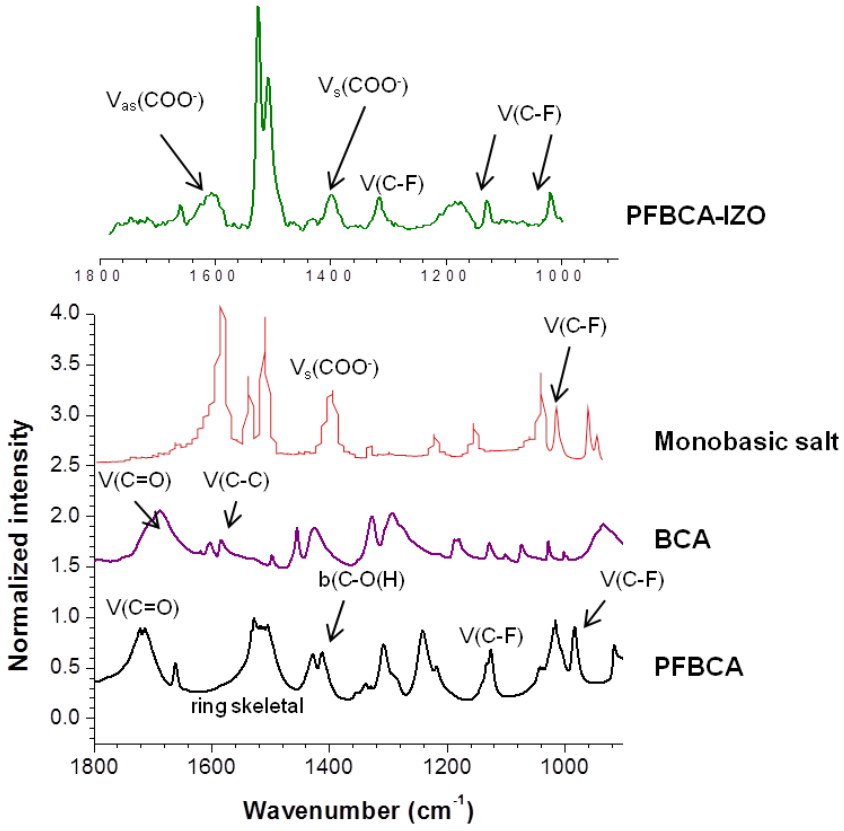

Figure 4.19 FT-IR vibrational spectroscopy data of isolated PFBCA (black) and its corresponding monobasic (red) salt. The FT-IR spectra of the un-fluorinated BCA is also sown (purple). The IRRAS of PFBCA-modified IZO is presented in green. The main vibrational modes used in the analysis are labeled. With Zachary Lachance (Pemberton Group, Univ. of Arizona)

It can be seen from the spectrum of the PFBCA-modified IZO that the C-F vibrational modes of the isolated salts are preserved and appear at approximately 1018, 1127 and 1312 cm^{-1}.[16, 18] The symmetric and asymmetric stretch of the caboxylate anion is seen in both the monodentate salt and the modified IZO at 1397 cm^{-1} and 1605 cm^{-1}, respectively. This is coupled with the disappearance of the carbonyl vibrational mode at approximately 1383 cm^{-1}. Qu *et al*. Generally, the mode of binding can be determined from the separation between the two carboxylate vibrations.[19] A separation of greater than 300 cm^{-1} suggest monodentate binding, 150-180 cm^{-1} indicates a bidentate bridging mode and 60-100 cm^{-1} indicates a bidentate chelating mode. Using similar analysis our separation value of 209 cm^{-1} suggests a monodentate binding.

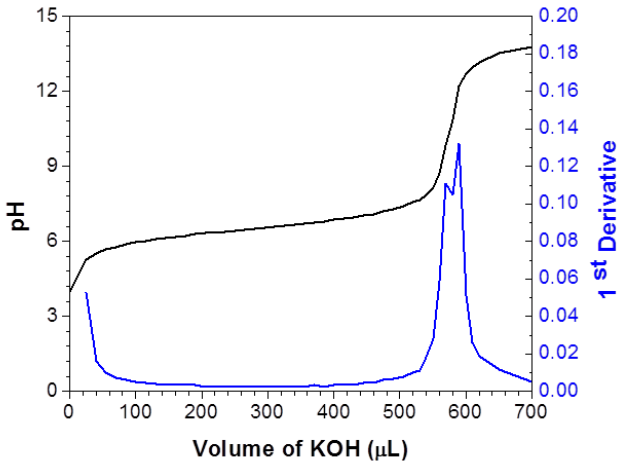

Figure 4.20 Titration and first derivative curves for PFBCA. Courtesy of Zachary Lachance (Pemberton Group, Univ. of Arizona).

4.4.3 UPS derived energy level diagrams for PFBPA-IZO and PFBCA-IZO substrates

Figure 4.21 shows the UPS-derived band diagram for oxygen plasma treated IZO, PFBPA-IZO and PFBCA-IZO samples.

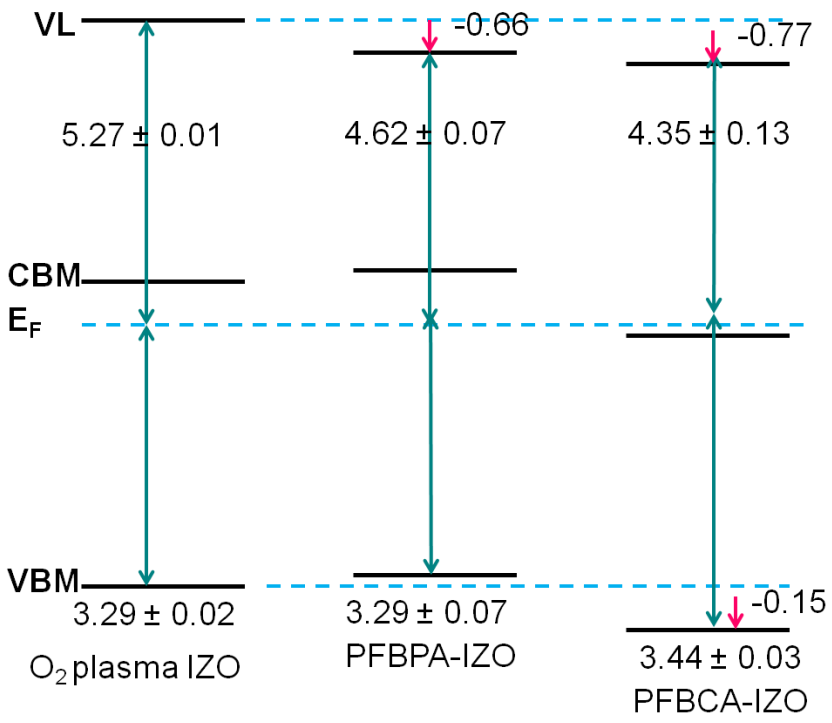

Figure 4.21 Energy level diagrams constructed from UPS for bare OP (far left) and ferrocene-modified oxygen plasma treated ITO. Significant changes in the valence band maximum and surface dipole are shown in red. A band gap of 3.6 eV was assumed and maintained throughout.

The figure shows that the work function in both the modified sample is reduced relative oxygen plasma treated substrate. Interestingly, the valence band maximum of the

PFBCA-modified sample shows a significant increase, which indicates that there is an increase in the density of electrons at the surface.

4.5 Experimental section

The IZO films (5-10 nm thick) were prepared by sputtering onto gold coated glass from a 70:30 (wt%) In2O3:ZnO target in a chamber with base pressure of 4.5 mTorr. PFBPA was synthesized according to a previously reported protocol[20] and PFBCA was obtained commercially (Alfa Aesar). Prior to modification the IZO was prepared by using a modified DSC protocol. Briefly, the IZO substrates were cut into 1″ × 1″ pieces and then subject to several cleaning steps: (1) scrubbing the substrates with dilute Triton X-100 solution with the aid of a lint-free cloth, (2) sonicating in Triton X-100 solution for 5 min then rinsing with distilled water, (3) sonicating in distilled water for 5 min, (4) sonicating in acetone for 5 min, (5) sonicating in ethanol for 5 min and (6) drying under nitrogen. The detergent solvent cleaned substrates were then Oxygen plasma treated (Plasma Etch, PE50) for 10 minutes after which they are immediately modified with the acids. The phosphonic and carboxylic acids surface modification were done in ethanol in 10 mM ethanol solutions. After modification, the samples are sonicated in ethanol for 5 min to remove any physisorbed layers before measurements were performed.

Titrations were done using 10 mM solutions of the modifier in ethanol (5 mL) and a 0.17 M aqueous solution of KOH as the titrant. The titrant was added in aliqupts of approximately 50 µL and the mixture stirred and allowed to equilibrate for 30 seconds after each addition. The titration was monitored potentiometrically. Monobasic and dibasic salts were generate as appropriate for the acid based on the previously obtained

titration curve by adjusting the pH of the acid solution. Upon achieving the desired pH the solvent was removed and the salt dried under vacuum and heating. FT-IT analysis is then performed on the salts in KBr pellets. The FT-IR spectra for the isolated acids were also done in KBr.

AFM was performed on the samples using an agilent N9524B microscope and PM-IRRAS measurements were conducted using a Nicolet Nexus 670 FT-IR spectrophotometer with a HINDS PEM-90 photoelastic Modulator at the University of Arizona by Zachary Lachance.

4.6 Conclusion:

In this chapter we set out to determine the binding mode of PFBPA and PFBCA to the surface of IZO. We were able to develop a model that chemically describes the surface of IZO. Based on a combination of IRRAS and XPS measurements we were able to predict that the phosphonic acid binds to the surface in a bidentate manner while the carboxylic acid is bound in a monodentate configuration.

4.7 Literature cited

[1] C. G. Granqvist, *Sol. Energy Mater. Sol. Cells* **2007**, *91*, 1529.

[2] D. S. Liu, C. S. Sheu, C. T. Lee, C. H. Lin, *Thin Solid Films* **2008**, *516*, 3196.

[3] C. Besleaga, L. Ion, V. Ghenescu, G. Socol, A. Radu, I. Arghir, C. Florica, S. Antohe, *Thin Solid Films* **2012**, *520*, 6803.

[4] C. Donley, D. Dunphy, D. Paine, C. Carter, K. Nebesny, P. Lee, D. Alloway, N. R. Armstrong, *Langmuir* **2002**, *18*, 450.

[5] C. Carter, M. Brumbach, C. Donley, R. D. Hreha, S. R. Marder, B. Domercq, S. Yoo, B. Kippelen, N. R. Armstrong, *J. Phys. Chem. B* **2006**, *110*, 25191.

[6] P. B. Paramonov, S. A. Paniagua, P. J. Hotchkiss, S. C. Jones, N. R. Armstrong, S. R. Marder, J. L. Bredas, *Chem. Mater.* **2008**, *20*, 5131.

[7] J. C. C. Fan, J. B. Goodenough, *J. Appl. Phys.* **1977**, *48*, 3524.

[8] E. L. Ratcliff, A. K. Sigdel, M. R. Macech, K. Nebesny, P. A. Lee, D. S. Ginley, N. R. Armstrong, J. J. Berry, *Thin Solid Films* **2012**, *520*, 5652.

[9] F. Chesneau, H. Hamoudi, B. Schuepbach, A. Terfort, M. Zharnikov, *J. Phys. Chem. C* **2011**, *115*, 4773.

[10] S. A. Paniagua, *Interfacial Engineering of Transparent Conductive Electrodes and Nanoparticles with Phosphonic Acids and Metal-Organic Dopants for Organic Electronic Applications*, Georgia Institute of Technology **2013**.

[11] D. P. Woodruff, T. A. Delchar, *Modern Techniques of Surface Science*, Second ed., Cambridge University Press, **1994**.

[12] M. Gliboff, L. Z. Sang, K. M. Knesting, M. C. Schalnat, A. Mudalige, E. L. Ratcliff, H. Li, A. K. Sigdel, A. J. Giordano, J. J. Berry, D. Nordlund, G. T.

Seidler, J. L. Bredas, S. R. Marder, J. E. Pemberton, D. S. Ginger, *Langmuir* **2013**, *29*, 2166.

[13] P. J. Hotchkiss, M. Malicki, A. J. Giordano, N. R. Armstrong, S. R. Marder, *J. Mater. Chem.* **2011**, *21*, 3107.

[14] P. J. Hotchkiss, S. C. Jones, S. A. Paniagua, A. Sharma, B. Kippelen, N. R. Armstrong, S. R. Marder, *Acc. Chem. Res.* **2012**, *45*, 337.

[15] S. A. Paniagua, P. J. Hotchkiss, S. C. Jones, S. R. Marder, A. Mudalige, F. S. Marrikar, J. E. Pemberton, N. R. Armstrong, *J. Phys. Chem. C.* **2008**, *112*, 7809.

[16] S. Yagyu, M. Yoshitake, N. Tsud, T. Chikyow, *Appl. Surf. Sci.* **2009**, *256*, 1140.

[17] K. Ohno, Y. Mandai, H. Matsuura, *J. Mol. Struct.* **1993**, *298*, 1.

[18] M. Boczar, K. Szczeponek, M. J. Wojcik, C. Paluszkiewicz, *J. Mol. Struct.* **2004**, *700*, 39.

[19] Q. Qu, H. Geng, R. Peng, Q. Cui, X. Gu, F. Li, M. Wang, *Langmuir* **2010**, *26*, 9539.

[20] P. J. Hotchkiss, H. Li, P. B. Paramonov, S. A. Paniagua, S. C. Jones, N. R. Armstrong, J.-L. Bredas, S. R. Marder, *Adv. Mater.* **2009**, *21*, 4496.

CHAPTER 5 DIELECTRIC NANOCOMPOSITES FOR ENERGY STORAGE APPLICATIONS

5.1 Dielectric polymer host materials for high energy density applications

The development of efficient, high-energy density dielectric materials for electrical energy storage is an enabling technology for the advancement of contemporary electronic devices such as integrated circuits, field effect transistors, mobile devices and hybrid electric vehicles.[1-4] Among this class of materials are polymeric systems which are well recognized for their high breakdown strength (> 300 V/μm), low dielectric loss (< 2%) and relatively fast discharge speed.[5-8] Recall from chapter 1 that the stored energy density (U) in dielectric films is generally expressed as shown in Equation 5.1:

$$U = \int E \, dD \qquad \text{(Equation 5.1)}$$

where *E* is the applied electric field and *D* is the electric displacement. Therefore, in addition to having a high breakdown strength, a large electric displacement– which is obtained through high permittivity– is also desirable in order to maximize the storage capacity of dielectric materials.[9] Unfortunately, most polymeric systems that are utilized in capacitor applications generally suffer from low dielectric constant (< 15) which, in turn, limits their achievable energy density. Biaxially oriented polypropylene (BOPP), for

example, has remained the commercial state-of-the-art for numerous years because of its high breakdown strength (~730 V/μm); however, its low permittivity (~2.2 at 1 kHz) limits the energy density to about 1.2 J/cm^3.[10, 11] The dielectric properties of some of the commonly used polymers are summarized in Table 5.1.

Table 5.1 Summary of the characteristics of commonly used dielectric polymers. Reproduced from Rabuffi[11]

Polymer film	Permittivity	Dielectric strength (V/μm)	Loss factor (% at 1 kHz)	Energy density (J/cc)
Polypropylene	2.2	640	< 0.02	1 - 1.2
Polyester	3.3	570	< 0.5	1 - 1.5
Polycarbonate	2.8	528	< 0.15	0.5 - 1
Polyethylene naphlate	3.2	550	< 0.15	1 - 1.5
Polyphenylene sulfide	3.0	200	< 0.03	1 - 1.5

Poly(vinylidene fluoride) (P(VDF)) and its derivatives offer a potential alternative for achieving high energy density dielectric films owing to both their high permittivity (> 12) and dielectric strength (> 300 V/μm).[11, 12] The large permittivity originates from the polar C-F bonds (~ 2.1 Debye) that are found along the polymer backbone, which facilitate the packing of the polymer chains into macroscopic semicrystalline domains.[13] P(VDF)-based polymers have several polymorphs, four of which are depicted in Figure 5.1. The chains in the alpha (α) and delta (δ) polymorphs are arranged in a trans-gauche-trans-gauche ($TGTG^-$) conformation and their crystalline domains occupy similar size unit cell. However, the dipole moments in the α-phase are oriented such that they cancel each other rendering the polymorph non-polar. In contrast, the dipole moments in the δ-

phase point in the same direction rendering the polymorph polar. The gamma (γ) polymorph has a trans-trans-trans-gauche (TTTGTTTG) arrangement with the C-F dipoles oriented at an angle; thereby making the phase polar. The β-phase has an all-trans ($T_{m>4}$) conformation with the dipoles arranged perpendicular to the chain axis, rendering the phase highly polar.

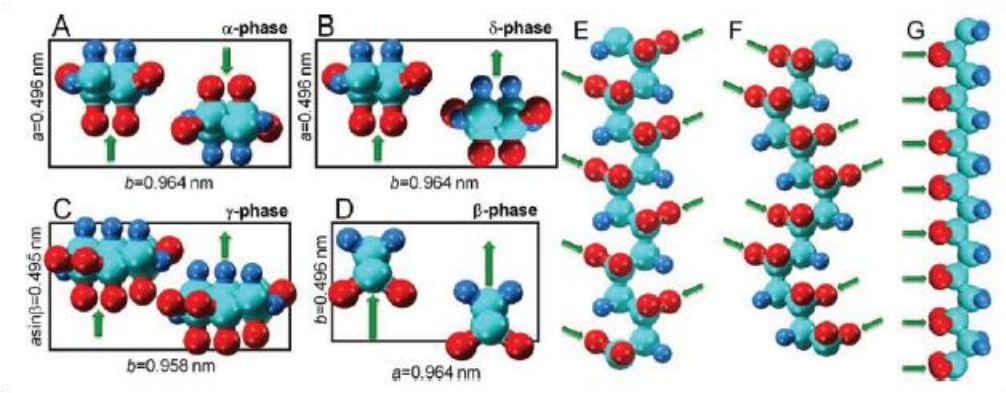

Figure 5.1 Unit cells of (A) α, (B) δ, (C) γ, and (D) β forms of PVDF crystals viewend along the c-axes and schematic chain conformation for (E) TGTG' (α/δ), (F) TTTGTTTG' (γ), and (G) $T_{m>4}$ (β) phases. Red, cyan and blue spheres represent F, C, and H atoms, respectively. The projections of the dipole moment are indicated by green arrows. Reproduced from Zhu and Wang.[12]

While these systems have substantial storage capacity, the P(VDF) homopolymer and various P(VDF) copolymers suffer from large polarization hysteresis which precludes efficient extraction (i.e. the total amount of charge) of the stored energy.[9]

One method of mitigating the large hysteresis is to prepare terpolymers that incorporate bulky monomeric groups into the main chain of P(VDF)-based polymers, which serve as molecular defect sites that promote a reduction in the Curie transition

temperature thereby facilitating the ferroelectric-paraelectric transition. [14] This makes it easier to achieve high dielectric constants under ambient conditions. Similar results have been obtained for terpolymers prepared by the incorporation of chlorotrifluoroethylene (CTFE) monomer units into the copolymer poly(vinylidene fluoride-trifluoroethylene) [P(VDF-TrFE) thereby converting a ferroelectric system into one that is a relaxor ferroelectric.[15-18] and consequently increasing their capacity to store energy (*vide infra*). Therefore, in addition to the high breakdown strength and large dielectric constant of P(VDF)-based terpolymers, their ferroelectric relaxor behavior makes them promising candidates for high-energy density capacitors.

5.2 Enhanced permittivity and energy density in neat P(VDF-TrFE-CTFE) terpolymer through control of morphology.

In addition to the chemical composition of the polymeric backbone, the dielectric properties of P(VDF)-based polymers can be significantly influenced by their crystalline structure and morphology.[19] These properties, in turn, are highly dependent on the processing conditions used to prepare the films. Several processing methods have been developed that allow for the controlled formation of various crystalline polymorphs, and consequently, the ability to tailor the microstructure of the polymers for various electroactive applications.[20-23] Although a fair amount of work has been done to examine the impact of the chemical composition of P(VDF)-based terpolymers on their crystalline phases and dielectric performance,[12, 15-18] much less attention has been given to their processing, albeit an integral component for optimization of these systems.

In this study, we report on the dielectric properties of a terpolymer thin film, poly(vinylidene fluoride-trifluoroethylene-chlorotrifluoroethylene) [P(VDF-TrFE-CTFE)], with a highly crystalline fibrillar morphology as obtained through a simple spin coating and thermal treatment process. The terpolymer investigated herein has an optimal composition of 78.8 mol % VDF, 7.2 mol % TrFE and 14 mol % CTFE, which yields a permittivity of ~50 at 1 kHz.[17, 24] The structure of the polymer is shown below.

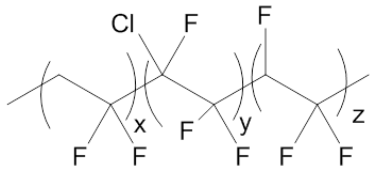

poly(vinylidene fluoride-trifluoroethylene-chlorotrifluoroethylene) [P(VDF-TrFE-CTFE)]

While this terpolymer system has typically been processed by drop casting, we show that the use of spin coating films followed by thermal treatment and then quenching from the melt allows for a marked enhancement in dielectric constant, as well as high energy density. Furthermore, we present a detailed study of the morphology and its impact on the dielectric properties that are relevant for capacitor applications. A thorough investigation of the energy storage capacity via polarization-electric field (P-E) and charge-discharge (C-D) measurement on the films is also presented.

The P(VDF-TrFE-CTFE) terpolymer films were prepared using two different processing methods (see *Experimental section*). The first method (**M1**), involved casting of the terpolymer film, drying at elevated temperature (50 ^{o}C), cooling to room

temperature, “lift-off” with distilled water and a final annealing cycle, prior to application of the top electrodes.[17] In the second method (**M2**), the terpolymer was dissolved in dry N,N-dimethylformamide (DMF) and then thin films were prepared by spin-coating followed by a soft bake, drying overnight at 120 °C (above the melting temperature), and finally thermal quenching.

5.2.1 Characterization of the morphology and phase composition of the terpolymer

The morphology of the as prepared films was evaluated using scanning electron microscopy (SEM). Figure 5.2 presents the SEM top surface image of the films **A** and **B** that were prepared from the as synthesized terpolymer using **M1** and **M2**, respectively.

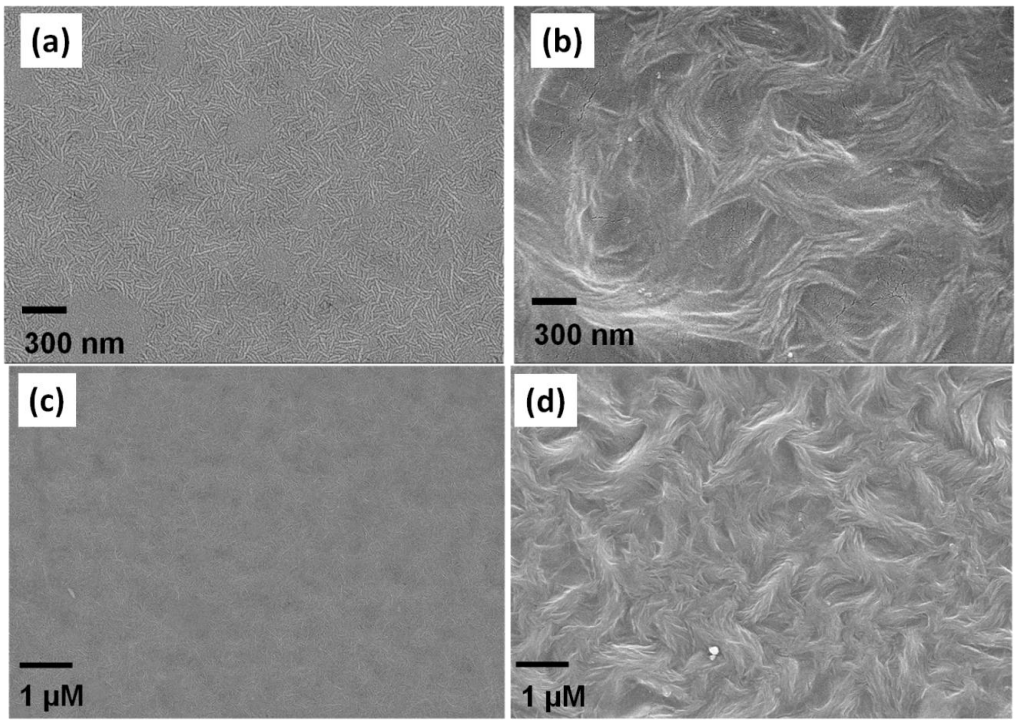

Figure 5.2 Top surface SEM image of neat P(VDF-TrFE-CTFE) films: (a and c) film A, and (b and d) film B high and low resolution, respectively. Images acquired by Yunsang Kim (Perry Group).

The SEM images reveal a qualitative difference in the morphology of the two terpolymer films. The images show distinct crystalline and amorphous phases in both films but the density and apparent size of crystalline domains observed in film **B** are much more pronounced. This suggests that thermal treatment of the terpolymer well above its melting point (~ 79 °C)[17] and subsequent nucleation and crystallization is important for the formation of the dense, fibrillar morphology observed in film **B**. This difference in morphology can have significant effects on the dielectric properties of the films as the character of the crystalline domains are known to be responsible for the high permittivity in P(VDF) based polymers.[13] AFM analysis of the films provided the RMS surface roughness values of 1.5 and 3.6 nm for films **A** and **B**, respectively (Figure 5.3).

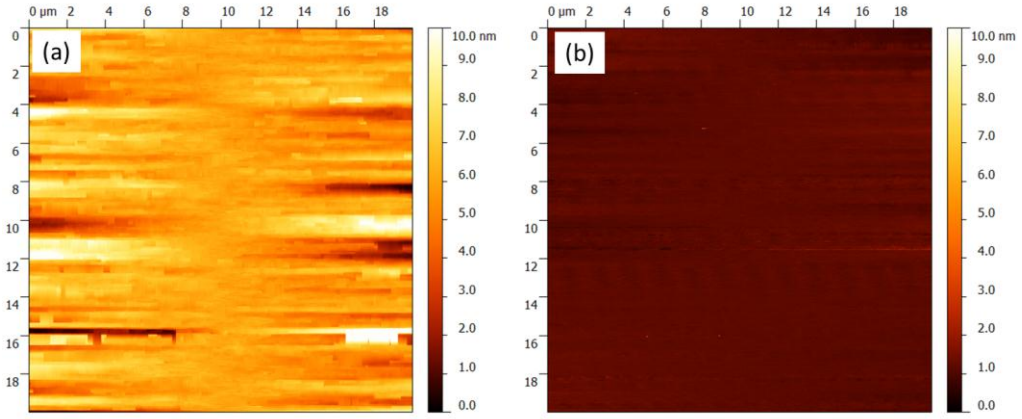

Figure 5.3 AFM images of neat terpolymer films prepared by the two different methods. Both films were prepared from the as synthesized terpolymer using M1 (left) and M2 (right).

Figure 5.4 shows the room temperature X-ray diffraction (XRD) patterns of films **A** and **B**. A thorough evaluation of each sample was done using a Gaussian peak fitting analysis and the results are presented in Table 5.2.

Table 5.2 Lattice constant and coherence length for the terpolymer prepared using different conditions

	Inter-chain spacing (Å)/[phase]	**Coherence length (nm)**
Film A	4.73/[non-polar]	20.27
	4.58/[polar]	4.05
Film B	4.78/[non-polar]	30.20
80 °C annealing	4.75/[non-polar]	26.45
	4.68/[polar]	4.23
No annealing	4.69/[polar]	2.15
P(VDF-TrFE) 70:30 mol%	4.45/[polar]	8.83

Film **B** showed a single α-phase (020) diffraction peak at approximately 18.54° (equivalent to an interchain crystal spacing of 4.75 Å), which is consistent with the angle of the reflection typically observed for the non-polar α phase in the terpolymer.[14, 25] The XRD of a copolymer poly(vinylidene fluoride-trifluoroethylene) [P(VDF-TrFE)] 70/30 mol% was included for comparison and was found to have a interchain crystal spacing of 4.45 Å. This demonstrates that the terpolymer has a larger interchain distance, which is often attributed to the incorporation of the bulky, chlorinated monomer into the polymeric backbone since chlorine has a greater van der Waals radius than fluorine. [14, 25] Film **A** shows a (020) diffraction peak at a two theta of 18.75°, which we attribute to an overlap of the (100) and (020) reflections of the α-phase. A higher angle diffraction peak

centered at 19.37° was also observed and was assigned to overlapping α-phase (110) and β-phase (110) reflections. The higher angle diffraction appears in the region where the ferroelectric β-phase of the P(VDF-TrFE) (two theta ~19.80°) is typically observed for copolymers with VDF content between 50 and 80 mol%.[13, 26]

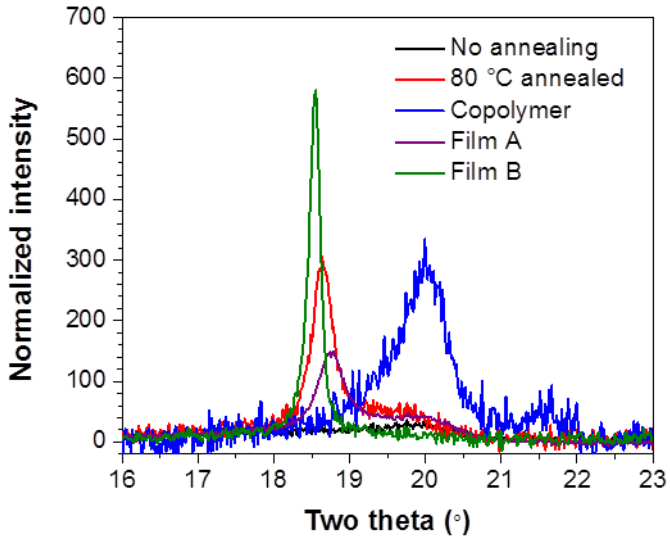

Figure 5.4 XRD (200, 110) reflection of terpolymer Films A and B. Films that represent intermediary steps in the M2 process (i.e. no annealing *vs*. annealing at 80 °C for 10 min) are also included. The spectrum of a copolymer p(VDF-TrFE) 70:30 mol % film is also shown. All the spectra were normalized for thickness. Data acquired by Dr Kathaperumal (Perry group)

On this basis we conclude that the **M2** processing technique gives rise to a predominance of non-polar domains, along with amorphous phase, in the terpolymer, while **M1** gives a mixture of polar and non-polar domains, again with amorphous phase.

In order to track the evolution of crystal formation during the second method, XRD data of films that represented intermediary steps in the **M2** process were evaluated.

The film that was not annealed (i.e. spin coated and allowed to dry at room temperature) showed a small amount of the β-phase but was mostly amorphous in nature. This suggests that in the absence of annealing the polar phase seems to be the thermodynamically stable crystal phase in the terpolymer. Annealing at 80 °C for 10 minutes provided a film with overlapping α-peaks (110 and 020) at 18.93° and 18.64°, respectively. Subsequent annealing at 120 °C overnight gives a predominantly non-polar (020) microstructure.[14, 25] This demonstrates that the high-temperature treatment followed by quenching is highly effective in promoting high α-phase content and relaxor ferroelectric behavior in the terpolymer.

Assessment of the coherence lengths of the crystallites (L) of the various phases was determined via XRD using Scherrer formalism (Equation 5.2)

$$L = \frac{0.9\,\lambda}{B\cos\theta} \qquad \text{(Equation 5.2)}$$

where λ is the x-ray wavelength, B is the full width at half maximum in radians and θ is the angular position of the diffraction peak.[27] The results of the Scherrer analysis are shown in Table 5.2. The size of crystallites in the non-polar phase progressed from being nonexistent under room-temperature drying conditions to 30.2 nm after high-temperature treatment at 120 °C followed by quenching. In the polar phases of the differently annealed films, the inter-chain spacing of the films remains relatively constant regardless of thermal treatment while their coherence lengths show a small difference between the annealed and non-annealed samples. It is evident from these results that not only is the

formation of the nonpolar phase promoted by quenching from high temperature but the size of the crystallites formed increases with the temperature of the thermal treatment.

FT-IR measurements were performed on films **A** and **B** in order to provide molecular structural information (Figure 5.5). The vibrational spectrum of film **A** shows three characteristic absorption bands at 505, 616, and 1290 cm^{-1} which are attributed to the CF_2 bending mode in the TTTGTTTG' conformation of the γ phase, the α phase TGTG' conformation, and the CF_2 stretching vibration of the all-trans ($T_{m>4}$) β phase, respectively.[16, 24] Film **B** shows a similar crystalline composition with the exception of a diminished γ phase. For comparison, the FT-IR spectrum of P(VDF-TrFE) prepared using **M2** is also presented. The copolymer film is comprised solely of a strong all-trans β phase suggesting that this polar phase is the thermodynamically stable conformation in the copolymer.[14, 26, 28] Therefore, while the introduction of CTFE units into the copolymer backbone contributes to the destabilization of the polar phase it promotes the formation of the α-phase and the consequent ferroelectric relaxor behavior.

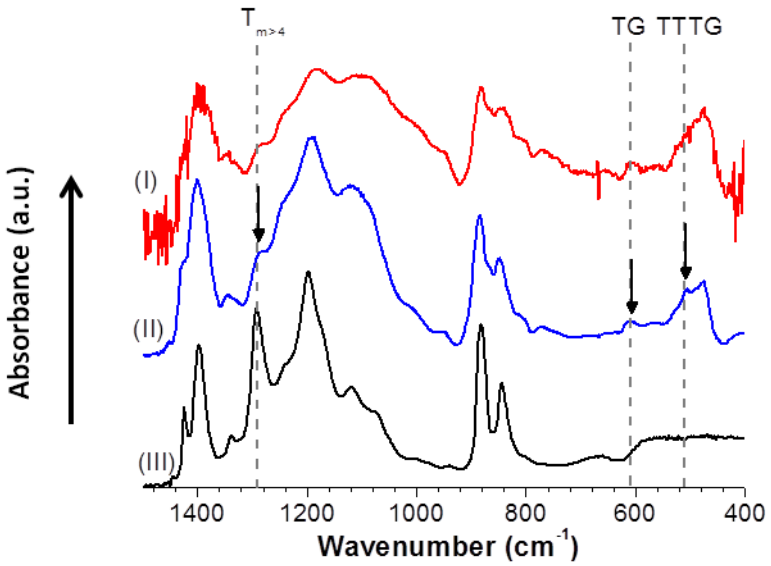

Figure 5.5 FT-IR spectra of the terpolymer films: (I) film B and (II) film A which were prepared by M2 and M1, respectively. The spectrum of a copolymer p(VDF-TrFE) 70:30 mol % (III) prepared via M2 was also included for comparison.

5.2.2 Dielectric characterization of terpolymer films

The effect of processing method on the dielectric constant and failure statistics of the films was investigated. Owing to the statistical nature of dielectric breakdown, the failure analysis was performed on the films using Weibull statistics.[29, 30] In this approach the cumulative probability of failure (P_F) at an applied electric field (E) is given by Equation 5.3.

$$P_F(E) = 1 - \exp\left[-(E-\gamma)/\alpha\right]^{\beta} \qquad \text{(Equation 5.3)}$$

where γ is the threshold electric field below which no breakdown occurs, α is the estimated value of E at which the cumulative probability is 63.2% and β is the Weibull parameter which represents the scattering in the measured dielectric strength values. In order to analyze the experimental data using the Weibull approach, the probability of failure is arranged using a median ranking approximation that can be expressed in equation 5.4

$$P_F(i,n) = \left[\frac{i-0.3}{n+0.4}\right] \qquad \text{(Equation 5.4)}$$

where n is the sample size, and i is the index (1, 2, 3,…n). The breakdown fields are arranged in ascending order and failure probability based on positioning is determined from equation 5.4 at each field. The parameters β and α are subsequently determined from a linear fit of log E *vs*. log[-ln(1-P)]. Figure 5.6 shows the examples of these plots for films A and B. Beta represents the slope of the fit and α is equal to the breakdown field when the probability of failure is 63.2% (i.e., 1-1/e).

Table 5.3 Dielectric characteristics of neat terpolymer films A and B prepared using the two methods.

	Film A [M1]	**Film B [M2]**
Thickness (μM)	20-40	3.9 ± 0.1
Relative permittivity (at 1 kHz)	~ 50	77 ± 10[a]
Dielectric strength (V/μm)	96 ± 40[b]	261 ± 62[b]
Weibull parameter (β)	2.9 ± 0.2[b]	5.6 ± 0.2[b]

[a] The error bars associated with the dielectric measurements reflect the standard deviation of the average values.
[b] Propagation of error from Weibull analysis was used to determine the uncertainty in Weibull parameter (β) and dielectric strength.

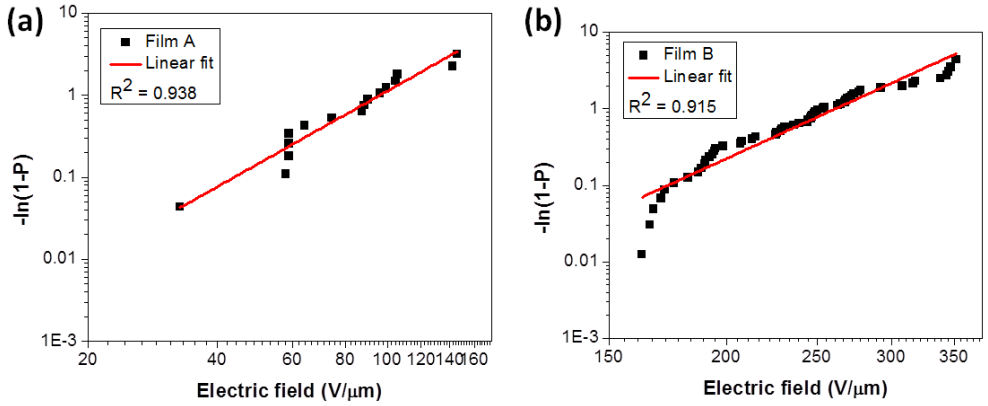

Figure 5.6 Weibull analysis plot for raw breakdown field data used to extract α and β for (a) Film A and (b) Film B.

Assuming a threshold of zero, the parameters can be substituted into equation 5.3 to determine the probability of failure as a function of electric field. The dielectric and breakdown analysis results for the two films are shown in Table 5.3. As mentioned above, Films A and B represent samples prepared from the pristine/as synthesized

terpolymer using M1 and M2, respectively. Dielectric spectroscopy measurements reveal that the film prepared using M2 has a higher permittivity than those prepared via M1. Film B has a rather high dielectric constant of 77 (at 1kHz) which, to the best of our knowledge, is the highest relative permittivity value reported for a neat organic fluoropolymer material. The increase in dielectric constant relative for B relative to film A is believed to originate from the increase in the amount of crystalline α-phase domains, as indicated by the microstructure in the SEM images (Figure 5.2), which are able to undergo substantial polarization in the presence of an electric field.[13] It is important to note that when film A is re-dissolved in dry DMF and processed into films via M2 (film C) the high permittivity observed in film B is reproduced (Table 5.4) thereby demonstrating the consistency of the processing methods. However, while the films A and B exhibit marked differences in permittivity they both demonstrate relatively low dielectric loss (tan $\delta < 0.04$) at 1 kHz.

Table 5.4 Dielectric characteristics of various neat terpolymer films prepared using the Methods 1 and 2 ([M1] and [M2]). The error bars associated with the dielectric measurements, with the exception of β, reflects the standard deviation of the average values. Propagation of error from Weibull analysis was used to determine the uncertainty in Weibull parameter (β) (measure of breakdown strength reliability).

	Film C [M2]	**Film D [M2]**	**Film E [M2]**	**Film F [M1]**
Thickness (μM)	8.5 ± 0.3	4.7 ± 0.1	3.1 ± 0.1	15 - 25
Relative permittivity (at 1 kHz)	72 ± 5	57 ± 5	62 ± 3	~ 50
Dielectric strength (V/μm)	128 ± 27	116 ± 49	222 ± 48	90
Weibull parameter (β)	5.5 ± 0.6	1.7 ± 0.1	1.9 ± 0.1	4.7

Film **C** was prepared by re-dissolving film **B** in dry DMF then preparing a fresh sample using **M2**. Film **D** represents a sample that has been prepared using **M2** from a

terpolymer solution that has been allowed to age for four months. Films **E** and **F** were prepared via **M2** and **M1** using atmosphere equilibrated and dry DMF, respectively.

The impact of solvent quality as well as polymer solution aging on the dielectric performance of the films was also examined and the results are presented in Table 5.4. Films **E** and **F** represent samples prepared using atmosphere equilibrated and dry DMF, respectively. The results show a reduction in the permittivity, dielectric strength and Weibull modulus of film **E**, relative to film **B**, although both films were prepared using **M2** which indicates that the presence of moisture in the DMF is deleterious to the properties. While the permittivity and E_B of film **F** did not improve relative to film **A** under the same preparation protocol (**M1**), the Weibull modulus showed significant improvement in film **F**. Furthermore, if the solution used to prepare the film is allowed to age for a period of four months under ambient conditions prior to making films using **M2** (film **D**) the dielectric properties are diminished relative to film **B**. Based on these findings it is evident that the use of anhydrous solvent is critical for obtaining high dielectric constant and dielectric strength terpolymer films with moderate Weibull moduli. Taken together, these results indicate that the details of the method used to prepare terpolymer films have a marked impact on the morphology, crystallinity and consequent electrical performance of the dielectric material. Specifically in the case of the terpolymer, the dielectric properties can be maximized by making films from freshly prepared, dry DMF solutions using the **M2** method reported here.

5.2.3 Assessing the energy storage capacity of the terpolymer films

Polarization-electric filed (P-E) measurements were performed on film **B** to determine its energy storage capacity. The stored energy can be determined from the integration of the region above the curve and the ordinate as illustrated in Figure 5.7. The results of the P-E measurements are shown in Figure 5.8. The unipolar P-E response of the film at fields up to ~ 470 V/μm are shown in Figure 5.8a; the loops show relatively narrow hysteresis, small remnant polarization, and relaxor ferroelectric behavior, all of which are desirable properties for achieving efficient, high energy density storage materials. However, the gradual widening of the loops with increasing field indicates that some energy loss is being incurred possibly from conduction and/or charge injection at high fields.[31, 32]

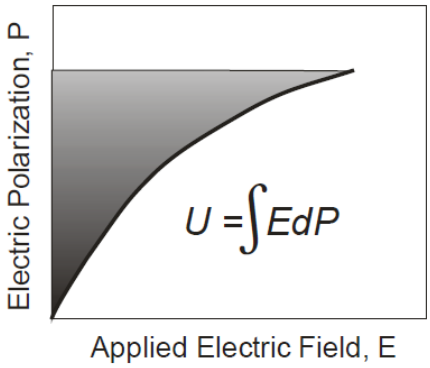

Figure 5.7 P-E curve of a ferroelectric material. The stored energy is equal to the shaded under the P-E curve.

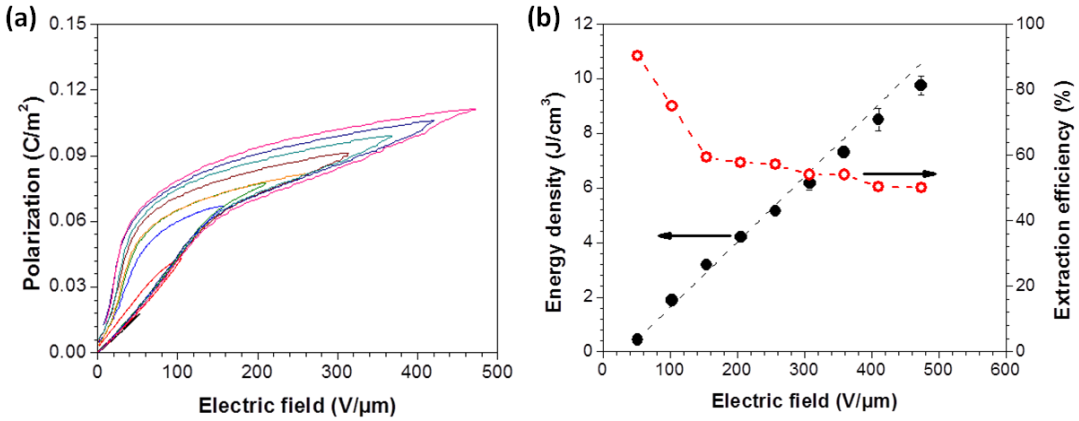

Figure 5.8 Unipolar P-E curves of film B prepared from the as synthesized terpolymer using M2 (a) and the corresponding recoverable energy density and extraction efficiency curves (b). Each unipolar P-E curve was obtained on a single device at different maximum field until catastrophic failure. Dashed lines serve as guides for the eye.

Additionally, the P-E curves also show a reduction in the polarization response at ~150 V/μm which is evidence of displacement saturation. Figure 5.8b shows the values of the discharged energy density and extraction efficiency as a function of the applied field as determined from the integration of the areas between the charge and discharge curves of the P-E loops and the ordinate.[9] Unlike linear dielectrics, which show a quadratic energy density dependence with electric field, the terpolymer exhibits a near-linear behavior as the field is increased. In addition, the extraction efficiency appears to taper off rapidly prior to the onset of dielectric saturation at ~150 V/μm. For example, film **B** which gave a maximum extractable energy density of ~9.7 J/cm^3 at ~ 470 V/μm did so only with an extraction efficiency of about 50%. It is clear that the onset of early polarization saturation (i.e. saturation at a field that is much lower than the breakdown field strength) and conduction/leakage at high fields imposes a limit on the achievable energy density and the extraction efficiency. This serves to reinforce the notion that consideration must

be given to extraction efficiency when assessing the discharged energy density for various capacitor applications. Therefore, it may be advantageous to develop high permittivity terpolymer systems in which the threshold for dielectric saturation is much closer to the breakdown field of the film. Recall that the impetus behind the synthesis of the terpolymer was the introduction of a bulky CTFE monomeric group into the main chain of P(VDF-TrFE) in order to reduce the size of the crystalline domains and simultaneously lower the energy barrier for ferroelectric-paraelectric phase transition giving rise to high dielectric constant.[28] Furthermore, in order to delay the onset of early dielectric saturation the polymer system would have to be optimized such that it has a lower permittivity value that allows for the energy density to be maximized at higher field.[9] It therefore stands to reason that a systematic study of the chemical composition of the bulky monomer as well as the crystallization behavior of the resulting terpolymer is needed to properly understand and control the relaxor ferroelectric behavior.

Key to the development of fluoropolymer energy storage materials are the design and processing of dielectrics that are capable of rapidly storing and nearly instantaneously delivering large amounts of energy in an efficient manner. As such we conducted charge-discharge (C-D) measurements on Film **B** to examine it energy storage capacity under pulsed conditions. A schematic of the set-up used in C-D measurements is shown in Figure 5.9. In this technique, the device under test (DUT) is initially charged by applying a known DC field through a charging circuit. The DUT is then discharged through a load resister of known value and the current output monitored through a known resistor. An oscilloscope integrates the output voltage over time to calculate the released energy.

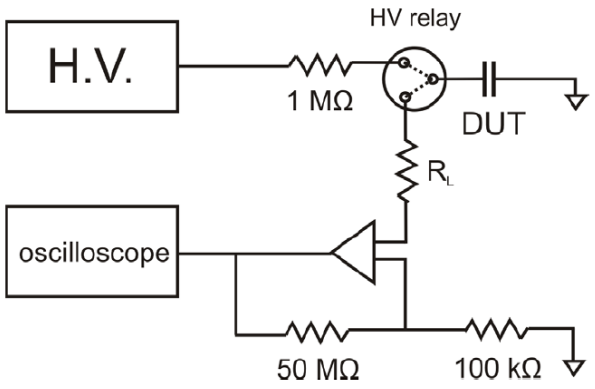

Figure 5.9 Schematic of charge-discharge circuit.

Figure 5.10 shows the C-D results. Film **B** shows a maximum extractable energy density of ~ 27 J/cm^3 which is almost three times as high as that achieved under P-E conditions. It is also important to highlight the fact that under pulsed conditions fields up to ~ 604 V/μm can be achieved prior to the occurrence of catastrophic failure, which is markedly higher than the fields reached under the longer timescale of breakdown testing. Since, both C-D and breakdown testing are performed until catastrophic failure, the superior performance of the terpolymer film under pulsed conditions is believed to be a result of the ability of the material to withstand electrical and mechanical stress developed in the dielectric during measurement, as well as the differences in the timescales of the techniques.

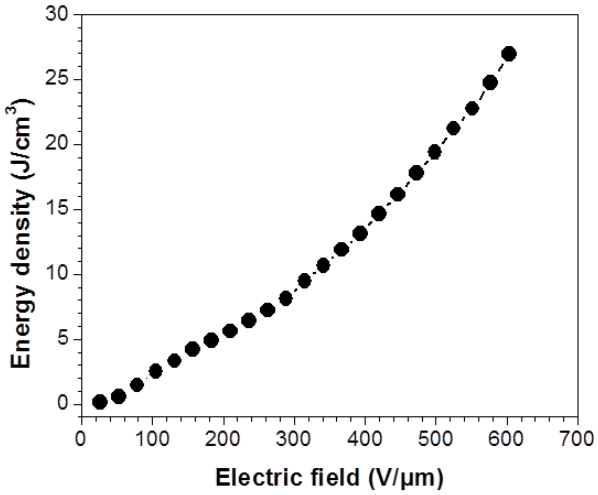

Figure 5.10 Discharged energy density of film B as determined from charge-discharge measurements. Standard deviation (1σ) in the measurements was less than 0.5 J/cm^{-3} for measurements.

5.3 Dielectric properties of nanocomposite films comprised of high permittivity P(VDF-TrFE-CTFE) terpolymer and phosphonic acid modified barium titanate nanoparticles

The nanocomposite approach towards the development of dielectric materials generally involves the incorporation of high permittivity particles into a low dielectric constant polymer matrix. In this study we examine the dielectric properties of nanocomposite thin films formed between phosphonic acid surface-functionalized barium titanate nanoparticles and poly(vinylidene fluoride-trifluoroethylene-chlorotrifluoroethylene) P(VDF-TrFE-CTFE), which exhibits marked reduction in permittivity contrast relative to other conventional systems. The permittivity of the neat

polymer and the particle was determined to be 77 and 127, respectively at 1 kHz. We hypothesize that the use of filler particles and a matrix with comparable permittivities will result in higher achievable dielectric strength and more reliable breakdown behavior. Concomitantly, it is expected that the improvements in dielectric strength will result in greater energy storage capacity in these nanocomposite thin films.

5.3.1 Characterization of $BaTiO_3$ nanoparticles.

In order to elucidate both structural and phase information on the BT particles used throughout this study the bare/unmodified BT nanoparticles were characterized by SEM, XRD and Raman spectroscopy. The morphology of the BT nanoparticles is shown in the SEM image of Figure 5.11, which reveals a wide distribution in the particle size (154 ± 45 nm).

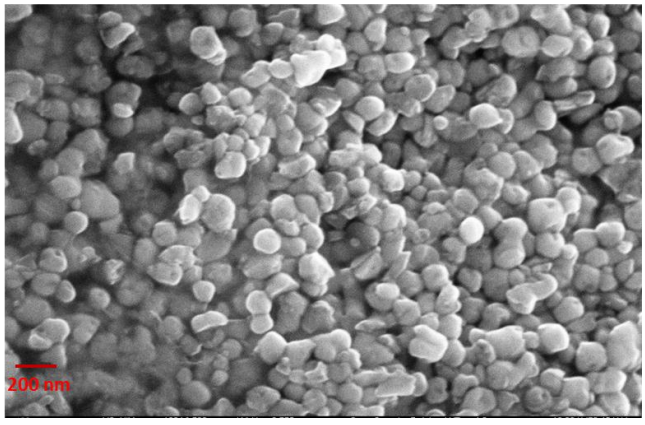

Figure 5.11 SEM of barium titanate nanoparticles. Image obtained by Yunsang Kim (Perry Group).

The Curie temperature of barium titanate nanoparticles of ~150 nm diameter is ~110 °C such that the tetragonal polymorph should be the thermodynamically stable phase at room temperature.[33] The XRD data (Figure 5.12a) of our BT nanoparticles shows a splitting of the [200] and [002] reflections at approximately 45°, indicative of the presence of tetragonal phase BT.[34] However, a peak fitting analysis using Gaussian bandshapes shows that the dominant reflection is at the lower of the two angles (2θ = 44.98), which indicates a substantially larger BT cubic phase content in our nanoparticle sample. The ratio of cubic to tetragonal phase was found to be 1.5:1.

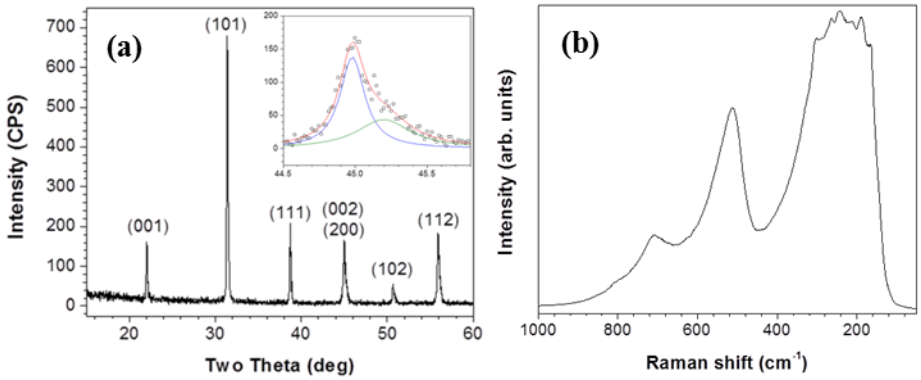

Figure 5.12 XRD (a) and Raman spectrum (b) of BT nanoparticles. The inset in the XRD highlights the splitting of the peak at 2θ of ~45°.

To further investigate the phase composition the BT nanoparticles, Raman spectroscopy was employed. The cubic phase of BT is Raman inactive but the presence of some

tetragonal phase BT is supported by the Raman spectrum in Figure 5.21b, which shows characteristic peaks for tetragonal barium titanate at 175, 265 and 718 cm^{-1}.[35-37]

5.3.2 Surface modification and characterization of barium titanate (BT) nanoparticles

Pentafluorobenzyl phosphonic acid (PFBPA) was used to modify the surface of BT nanoparticles according to a previously reported method with minor changes.[38] A schematic of the modification process is given in Figure 5.31.

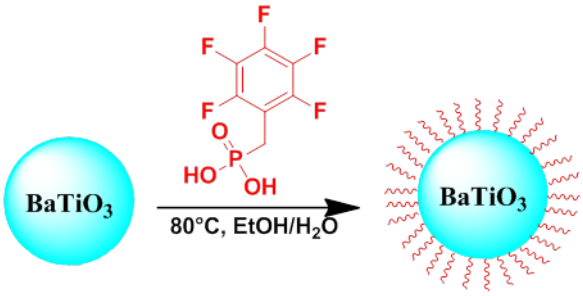

Figure 5.13 Schematic of the surface modification of barium titanate with PFBPA acid.

The phosphonic acid was first synthesized by converting pentaflurobenzylbromide to the phosphonate via an Arbuzov reaction followed by subsequent hydrolysis with bromotrimethylsilane, to form the phosphonic acid. The commercial BT nanoparticles used in this study were obtained from Cabot Corporation. Prior to the surface

modification, BT nanoparticles were subjected to ball milling for two days in the presence of yittria-stabilized zirconia (grinding media) and ethanol in order to break up aggregates. Energy dispersive x-ray measurements on the de-aggregated particles only found trace amounts of zirconia (1.19 atomic %). The nanoparticles were then suspended in a 95:5 (v/v) ethanol/water solvent mixture (0.4 g/10 mL) and the mixture ultrasonicated for 4 h at 15-25 °C. The phosphonic acid modifier (0.17 mmol/g BT) was added to the suspension and the mixture stirred and heated at 80 °C for 1 h. The functionalized nanoparticles were isolated by using six centrifugation/wash cycles (~10,500 rpm) in ethanol with a 10 min ultrasonication step between washes. The modified nanoparticles were then dried overnight in a vacuum oven at 80 °C. Control samples were made using the same protocol but without the addition of PFBPA surface modifier to the nanoparticle suspension.

In order to verify the modification of BT with PFBPA, FT-IR measurements were performed. FT-IR analysis of the region 700 and 1600 cm^{-1} region, as shown in Figure 5.14, provided evidence of the binding of the phosphonic acid to BT.

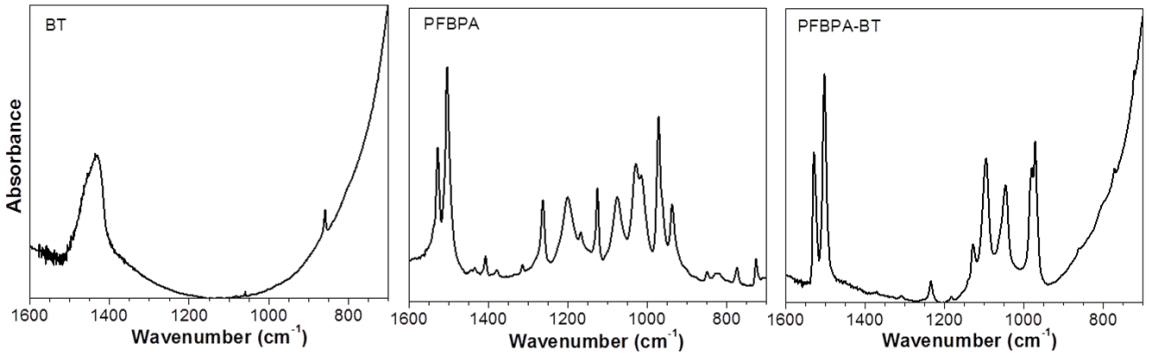

Figure 5.14 FT-IR spectra of unmodified BT (left), PFBPA (center) and PFBPA-BT (right) in the P-O stretching region. The BT and PFBPA-BT spectra were normalized to the Ti-O vibration mode at ~ 540 cm^{-1}. All spectra were obtained from KBr pellets.

The FT-IR spectrum of pristine BT shows a significant amount of $BaCO_3$ impurity at ~1430 cm^{-1} as well as the rising edge of the Ti─O vibration mode at ~540 cm^{-1}.[39] The C─F stretching (1126 cm^{-1}) and the aromatic vibration modes (~ 1500 and 1530 cm^{-1}) of PFBPA are both preserved in the modified BT. In contrast, there was significant changes in the P═O and P─O stretching region for PFBPA-BT. Upon surface functionalization of BT the P─O stretching mode in the free phosphonic acid (1090-990 cm^{-1}) transforms into P─O─M bonds (1045 and 1095 cm^{-1}), where M represents surface metal, while the P═O vibration (1200 cm^{-1}) completely disappears. This is consistent with majority of the acid being bound to the surface in a tridentate manner.[40, 41] The coverage of the ligand on the surface can be deduced from the following equation:

$$\frac{SA_{NP} \times MW_L}{A \times BA_L} = \frac{M_L}{M_{NP}}$$

where SA_{NP} is the surface area of the nanoparticle (can be deduced from BET), MW_L is the molecular weight of the ligand, A is Avogadro's constant, BA_L is the binding area of the ligand, and M_L/M_{NP} is the mass of ligand per gram of particle. Based on a theoretical footprint of a phosphonic acid monolayer (24 $Å^2$)[42] and the BET surface area (5.124 m^2/g) the coverage was estimated from the weight loss obtained from TGA (Figure 5.15) to be at least 2 monolayers.

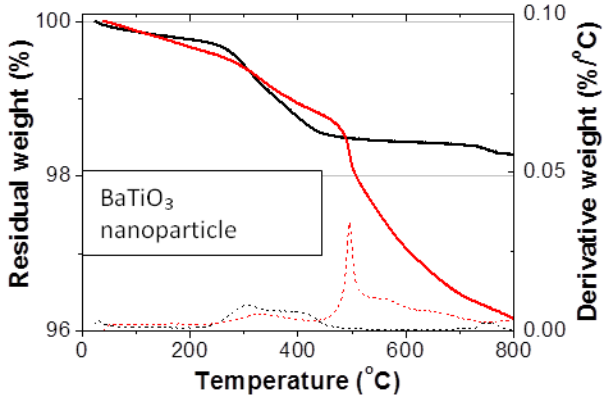

Figure 5.15 Thermogravimetric analysis of unmodified (in black) and PFBPA-modified BT particles (in red) for BT. Residual weight is shown in solid lines and the derivative of residual weight is shown in dashed lines.

5.3.3 Preparation and characterization of nanocomposite thin films

The PFBPA-modified BT nanoparticles were dispersed in P(VDF-TrFE-CTFE) terpolymer in order to form the nanocomposite thin films. The terpolymer and modified nanoparticles were both added to dry N,N-dimethylformamide and mixed/ ball milled for

14 days in the presence of grinding media. Thin films were prepared from the resulting suspensions by spin-coating the mixture onto oxygen plasma treated (Plasma Etch; 2 min) aluminum-coated glass substrates which served as the bottom electrode. The films were soft baked at 80 °C for ~ 10 min then dried overnight under vacuum at 120 °C. The post ball milling steps are similar to **M2**.

The microstructure/morphology of the nanocomposite films was investigated by SEM and AFM. Figure 5.16 shows the top surface SEM images that were obtained to assess the effectiveness of the dispersion of the nanoparticles in the terpolymer matrix. Overall, the nanoparticles appeared to be homogeneously dispersed in the polymer matrix (i.e., no significant aggregation of particles) and yielded relatively high quality films. Interestingly, the high resolution surface images of the terpolymer show a dense network of fibular crystalline domains, which are well known to be the origin of the high permittivity in PVDF based co-polymers.[13] These fibril domains are gradually diminished as the particle loading increases, which can impact on the magnitude of the permittivity. In addition to the reduction in the fibril domain, the images show a gradual increase of cracks and pinhole defects with increased BT nanoparticle volume fraction. The AFM image shows that the surface roughness of the thin films increases with particle loading from 34 nm in the neat polymer up to 300 nm in the nanocomposite film with 50% volume loading of particles (Figure 5.17).

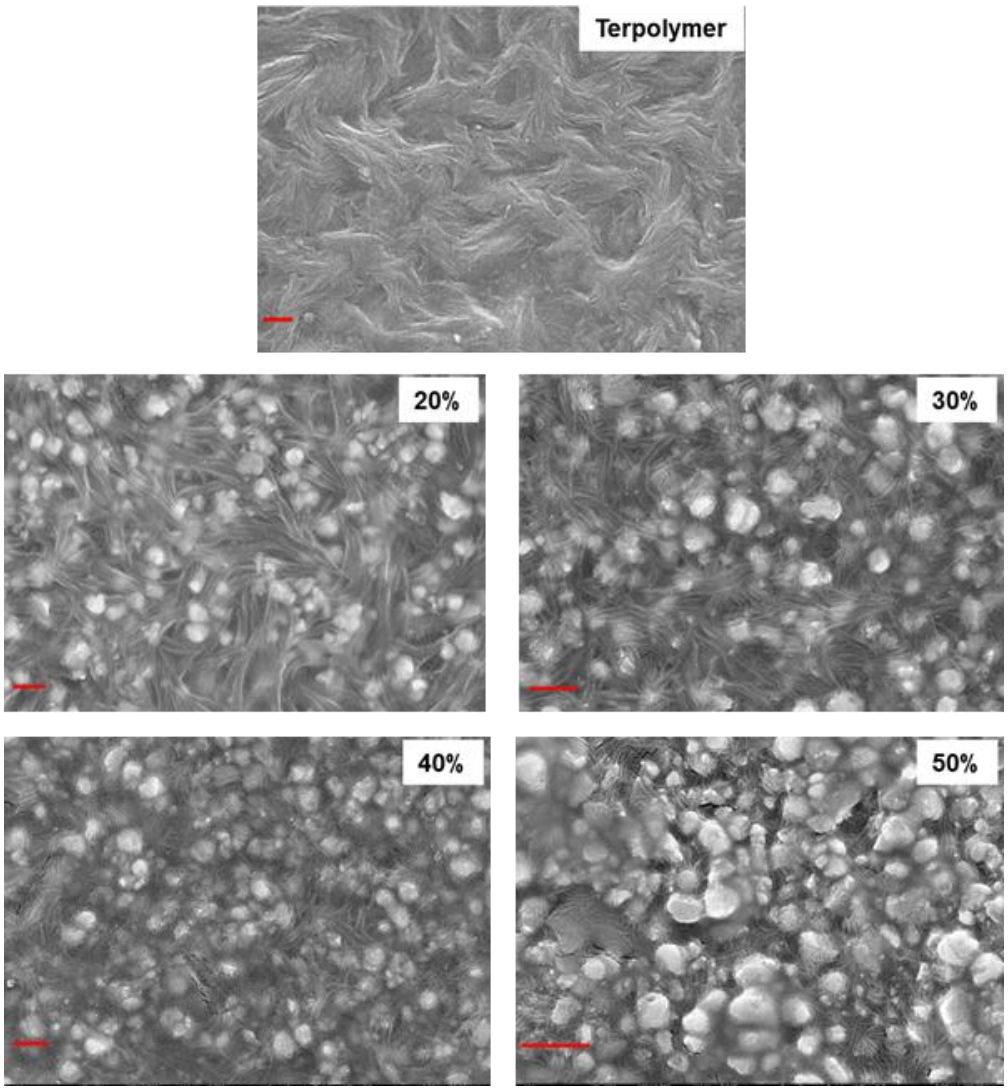

Figure 5.16 SEM high magnification top surface images of the neat terpolymer and nanocomposite thin films with different BT volume fraction. All scale bars are 300 μm.

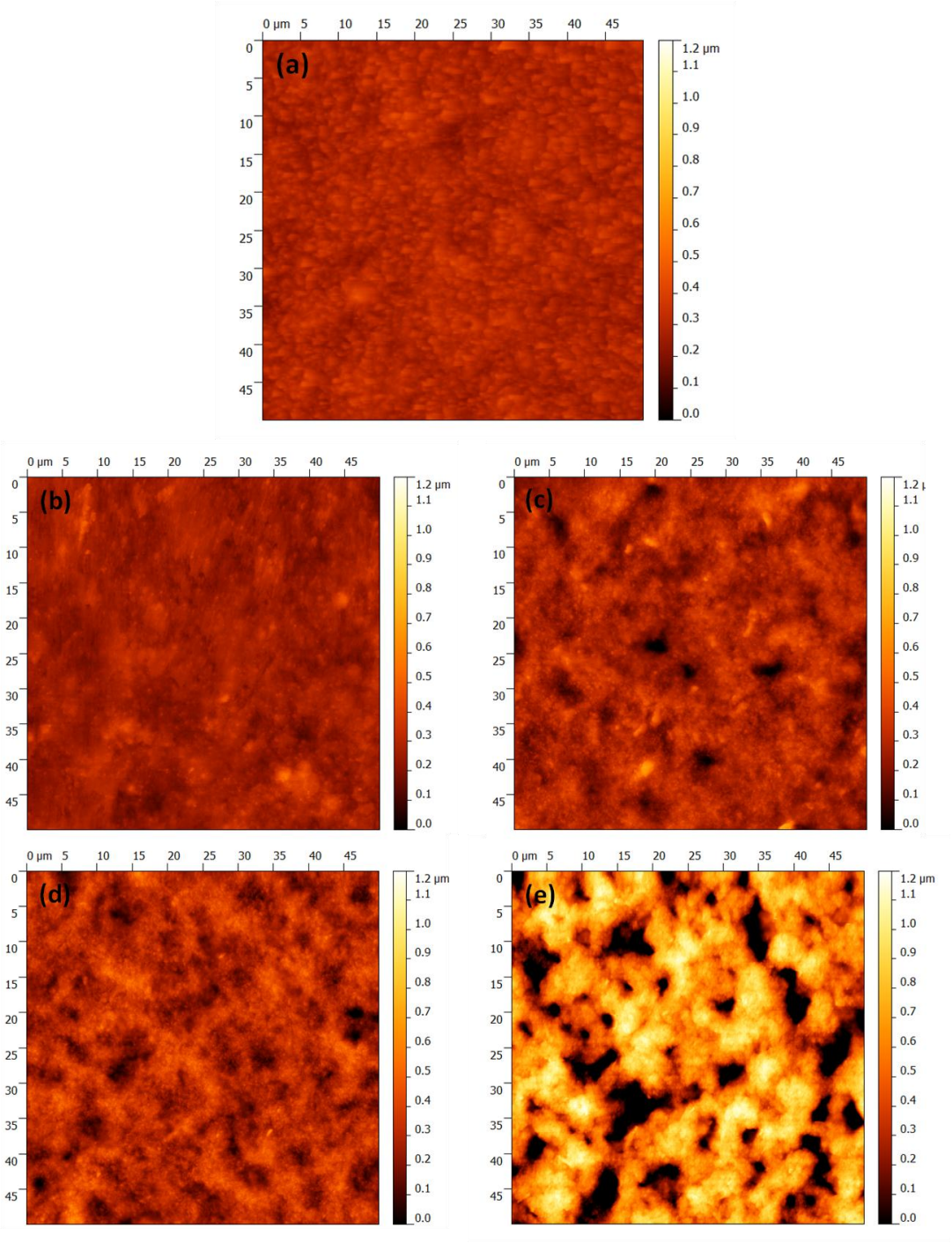

Figure 5.17 AFM images of neat terpolymer (a) and nanocomposite films (b-e). The RMS roughness as determined from 50 µm × 50 µm scans are: 34 nm (neat polymer), 42 nm (20% BT), 74 nm (30% BT), 87 nm (40% BT), and 300 nm (50% BT).RMS.

5.3.4 Dielectric characterization of terpolymer nanocomposite films

Dielectric spectroscopy was used to ascertain the effective permittivity and corresponding loss tangent of the dielectric films. The results presented in Figure 5.18a show minimal change in the effective permittivity of the nanocomposite thin films with increased particle loading for film thicknesses ranging from 2.8 to 3.9 µm. This is likely to be due to the nominal permittivity difference between the nanoparticle and the polymer matrix as well as the reduction in fibril domains with particle loading as was observed elsewhere by Li et al.[43]

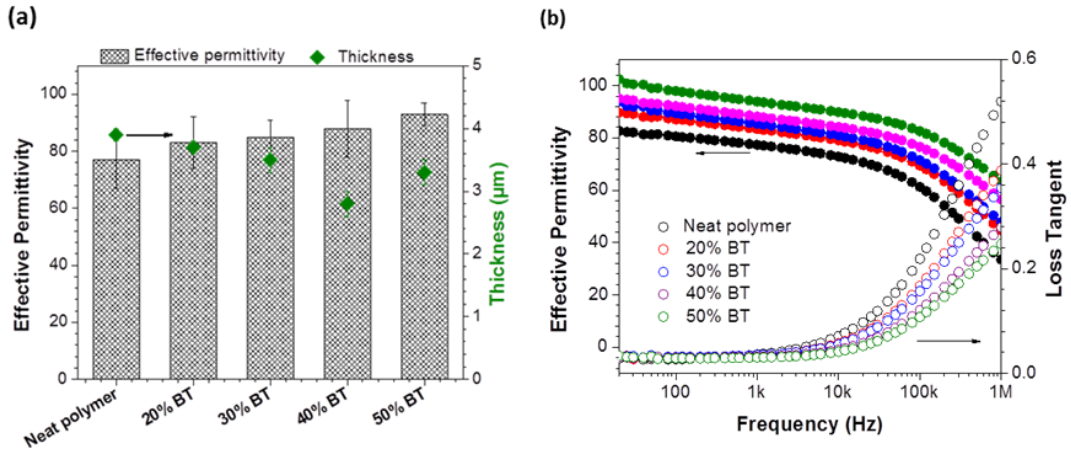

Figure 5.18 Measured permittivity of nanocomposite films at 1 kHz with the corresponding film thicknesses (a) and permittivity and loss tangent of the thin films over a frequency range of 20 Hz to 1 MHz (b).

A comparison plot of the real part of permittivity and the loss tangent for the nanocomposites over the frequency range of 20 Hz to 1 MHz is shown in Figure 5.18b.

The thin films show a sharp reduction in permittivity beyond 30 kHz and, concomitantly, a sharp increase in the loss tangent. In addition, with increased particle loading there is a marked reduction in the loss tangent which indicates that the dielectric dissipation mostly originates in the polymer matrix.[44]

The dielectric strength of the nanocomposite films were measured and analyzed within the context of Weibull distribution as was shown before for the neat terpolymer. Recall that the Weibull modulus represents the scattering in the measured dielectric strength values and serves as a measure of the reliability of the devices.

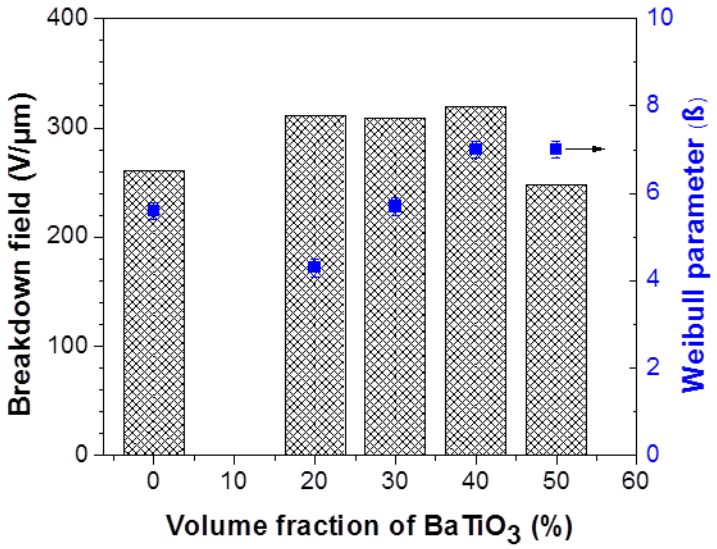

Figure 5.19 Breakdown strength and Weibull modulus of terpolymer and nanocomposite films at different BT particle loading.

Figure 5.19 shows the impact of increasing particle loading on the dielectric strength of the nanocomposites. Generally, the inclusion of particles into polymer matrices often

results in lower dielectric strength composites relative to the neat polymer.[4, 17, 45] To the contrary, we find that particle loadings up to 40% showed improved dielectric strength. This behavior was found to be consistent at all fields except for the 50% composite which underperforms relative to the pristine polymer in the region above 200 V/μm. This may perhaps be better appreciated from the plot of the cumulative distribution function shown in Figure 5.20.

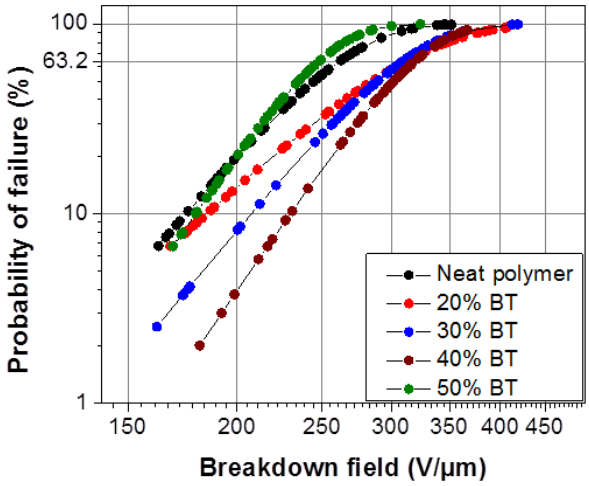

Figure 5.20 Cumulative probability of failure as a function of applied electric field.

A similar improvement in dielectric strength as a function of increased filler loadings has been previously observed for titania in polyvinyl alcohol by Tuncer[46] and Kilaru[47] and was postulated to be the result of the nanoparticles acting as trap/scattering sites in the pathway of charge carriers. As a result, charge carriers travel shorter distances, become less mobile, and have lower kinetic energy thereby increasing the lifetime to breakdown. Kilaru *et al.*[47] were able to provide direct evidence of this phenomenon in a

fluoropolymer that was loaded with various amounts of BT by charge-voltage analysis. In these studies it was observed that hysteresis in the current density-voltage (J-V) curves increases (i.e., the curves become wider) with particle loading. This behavior was attributed to the scattering of the charges injected from the electrode during the potential sweep. It therefore stands to reason that a similar phenomenon is likely in our system, which is indeed the case as will be demonstrated in the next section.

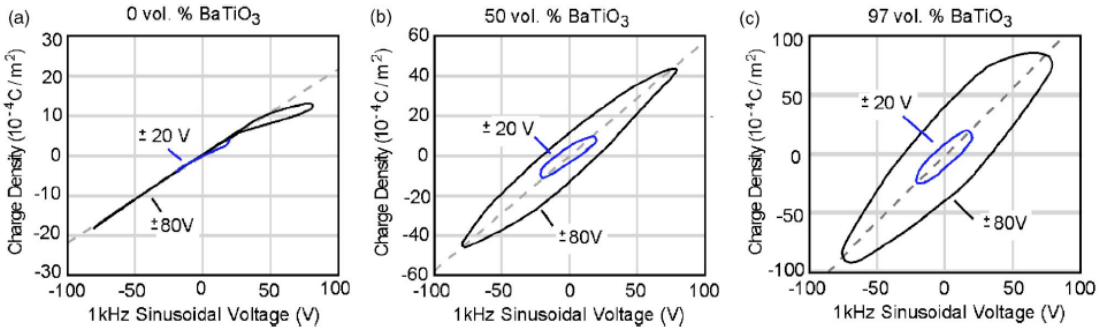

Figure 5.21 Charge-voltage analysis at +/−20 and +/−80 V at 1 kHz sinusoidal voltage for the minimum through maximum achievable $BaTiO_3$ content in the nanocomposite film. The 97 vol% $BaTiO_3$ is the specification for the original as deposited $BaTiO_3$/fluoropolymer ratio and is larger than the actual vol % of $BaTiO_3$ since an additional layer of the pure fluoropolymer was added on top coat is added. Reproduced from Kilaru *et al*.[47]

Beyond 40% BT loading, the dielectric strength plummets and is likely to be due to an increase in particle-particle contact and film porosity.[48, 49] However, it is important to note that at particle loadings of 20-40% there is an improvement in the Weibull modulus (β) relative to the neat polymer. The higher β values are indicative of a reduction in the spread of the breakdown behavior of the thin films.

5.3.5 Assessing the energy storage capacity of the terpolymer films

The effect of the particle loading on the energy density was analyzed by polarization-electric field (P-E) measurements. It is generally accepted that the inclusion of high permittivity particles into a polymer matrix changes the electric-field distribution in the nanocomposite and could potentially lead to higher energy densities.[45, 49, 50] Recall that the extractable energy density of the nanocomposite thin films can be calculated from the P-E curves (Figure 5.22) by integrating the area between the loop and the ordinate.

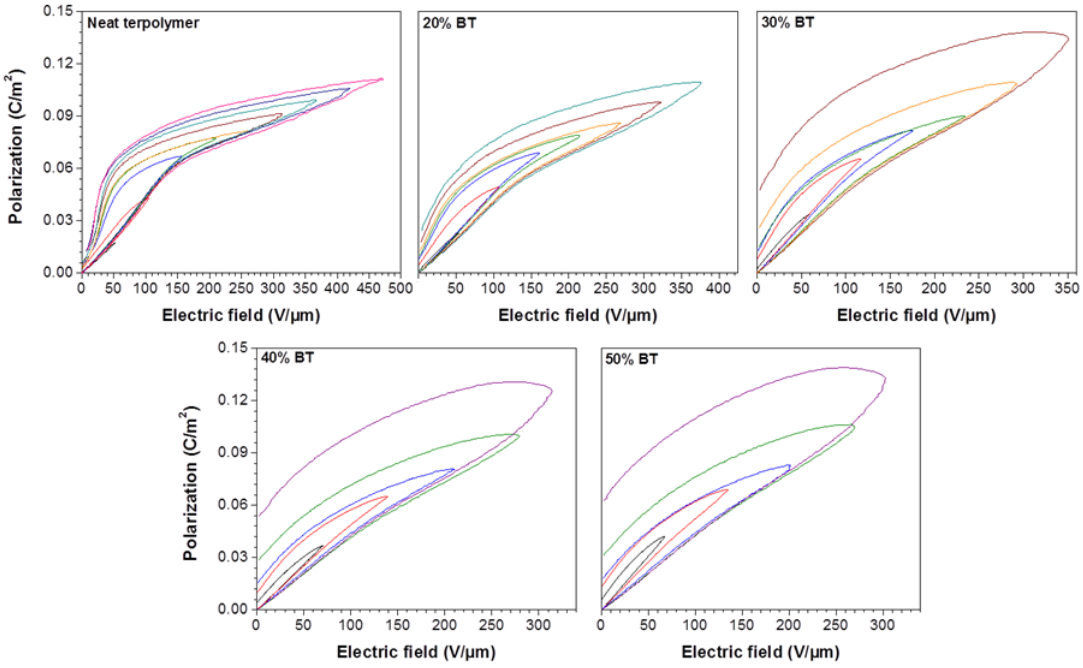

Figure 5.22 Unipolar P-E responses for neat terpolymer and nanocomposite thin films. Each unipolar P-E curve was obtained on a single device at different maximum field until catastrophic failure.

Therefore, the gradual widening of the P-E loops is indicative of losses in the system. In the case of the neat terpolymer, a relaxor ferroelectric behavior[12] is observed and maintained up to fields as high as 470 V/μm with minimal hysteresis loss. The P-E loop of the neat terpolymer also shows evidence of dielectric saturation at approximately 150 μV/m. Interestingly, the saturation is gradually reduced with increased filler content. In the regime beyond ~ 200 V/μm the nanocomposite films exhibit large hysteresis and the loop widening increases significantly with particle loading. The transformation of the shape of the loops at higher fields is indicative of charge injection and trapping in the nanocomposite thin films as was discussed in the previous section. It should be pointed out here that the observed hysteresis has some contribution from the ferroelectric $BaTiO_3$ particles themselves and should be taken into account.

Figure 5.23a shows the extractable energy density as a function of electric field. It can be seen that all the nanocomposites, with the exception of the 20% film below 200 V/μm, demonstrated higher polarization relative to the neat polymer. However, at higher fields the nanocomposite film with 20% BT loading recovers and outperforms the terpolymer giving a maximum energy density of 8.9 J/cm^3 at 378 V / μm.

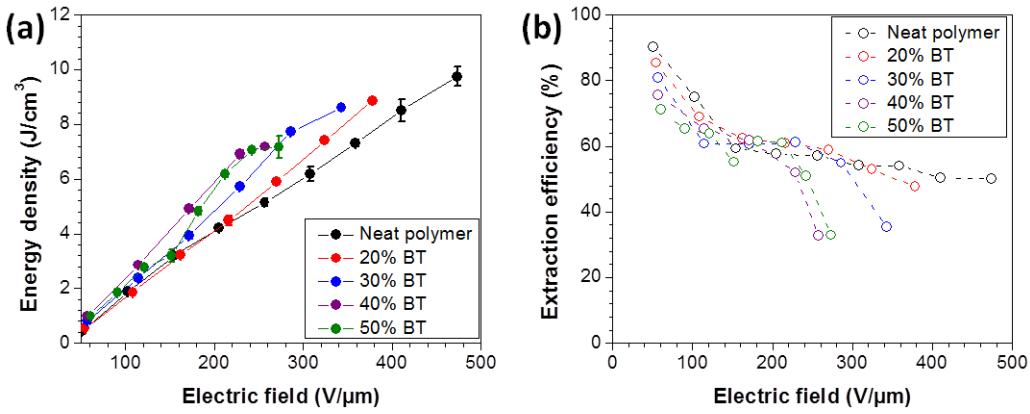

Figure 5.23 Extractable energy densities (a) and extraction efficiency (b) based on the analysis of the unipolar P-E loops.

In addition, the performance of the film with 50% nanoparticle loading is consistently inferior to that of the 40% nanocomposite. The reduction in the polarization exhibited by the 50% film is likely due to increased particle-particle interaction (due to the close proximity of the particles at these high loadings) and porosity in the films. Taken together, both these observations may be indicative of an upper and lower limit on the volume fraction of the nanoparticles that can be introduced into the polymer matrix for optimal energy extraction. Further, the overall enhanced polarization observed in the nanocomposite films could account for the improved recoverable energy density. It is also important to note that while the neat terpolymer exhibited superior dielectric strength the films with particle loadings of 20% and 30% v/v performed comparably well in the high field regime prior to the onset of losses shown in the unipolar P-E loops.

While it is essential to know the extractable energy density in these thin films, it is equally important to deduce how efficiently the stored energy is recovered. Figure 5.23b shows the extraction efficiency curves obtained from the P-E loop analysis. The plots

demonstrate that the introduction of BT nanoparticles into the terpolymer matrix has minimal impact below 200 V/μm. At higher fields, however, the BT particle loading compromises the efficacy of the charge-recovery process. Therefore, preservation of the gains in polarization achieved through the introduction of high permittivity particles into the polymer matrix may prove challenging at high fields. The overall inferior performance of the other nanocomposite films relative to the neat polymer is likely to have originated from the particles ability to act as scattering centers. As such, while the introduction of the BT particles into the polymer matrix can improve the dielectric strength of the neat polymer (Figure 5.19) due to the filler's ability to act as trap sites for injected charges, this capability may also be responsible for the diminished ability to recover the stored charges at high fields. The impetus is therefore to find a means of balancing particle loading, recoverable energy density and extraction efficiency. In the present study our case the extraction efficiency of the 20% film seems to be a good compromise in all dimensions and at all fields.

The extractable energy density of the thin films was also evaluated by charge-discharge (C-D) measurements to assess their performance under pulsed conditions. Figure 5.25a shows that there was little change in maximum energy density (U_{C-D}^{max}) with varying volume fraction of particle at low fields (~152 V/μm) which may be an indication that under pulsed condition the attainable energy density is mostly determined by the polymer.

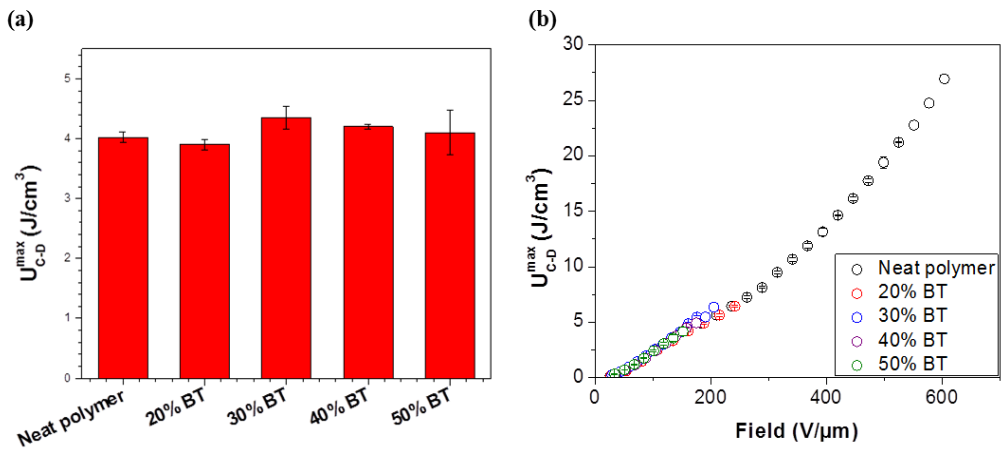

Figure 5.24 Measured maximum energy density of nanocomposite thin films under pulsed conditions at an applied field of 152V/μm. (b) Energy density measurement of nanocomposite and P(VDF-TrFE-CTFE) as a function of electric field by using a charge-discharge circuit.

The average maximum energy density of the nanocomposite thin films ranged from 3.9 to 4.4 J/cm^3. These values are within the range of the recoverable energy density obtained from P-E measurements at similar fields. Since the measurements were performed until device failure energy density of the nanocomposite films under pulsed conditions were severely limited to very low field (< 300 V/μm) as shown in Figure 5.25b. In contrast, the polymer was able to reach a maximum energy density of 27 J/cm^3 at a field of 604 V/μm. In addition, the measureable field strengths of the nanocomposites were also lower than the values obtained from Weibull device failure analysis. It is believed that the discrepancies between the Weibull and the pulsed measurements stem from a combination of built up electrical stresses during the C-D[51] as well as the use of larger electrode areas (*see experimental*).

5.4 Molecular engineering of interfaces for improved dielectric strength and energy storage: A preliminary look at the impact of surface modifiers

Surface modification of nanaoparticles prior to their dispersal in a suitable polymer host is an integral part of the nanocomposite preparation process. As outlined in the introductory chapter modification of BT nanoparticles with suitable phosphonic acid ligands prior to their dispersal in a suitable polymer matix can lead to improved homogeneity, reduced particle aggregation and effective surface passivation relative to the composite containing unmodified particles.[38] The surface functionalization of the particles leads to marked improvements in the measured dielectric strength and energy density of the composites. While notable progress has been made in the Perry Group at Georgia tech using this approach, a clear/systematic understanding of the result was not pursued. Also, the modifiers were solely chosen with the objective of minimizing the surface energy difference between the particles and the polymer host; therefore, not much thought was given to molecular structure and its impact on the dielectric performance of the films. As such, in this study we begin to examine the role of surface modifiers in tailoring the dielectric properties of nanocomposite dielectric films. It was hypothesized that the molecular structure of the modifier used to coat the nanoparticles can play a significant role in tuning the frontier energy levels at the BT surface thereby creating an additional barrier to the propagation of charge between the matrix and the filler. Additionally, the physical interaction between the matrix and the particle can also be altered by the choice of modifier thereby limiting the mobility of the polymer chain within the vicinity of the particle surface.[52, 53] The polariazability of nanocomposite

films in the presence of an electric field is affected by chain mobility. Therefore, the physical interaction at the particle-polymer interface and this could have significant effects on the dielectric performance of the nanocomposite thin films.

Given the propensity of the surface modifiers to change the chemical and dielectric characteristic of the interface, it is important to examine the role that their molecular structure plays in the performance of nanocomposite films. This study presents a preliminary look at the influence of fluoraryl surface modifiers with variable dipole moments and similar surface energy on the dielectric properties of nanocomposite thin films. The modifiers examined herein are pentafluorobenzyl phosphonic acid (PFBPA, OLS-II-62), 2,6-bis(trifluromethyl)benzylphosphonic acid (bis-CF3BPA, AJG-III-045a), 4-(trifluromethyl)benzylphosphonic acid (4-CF3BPA, AJG-II-298a) and 3,4,5,-trifurobenzylphosphonic acid (3,4,5F3BPA, GHF-I-023a). The structure of the molecules and their TGA-derived coverage are presented Figure 5.25.

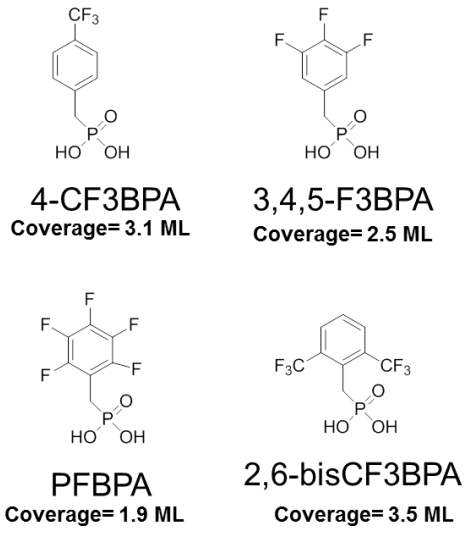

Figure 5.25 Structure of dipolar surface modifiers used to functionalize BT. The surface coverage of the modifier on the nanoparticle as determined from TGA is also shown.

5.4.1 Particle modification and film preparation

Successful modification of the particles with the ligands was confirmed by FT-IR (Figure 5.26) and TGA analysis was used to determine coverage. The modified particles were used to prepare 40% v/v nanocomposite solution poly(vinylidene-co-hexafluoropropylene) P(VDF-HFP) (M2 protocol was used) ,which were in turn used to prepare thin films parallel plate capacitors used to study the impact of the modifiers on the dielectric performance of the nanocomposites. SEM was utilized to investigate the morphology of the nanocomposite films. The surface and cross-sectional images depicted in Figure 5.27. No qualitative distinction between films formed using different coupling agents. Overall, the nanoparticles appeared to be dispersed in the polymer with very little evidence of aggregation.

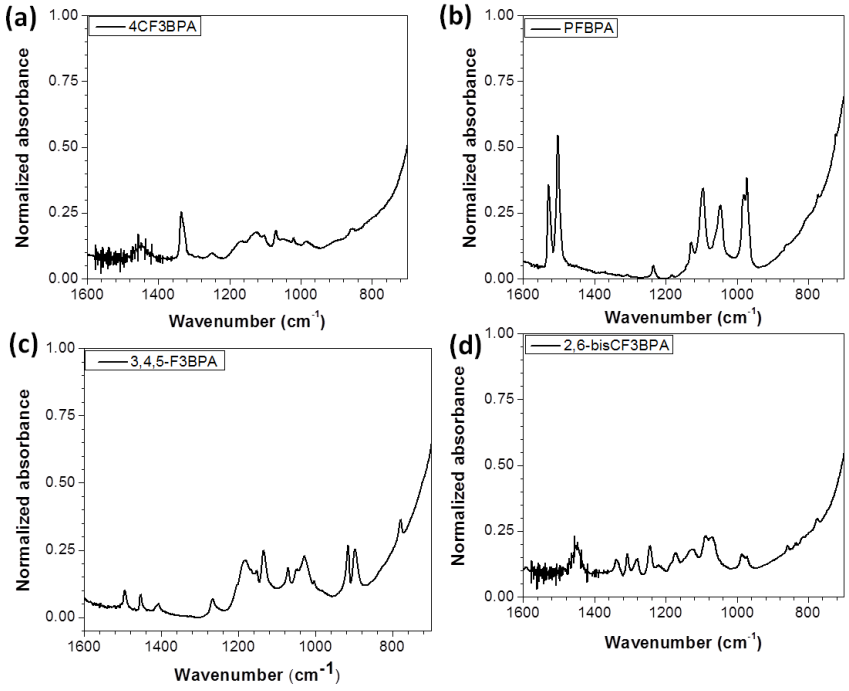

Figure 5.26 FT-IR spectra of modified BT particles (a), 4-CF3BPA, (b) PFBPA (c) 3,4,5-F3BPA and (d) 2,6-bisCF3BPA. in the P-O stretching region. All spectra were obtained from KBr pellets.

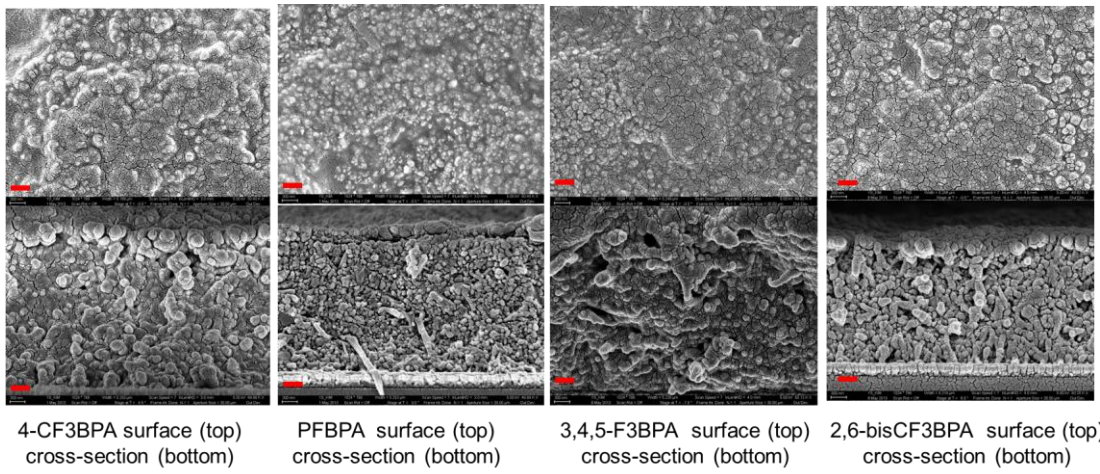

Figure 5.27. SEM top surface and freeze-fractured cross section images of the nanocomposite thin films formed with BT functionalized with the various surface modifiers. All scale bars are 300 μm. [SEM images obtained by Yunsang Kim; Perry Group]

5.4.2 Dielectric characterization of nanocomposites

The effective permittivity of the nanocomposites were evaluated as a function of frequency up to 1 MHz and the results are presented in Figure 5.28. The results show clear variation in effective permittivity among the nanocomposites prepared using different surface modifiers; the films containing PFBPA and 2,6-bis-CF3BPA surface modified particles had a higher dielectric constant than the other two films. The observed differences in effective dielectric constant between the films is presumably due to changes in the polarizability characteristics of the interface region which will affect the overall permittivity of the films.

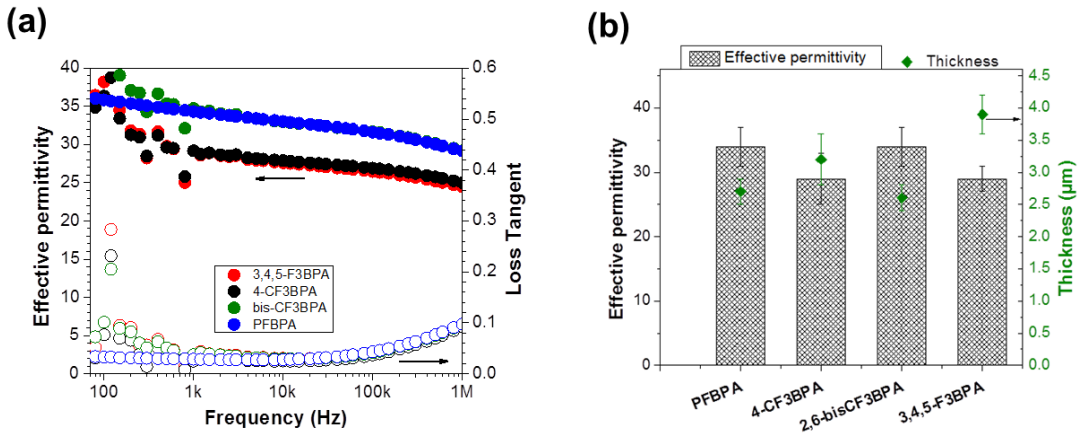

Figure 5.28. Dielectric spectroscopy of the thin from 20 Hz to 1MHz (a) and measured permittivity of nanocomposite films at 1kHz with the corresponding film thicknesses (b).

The loss experienced in the films is ~ 0.1 at 1 MHz which significantly lower than that of the neat polymer (~0.2) at the same frequency. It is also worth mentioning that below 1

kHz there is substantial variation in the permittivity and loss values which might be indicative of some amount of ionic conduction in the host matrix.

Weibull statistics was used to analyze the breakdown behavior of the nanocomposites in a manner similar to that shown in the previous two sections. Stark differences were observed in the dielectric strength of the films as is shown in Figure 5.29; breakdown field ranging from 137 to 330 V/μm were attained.

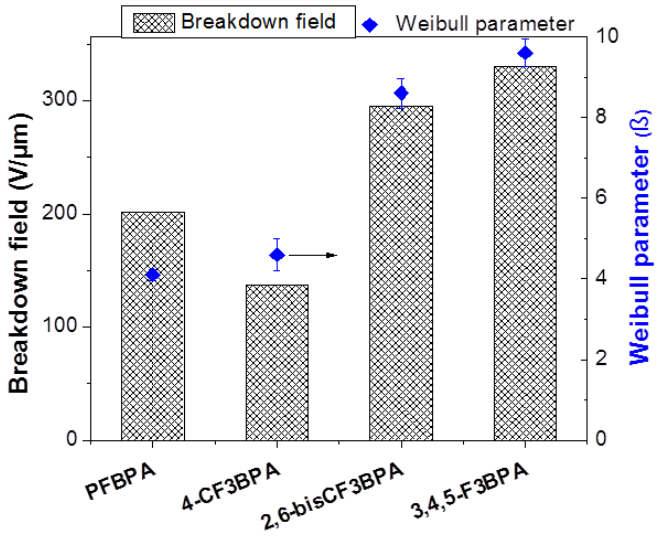

Figure 5.29. Breakdown strength and Weibull parameter of nanocomposite thin films prepared using BT120 functionalized with the various surface modifiers

The results indicate that the films prepared from particles modified with 3,4,5-F3BPA and bis-CF3BPA ligands significantly outperforms the other two composites giving field strengths of 330 and 295 V/μm, respectively. The Weibull parameter values for the nanocomposites ranged from 4.1 to 9.6 with the films that were found to have superior dielectric strength having values of 8.6 (bis-CF3BPA) and 9.6 (3,4,5-F3BPA). The results

serve to further substantiate the notion of manipulating the dielectric performance of nanocomposite via controlling the properties of the interphase region through suitable modifiers.

5.4.3 Energy densities of nanocomposite thin film

The recoverable energy density and extraction efficiency under a polarizing electric field was examined for the nanocomposite films by integrating the area between the charging and discharging unipolar curves) and the ordinate as was done in the previous chapter (Figure 5.30).

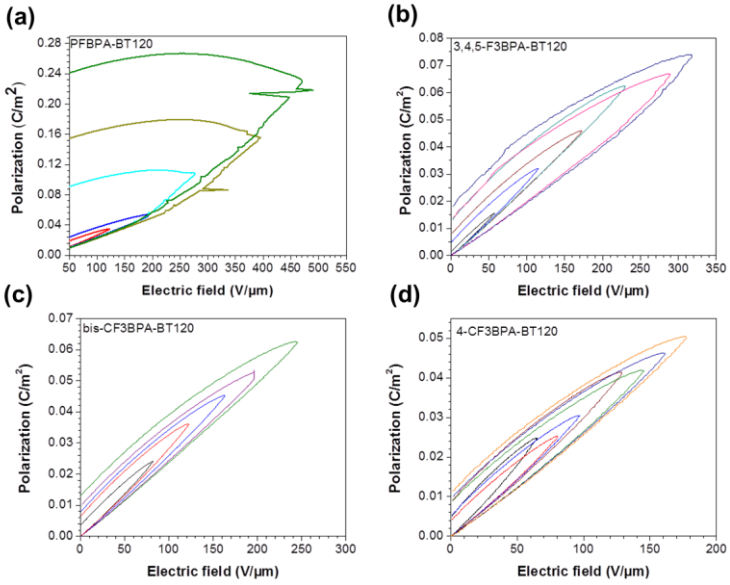

Figure 5.30.Unipolar P-E responses for nanocomposite thin films. Each unipolar P-E curve was obtained on a single device at different maximum field until catastrophic failure.

Figure 5.31 shows the energy density and extraction efficiency after integration. Here too, it is observed that the used of different surface modifiers to functionalize the BT can significantly affect both the extractable energy density and efficiency. The recoverable energy density ranged from 2.7 to 6.6 J/cm^3 across the modifiers with the 3,4,5-F3BPA and bis-CF3BPA ligands significantly outperforming the others. The nanocomposites prepared using the 3,4,5-F3BPA-modified BT particles was able to sustain fields up to 318 V/µm which is relatively close to the 330 V/µm determined from the breakdown measurements. However, it is important to note that the extraction efficiency at this field is ~50%. Similarly, films prepared using the bis-CF3BPA-modified BT particles were able to sustain fields up to 246 V/µm with an extraction efficiency of 63%.

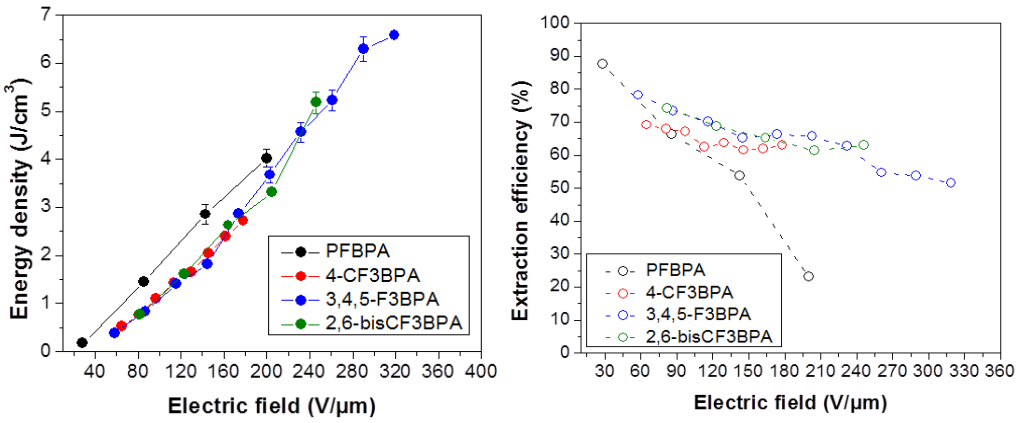

Figure 5.31.Calculated recoverable energy densities (left) and extraction efficiency (right) based on P-E analysis.

It is clear that both the recoverable energy density and the extraction efficiency can be tailored by the use of surface modifiers. The extractable energy density was also examined under pulsed conditions and the results are shown in Figure 5.32.

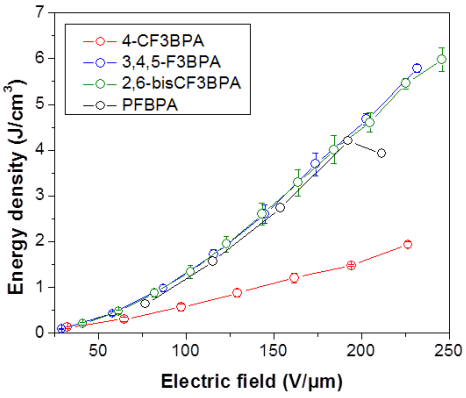

Figure 5.32. Calculated recoverable energy densities (left) and extraction efficiency (right) based on C-D analysis.

Here too it is seen that the extractable energy density ranges from 1.9 to 5.9 J/cm^3 for the devices tested, which is fairly similar with the values obtained by P-E measurement. Interestingly, the same two modifiers (i.e. 3,4,5-F3BPA and bis-CF3BPA) were found to perform the best among the lot.

5.4.4 A Closer look at the molecular surface modifiers

In an effort to begin to explain the dielectric behavior of the nanocomposite films the potential effect of the surface modifiers on the BT nanoparticle was explored. It was hypothesized that the observed differences in performance was due to changes in the work function of the BT and consequently the energy barrier at the polymer-particle interface. Calculated dipole moments of the molecules used in this study and their corresponding measured work function change on an ITO surface is presented in Table 5.5.

Table 5.5 Calculated dipole moment and work function change for the various surface modifiers on ITO.

	Dipole Moment [Debye]*	Work Function Change [eV]**
4-CF3BPA	-2.17	1.01
3,4,5-F3BPA	-2.22	0.66
PFBPA	-1.49	0.61
2,6-bisCF3BPA	0.52	0.10

The dipole moments were determined from a surface bound optimized geometry and the reported changes in work function (WF) are relative to detergent solvent clean ITO (4.61 eV). [Calculations and measurements were done by Anthony Giordano (Marder Group)]

From the results portrayed Table 5.5 it is evident that the surface modifiers can have different effects on the frontier energy levels of the metal oxide (ITO) and the trend in WF changes tracks relatively well with the dipole moments of the molecule. It is presumed that similar trends will be observed when these molecules are bound to BT. Previous work done within the group by Hotchkiss *et al.*[54] found that the surface energy for these fluoroaryl molecules were within the range of 35 to 38 mJ/m^2 as determined from contact angle measurements. This suggests that the interaction between the molecule, and by extension the BT particle, is relatively the same. As such the difference in the dielectric performance between the composites may be a result of differences in injection barriers and frontier orbital levels at the BT/polymer interface. Unfortunately, the trend observed in the dielectric data does not support this conclusions as the two molecules that perform the best have dipoles moments pointing in opposite directions

(i.e. towards and away from the surface). This suggest that other factors are at play which were not considered, so further systematic studies must be done to decipher the underlying factors that contribute to the observed differences.

5.5 Experimental section

5.5.1 Neat polymer and nanocomposite thin film processing:

In the **M1** processing method, 1.5-2 mL of a 10 wt % terpolymer solution in ambient atmosphere equilibrated N,N-dimethylformamide (DMF) was filtered, cast onto a glass slide and then dried at 72 °C in a vacuum oven for 2 h. The film was then cooled to room temperature before its removal from the glass substrate by "lift-off" in distilled water and placed in a vacuum oven at 50 °C. After 2 h the films are subjected to further annealing at 65 °C, 14 °C below its melting temperature, for 5 h prior to electrode deposition. In the second method (**M2**), the terpolymer was dissolved in dry DMF and stirred at room temperature for at least 8 h. Thin films were then prepared from the polymer solution by spin-coating ~1.5 mL onto oxygen plasma (Plasma Etch, 2 min.) treated aluminum bottom electrode coatings on glass substrates. The spin-coated films were then soft baked at 80 °C for ~ 10 min then treated overnight under vacuum at 120 °C. In order to evaluate the dielectric properties of the polymer, parallel plate capacitors were fabricated by depositing aluminum top electrodes on the spun film. The PFBPA-modified BT nanoparticles were dispersed in the polymer matrix in order to form the nanocomposite thin films. The polymer and modified nanoparticles were both added to dry N,N-dimethylformamide in a 30 mL high density polyethylene (HDPE) vial and ball milled for 14 days in the presence of grinding media (yittria-stabilized zirconia; Inframat

Advanced Materials, LLC., Farmington, CT). The grinding media used were of three different sizes; 0.5 mm diameter, 5 mm diameter and 10 mm diameter. Pre-calculated masses of the polymer, depending on the desired volume loading of barium titante, were measured and placed in 10 mL glass vials. The corresponding amounts of barium titanate were measured and placed into previously cleaned HDPE bottles and the bottles appropriately labeled according to particle volume loading. The three different sizes of grinding media were added to each bottle in the following amounts:

0.5 mm beads 26 g
5 mm beads 5 g
10 mm beads 6 g

DMF (8-9 mL) was added to each bottles and the container closed and sealed with parafilm. The bottles were placed on the ball mill for two days after which the pre-weighed polymer were added to their respective vials and the bottles returned to the ball mill for an additional 12 days. Films were subsequently prepared from the resulting suspensions by spin-coating the mixture onto oxygen plasma treated (Plasma Etch; 2 min) aluminum-coated glass substrates which served as the bottom electrode. The films were soft baked at 80 °C for ~ 10 min then dried overnight under vacuum at 120 °C.

5.5.2 Thin film characterization:

The morphology of the films was characterized by both scanning electron (Zeiss Ultra 60) and atomic force microscopies (Agilent N9524B). Further characterization of the films was performed using Fourier transform infrared (FT-IR, Perkin-Elmer Spectrum 1000) spectra and X-ray diffraction (XRD, PANalytical, X'Pert PRO Alpha-1). Profilometry (Dektac 6M, Veeco) was used to determine the thickness of the films.

5.5.3 Device fabrication and characterization:

Parallel plate capacitors of the thin films were fabricated in order to evaluate their dielectric properties. For films prepared via the first method (**M1**), a 25 nm thick gold electrode was sputtered onto both sides of the terpolymer films (Denton Vacuum Desk IV sputter coater) and their dielectric properties characterized on a HP LCR meter (HP 4284A). In the case of the films prepared using method 2 (**M2**), circular aluminum top electrodes (0.25 mm^2 and 1.0 mm^2) were deposited on the spin-coated films through a shadow mask by using a thermal evaporator (Kurt J. Lesker PVD75, rate = 3 Å s^{-1}). Automated dielectric characterization of the devices was performed using a Lab VIEW software interface. Samples with electrode area of 0.25 mm^2 were used to perform dielectric strength measurements through the use of a Keithley 248 power supply by ramping the applied voltage from 50 V_{DC} at a rate of 10 Vs^{-1} until catastrophic failure, as evidenced by a spiking of the current, of the device under test. An Agilent 4284 LCR meter was used to measure the frequency-dependent effective permittivity and dissipation factor over the range of 20 Hz to 1 MHz. Unipolar P-E measurements were conducted using a high voltage amplifier (Trek 610-D) in conjunction with a charge integrator circuit under unipolar sawtooth waveforms with a period of 0.01 s. The energy storage capacity of the thin films was measured at multiple electric field strengths using a C-D circuit and making use of an electrode area of 1 mm^2.

5.6 Conclusion

In summary, we have demonstrated a simple, improved processing method that yields p(VDF-TrFE-CTFE) films, with an improved fibrillar morphology dominated by α-phase, that leads to an enhanced dielectric constant of 77 ± 10 at 1kHz. Under P-E analysis, the terpolymer films show a sizeable high-energy density (9.7 J/cm^3) and moderate charge extraction efficiency at high fields (< 470 V/μm). Significantly, under pulsed conditions an almost three-fold enhancement in the maximum energy density (27 J/cm^3) was realized at a maximum electric field of > 600 V/μm. Taken together, these results demonstrate the importance of the processing conditions and morphology of this class of polymers for high electrical energy storage and pulsed-power applications.

We have also demonstrated the use of phosphonic acid-modified barium titanate nanoparticles and a terpolymer [P(VDF-TrFE-CTFE)] to prepare homogeneous nanocomposite thin films with diminished dielectric contrast and high energy density. While the reduced dielectric contrast between the particle and polymer had a small impact on the effective permittivity of the nanocomposite there was an incremental reduction in the loss tangent as a function of particle loading. In addition, moderate Weibull parameters were obtained (7 at 40% and 50%) and high breakdown field of 319 V/μm at 40% BT. The improvements are believed to be a result of having a more homogeneously distributed local electric fields as well as the effective optimization of the BT particle loading. A maximum energy density of 8.9 J/cm^3 was obtained under P-E analysis for the 20% film. The P-E data showed that while higher the nanocomposites generally exhibit greater polarizability and, as a consequence, energy density compared to the polymer, the efficiency with which the charges can be recovered is compromised

with filler loading. Under pulsed conditions where the discharge time is on the order of 5-20 ms, the neat polymer outperforms at field greater than ~200 V/μm. These studies suggest that the polymer matrix and filler particles must be carefully chosen in order to achieve high energy densities and breakdown criteria for specific applications.

Our preliminary examination of the effect of various fluororaryl, dipolar surface modifiers on the dielectric properties of nanocomposite thin films shows that the effect can be very significant. Although we do not fully understand the mechanisms behind the observed changes the results substantiate the importance of trying to the role that the structure of the modifiers play in tailoring the dielectric properties of the thin films. Polarization-electric field measurements showed that the choice of modifier also had a marked impact on the achievable energy density, giving values that ranged from 2.7 – 6.6 J/cm^3. Weibull analysis of the breakdown statistics of nanocomposite thin films gave breakdown fields ranging from 137 - 330 V/μm and modulus parameter (beta values) spanning from 4.1 - 9.6.

5.7 Literature Cited

[1] Y. Cao, P. C. Irwin, K. Younsi, *IEEE. T. Dielect. El. Insul.* **2004**, *11*, 797.

[2] Q. Wang, L. Zhu, *J. Polm. Sci. Pol. Phys.* **2011**, *49*, 1421.

[3] H. S. Nalwa, *Handbook of Low and High Dielectric Constant Materials and Their Applications*, Academic Press, New York, **1999**.

[4] P. Barber, S. Balasubramanian, Y. Anguchamy, S. Gong, A. Wibowo, H. Gao, H. J. Ploehn, H. C. zur Loye, *Materials* **2009**, *2*, 1697.

[5] W. J. Sarjeant, J. Zirnheld, F. W. MacDougall, *IEEE. T. Plasma Sci.* **1998**, *26*, 1368.

[6] W. J. Sarjeant, I. W. Clelland, R. A. Price, *Proc. IEEE.* **2001**, *89*, 846.

[7] H. W. Starkweather, P. Avakian, R. R. Matheson, J. J. Fontanella, M. C. Wintersgill, *Macromolecules* **1992**, *25*, 6871.

[8] K. Yao, S. Chen, M. Rahimabady, M. S. Mirshekarloo, S. Yu, F. E. H. Tay, T. Sritharan, L. Lu, *IEEE. T. Ultrason. Ferro.* **2011**, *58*, 1968.

[9] B. Chu, X. Zhou, K. Ren, B. Neese, M. Lin, Q. Wang, F. Bauer, Q. M. Zhang, *Science* **2006**, *313*, 334.

[10] J. Ho, R. Ramprasad, S. Boggs, *IEEE. T. Dielect. El. Insul.* **2007**, *14*, 1295.

[11] M. Rabuffi, G. Picci, *IEEE. T. Plasma Sci.* **2002**, *30*, 1939.

[12] L. Zhu, Q. Wang, *Macromolecules* **2012**, *45*, 2937.

[13] A. J. Lovinger, *Science* **1983**, *220*, 1115.

[14] A. J. Lovinger, D. D. Davis, R. E. Cais, J. M. Kometani, *Polymer* **1987**, *28*, 617.

[15] F. Xia, Z. Y. Cheng, H. S. Xu, H. F. Li, Q. M. Zhang, G. J. Kavarnos, R. Y. Ting, G. Abdul-Sedat, K. D. Belfield, *Adv. Mater.* **2002**, *14*, 1574.

[16] H. S. Xu, Z. Y. Cheng, D. Olson, T. Mai, Q. M. Zhang, G. Kavarnos, *Appl. Phys. Lett.* **2001**, *78*, 2360.

[17] Y. Y. Lu, J. Claude, B. Neese, Q. M. Zhang, Q. Wang, *J. Am. Chem. Soc.* **2006**, *128*, 8120.

[18] T. C. Chung, A. Petchsuk, *Macromolecules* **2002**, *35*, 7678.

[19] R. Gregorio, E. M. Ueno, *J. Mater. Sci.* **1999**, *34*, 4489.

[20] V. Sencadas, R. Gregorio, S. Lanceros-Mendez, *J. Macromol. Sci. B* **2009**, *48*, 514.

[21] M. C. Branciforti, V. Sencadas, S. Lanceros-Mendez, R. Gregorio, *J. Polm. Sci. Pol. Phys.* **2007**, *45*, 2793.

[22] V. Sencadas, R. Gregorio, S. Lanceros-Mendez, *J. Non-Cryst. Solids* **2006**, *352*, 2226.

[23] H. M. Bao, J. F. Song, J. Zhang, Q. D. Shen, C. Z. Yang, Q. M. Zhang, *Macromolecules* **2007**, *40*, 2371.

[24] Y. Lu, J. Claude, Q. Zhang, Q. Wang, *Macromolecules* **2006**, *39*, 6962.

[25] R. Hasegawa, Takahash.Y, H. Tadokoro, Y. Chatani, *Polym. J. (Tokyo, Jpn.)* **1972**, *3*, 600.

[26] K. Tashiro, K. Takano, M. Kobayashi, Y. Chatani, H. Tadokoro, *Polymer* **1984**, *25*, 195.

[27] D. A. Skoog, F. J. Holler, S. R. Crouch, *Principles of instrumental analysis*, 6th ed. ed., Thomas higher education, California, **2007**.

[28] Z. Y. Cheng, D. Olson, H. S. Xu, F. Xia, J. S. Hundal, Q. M. Zhang, F. B. Bateman, G. J. Kavarnos, T. Ramotowski, *Macromolecules* **2002**, *35*, 664.

[29] W. Weibull, *J. Appl. Mech-T. Asme.* **1951**, *18*, 293.

[30] L. A. Dissado, J. C. Fothergill, S. V. Wolfe, R. M. Hill, *IEEE Trans. Electr. Insul.* **1984**, *19*, 227.

[31] F. Xia, Q. M. Zhang, *Appl. Phys. Lett.* **2004**, *85*, 1719.

[32] K. C. Gao, *Dielectric Phenomena in Solids*, Elsevier Academic Press, San Diego, **2004**.

[33] Z. Zhao, V. Buscaglia, M. Viviani, M. T. Buscaglia, L. Mitoseriu, A. Testino, M. Nygren, M. Johnsson, P. Nanni, *Physical Review B* **2004**, *70*.

[34] K. Suzuki, K. Kijima, *J. Alloys Compd.* **2006**, *419*, 234.

[35] S. W. Lu, B. I. Lee, Z. L. Wang, W. D. Samuels, *J. Cryst. Growth* **2000**, *219*, 269.

[36] M. B. Smith, K. Page, T. Siegrist, P. L. Redmond, E. C. Walter, R. Seshadri, L. E. Brus, M. L. Steigerwald, *J. Am. Chem. Soc.* **2008**, *130*, 6955.

[37] Didomeni.M, S. H. Wemple, S. P. S. Porto, *Phys. Rev.* **1968**, *174*, 522.

[38] P. Kim, S. C. Jones, P. J. Hotchkiss, J. N. Haddock, B. Kippelen, S. R. Marder, J. W. Perry, *Adv. Mater.* **2007**, *19*, 1001.

[39] M. D. B. Lopez, G. Fourlaris, B. Rand, F. L. Riley, *J. Am. Ceram. Soc.* **1999**, *82*, 1777.

[40] S. A. Paniagua, P. J. Hotchkiss, S. C. Jones, S. R. Marder, A. Mudalige, F. S. Marrikar, J. E. Pemberton, N. R. Armstrong, *J. Phys. Chem. C.* **2008**, *112*, 7809.

[41] P. J. Hotchkiss, S. C. Jones, S. A. Paniagua, A. Sharma, B. Kippelen, N. R. Armstrong, S. R. Marder, *Acc. Chem. Res.* **2012**, *45*, 337.

[42] W. Gao, L. Dickinson, C. Grozinger, F. G. Morin, L. Reven, *Langmuir* **1996**, *12*, 6429.

[43] J. J. Li, S. I. Seok, B. J. Chu, F. Dogan, Q. M. Zhang, Q. Wang, *Adv. Mater.* **2009**, *21*, 217.

[44] X. J. He, K. Yao, B. K. Gan, *J. Appl. Phys.* **2005**, *97*.

[45] J. P. Calame, *J. Appl. Phys.* **2006**, *99*.

[46] E. Tuncer, I. Sauers, D. Randy James, A. R. Ellis, M. Parans Paranthaman, A. Goyal, K. L. More, *Nanotechnology* **2007**, *18*.

[47] M. K. Kilaru, J. Heikenfeld, G. Lin, J. E. Mark, *Appl. Phys. Lett.* **2007**, *90*.

[48] P. Kim, N. M. Doss, J. P. Tillotson, P. J. Hotchkiss, M.-J. Pan, S. R. Marder, J. Li, J. P. Calame, J. W. Perry, *ACS Nano* **2009**, *3*, 2581.

[49] J. F. Wager, P. D. Keir, *Annu. Rev. Mater. Sci.* **1997**, *27*, 223.

[50] J. P. Calame, *J. Appl. Phys.* **2011**, *110*.

[51] R. C. Smith, C. Liang, M. Landry, J. K. Nelson, L. S. Schadler, *IEEE. T. Dielect. El. Insul.* **2008**, *15*, 187.

[52] H. T. Vo, F. G. Shi, *Microelectron. J.* **2002**, *33*, 409.

[53] S. Ramesh, B. A. Shutzberg, C. Huang, J. Gao, E. P. Giannelis, *IEEE. T. Adv. Pack.* **2003**, *26*, 17.

[54] P. J. Hotchkiss, H. Li, P. B. Paramonov, S. A. Paniagua, S. C. Jones, N. R. Armstrong, J.-L. Bredas, S. R. Marder, *Adv. Mater. (Weinheim, Ger.)* **2009**, *21*, 4496.

CHAPTER 6 SUMMARY AND OUTLOOK

The field of organic electronics has garnered a lot of scientific interest over the past decade due to the potential of making relatively low-cost, light-weight, flexible devices using simplified processing techniques. Performance in these devices depends critically on the properties of the active layers, electrodes, and the interfaces between them. The body of work presented in this thesis focuses on the metal oxide-organic interfaces often encountered in organic electronics and capacitors based on nanocomposite dielectrics and illustrates the use of small-molecule surface modifiers to probe (chapters 2 and 3) and control (chapters 4 and 5) the properties of said interfaces. While the information was presented with the relatively narrow scope of those chapters, the knowledge gleaned herein can be applied to a wider range of technologies such as organic light-emitting diodes, and organic field-effect transistors.

Redox monolayers provide a convenient platform on which to test the kinetics of charge-transfer at the organic-inorganic interface. Chapters 2 and 3 utilized this approach to examine the kinetics between several ferrocene-based modifiers and ITO. In the second chapter the experimental results obtained from solution-phase studies revealed that the chemistry taking place at the electrode surface can be complicated by adsorption processes depending on the propensity of the molecule to bind to the surface. Furthermore, the technique of CV, which is commonly used in experiments of this type, is limited in its ability to distinguish between a free diffusional and a surface-confined

species and so surface-adsorption effects can be overlooked if appropriate scan-rate-dependent experiments are not performed or CSWV experiments are not used to distinguish between free and surface-bound species. In the third chapter the molecules are tethered to the surface of the ITO via their various anchoring groups and the charge-transfer kinetics investigated by CV. The experimental results show that the choice of anchoring group has minimal impact on the rate constant of charge-transfer (i.e. the molecules experience a similar barrier to charge-transfer). That said, it would be of interest to extend these studies to correlate the structure-property relationship of the tail group to electrochemically determined rate constant. Here, redox-terminated modifiers could be designed that incorporate commonly used tail groups as the linker moiety. These molecules would have a Fc-R-PO_3 structure, for example, where R can be alkyl or aryl groups. This would allow for the direct assessment of the role that commonly used tail groups play in mediating charge-transfer. Such studies provide a direct path to assess the impact of factors including, but not limited to, the choice of substituent, dipole moment, and distance from a redox group from the oxide surface play in the kinetics of charge-transfer. The results obtained from these studies may give insight into the rational design of surface modifiers to control electron-transfer rates while simultaneously achieving other functions including work-function modification and effective wetting of the oxide surface by organic films.

One issue encountered in the electrochemical studies that were conducted using pre-modified electrodes is the lateral interactions between the ferrocene centers which could preclude the accurate determination of charge injection rates across the organic-inorganic interface. This problem can be mitigated by using alkyl diluents to minimized

communication between ferrocene moieties. Ideally, in the case of independently anchored redox sites the full width at half maximum (FWHM) is 90.6/n (mV) at room temperature. Deviations from this value can be used as a measure of interactions between sites and/or site heterogeneity. Experiments can be designed that look at the kinetics of charge-transfer as a function of the degree of dilution of the ferrocene modifier on the surface of the metal oxide.

Organic electronic devices, much like any other types of electronic platforms, experience power loses through dissipation due to internal resistance. This resistance is comprised of two main components (i) a shunt resistance (R_p) due to pinholes and secondary detrimental processes such as charge recombination and (ii) a series resistance (R_s) which is related to the combined resistance to charge mobility in the active layers, the innate electrode resistance, and the contact resistance at the interface between adjacent layers.[1] The inherent internal resistance of metal oxides, such as ITO, limits the rate of propagation of the charge transferred to it away from the interface resulting in additional losses in energy. As such, there are several ongoing efforts to develop new metal oxides that offer lower internal and contact resistances, relative to ITO. Toward this end, the electrochemical techniques discussed in this study will be useful in screening and characterizing new metal oxides for various organic electronic devices. Heterogeneity in the surface composition of the electrode, for example, has been reported to affect the recombination of charges at the TCO-organic interface in OPVs.[2, 3] The redox surface modifiers reported in this work can be used to examine electron-transfer rates for electrodes having varying surface compositions. This will allow us to determine

what compositional factors have to be controlled to achieve good charge collection/injection.

The density of state (DOS) of the conduction band varies among TCOs depending of their primary orbital structure. The extent of coupling between the redox-active part of the modifier and the states of the electrode may vary among different metal oxide electrodes. It would therefore be of interest to examine the kinetics of charge-transfer among between a redox surface modifier and various TCOs. This would provide insight into the role that the electronic structure of the metal oxide plays in modulating charge-transfer kinetics. In literature, the DOS of metal oxides is usually evaluated by examining the effective mass of the conducting electrons within the band. Larger effective mass signifies a greater DOS near the conduction band edge. Table 6.1 below lists the properties of several TCOs for which the DOS have been previously assessed based on the effective mass. It demonstrates that conduction bands made primarily of d orbitals have a greater DOS than those made of s and p orbitals. This study will allow us to evaluate the dependence of the rate of charge injection on the DOS of the electrode. In addition, one can assess whether or not the anchoring group exhibit preferential coupling to specific orbitals/electrodes. It is important to point out that it is the band structure close to the surface that is important and this may differ from that of the bulk and, moreover, may be changed to varying extent depending on the binding of different modifying groups. The conduction band edge position for TiO_2 and ZnO, for example, has been shown via electrochemistry to be very similar[4] but the structural make-up of their bands is very different.

Table 6.1. Primary conduction band orbitals, optical band gap and DOS of various TCOs.[5-7]

TCO Material	Primary CB Orbitals	DOS (effective electron mass [m_e])
TiO_2	3d Orbitals of Ti^{4+}	5-10 m_e
ZnO	s, p orbitals of Zn^{2+}	0.3 m_e
ITO	5s and 5p of In	0.3 m_e
Nb_2O_5	d orbitals of Nb^{5+}	3.0 m_e
SnO_2	s, p orbitals of Sn^{4+}	0.3 m_e

Based on the DOS alone it is expected that there will be a greater rate of charge injection into/from the TiO_2 electrode. These TCOs can serve to elucidate the role that electronic structure/orbital identity plays in electron transfer. The use of Nb_2O_5 may be help to further explore the influence the role of conduction band structure on charge injection. SnO_2 conduction band orbital make-up and DOS are similar to that of ZnO but the band edge energies are different. A comparison between the two will allow for the investigation of the influence of energy level alignment on the kinetics of charge transfer.

Complementary information to that obtained from electrochemical data can be garnered from photo-induced charge-transfer dynamics by employing transient spectroscopy techniques to probe the metal-oxide organic interface. Here, photoactive surface modifiers can be tethered to the metal oxide electrode surface and examined surface using pump-probe techniques. This approach can prove to be very useful in deconvoluting the role that parameters such as molecular orientation and structure plays in mediating the kinetics of charge transfer. Additionally, careful analysis of the

transients can provide insight into the kinds of species generated during the photo-excitation process, their lifetimes, and the kinetics associated with the charge recombination at the hybrid interface.

In chapter 4 the binding of a phosphonic and carboxylic acid on the surface of IZO was examined. The results show that the molecules are bound to the surface in a bidentate and monodentate manner, respectively. As explained in the introductory chapter, understanding the binding configuration of these molecules on the surface provides insight into the molecular orientation on the surface, which can be directly correlated to changes in work function. The next rational step in this particular project is to determine the orientation of these molecules on the surface of IZO. Further, it is of interest to examine other functional groups such as sulfonic acids, hydroxamic acids and thiols; our collaborators in the Pemberton Group at the University of Arizona are currently conducting these studies on IZO electrodes. The distribution of binding modes of these molecules on the surface of metal oxides as well as their molecular packing (i.e. whether the molecules form homogeneous monolayers, or islands on the surface) will have a direct effect on molecular orientation and the net surface dipole and consequently, the ability to tune work function. It is therefore important to understand how the modifiers are tethered to and distributed on the metal oxide surface.

IZO is presented in this thesis as an alternative to ITO; however, several other TCOs are currently being explored for organic electronic applications including zinc oxide (ZnO), molybdenum oxide (MoO_3) gallium-doped zinc oxide (GZO). Understanding the chemical and physical nature of these complex metal oxide surfaces is key to their integration into the various device platforms. This requires developing

accurate theoretical and chemical models to describe the surface composition and structure of the metal oxides. Specifically, the nature of the surface termination, the chemical nature of defect sites, the binding and coverage of various surface modifiers and the kinetics of charge transfer across these electrodes, and the trends in energy level alignment have to all be reconciled in order to develop the appropriate chemical description of the surface. The combined results from these studies will hopefully provide experimental guidelines for designing molecules with the appropriate binding group for modification of specific metal oxides.

In organic electronic devices there is always competition between charge extraction and recombination. As such, many of these platforms now integrate interlayers into their device architecture that are capable of selectively allowing the passage of one type of charge. From both a synthetic and practical point of view it would be interesting to design donor-acceptor type monolayers that are capable of serving as charge-selective layers (i.e. buffer layers). In addition to regulating the passage of charge across the hybrid interface, these molecules would simultaneously serve to adjust the work function of the metal oxide electrode, and regulate the physical interaction between the electrode and the active layer.

While the evolution of the chemical composition at the interface as a function of various modification conditions (namely time and temperature) was explored, the evolution of band structure at the interface as a function of the same parameters was not investigated. There still remains a need to understand how the interfacial energy levels evolve and what the contributors to the observed changes are. With all these newly explored metal oxides, fundamental studies will need to be done that explore binding

modes and orientation, surface pretreatment, surface modification conditions and their impact on work function tuning. This will further contribute to the building of a molecular picture for the adsorption of various surface modifiers on metal oxide surfaces.

The processing of dielectric nanocomposites through control of the polymer morphology and nanoparticle surface energy was explored in chapter 5. Using simple spin coating techniques and thermal treatment, a permittivity of 77 was achieved in a poly(vinylidene fluoride-trifluoroethylene-chlorotrifluoroethylene) polymer matrix. An energy density of 27 J/cm^3 and field strength 604 V/μm was also observed. Nanocomposites prepared using this polymer system and PFBPA-functionalized barium titanate nanoparticles afforded breakdown fields above 300 V/μm at particle loadings as high as 40 % v/v. A maximum permittivity and energy density of 83 and 9 J/cm^3 was observed in the nanocomposite thin films.

Some of the most interesting results of this chapter came from the study that investigated the impact for dipolar fluoroaryl modifiers on the dielectric performance of nanocomposite thin films. The results of this study show that by simply changing the ligand used to modify the interface we can tune the energy density from 2.7 – 6.6 J/cm^3. The observed breakdown field strength spanned the range 137 – 330 V/μm. Based on these studies it is of interest to understand how the properties of the interface between the particle and polymer depend on the structure of the ligand. Integral to the development of nanocomposites is the design of ligands that can give rise to high dielectric constants and low leakage currents; therefore, gaining insight into how the ligand structure and length affect carrier generation from the surface of BT is important. Here, understanding the role of factors such as conjugation, linker length, the role of fluorocarbons moieties compared

to their hydrocarbon counterparts, and the spacing that optimizes the tradeoff between $BaTiO_3$ particle content and minimizing electron tunneling between particles need to be considered. Specifics, such as the understanding the mechanism of charge transport in these ligands as well as the impact of temperature and voltage on the various modes, are of interest. A comprehensive understanding of these properties becomes very important when nanometer size ceramic particles are used in composites since at these length scales the filler particles present a high surface area per unit volume, which can have a profound impact on the macroscopic dielectric properties.

The data presented in chapter 5 suggest a significant effect of the modifiers on the measured work function values. For example, compared to ITO, which has a work function of 4.6 eV, 4-CF3BPA- and 2,6-bis-CF3BPA-modified ITO exhibit a change in work fuction of 1.0 and 0.1 eV, respectively. A more detailed structure-property study in this regard on the relationship between the change in work function and leakage current, dielectric strength, and P-E measurements would enable us to develop nanocomposites having large extractable energy density and efficiency via enhanced dielectric strength.

Another rational step would be to examine how the structure at the polymer-particle interface changes with particle size and choice of surface modifier. Such studies would allow us to tailor the interface between the particle and polymer in a manner that promoted proper wetting between the organic and inorganic phase and simultaneously improves the breakdown behavior of the thin films. The use of modeling and systematic design and synthesis of polymers will greatly help in understanding the interfacial interactions of interest. In addition, it was concluded in chapter 5 that the nanoparticles were acting as trap sites for mobile charges in the matrix. Understanding how trapping in

nanocomposite films can be tailored through systematic surface modification of the particles can prove useful for the development of capacitor technology. Different polymer host system and particles should also be explored.

Overall this body of work seeks to expand the knowledgebase of the scientific community on the use of surface modifiers to control and probe interfaces. It is the hope of the author that the information contained within this document will serve a platform from which future scientific studies can be launched.

6.1 Literature Cited

[[1] S. Choi, W. J. Potscavage, Jr., B. Kippelen, *J. Appl. Phys.* **2009**, *106*.

[2] N. R. Armstrong, C. Carter, C. Donley, A. Simmonds, P. Lee, M. Brumbach, B. Kippelen, B. Domercq, S. Y. Yoo, *Thin Solid Films* **2003**, *445*, 342.

[3] E. L. Ratcliff, A. K. Sigdel, M. R. Macech, K. Nebesny, P. A. Lee, D. S. Ginley, N. R. Armstrong, J. J. Berry, *Thin Solid Films* **2012**, *520*, 5652.

[4] J. B. Asbury, E. Hao, Y. Q. Wang, H. N. Ghosh, T. Q. Lian, *J. Phys. Chem. B* **2001**, *105*, 4545.

[5] V. Thavasi, V. Renugopalakrishnan, R. Jose, S. Ramakrishna, *Mat. Sci. Eng.R.* **2009**, *63*, 81.

[6] M. Mizuno, T. Miyamoto, T. Ohnishi, H. Hayashi, *JPN J Appl. Phys. 1* **1997**, *36*, 3408.

[7] I. Hamberg, C. G. Granqvist, K. F. Berggren, B. E. Sernelius, L. Engstrom, *Phys. Rev. B* **1984**, *30*, 3240.

APPENDIX A **Pyrenylpropyl Phosphonic Acid Surface Modifier for Mitigating the Thermal Resistance of Carbon Nanotube Contacts**

A.1 Introduction

Forests comprised of nominally vertically aligned carbon nanotubes (CNTs), having outstanding thermal and mechanical properties, are excellent candidates for thermal interface materials (TIMs).[1-12] However, despite nearly a decade of research TIMs based on vertically aligned CNT (VACNT) forests have yet to harness effectively the high thermal conductivity of individual CNTs. One of the key obstacles that has limited the effectiveness of VACNT TIMs is the presence of high thermal contact resistances between the CNT free ends and the surfaces comprising the interface.[2-4, 13] Previous approaches to mitigate the contact resistance have focused on methods for bonding the free ends of the CNTs to the interface.[2, 5-10, 12] A few of the more successful bonding methods that have been developed are summarized in Table A.1. While, many of the methods have produced TIMs with thermal resistances that are comparable to conventional metallic solder TIMs (5 $mm^2 K W^{-1}$)[14], they are generally challenging to implement consistently, or require cumbersome processing. Specifically, Tong et al.[2] using indium to weld multiwall CNT (MWCNT) tips to glass noted that while thermal resistances on the order of 1 $mm^2 K W^{-1}$ were measured the thermal resistance across the entire area of the sample varied significantly, a result they attributed to inconsistent bonding at the interface. Later, Barako et al.[11] using In to bond 500 μm tall MWCNTs to glass was able to obtain thermal resistances as low as 28 $mm^2 K W^{-1}$.

TableA.1 Literature summary of thermal interface materials (TIMS)

Interface	CNT Forest Height [μm]	Measurement Pressure [kPa]	Thermal Resistance [mm^2 K W^{-1}]	Implementation Process
Bonded CNT Forests:				
Si-MWCNT-In-SiO_2[2]	10	0	~1	Metal Evaporation, Bonding (Pressure NA[a], 180 °C)
Si-MWCNT-Pd-Ag[8]	20	34	11	Drop Casting, Bonding (273 kPa, 250 °C)
Si-MWCNT-Au-Ag[7]	30	0	4.5 ± 0.5	Metal Evaporation, Bonding (Pressure NA[a], 220 °C)
Si-Au-Patterned MWCNT-Au-Si[6]	~60	63	4.4	Metal Evaporation, Bonding (63 kPa[b], 150 °C)
Si-MWCNT-Polymer-Ag[12]	10-115	7	5-44	Spray Coating, Bonding (138 kPa, RT[c])
Si-MWCNT-Al/Ni-SiO_2 [11]	500	200-500	15-50	Bonding (100 kPa)
Si-MWCNT-In-SiO_2[11]	500	100-600	28-71	Bonding (100 kPa, 180 °C)
Cu-MWCNT-Si[5]	NA	0	10	Spin Coating, Microwave Bonding (6.425 GHz, 750 kPa, 160 °C)
This Work:				
Si-MWCNT-Cu-Ag	15	7	4.6±0.5	Solution Bath, Bonding (300 kPa, RT[c])
Conventional Materials:				
Greases[30]			10	
Gels[30]			8	
Phase Change[30]			10	
Solder[14]			5	

[a] NA: Data not available [b] By patterning the MWCNT forest into pillars the apparent area of CNT contact was reduced to only 7% of a full coverage forest, which increased the pressure at the MWCNT tips by a factor of 14.
[c] RT: Room temperature

Several authors[6, 7, 9] have coated both MWCNT tips and the surface of the interface with films of Au and diffusion bonded the MWCNT tips under high temperature and pressure

to produce resistances as low as ~ 4 mm^2 K W^{-1}.However, unlike bonding with In or other solders Au does not melt and reflow during the bonding process and is instead restricted to diffusing between contacting surface asperities, limiting the contact area and making it difficult to achieve adequate bonding. As stated by Wasniewski et al.[9], Au diffusion bonding "results proved very difficult to replicate; challenges with achieving strong, uniform diffusion bonds precluded positive test results." Ni et al.[10] reported achieving thermal resistances as low as 1.4 mm^2 K W^{-1}, by modifying and bonding CNT films with the polymer HLK5. However, some important experimental details, including the CNT forest thickness, CNT chemical modification procedure, bonding procedure, and measurement uncertainty analysis were absent from this report, therefore it was not included in Table 1. The remaining approaches summarized in Table A.1 similarly produced either relatively high thermal resistances (over 5 mm^2 K W^{-1}), and/or required processing that could not be scaled in a practical manner. The method developed by Lin et al.[5] to chemically modify and anchor MWCNTs to Si substrates includes spin coating followed by a two-stage microwave bonding process lasting 1.5 hours with a peak temperature and pressure of 160 °C and 750 kPa respectively. As such, there is a significant need for a method of bonding CNT free ends that can repeatedly produce low thermal contact resistances uniformly over device areas, 1-4 cm^2, with minimally harsh and scalable processing. Here we show that a simple organic surface modifier, a pyrenylpropyl phosphonic acid, can be synthesized and applied in a straightforward approach to consistently reduce the thermal resistance of MWCNT contacts by approximately 9-fold.

The bifunctional interface modifier was designed such that it was terminated at one end with a pyrene moiety that is known to associate with CNT sidewalls through π-π stacking interactions.[15, 16] The opposite end of the molecule is terminated with a phosphonic acid functionality, which has been shown to form robust covalent bonds to native metal oxide surfaces [17-21] that are commonplace in electronic device architectures. The effectiveness of this approach was investigated by determining the thermal resistance of nominally vertically aligned MWCNT forests coupled to Cu oxide using the pyrenylpropyl phosphonic acid (PyprPA) modifier and comparing this value to that obtained for MWCNT forests in non-bonded dry contact with the oxidized surface of Cu films. In tests of multiple samples of each type, the non-bonded MWCNT forests were found to have thermal resistances of 20-60 mm^2 K W^{-1} whereas the forests coupled with the PyprPA modifier had thermal resistances of 4-5 mm^2 K W^{-1}, attributing the PyprPA modification and coupling process to a greater than 85% reduction in the thermal resistance as well as a substantial reduction in the sample-to-sample data scatter. Further experiments suggest that the PyprPA modifier might also be utilized to reduce the electrical contact resistance of MWCNT-Cu oxide interfaces by as much as 90%, which would render it of interest for CNT interconnects and possibly even graphene-based electronic devices. The attachment strength of PyprPA coupled MWCNT forest-Cu oxide interfaces was measured through a tensile failure mode to be 290-390 kPa, of the same order as Au diffusion bonded CNT TIMs.[7]

A.1.1 Pyrenylpropyl Phosphonic Acid

The phosphonic acid was synthesized as illustrated in Figure A.1 in two steps from 1-(3-iodopropyl)pyrene 1, which was obtained using the method of Gastaldi and

Stien.[22] Iodide 1 was then converted to phosphonate 2 and, with subsequent hydrolysis, to phosphonic acid 3.

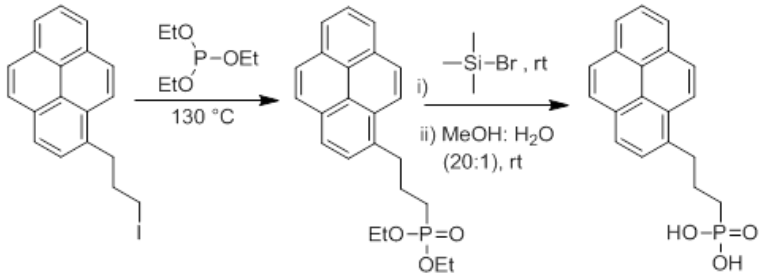

Figure A.1 Synthesis of pyrenylpropyl phosphonic acid. 1 iodide precursor, 2 phosphonate, and 3 phosphonic acid.

A.1.2 Carbon nanotube synthesis

CNT forests were grown on single crystal Si substrates 1×1 cm in size. A trilayer catalyst stack consisting of Ti, Al, and Fe films was first deposited onto the substrates using evaporation in thicknesses of 60, 10, 3 nm respectively. The CNT growth took place in an Aixtron Black Magic© system using a low pressure chemical vapor deposition (CVD) process with H_2, N_2, and C_2H_2 as the feedstock gases at a temperature of 850 °C and pressure of 10 mbar. A growth time of 5 min was used and produced nominally vertically aligned forests of multiwall CNTs approximately 10-15 μm in height with a D/G ratio determined by Raman spectroscopy of approximately 0.85 (Figure A.2). Previous transmission electron microscopy (TEM) characterization performed on CNTs grown by this recipe had an average diameter of 8 nm.[1] CNT forest growth for electrical resistance measurements was performed on 25 μm thick Cu substrates using an identical

process, except 100 nm of Ni was added to the bottom of the catalyst stack as a diffusion barrier.

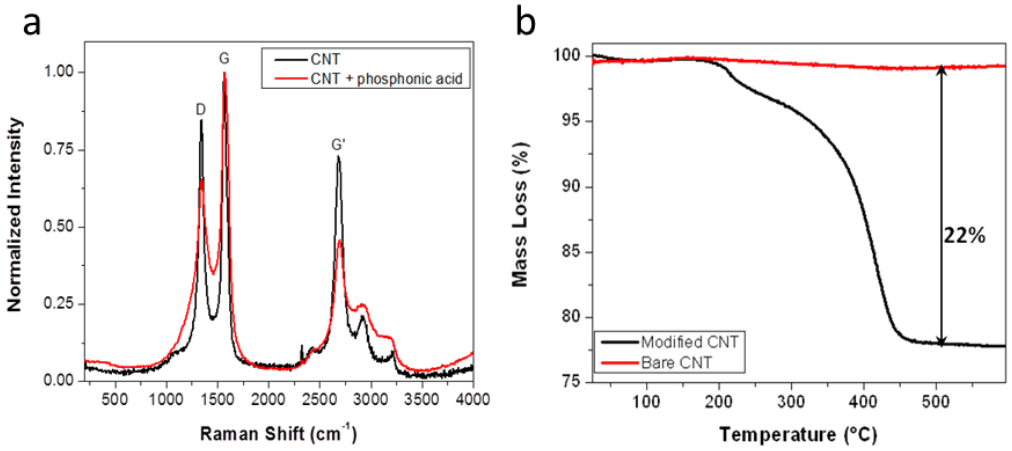

Figure A.1 Raman and TGA. a) Raman spectra of modified and unmodified CNT. b) TGA of modified and unmodified CNT showing 22% mass loss.

A.1.3 Modification of the CNTs

MWCNTs were modified with the PyprPA using a protocol similar to that outlined by Simmons et al.[23] CNT (10 mg) was added to 50 mL of DI water and ultrasonicated for 4 h before a phosphonic acid solution (1.5 mM, in methanol) was added and the mixture stirred overnight. Several centrifugation/wash cycles in DI water was undertaken to remove the excess phosphonic acid after which the modified tubes were dried in a vacuum oven at 80 °C. Prior to annealing in the oven, the degree of removal of the excess acid was assessed by monitoring the UV-vis spectra of the PyprPA in the DI water supernatant (Figure A.3). It was observed that after the nine washes, very little acid was removed in subsequent cycles which suggest that the majority of the remaining molecules were directly associated with the CNT.

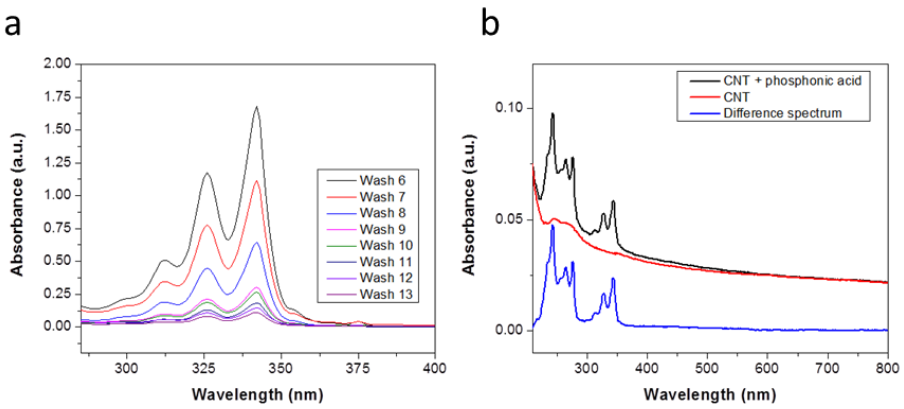

Figure A.2 Modification of CNTs with pyrenylpropyl phosphonic acid. a) Monitoring the supernatant after modification to assess the removal of excess modifier from the CNTs. b) UV-Vis spectra used to approximate the amount of the modifier per micro gram of CNT.

A comparison spectra is shown in Figure A.1.4.

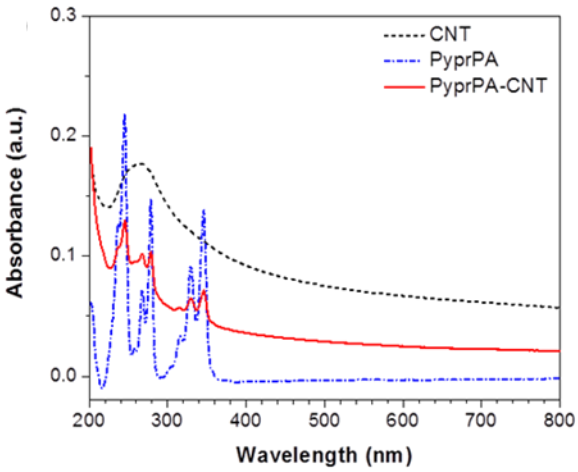

Figure A.3 Comparison of the UV-Vis spectra of the MWCNT, phosphonic acid moiety, and the modified nanotube

In order to approximate the amount of the acid that was bound to the CNTs, calibration curves for both the CNTs and the pyrene modifier were generated using the absorptions at 254 and 344 nm, respectively (Fig. A.3) in 1% sodium dodecyl sulfate. Based on the difference spectrum between the UV-Vis of the modified CNTs and the pristine nanotube the amount of the phosphonic acid per microgram of CNT was found to be 1.2×10^{-4} mol μg^{-1}. A CNT spectrum was chosen such that the absorption within the 600 – 800 nm region closely approximates that of the modified CNT as have been demonstrated elsewhere.[2]

Raman spectroscopy and themogravimetric analysis (TGA) were performed on the CNT-phosphonic acid hybrid. The Raman spectra (Figure. A.2) of the pristine and modified CNTs showed the characteristic bands[3] but no clear shift in the band positions between the modified and unmodified CNTs was observed as reported elsewhere.[4, 5] The TGA showed approximately 22 wt% loss which commenced at around 200 °C indicating relatively good thermal stability.

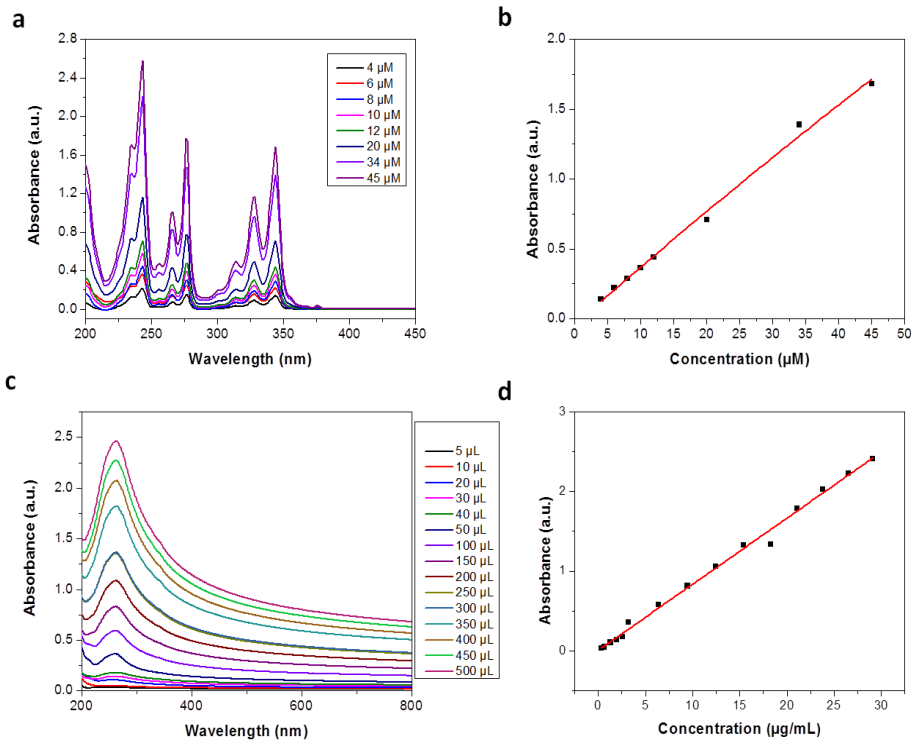

Figure A.4 Calibration curves. a) UV-Vis of various concentration of pyrene-based phosphonic acid. b) calibration curve, of pyrene moiety. c) UV-Vis of various concentration of CNTs. d) calibration curve, of CNTs.

A.1.4 Modification of the copper oxide films with phosphonic acid

Prior to modification, the copper substrates were cleaned by sonicating them consecutively in dilute triton X, DI water and ethanol for 10 min each. The oxide films were then dried under a stream of nitrogen and oxygen plasma etched for 2 min (Plasma Etch-50) before they were immersed in a 1.5 mM solution of the pyrenylpropyl phosphonic acid solution (ethanol:chloroform; 1:1) for 24 h. After modification, the films were sonicated for 30 min in the aforementioned solvent system to remove any physisorbed molecules before they were examined by x-ray photoelectron spectroscopy

(XPS). All XPS measurements were carried out on a Kratos Axis Ultra^{DLD} spectrometer using a monochromatic Al(Kα) source. All the measurements were acquired at normal take-off angle of 0º relative to the surface normal at pass energies of 160 eV and 20 eV for surveys and high resolution data, respectively.

The high resolution spectra of Cu 2p region is shown in Figure A.5 for both the modified and unmodified copper oxide films; peak assignments were consistent with that shown by Barr.[6] An XPS overlay of the modified and unmodified copper is shown in Figure A.6. Presence of the P (2p) peak in the modified substrate indicate successful functionalization of copper.

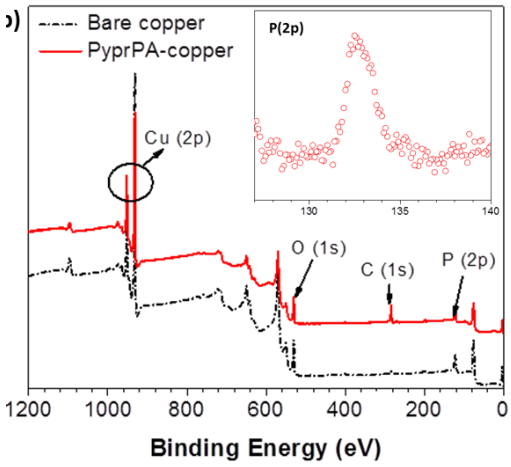

Figure A.5 Modification of copper oxide with phosphonic acid.XPS survey spectra of the modified and unmodified copper substrate. The phosphorus 2p peak is show in the inset.

The surface coverage was approximated by evaluating the degree attenuation of the Cu 2p photoelectrons by the organic overlayer. The attenuation of the Cu (2p) signal (A_{Cu}) is represented by the equation below

$$A_{Cu} = S_{Cu}^{ML}/S_{Cu} = \exp[-d/\lambda_{ML} \sin \theta] \quad \text{(Equation A.1)}$$

where S_{Cu}^{ML} is the signal from the modified surface, S_{Cu} is the signal from the bare Cu substrate, d is the thickness of the monolayer, λ_{ML} is the attenuation length of the copper photoelectrons in the organic layer and θ is the take-off angle between the sample and the detector. The attenuation length was approximated from the inelastic mean free path (IMFP) using the Cumpson method.[7] In this approach the IMFP is determined based on the connectivity and electronic environment of the molecule using a quantitative structure-property relationship model. Subsequently, elastic scattering is assumed to be negligible therefore IMFP ~ λ_{ML}. Using this approach, the thickness of the monolayer was found to be 10.35 ± 0.34 Å. Theoretical calculations on the Hartree-Fock optimized molecular structure (basis set 6-31 G) suggest that for a monolayer coverage the maximum thickness should be about 13.62 Å (Fig. A.5b).

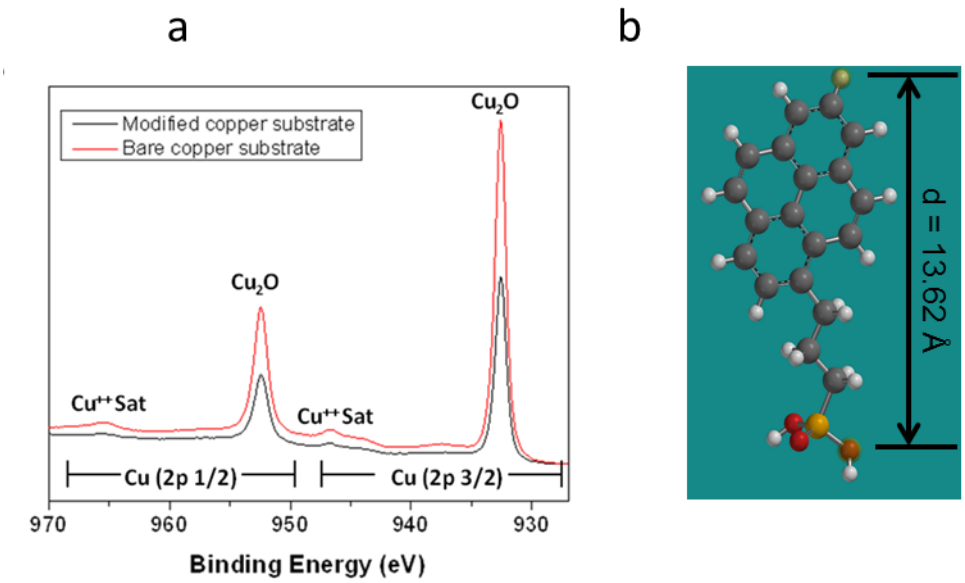

Figure A.6 Assessment of coverage. a) High resolution spectra of the Cu 2p region which shows the attenuation of the signal upon modification with the phosphonic acid. b) optimized geometry (Hartree-Fock, basis set 6-31 G) in which the molecular length is estimated to be 13.62 Å

A.1.5 Thermal Characterization

For thermal characterization the PyprPA modifier was used to couple the free tips of vertical multiwall MWCNT forests, roughly 15 µm in height with an average tube diameter of 8 nm (Figure A.8a) to 300 nm thick Cu films evaporated on 25 µm Ag foil substrates (Alfa Aesar 11498). A surface oxide layer was established on the Cu films as described in the Methods to facilitate experimental control,

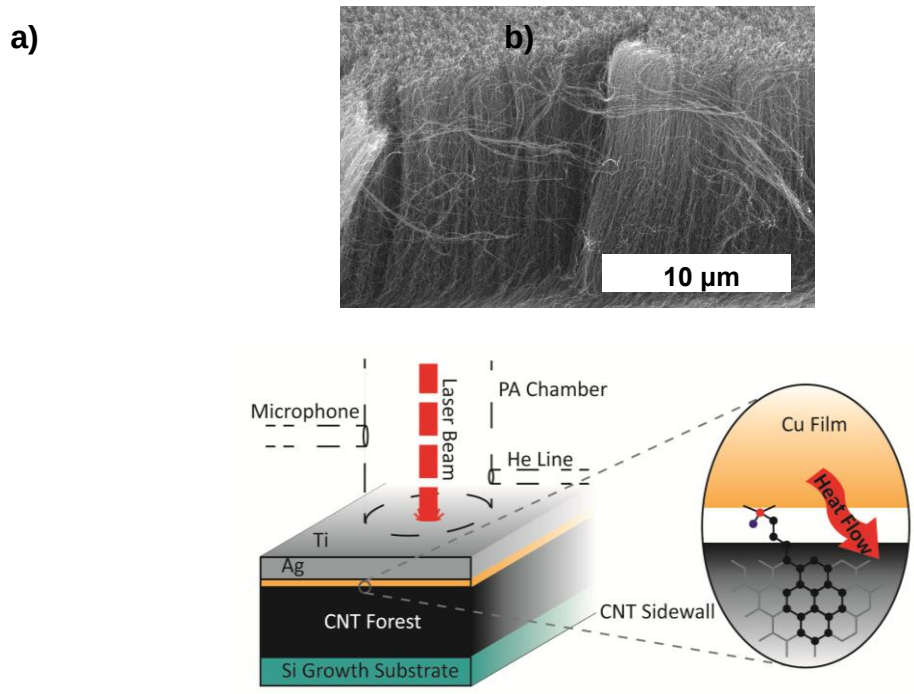

FigureA.7 Sample and photoacoustic measurement configuration. a) Representative scanning electron micrograph of a MWCNT forest used for PyprPA interface coupling. b) Photoacoustic measurement configuration (left) used to measure the thermal resistance of MWCNT forests coupled to oxidized Cu surfaces with the PyprPA modifier (right).

although the native oxide layer may be sufficient for the coupling process. The final sample configuration for thermal measurements can be seen in Figure A.8b. The thermal resistance of both MWCNT forests coupled with the PyprPA and those in dry contact with oxidized Cu films was measured using a photoacoustic (PA) technique. The PA technique is a nondestructive method for measuring the thermal conductivity of materials, including thin films, and the thermal resistance of interfaces. An overview of the technique and the underlying theory has been reported previously[3, 25] .

A.1.6 Photoacoustic characterization

The PA technique is a nondestructive method for measuring the thermal conductivity of materials, including thin films, and the thermal resistance of interfaces. An overview of the technique and the underlying theory has been previously reported by Wang and Hu.[8, 9] In brief, a modulated cw laser (λ=1100 nm) is used to periodically heat the sample's surface. Upon absorption, the heat flows both downward through the sample and into a layer of He gas contained in a sealed chamber above the sample. The periodic nature of the heating causes periodic pressure fluctuations in the He gas layer that are detected using a microphone embedded in the chamber wall. The phase of the microphone signal relative to heating pulse is extracted using lock-in amplification over a range of modulation frequencies to thermally profile the sample from bottom to top. The phase vs. frequency data are used to adjust unknown thermal properties in a theoretical model, which is based on 1D heat flow through layered media, and fit the model to the data. In this work it is used to extract the total resistance of the interface, the details of which are now discussed.

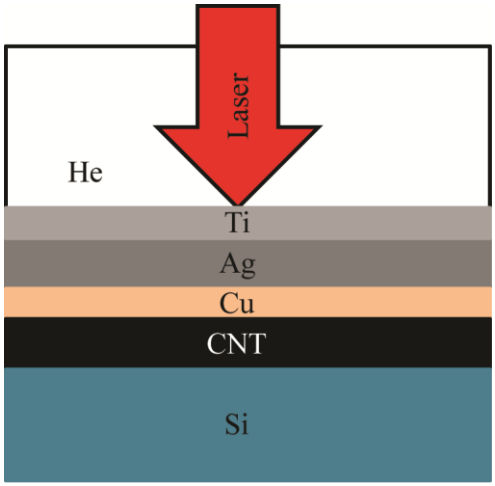

Figure A.8 Sample geometry for photoacoustic data analysis.

The steady state periodic heat flow through each layer of the sample structure (Figure A.9) is described by a one dimensional heat diffusion equation (HDE) with heat generation due to laser absorption is given by the equation below :

$$\frac{\partial^2 \theta_i}{\partial x^2} = \frac{1}{\alpha_i}\frac{\partial \theta_i}{\partial t} - Q^{\circ}_{laser,i}(x)e^{j\omega t} \qquad \text{(Equation A.2)}$$

where, θ is the temperature rise, α is the thermal diffusivity, Q°_{laser} is a group of parameters accounting for the heat generation to laser absorption, ω is the angular frequency of laser modulation, and *i* is the layer index. Since the top Ti layer is more than 3 times thicker than its absorption length effectively all of the laser energy will be absorbed in the Ti layer. The HDE for each layer is coupled through continuity of heat flux and temperature discontinuity, due to contact resistance, conditions at each boundary:

$$k_i \frac{\partial \theta_i}{\partial x} = k_{i+1}\frac{\partial \theta_{i+1}}{\partial x} \qquad \text{(Equation A.3)}$$

$$k_i \frac{\partial \theta_i}{\partial x} - \frac{1}{R_{i,i+1}}(\theta_i - \theta_{i+1}) = 0 \qquad \text{(Equation A. 4)}$$

where, *k* is thermal conductivity, and $R_{i,i+1}$is the contact resistance between layers *i* and *i+1*. In the data fitting process all thermophysical and optical properties for the Ti, Ag, Cu, and Si layers are considered to be known, taken from references[10, 11], and are fixed. The fitting parameters are k_{CNT}, α_{CNT}, and the thickness of the CNT layer (l_{CNT}), in

addition to the contact resistances of the Ti-Ag, Ag-Cu, Cu-CNT, and CNT-Si interfaces. Data fitting is conducted using a non-linear least squares (Levenberg-Marquardt) algorithm.[12] The initial guess values and bounds for each of the fitting parameters are given in Table A2 below. To further ensure that the algorithm converges to a global minimum each fitting parameter is separately varied by 5, 20, 500, and 2,000% to create four additional sets of guess values. Since there are seven fitting parameters in this work the data is fit to 28 additional sets of guess values. The data fitting procedure is used to extract the total resistance of the interface, comprised of the sum of the contact resistances of the Cu-CNT and CNT-Si interfaces and the resistance of the CNT layer. Due to the large number of fitting parameters for the sample structure the confidence interval is too large to meaningfully resolve properties on an individual basis. It is worth noting that the Cu oxide layer is only a native layer on the surface of the Cu film, therefore its thickness is on the order of a few nm and the thermal resistance of the layer can be lumped into the Cu-CNT contact resistance without a significant loss in accuracy.

Table A.2 Initial guess value and bounds for fitting parameters.

	α_{CNT} [m^2/s]	k_{CNT} [W/m-K]	l_{CNT} [μm]	$R_{Ti\text{-}Ag}$ [mm^2-K/W]	$R_{Ag\text{-}Cu}$[1] [mm^2-K/W]	$R_{Cu\text{-}CNT}$ [mm^2-K/W]	$R_{CNT\text{-}Si}$ [mm^2-K/W]
Guess	$1.3\cdot10^{-5}$	10	12	$1.0\cdot10^{-3}$	$1.0\cdot10^{-2}$	3	1
Min.	$3.0\cdot10^{-7}$	1	8	$1.0\cdot10^{-5}$	$1.0\cdot10^{-4}$	0.01	0.01
Max.	$1.3\cdot10^{-3}$	500	15	0.5	1	1000	1000

[1] A 80nm layer of Ti was deposited between the Ag and Cu to promote adhesion and was lumped into the Ag-Cu interface resistance in the model. Due to this fact the initial guess value and bounds for the Ag-Cu interface are larger than for the Ti-Ag interface.

The base pressure in the PA acoustic chamber, located immediately above the sample surface (Figure. A8), can be altered to examine the thermal resistance of the sample as a function of the pressure applied to it. PA tests were conducted at cell pressures of 7 kPa, a slight positive pressure to ensure that the chamber was filled with helium, and 138 kPa, to apply modest pressure to the interface. Five samples treated with the PyprPA modifier were prepared and PA tests were conducted at 3-4 different locations on each sample, providing 16 total measurements. Similarly, four dry contact samples were prepared and measurements were taken at 2-3 different locations on each sample, providing 11 total measurements. The beam diameter at the sample surface was approximately 1 mm and the surface area of each sample was 1 cm^2. By testing 2-4 different locations on the surface of each sample the efficacy of the coupling procedure over device-sized areas was examined. The total thermal resistance, comprised of the sum of the contact resistance at the MWCNT tip-Cu interface, the resistance of the MWCNT forest, and the contact resistance at the MWCNT-Si growth substrate interface, for both sample configurations and both PA chamber pressures is displayed in Fig. A10. The error in the measurement has contributions from both the resolution of the experimental setup and variations in thermal resistance from sample to sample.

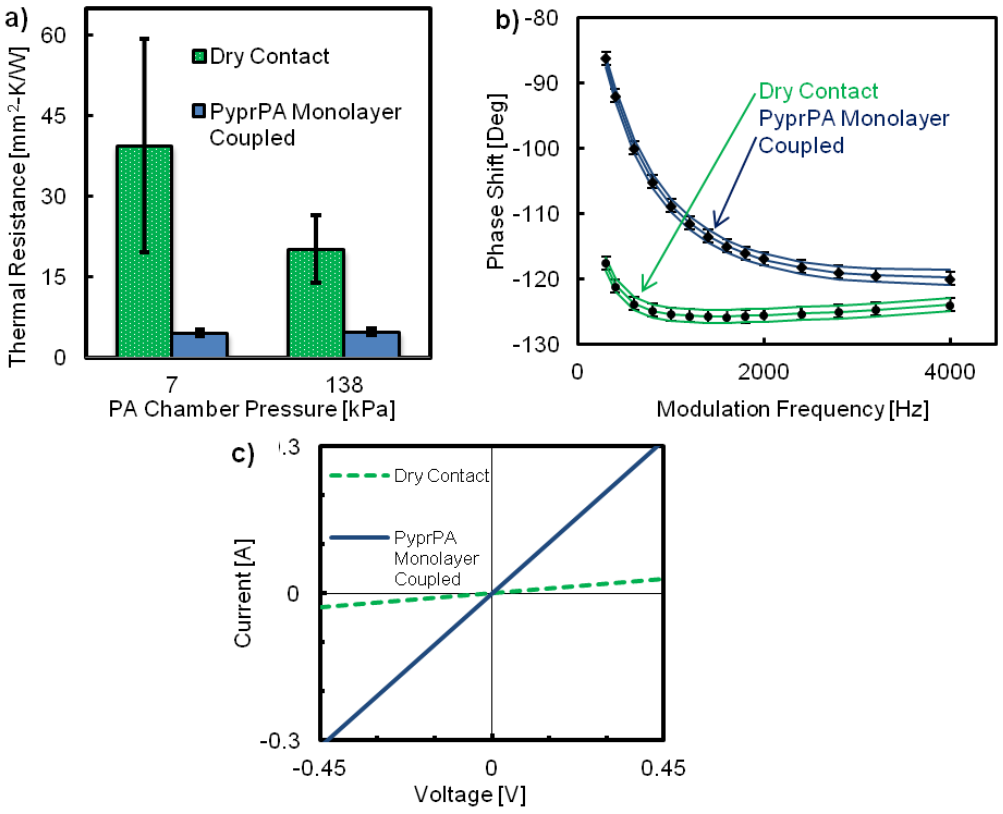

Figure A.9 Photoacoustic characterization of MWCNT forests in dry contact and PyprPA coupled configurations. a) Coupling the MWCNT tip interface with the PyprPA modifier reduces the thermal resistance of the interface material by 85-75% on average and alleviates the pressure dependence. Error bars include measurement uncertainty and variations in thermal resistance from multiple measured samples. b) A representative photoacoustic measurement data set for a PyprPA coupled MWCNT forest, including theoretical curve fits to the data and to data sets shifted by the measurement uncertainty of ± 1 degrees (solid lines). c) Coupling the MWCNT tip interface with the PyprPA modifier may reduce the electrical resistance of the interface material by up to 90%.

The total thermal resistance of the dry contact samples was measured to be 40 ± 20 and 20 ± 6 mm^2 K W^{-1} at pressures of 7 and 138 kPa, respectively. Analogous trends have been observed in previous studies[6, 26] and were analyzed theoretically by Cola et al.[27] In essence, increasing the pressure applied to the interface compresses the MWCNT forest and brings additional MWCNTs into contact with the Cu surface in

addition to increasing the contact length of MWCNTs already in contact with the surface. The net effect is an increase in the contact area, or the area available for heat conduction, resulting in a decrease in the thermal contact resistance.

The total thermal resistance of the samples coupled with a monolayer of the PyprPA modifier using the procedure outlined in Methods was measured to be 4.6 ± 0.5 and 4.9 ± 0.5 mm^2 K W^{-1} at pressures of 7 and 138 kPa respectively. The PyprPA modification and coupling procedure reduced the thermal resistance of the MWCNT forest by 88%-76% on average. The fact that the thermal resistance of the coupled samples did not exhibit a significant dependence on pressure, over the range considered, suggests that the contact area is constant and that the interface is well bonded. Moreover, the low thermal resistances achieved by coupling were consistent across the entire area of the sample (1 cm^2) demonstrating the strong uniform bonding over device-sized areas. Three additional PyprPA-coupled samples were fabricated in which the PyprPA:CuO was not sonicated prior to coupling this surface to the MWCNT forest. This was done to assess whether steps to attempt to create only a monolayer of PyprPA at the interface were required. The thermal resistance of the samples without sonication prior to MWCNT coupling were measured to be 9 ± 6 and 7 ± 3 mm^2 K W^{-1} at PA chamber pressures of 7 and 138 kPa respectively, which is an approximately 45% increase in the thermal resistance over MWCNT forests coupled to sonicated PyprPA:CuO substrates at 7 kPa. This increase in resistance can be attributed to the disorder and weak bonding associated with multiple layers of PyprPA not removed by the sonication step before coupling the surface to MWCNTs.

For all of the aforementioned MWCNT-PyprPA:CuO samples the MWCNT forest was wet with a few drops of solvent and subsequently dried during the coupling process. It has been previously suggested that capillary forces present during the drying process may drive MWCNTs towards the PyprPA:CuO surface and enhance the contact area.[12] To elucidate the role of solvent in the MWCNT-PyprPA:CuO coupling process two additional sample types were fabricated. For the first type (PyprPA-only) the sample was fabricated following the same PyprPA:CuO-sonication-MWCNT coupling procedure except no solvent was dripped onto the top of the MWCNT forest to wet the interface beforehand. For the second type (solvent-only) the CuO film was not modified with PyprPA prior to the coupling process. The thermal resistance of two PyprPA-only samples was measured to be 9 ± 4 and 8 ± 2 $mm^2 KW^{-1}$ at 7 and 138 kPa, respectively. Likewise, two solvent-only samples were prepared and the thermal resistance was measured to be 7 ± 2 $mm^2 KW^{-1}$ at 7 kPa and 7 ± 1 $mm^2 KW^{-1}$ at 138 kPa the first time each sample was characterized using PA. However, the MWCNT-CuO interface was observed to be very weakly adhered. As such, when the solvent-only samples were removed and reinserted into the PA setup to measure the thermal resistance at a different location on the sample the MWCNT-CuO interface delaminated and the thermal resistance was measured to increase. After full delamination of the MWCNT-CuO interface the thermal resistance was measured to be approximately 19 ± 1 and 11 ± 1 $mm^2 KW^{-1}$ at 7 and 138 kPa respectively.

The exact contributions of the PypPA modifier and solvent cannot be resolved from these results; however it is clear that both the solvent and PyprPA modifier play significant and different roles in decreasing the thermal resistance of the interface. For the

PyprPA-only samples the thermal resistance was roughly 22% reduced from the dry contact samples at 7 kPa. This demonstrates a significant benefit to having stronger covalent interactions between the phosphonic acid and the Cu oxide and π-π stacking interactions between the pyrenyl group and the MWCNT forest mediated by the PyprPA modifier, as compared to only having van der Waals interactions in the dry contact arrangement. The notion that interfacial heat transfer can be enhanced by improving the strength of bonding at the interface is well accepted,[27, 28] although it has only recently been observed for surface modifiers experimentally.[29] It should however be noted that without direct knowledge of the contact area at the interface it remains unclear if the reduction in thermal resistance of the PyprPA-only samples can be entirely attributed to enhanced bond strength as a result of the modifier. For the solvent-only interfaces the thermal resistance was 18% less than dry contact samples at 7 kPa before delamination occurred. This suggests that capillary forces during the drying process do in fact pull MWCNTs towards the CuO surface and considerably increase the contact area. It is unlikely that the solvent influences thermal transport within the CNT forest in a manner that would significantly reduce the total thermal resistance, especially for forests as short as the ones used in this study, as several prior studies have shown that the total thermal resistance of CNT interfaces is dominated by the contact resistances.[1-3] After routine handling the van der Waals bonded MWCNT-CuO interface of the solvent-only samples delaminated causing the thermal resistance of the samples to increase, whereas all samples coupled with the PyprPA remained adhered further demonstrating the benefit of the stronger covalent and π-π bonding present with the modifier.

A.1.7 Thermal Stability, Attachment Strength, and Electrical Characterization

To further assess the utility of the MWCNT-PyprPA:CuO system for thermal and electrical applications the attachment strength and current-voltage characteristics of MWCNT-PyprPA:CuO interfaces were examined. The attachment strength of the PyprPA coupled samples used in PA tests (3 total) was measured through a tension failure mode (Figure A11) to be 340 ± 50 kPa, which is of similar order to the strength of Au-Au diffusion bonded MWCNT forest interfaces.[7] All samples failed at the PyprPA:CuO interface and no appreciable differences in attachment strength were observed between all three PyprPA coupled interface configurations (*i.e.*, solvent, with and without sonication, and dry coupled interfaces). Samples for current-voltage scans were fabricated by growing MWCNTs on electrically conductive Cu substrates and coupling them to PyprPA:CuO films.

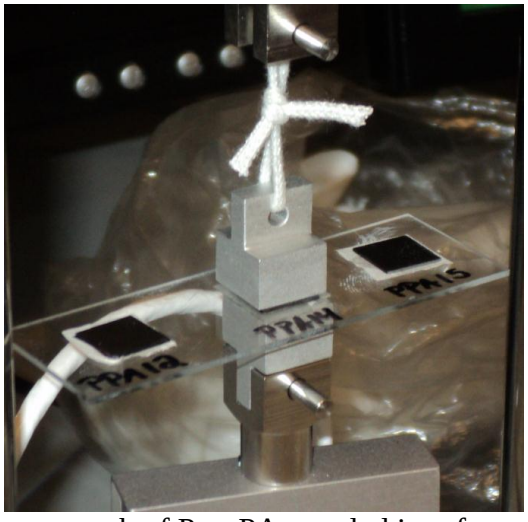

Figure A.6.10 Attachment strength of PyprPA coupled interfaces was measured through a tensile failure mode to be 340 ± 50 kPa.

Current-voltage scans were conducted using a 2-probe technique by contacting the Cu growth substrate and modified Cu surface (Figure A.11). As such the measurement includes contributions from the oxidized Cu film, MWCNT forest, Cu growth substrate and all intermediate interfaces; hence, it is not meaningful to extract the resistance from this data. Furthermore, the measurement is sensitive to the separation distance between the probes and the pressure applied to them. Care was taken to place the probes as consistently as possible; however, it was not precisely controlled. Coupling the MWCNT tip sidewall interface with a monolayer of PyprPA reduced the total electrical resistance by approximately 90% over dry contact. The reduction in electrical resistance was approximately 85% for samples that were not sonicated to facilitate the presence of a monolayer of PyprPA in the interface (Figure A.12).

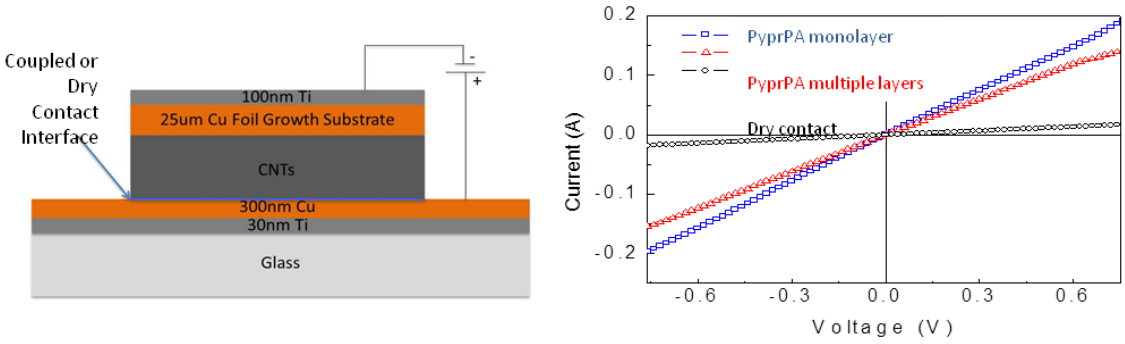

Figure A.11 PyprPA coupling of interfaces may reduce the electrical resistance by approximately 90% over interfaces in dry contact.

All PyprPA coupled interfaces displayed a linear relationship, suggestive of ohmic behavior, over the scan range from -0.45 to +0.45 V as shown in Figgure A.10c and therefore might be useful for CNT interconnects.

A.2 Conclusions

In summary, we have synthesized a pyrene-propyl phosphonic acid modifier for coupling CNTs to metal oxide surfaces in a simple and scalable manner to reduce the thermal contact resistance. When used to couple vertical MWCNT forests to oxidized Cu surfaces the PyprPA modifier reduced the thermal contact resistance by approximately 9-fold over MWCNT forests in non-bonded dry contact. As a thermal interface material PyprPA coupled MWCNT forests had a thermal resistance of 4.6 ± 0.5 mm^2 K W^{-1}, which is on par with the resistance of conventional thin-film metallic solders.[14] Electrical characterization of PyprPA coupled and dry contact CNT interfaces indicate that the modifier may reduce the electrical contact resistance by a similar magnitude. The results of this work suggests that surface modifiers such as the one synthesized here could be used with relatively simple and repeatable processing steps to reduce contact resistances in CNT based architectures for thermal and electrical transport.

A.3 Experimental

A.3.1 Pyrenylpropyl phosphonic acid synthesis:

The phosphonic acid was synthesized over two steps from 1- (3-iododpropyl)pyrene which was obtained using the method of Gastaldi and Stien[22]. The iodide (1.35 g, 3.65 mmol) was heated with triethylphosphite (1.82 g, 10.94 mmol) at 130 °C overnight. Excess triethylphosphite and other volatiles were removed under vacuum (approximately 20 mTorr) with heating (100 °C) to give waxy solid (798 mg, 57% yield). ^{1}H-NMR (300 MHz, $CDCl_3$): δ 8.27 (d, *J* = 9 Hz, 1H), 7.97-8.18 (m, 7H), 7.86 (d, *J* = 89 Hz, 1H), 4.02-4.13 (m, 4H), 3.45 (t, *J* = 6 Hz, 2H), 2.14-2.23 (m, 2H), 1.88 (m, 2H), 1.29 (t, *J* = 7.5 Hz, 6H).). ^{13}C{^{1}H} NMR (75.5 MHz, $CDCl_3$) δ 135.31, 135.30, 131.38, 130.84, 130.00, 128.69, 127.46, 127.42, 127.33, 126.75, 125.85, 125.07, 124.95, 124.79, 124.78, 123.4, 61.52 (d, *J* = 6.04 Hz), 33.95 (d, *J* = 16 Hz), 25.42 (d, *J* = 145.7 Hz), 24.51, 16.46 (d, *J* = 5.3 Hz). ^{31}P{^{1}H} NMR (162 MHz, $CDCl_3$) δ 32.6. Anal. Calcd for $C_{23}H_{25}O_3P$: C, 72.62; H, 6.62. Found: C, 72.36; H, 6.76. HRMS (m/z) $[M]^+$ Calcd for $C_{23}H_{25}O_3P$: 380.1534. Found, 380.1541. The phosphonic acid was obtained by dissolving the phosphonate (0.38 g, 1 mmol) in dry dichloromethane and adding bromotrimethylsilane (0.46 g, 3 mmol) dropwise. The solution was stirred overnight. The volatiles were then removed by rotary evaporation after which a methanol: water solution (20:1) was added to the residue and the contents of the flask were stirred overnight. The reaction mixture was then concentrated by rotary evaporation to give a solid. The solid was washed with methanol and dried under vacuum to give an off-white powder (144 mg, 44% yield). ^{1}H-NMR (300 MHz, DMSO): δ 8.37 (d, *J* = 9 Hz, 1H), 8.02-8.28 (m, 7H), 7.94 (d, *J* = 9 Hz, 1H), 3.40(t, J = 7.5 Hz, 2H), 3.37-3.41(m, 2H), 1.66 (p, *J* = 9Hz,

2H). ^{13}C {^{1}H} NMR (75.5 MHz, DMSO): δ 136.44, 130.90, 130.42, 129.32, 128.16, 127.65, 127.47, 127.26, 126.54, 126.15, 124.96, 124.93, 124.81, 124.24, 124.15, 123.55, 33.3 (d, *J* = 16 Hz), 27.41 (d, *J* = 140 Hz), 25.63 (d, *J* = 4.5 Hz). ^{31}P{^{1}H} NMR (162 MHz, DMSO): δ 27.91. Anal. Calcd for $C_{19}H_{17}O_3P$: C, 70.37; H 5.28. Found: 70.63; 5.26. HRMS (m/z): $[M]^+$ calcd for $C_{19}H_{17}O_3P$: 324.0915; found, 324.0915.

A.3.2 Interface coupling procedure

Before modification took place the as-evaporated Cu films were exposed to an O_2 plasma at 200 mTorr pressure for 2 min to facilitate formation of a consistent surface oxide layer. Upon removal from the plasma chamber the Cu films were immediately placed in a 1.5 mM solution of the PyprPA modifier in ethanol:chloroform (1:1). The Cu films were soaked for 1-12 days, during which time the modification took place. The minimum soak time required to form a monolayer was not explored. For coupling the MWCNT forests, the PyprPA-modified Cu oxide film (PyprPA:CuO) was removed from the PyprPA solution and sonicated in a solution of ethanol:chloroform (1:1) for 5 min to remove excess PyprPA with the intent of leaving only a monolayer covalently bonded to the Cu oxide surface. The top of the MWCNT forest was then wetted with a few droplets of ethanol:chloroform (1:1) and the PyprPA:CuO film was placed onto the wet forest. 300 kPa of pressure was applied to the still wet interface and it was allowed to dry for at least 5 hours at room temperature.

A.3.3 Current-voltage scans

The current-voltage characteristics of PyprPA modified interfaces were assessed using a 2-probe technique. To create electrical contact CNTs were grown on conductive 25 μm thick Cu substrates (Alfa Aesar 13382). Ni, Ti, Al, Fe films were evaporated onto

the Cu substrates in thicknesses of 100, 30, 10, 3 nm respectively as a catalyst stack and CNTs were grown using the same low pressure CVD process described above. PyprPA modification of the CNT-Cu oxide interface was identical to the procedure used to prepare samples for photoacoustic testing. Contact was made to the Ti coated backside of the Cu growth substrate and to the extended portion of the Cu oxide film. The scan was conducted from -0.6 to +0.6 V and for PyprPA coupled interfaces revealed a linear relationship with current, indicative of ohmic behavior. Coupling of the interface with a monolayer of the PyprPA modifier reduced the electrical resistance of the interface by roughly 90% over dry contact interfaces, while coupling with multiple physisorbed layers decreased the resistance by roughly 85% (Figure A 10).

A.4 Literature cited

[1] X. J. Hu, A. A. Padilla, J. Xu, T. S. Fisher, K. E. Goodson, *J. Heat Transfer* **2006**, *128*, 1109.

[2] T. Tong, Y. Zhao, L. Delzeit, A. Kashani, M. Meyyappan, A. Majumdar, *IEEE Trans. Compon. Packag. Technol.* **2007**, *30*, 92.

[3] B. A. Cola, J. Xu, C. R. Cheng, X. F. Xu, T. S. Fisher, H. P. Hu, *J. Appl. Phys.* **2007**, *101*.

[4] M. A. Panzer, H. M. Duong, J. Okawa, J. Shiomi, B. L. Wardle, S. Maruyama, K. E. Goodson, *Nano Lett.* **2010**, *10*, 2395.

[5] W. Lin, R. W. Zhang, K. S. Moon, C. P. Wong, *Carbon* **2010**, *48*, 107.

[6] A. Hamdan, J. Cho, R. Johnson, J. Jiao, D. Bahr, R. Richards, C. Richards, *Nanotechnology* **2010**, *21*.

[7] R. Cross, B. A. Cola, T. Fisher, X. F. Xu, K. Gall, S. Graham, *Nanotechnology* **2010**, *21*.

[8] S. L. Hodson, T. Bhuvana, B. A. Cola, X. F. Xu, G. U. Kulkarni, T. S. Fisher, *J. Electon. Packag.* **2011**, *133*.

[9] J. R. Wasniewski, D. H. Altman, S. L. Hodson, T. S. Fisher, A. Bulusu, S. Graham, B. A. Cola, *J. Electon. Packag.* **2012**, *134*.

[10] Y. X. Ni, H. L. Khanh, Y. Chalopin, J. B. Bai, P. Lebarny, L. Divay, S. Volz, *Appl. Phys. Lett.* **2012**, *100*.

[11] M. T. Barako, Y. Gao, A. M. Marconnet, M. Asheghi, K. E. Goodson, in *13th Ieee ITherm*, San Diego, **2012**, pp. 1225.

[12] J. H. Taphouse, T. L. Bougher, V. Singh, P. P. Abadi, S. Graham, B. A. Cola, *Nanotechnology* **2013**, *24*, 105401.

[13] J. K. Yang, Y. Yang, S. W. Waltermire, T. Gutu, A. A. Zinn, T. T. Xu, Y. F. Chen, D. Y. Li, *Small* **2011**, *7*, 2334.

[14] D. D. L. Chung, *Appl. Therm. Eng.* **2001**, *21*, 1593.

[15] S. G. Stepanian, V. A. Karachevtsev, A. Y. Glamazda, U. Dettlaff-Weglikowska, L. Adamowicz, *Mol. Phys.* **2003**, *101*, 2609.

[16] Q. Yang, L. Shuai, J. Zhou, F. C. Lu, X. J. Pan, *J. Phys. Chem. B* **2008**, *112*, 12934.

[17] P. H. Mutin, G. Guerrero, A. Vioux, *Comptes Rendus Chimie* **2003**, *6*, 1153.

[18] P. H. Mutin, G. Guerrero, A. Vioux, *J. Mater. Chem.* **2005**, *15*, 3761.

[19] P. Kim, N. M. Doss, J. P. Tillotson, P. J. Hotchkiss, M. J. Pan, S. R. Marder, J. Y. Li, J. P. Calame, J. W. Perry, *Acs Nano* **2009**, *3*, 2581.

[20] P. J. Hotchkiss, M. Malicki, A. J. Giordano, N. R. Armstrong, S. R. Marder, *J. Mater. Chem.* **2011**, *21*, 3107.

[21] S. A. Paniagua, P. J. Hotchkiss, S. C. Jones, S. R. Marder, A. Mudalige, F. S. Marrikar, J. E. Pemberton, N. R. Armstrong, *J. Phys. Chem. C.* **2008**, *112*, 7809.

[22] S. Gastaldi, D. Stien, *Tetrahedron Letters* **2002**, *43*, 4309.

[23] T. J. Simmons, J. Bult, D. P. Hashim, R. J. Linhardt, P. M. Ajayan, *Acs Nano* **2009**, *3*, 865.

[24] X. Wallart, C. H. de Villeneuve, P. Allongue, *J. Am. Chem. Soc.* **2005**, *127*, 7871.

[25] H. P. Hu, X. W. Wang, X. F. Xu, *J. Appl. Phys.* **1999**, *86*, 3953.

[26] B. A. Cola, X. F. Xu, T. S. Fisher, *Appl. Phys. Lett.* **2007**, *90*.

[27] B. A. Cola, J. Xu, T. S. Fisher, *Int. J. Heat Mass Transfer* **2009**, *52*, 3490.

[28] R. Prasher, *Appl. Phys. Lett.* **2009**, *94*, 041905.

[29] M. D. Losego, M. E. Grady, N. R. Sottos, D. G. Cahill, P. V. Braun, *Nat. Mater.* **2012**, *11*, 502.

[30] R. Prasher, *Proc. IEEE* **2006**, *94*, 1571.